Technology Collaboration Programme
by iea

SAND2021-4835R

International Energy Agency
Photovoltaic Power Systems Programme

Task 13 Performance, Operation and Reliability of Photovoltaic Systems

PVPS

Bifacial Photovoltaic Modules and Systems: Experience and Results from International Research and Pilot Applications

2021

Report IEA-PVPS T13-14:2021

Sandia National Laboratories is a multimission laboratory managed and operated by National Technology & Engineering Solutions of Sandia, LLC, a wholly owned subsidiary of Honeywell International Inc., for the U.S. Department of Energy's National Nuclear Security Administration under contract DE-NA0003525.

What is IEA PVPS TCP?

The International Energy Agency (IEA), founded in 1974, is an autonomous body within the framework of the Organization for Economic Cooperation and Development (OECD). The Technology Collaboration Programme (TCP) was created with a belief that the future of energy security and sustainability starts with global collaboration. The programme is made up of 6.000 experts across government, academia, and industry dedicated to advancing common research and the application of specific energy technologies.

The IEA Photovoltaic Power Systems Programme (IEA PVPS) is one of the TCP's within the IEA and was established in 1993. The mission of the programme is to "enhance the international collaborative efforts which facilitate the role of photovoltaic solar energy as a cornerstone in the transition to sustainable energy systems." In order to achieve this, the Programme's participants have undertaken a variety of joint research projects in PV power systems applications. The overall programme is headed by an Executive Committee, comprised of one delegate from each country or organisation member, which designates distinct 'Tasks,' that may be research projects or activity areas.

The IEA PVPS participating countries are Australia, Austria, Belgium, Canada, Chile, China, Denmark, Finland, France, Germany, Israel, Italy, Japan, Korea, Malaysia, Mexico, Morocco, the Netherlands, Norway, Portugal, South Africa, Spain, Sweden, Switzerland, Thailand, Turkey, and the United States of America. The European Commission, Solar Power Europe, the Smart Electric Power Alliance (SEPA), the Solar Energy Industries Association and the Cop- per Alliance are also members.

Visit us at: www.iea-pvps.org

What is IEA PVPS Task 13?

Within the framework of IEA PVPS, Task 13 aims to provide support to market actors working to improve the operation, the reliability and the quality of PV components and systems. Operational data from PV systems in different climate zones compiled within the project will help provide the basis for estimates of the current situation regarding PV reliability and performance.

The general setting of Task 13 provides a common platform to summarize and report on technical aspects affecting the quality, performance, reliability and lifetime of PV systems in a wide variety of environments and applications. By working together across national boundaries we can all take advantage of research and experience from each member country and combine and integrate this knowledge into valuable summaries of best practices and methods for ensuring PV systems perform at their optimum and continue to provide competitive return on investment.

Task 13 has so far managed to create the right framework for the calculations of various parameters that can give an indication of the quality of PV components and systems. The framework is now there and can be used by the industry who has expressed appreciation towards the results included in the high-quality reports.

The IEA PVPS countries participating in Task 13 are Australia, Austria, Belgium, Canada, Chile, China, Denmark, Finland, France, Germany, Israel, Italy, Japan, the Netherlands, Norway, Spain, Sweden, Switzerland, Thailand, and the United States of America.

COVER PICTURE

Bifacial photovoltaic modules at Sandia National Laboratories, Joshua S. Stein

ISBN 978-3-907281-03-1

INTERNATIONAL ENERGY AGENCY

PHOTOVOLTAIC POWER SYSTEMS PROGRAMME

IEA PVPS Task 13

Performance, Operation and Reliability of Photovoltaic Systems

Bifacial Photovoltaic Modules and Systems: Experience and Results from International Research and Pilot Applications

Report IEA-PVPS T13-14:2021

April 2021

ISBN 978-3-907281-03-1

AUTHORS

Main Authors

Joshua S. Stein, Sandia National Laboratories, USA
Christian Reise, Fraunhofer ISE, Freiburg, Germany
Johanna Bonilla Castro, TÜV Rheinland, Cologne, Germany
Gabi Friesen, SUPSI, Switzerland
Giosuè Maugeri, RSE, Italy
Elías Urrejola, ATAMOSTEC, Chile
Samuli Ranta, TUAS, Finland

Contributing Authors

Muhammad A. Alam, Purdue University, USA
Marc Abou Anoma, SunPower Corporation, USA
Silvana Ayala Pelaez, National Renewable Energy Laboratory, USA
Djaber Berrian, ISC Konstanz, Germany
Emmanuelle Bertrand, LABORELEC, Belgium
Matthieu Chiodetti, EDF, France
Dimitrij Chudinzow, University of Stuttgart, Germany
Hervé Colin, INES, France
Ignacia Devoto, ISC Konstanz, Germany
Roger French, Case Western Reserve University, USA
Edward Fuentealba, University of Antofagasta, Chile
Florent Haffner, INES, France
Andreas Halm, ISC Konstanz, Germany
Joan Haysom, J.L. Richards & Associates Limited, Canada
Karin Hinzer, University of Ottawa, Canada
Imre T. Horvath, IMEC, Belgium
Hugo Huerta, TUAS, Finland
M. Ryyan Khan, Purdue University, USA
Markus Klenk, ZHAW, Switzerland
Radovan Kopecek, ISC Konstanz, Germany
Joris Libal, ISC Konstanz, Germany
Mattias Lindh, RISE, Sweden
Bill Marion, National Renewable Energy Laboratory, USA
Mark Mikofski, DNV GL, USA

Ruben Roldan Molinero, SUPSI, Switzerland
Mark Monarch, National Renewable Energy Laboratory, USA
Anja Neubert, DNV GL, Germany
M. Tahir Patel, Purdue University, USA
Anna Malou Petersson, RISE, Sweden
Gizem Nogay Poulin, CSEN, Switzerland
Santhosh Ramesh, IMEC, Belgium
Oume Lgheit Rhazi, EDF, France
Nicholas Riedel-Lyngskær, Fotonik Technical University of Denmark, Denmark
Daniel Riley, Sandia National Laboratories, USA
Annie C.J. Russell, University of Ottawa, Canada
Andreas Schneider, ISC Konstanz, Germany
Cameron T. Stark, Sandia National Laboratories, USA
Tudor Timofte, ISC Konstanz, Germany
Daniel Tune, ISC Konstanz, Germany
Jill Tymchak, J.L. Richards & Associates Limited, Canada
Christopher E. Valdivia, University of Ottawa, Canada
Felipe Valencia, ATAMOSTEC, Chile
Menghong Wang, Case Western Reserve University, USA

Editors

Joshua S. Stein, Sandia National Laboratories, USA
Boris Farnung, VDE Renewables, Germany

TABLE OF CONTENTS

ACKNOWLEDGEMENTS

This paper received valuable contributions from many IEA-PVPS Task 13 members and other international experts. Many thanks to Holly Larsen from Sandia National Laboratories for technical editing and to Sophia Archibeque from Sandia National Laboratories for help organizing and formatting references.

This report is supported by the German Federal Ministry for Economic Affairs and Energy (BMWi) under contracts no. 0324304A and 0324304B and by the Swiss Federal Office of Energy (SFOE) under contract no. SI/501788-01.

Sandia National Laboratories is a multimission laboratory managed and operated by National Technology & Engineering Solutions of Sandia, LLC, a wholly owned subsidiary of Honeywell International Inc., for the U.S. Department of Energy's National Nuclear Security Administration under contract DE-NA0003525.

The authors would like to thank the following people for reviewing this report, Laura Bruckman, Jan Vedde, and Matthias Littwin.

LIST OF ABBREVIATIONS

2P	Two modules stacked in portrait
2D	Two dimensional
3D	Three dimensional
AC	Alternating current
Al-BSF	Aluminum back surface field
AOI	Angle of incidence
ASPIRE	Arctic Solar Photovoltaics: Innovation for Renewable Energy
ATAMOSTEC	Atacama Module and System Technology
BEST	Bifacial Experimental Single Axis Tracking Field
BF	Bifaciality factor
BG	Bifacial gain
BiFi	Bifacial power gain
BSF	Back surface field
BIFOROT	Bifacial outdoor rotor tester
BOS	Balance of system
BSI	Back side irradiance
BSTC	Bifacial standard test conditions
CHARS	Canadian High Arctic Research Station
CoV	Coefficient of variation
DC	Direct current
DCM	Daylight coefficient method
DHI	Diffuse horizontal irradiance
DNI	Direct normal irradiance
DTU	Technical University of Denmark
EDF	Électricité de France
EMPIR	European Metrology Programme for Innovation and Research
EVA	Ethyl vinyl acetate
E-W	East–West
GCR	Ground coverage ratio
GE	Generated energy
GHI	Global horizontal irradiance
GRI	Ground reflected irradiance
Gv-BF	E-W facing ground sculpted vertical bifacial
HIT	Hetero junction with intrinsic thin layer
HJT	Hetero junction
HPC	High performance computing

HSAT	Horizontal single axis tracker
IAM	Incident angle modifier
IBC	Interdigitated back contacted
IDM	Irradiance distribution module
IEA	International Energy Agency
IEC	International Electrotechnical Commission
IMEC	Interuniversity Microelectronics Centre
IMP	Maximum power current
INES	Institut National de l'Énergie Solaire
ISC	International Solar Energy Research Center
ITRPV	International Technology Roadmap for PV
IV	Current and voltage
IWEC	International Weather for Energy Calculation
LCOE	Levelized cost of energy
LeTID	Light and elevated temperature induced degradation
MAE	Mean absolute error
MBE	Mean bias error
MODIS	Moderate resolution imaging spectroradiometer
MPPT	Maximum power point trackers
MPR	Module performance ratio
MQT	Module design qualification testing
MST	Module safety qualification testing
NOAA	National Oceanic and Atmospheric Administration
NREL	National Renewable Energy Laboratory
N-S	North–South
OECD	Organization for Economic Co-operation and Development
NSRDB	National Solar Radiation Database
PERC	Passivated emitter and rear
PERC+	Bifacial version of passivated emitter and rear
PERT	Passivated emitter rear totally diffused
PID	Potential induced degradation
PID-s	Shunting type PID
POA	Plane of array
POE	Polyolefin elastomer
PR	Performance ratio
PSDA	Atacama Desert Solar Platform
PUMET	Purdue University Meteorological Tool
PUB	Purdue University Bifacial Module Calculator

PV	Photovoltaic
PVK	Perovskite
PVPS	Photovoltaic Power Systems Programme
R&D	Research and development
RMD	Relative mean absolute difference
RMSE	Root mean squared error
RSE	Ricerca sul Sistema Energetico
SAM	System Advisor Model
SAT	Single axis tracker
s-BF	South facing optimally tilted and elevated bifacial plant
SQ	Shockley-Queisser
STC	Standard test conditions
SUPSI	University of Applied Sciences and Arts of Southern Switzerland
SURFRAD	Surface Radiation Budget Network
t-BF	East–West tracking bifacial plant
TMY	Typical meteorological year
TNO	Netherlands Organization for Applied Scientific Research
TUAS	Turku University of Applied Sciences
UTC	Coordinated universal time
v-BF	Vertical bifacial
WG2	Working Group 2
WG3	Working Group 3
ZHAW	Zürcher Hochschule für Angewandte Wissenschaften (Zurich University of Applied Sciences)

EXECUTIVE SUMMARY

Bifacial photovoltaic cells, modules, and systems are rapidly overtaking the market share of monofacial PV technologies. This is happening due to new cell designs that have replaced opaque, monolithic back surface foil contacts with isolated contacts, which allow light to reach the cell from the rear side. Minor adjustments to cell processing steps have resulted in bifacial solar cells with rear side efficiencies from >60% to over 90% of the front side. Bifacial cells now come in many varieties (e.g., PERC+, n-PERT, HIT, etc.) and many cell lines have converted to producing bifacial cells.

P-type solar cell limitations are driving the PV industry's attention toward high efficiency n-type solar cells, including n-PERT solar cells, which are promising for two reasons:

- Their process sequence calls for machinery that is generally compatible with current solar cell production lines.
- The n-PERT cell concept permits very high bifaciality, up to 95%

Today, busbar-less heterojunction (HJT) cells fabricated in a pilot-line on mass production equipment can reach efficiencies greater than 24%. With its high efficiency potential and lean manufacturing process flow, HJT cell technology is expected to gain greater global photovoltaic market share in the coming years. Even multijunction designs for bifacial cells are being considered. A multijunction bifacial cell based on a perovskite top cell and silicon HJT bottom cell appears promising.

Bifacial cells have valuable applications in both monofacial and bifacial modules. Placing bifacial cells in a monofacial package with white back encapsulant or a reflective backsheet results in a significant boost to front-side module rating and several companies are investigating this application. However, most bifacial cells end up in bifacial double-glass modules (or bifacial modules with a transparent polymer backsheet). Rating and safety standards are actively being updated to account for differences in the behavior and performance of these modules. A new IEC Technical Specification was released in 2019 (IEC TS 60904-1-2) that guides the measurement of the electrical characteristics of bifacial modules. Additional product certification requirements for bifacial PV modules are mainly related to the higher operating currents of these modules and the associated potential safety issues.

As bifacial modules have been deployed in the field, several bifacial-specific degradation issues have been discovered and are actively being researched. Light and elevated temperature induced degradation (LeTID) can specifically affect PERC cells if a stabilization process during cell manufacturing is not followed. The addition of isolated metal contacts on the rear side of bifacial cells may expedite hydrogen induced degradation processes. Potential induced degradation (PID) results from the migration of ions within the module package. When there is a potential gradient in the module, sodium ions from the glass can migrate to the cell surface and interfere with cell operation at stacking faults. A buildup of ions can also lead to surface passivation loss which results in degraded performance. Use of polyolefin encapsulants largely prevents PID. Double-glass bifacial modules using EVA encapsulant can be more susceptible to PID due to the increased availability of sodium ions from the glass.

Bifacial cell and module innovations have led to new optimized bifacial system designs. The reflectivity of the ground (albedo) is one the most important site characteristics influencing bifacial PV performance. Sites that experience significant snowfall typically benefit from bifa-

cial PV because of the increased albedo during these periods. Bifacial PV performance advantage is expressed as “bifacial gain”, which is the additional fraction of total energy that a bifacial PV system will produce compared with a monofacial system of the same orientation and size. Bifacial gain increases with albedo, diffuse fraction, array height, row spacing, and space between modules. The light received on the rear side of the array is much more nonuniform than light hitting the front. This nonuniformity leads to some electrical mismatch within each module and also can affect strings of modules depending on the configuration. Another characteristic of bifacial arrays is that they operate at higher DC current levels than monofacial arrays; therefore, system designers may need to adjust calculations for wire, fuse, and inverter sizing. International electrical design and safety codes are actively being reviewed to account for bifacial PV technologies.

Bifacial systems come in many forms. Many are nearly identical to monofacial designs such as fixed-tilt and single-axis trackers. Performance gains of bifacial over monofacial for these system designs vary depending on site conditions and system design details. Ground reflectance or albedo and the bifaciality of the modules are generally the most important factors. Bifacial modules on single-axis tracker fields over typical natural ground covers (albedo = 0.2 to 0.3) generally see bifacial gains less than 10%. These values increase significantly when the ground is covered with snow. Other system designs, such as east-west (E-W) vertically orientated arrays, are especially suited to bifacial PV technologies and offer some unique advantages such as a wider period of power generation that better matches typical load profiles, very low soiling rates, and such designs leave much of the land available for other uses, such as livestock. In addition, vertical bifacial PV has performance advantage at high latitudes due to the large variation in solar azimuth angle during the summer. In all cases, bifacial modules near the edge of rows will receive an extra amount of light due to the fact that there are fewer nearby modules and structures that shade the nearby ground. Such “edge effects” can be especially important for smaller arrays or arrays that are separated from one another. For example, elevated parking structures, fixed-tilt arrays on flat white roofs, and vertical sound barriers all benefit from the additional energy available near the edge of the array. Despite this benefit, economies of scale are also important. A recently published global analysis of bifacial PV economics determined that bifacial PV installed on single-axis trackers resulted in the lowest levelized cost of electricity for the vast majority of potential PV sites on the planet (93% of the Earth’s land area) [1].

A survey of field performance measurements from 27 different bifacial PV test systems compared bifacial gains with an array of design and site parameters and found that none of the parameters alone correlated well with the bifacial gain. A major limitation of small bifacial research systems is that their performance is dominated by “edge effects” or the increased light that reaches the back of the array due to the lack of adjacent modules and rows that for large systems result in less light reaching the array. Therefore, one should not expect the same performance measured on a small system when planning for a larger system. Instead comprehensive performance models are required to understand these relationships. These models differ primarily in how they calculate the amount of light that reaches the rear side of the array. There are two main types of bifacial models: (1) models based on view factors and (2) models that use ray-tracing. View factor models are less numerically expensive and generally assume infinitely long rows due to their two-dimensional formulations. As such view factor models are unable to represent detailed geometries. For detailed evaluations, ray-tracing models are recommended despite the computational challenges.

A bifacial PV modelling comparison was organized to evaluate the state of the art of bifacial PV performance models. Four hypothetical system designs and two designs based on field measurements were defined and the necessary input parameters and weather files were

provided to volunteers from 13 different research and commercial entities, each with their own bifacial PV performance model. These models are described in detail in this report. The comparison showed that the current bifacial models result in a range of results, with some models being unable to simulate all of the scenarios. The resulting predicted bifacial gains varied by as much as a factor of two. This exercise demonstrated the value of defining standard test cases to verify and validate bifacial performance models.

The last section of this report provides a summary of eleven bifacial field test sites around the world along with examples of field results. Many of these sites include a variety of bifacial test arrays with different orientations, designs, and site conditions. Many test labs are experimenting with enhancing albedo using white rocks or reflective cloths. These tests have been instrumental in validating performance models and better understanding the important role of albedo in bifacial performance. Measured bifacial gains from fixed tilt sites from sites in the US and France demonstrate how bifacial gains vary with season due to the changing sun path, with the highest gains in the summer when the solar elevation reaches it maximum. In the winter, the lower solar elevation angles result in more of the ground being covered in shadows and less light reaches the rear side of the array.

1 INTRODUCTION

Bifacial photovoltaic cell and module technologies are rapidly increasing their market shares. The International Technology Roadmap for Photovoltaic (ITRPV) 2019 Results [2] notes that as of 2020 bifacial cells account for about 20% of the total world PV cell market. By 2030, it is predicted that this share will increase to 70%. For bifacial PV modules, the market share for 2020 stands at about 12% and is predicted to increase to about 30% by 2030. This means that it is possible that much of the future bifacial cell production will be used in monofacial modules paired with white back encapsulant and/or reflective backsheets to enhance front side power rating.

Currently there are a number of active research teams around the world studying bifacial module and system performance in order to optimize the design of these technologies and lower the levelized cost of electricity (LCOE). A recent study examined which type of PV system design resulted in the minimum LCOE for sites across the globe [1]. It determined that bifacial modules on horizontal single-axis trackers (HSAT) were the optimal design for 93% of the Earth's land area. Monofacial HSAT systems were the lowest LCOE for only 3.1% of the land area. For 3.8% of the land area at latitudes >70°, bifacial modules on two-axis trackers have had the lowest LCOE. If this trend holds for the next decade, it is likely that the proportion of bifacial to monofacial modules may exceed the current predictions.

In order for bifacial modules and systems to succeed in the marketplace, a robust set of industry standards for rating, characterization, and safety need to be developed. Accurate models of module and system performance are required and need to be validated. Development and testing of new materials required for bifacial module designs must be conducted. Studies of field performance and reliability need to be conducted. This report is an international compilation of current knowledge about bifacial PV cells, modules, systems, and models.

Chapter 2 reviews the variety of bifacial PV cells that are available today. Chapter 3 covers bifacial modules, including test standards, certification, and bifacial-specific cell and module degradation issues. Chapter 4 discusses bifacial systems and includes subsections on albedo, bifacial gain, nonuniform rear-side irradiance, elevated DC current from bifacial systems, fixed tilt systems, single-axis tracked systems, and a global overview of optimal bifacial system designs. Chapter 5 examines a survey of field performance results obtained from the contributors to this report as well as a literature review. Chapter 6 presents a bifacial performance modeling comparison that was conducted among many of the contributors to this report. Each participant used the model of their choice to simulate the irradiance incident upon and energy produced by a number of specific bifacial PV system designs that were provided. Finally, Chapter 7 presents technical summaries of eleven bifacial field test sites that are researching bifacial PV performance across the globe.

2 BIFACIAL CELL TYPES

(Gizem Nogay Poulin and Joshua S. Stein)

2.1 Introduction to bifacial cells

Until recently, most crystalline silicon photovoltaic (PV) cells were made of p-type silicon with an aluminum rear contact that is opaque to light. These cells, called aluminum back-surface field cells (Al-BSF), are monofacial: they can accept only light entering the cell from the front side. More advanced cell designs—such as passivated emitter and rear cell (PERC), passivated emitter rear totally diffused (PERT), passivated emitter rear locally diffused, and silicon heterojunction with 15 thin layer (HIT)—can employ a localized back contact that requires metallization of only a portion of the cell's rear side. These advanced cells are bifacial, able to accept light from the rear as well as the front side, as shown in Figure 1.

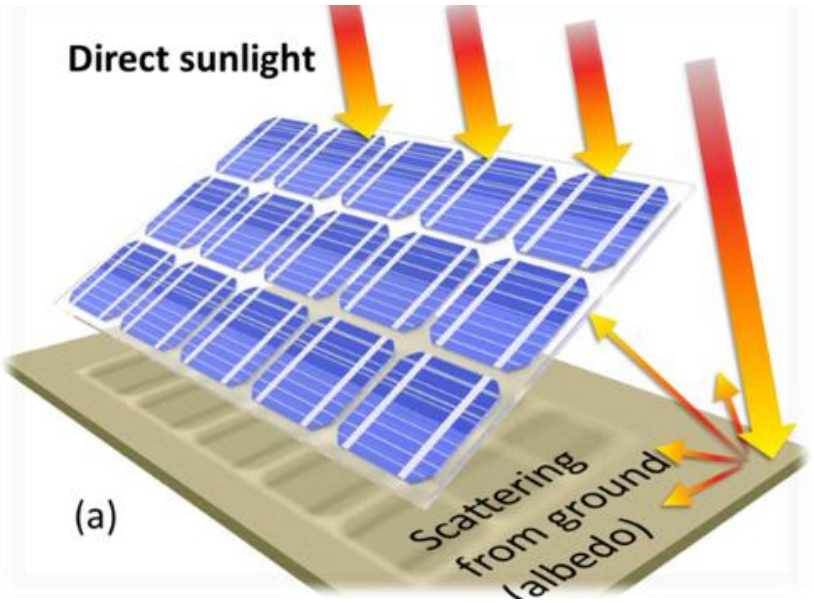

Figure 1: Bifacial PV modules convert light hitting the front and rear sides of the module to electrical energy.

Transition from monofacial to bifacial configuration can improve the energy yield of PV power plants up to 25 to 30% [3], [4] at a reasonable increase in production costs, according to National Renewable Energy Laboratory (NERL) calculations, shown in Figure 2 [5].

Summaries outline the history and progression of bifacial solar cell concepts and designs [6], [7]. The first patented bifacial solar cell design, awarded in 1960 [8], used a p+ junction on both sides of an n-type silicon wafer, with contacts attached to the side of the cell. Despite subsequent study of related cell designs, bifacial PV did not become widely popular until the PERC cells were produced at industrial scale. Bepvnovlow is a discussion of the performance potential and industrial compatibility of common bifacial cell technologies.

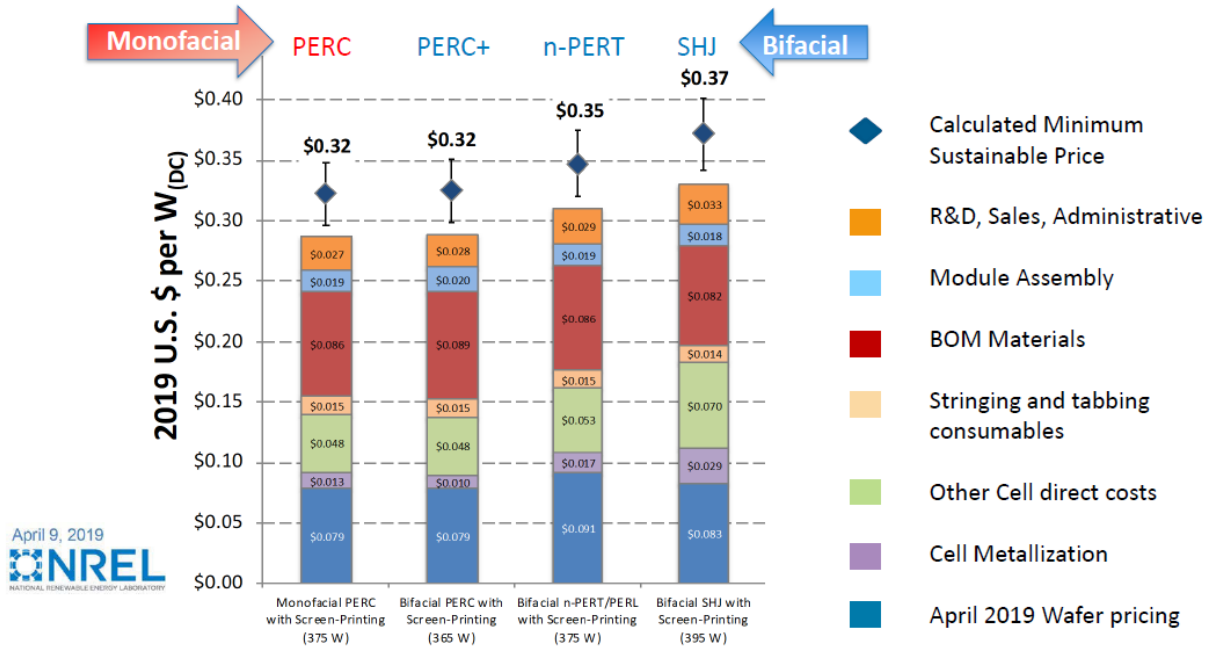

Figure 2: Monofacial versus bifacial module manufacturing cost calculation.

2.2 PERC cells

Al-BSF cells experienced a rapid production increase in 2004 to 2008, accounting for the vast majority of industrial-scale solar cells produced in that period. These cells presented three main technical drawbacks [3]:

- Rear-side recombination at the full-area aluminum back contact
- Partial absorption of infrared light at the rear
- A low carrier lifetime in p-type silicon

PERC technology [9], developed in the laboratory in 1989, addressed the first two limitations by introducing localized metal contacts and partial passivation at the rear side of the cells. However, 25 years of development were needed until process advances enabled mass production of PERC cells. Monofacial PERC cells are rapidly replacing Al-BSF cells in industrial manufacturing. According to the International Technology Roadmap for PV (ITRPV), PERC comprised 50% of the worldwide PV industry in 2019 and will reach approximately 80% within the next years [2].

However, monofacial PERC is near its upper efficiency limit of 22.5%. Making PERC cells bifacial (PERC+) is one way to improve their output power, as their bifaciality (rear efficiency divided by front efficiency) potential is around 80% [5]. Changing the production line from monofacial to bifacial does not add significantly to manufacturing costs, as shown in Figure 2.

Figure 3 presents the typical structure of a bifacial PERC+ cell. The front side n+ emitter region is produced with $POCl_3$ diffusion in a tube furnace and typically passivated with a SiN_x dielectric layer, which also acts as anti-reflective coating. Converting a monofacial PERC into a bifacial PERC+ requires replacing the full-area rear Al screen-print with an Al finger grid screen design. The Al screen—with a finger pitch identical to the local line-shaped laser contact opening pitch—must be aligned to ensure the overlap of Al fingers and laser contact opening introduced through rear passivation stack (typically AlO_x/SiN_y) [7]. Finally, the local

Al-BSF are formed during the firing process, with Al in direct contact with silicon wafer. With bifacial PERC+ cells, the finger grid design allows a decrease in Al paste consumption from 1.0 g to 0.2 g per wafer [3].

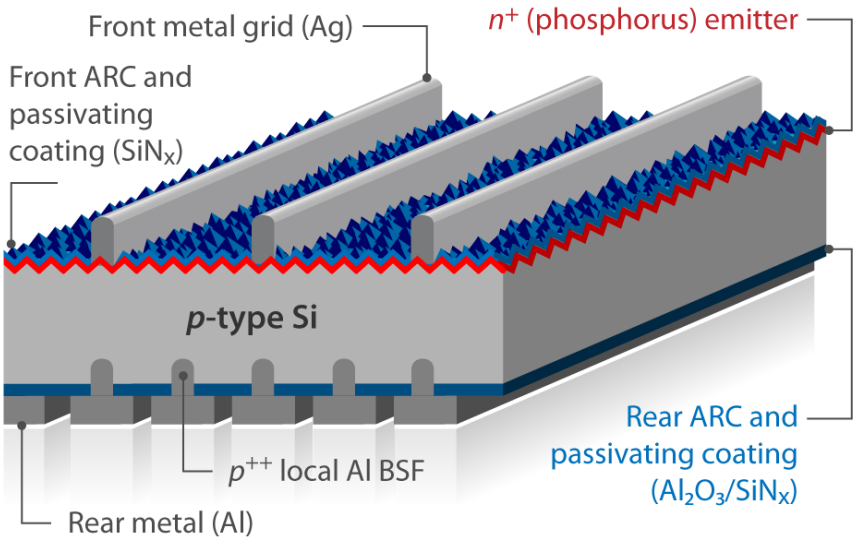

Figure 3: Typical bifacial p-type PERC+ cell scheme.

Several issues are critical in bifacial PERC+ cell development:

- Optimization of the thickness of the rear-side passivation stack of PERC+ for anti-reflective properties
- The high specific resistivity of screen-printed Al fingers, which requires design of the rear Al finger grid to minimize series resistance losses

Improving efficiency is a priority. Currently, bifacial p-type Czochralski grown PERC+ are mass-produced with average efficiencies above 21.5% [10]. Trina Solar has announced a certified efficiency of 23.39% for a 252 cm^2 PERC+ cell with nine-busbar technology using standard manufacturing equipment [11]. Externally confirmed efficiencies up to 24.1% have been reported for large-area (>244 cm^2) PERC+ still in R&D [12]. However, as very limited process information has been shared, the structure of this cell and its compatibility with current industrial lines are not known.

The next step for PERC+ efficiency improvement may be integration of the passivating contacts created with a thin interfacial oxide and a highly doped polysilicon layer on top (e.g., the TOPCon, POLO, Poly-Si) in mass production. A recent simulation study from Fraunhofer Institute for Solar Energy Systems shows that introducing the passivating contact fully at the rear and aligned locally to the front fingers can boost PERC efficiency by approximately 1% absolute [13].

At the module level, SolarWorld pioneered mass production of PERC+ glass/glass bifacial modules in 2015. Since then, various companies, such as Neo Solar Power Energy Corporation, Trina Solar, and LONGi Solar, have followed SolarWorld's technology route to offer commercial PERC+ products.

Nonetheless, several factors limit today's mainstream p-type solar cell technologies:

- The low bulk lifetime of the p-type material
- High sensitivity to metal impurities [14]

- Light-induced degradation caused by boron-oxygen complexes [15]

2.3 N-PERT

P-type solar cell limitations are driving the PV industry's attention toward high efficiency n-type solar cells, including n-PERT solar cells, which are promising for two reasons:

- Their process sequence calls for machinery that is more or less compatible with current solar cell production lines.
- The n-PERT cell concept permits very high bifaciality, up to 95% [16].

Figure 4 shows the n-PERT cell structure. Typically, the n-PERT cell features a p+ boron-doped emitter at the front side that is passivated with dielectric layers, such as Al_2O_3/SiN_x or SiO_2/SiN_x. An n+ phosphorous-doped back-surface field cell (BSF) covers the rear side, passivated by a SiN_x dielectric layer approximately 80 nm–thick. Several approaches can form the doped regions within the wafers:

- Performing two subsequent diffusion processes in tube furnace with POCl3 for n+ and BBr3 (or BCl3) for p+ doping
- Depositing a diffusion source on the surface and performing subsequent high temperature treatment to promote dopants in diffusion towards the wafer
- Using ion implantation and high temperature annealing for dopant activation

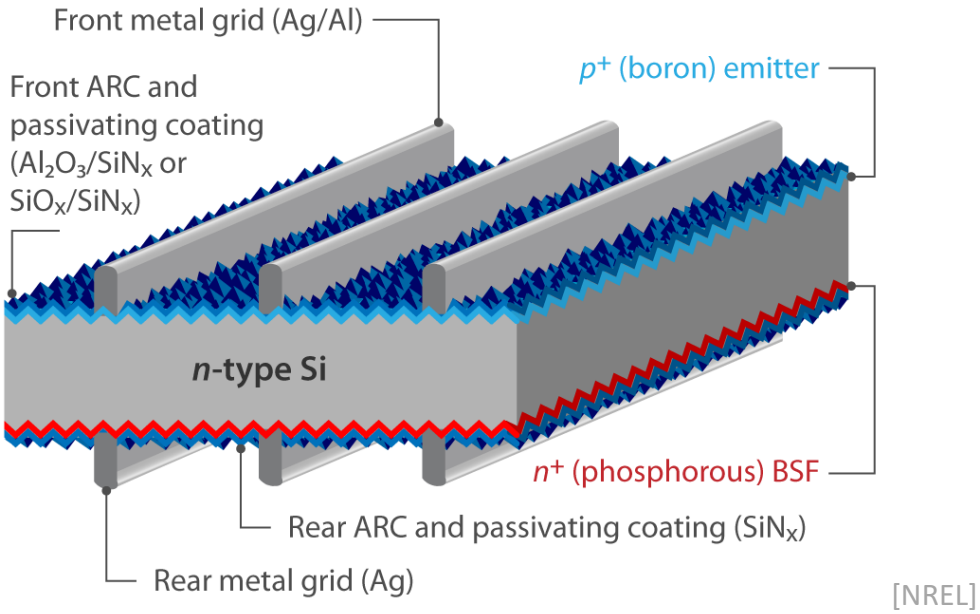

Figure 4: Typical bifacial n-PERT cell scheme.

Industry commonly prefers the first approach over the others because tube diffusion furnaces offer high throughput and moderate operating and investment costs. However, because tube gas-diffusion processes are two-sided, unintended parasitic doping of the wrong side is an issue. Two methods can address this issue: using either diffusion barriers to avoid parasitic doping or using single-side etching to remove the parasitic doping after the diffusion [7]. Screen-printing metallization is used to create metal contacts in industrial n-PERT solar cells. The process uses Al containing Ag paste for the front p-type emitter and Ag paste for the rear n-type BSF [17].

After the development of the first n-PERT cell concept in 2002 at the University of New South Wales [18], research has focused on improving the concept's efficiency and compatibility with industrial mass production. Average efficiencies now exceed 21.5% in mass-produced cells [19]. Interuniversity Microelectronics Centre (IMEC), in collaboration with Jolywood, recently reported a 23.2% efficient fully screen–printed bifacial n-PERT cell (bifaciality above 80%) with twelve busbars design [20].

Mirroring the PERC+ upgrade scenario, several research institutes are exploring a novel approach for integrating the passivating contacts by applying thin oxide and doped polysilicon layer stacks to the rear side of n-PERT cells to minimize recombination losses. Use of n+ passivating contacts on small-area monofacial lab-scale cells and a dedicated metallization scheme based on photo-lithography has led to efficiencies up to 25.7% [21]. With screen-printing at the R&D level, efficiencies up to 24.2% have been externally confirmed for large-area (>244 cm^2) bifacial n-PERT cells that integrate passivating contact technology to the rear side of the cell [22]. The Chinese photovoltaic companies Yingli Solar, Shenzhou International, Jolywood Solar Technology Co., and Jiangsu Linyang Energy Co. are mass producing bifacial n-PERT solar modules that feature a front efficiency of over 21% and bifaciality factor of 80 to 85% [23].

2.4 Hetero-junction cells

Hetero-junction solar cells (HJT) decrease recombination-related losses in conventional solar cells by using carrier-selective passivating contact structures that simultaneously provide surface passivation and carrier selectivity in place of the highly recombination active-direct contact regions between the silicon absorber and the metallization [24]. Early reports on silicon HJT solar cells were published by Fuhs et al. [25]. However today, this cell concept is associated with Sanyo Corporation—now Panasonic Corporation—which developed and patented the technology as hetero-junction with intrinsic thin layer (HIT) [26].

Figure 5 presents the typical bifacial HJT solar cell structure in front-junction configuration. Generally, HJT cells are based on n-type mono-Si wafers because HJT production does not include a high-temperature treatment that would aid in impurity gettering and deactivating boron-oxygen defects. However, recent results on p-type substrates show promise [27].

In HJT cell structure, surface passivation is provided by intrinsic amorphous silicon [a-Si:H(i)] deposited with plasma-enhanced chemical vapor deposition on both sides of the wafer; carrier selectivity is provided by in-situ doped a-Si:H layers on top. N- and p-type doped a-Si:H layers are applied to opposite sides of the wafer, respectively, to form electrical contacts to the electrons and holes in the wafer. To enhance lateral transport of the collected carriers toward the metallic grids, transparent conductive oxides are sputtered on top of the doped a-Si:H layers on both sides of the wafer.

As the surface passivation of HJT contacts can degrade upon annealing at temperatures above 250°C, special Ag pastes compatible with a low curing temperature are used for metallic grids. Owing to the high-quality chemical passivation provided by a-Si:H, HJT technology enables very high V_{oc} values. In experiments, values of up to 750 mV—very close to the theoretical limit—were reported for a 98-um-thick c-Si wafer. Further, conversion efficiencies greater than 25% have been demonstrated for large-area HJT solar cells in two configurations: the front-back contacted [28] and the interdigitated back-contacted (IBC) [29].

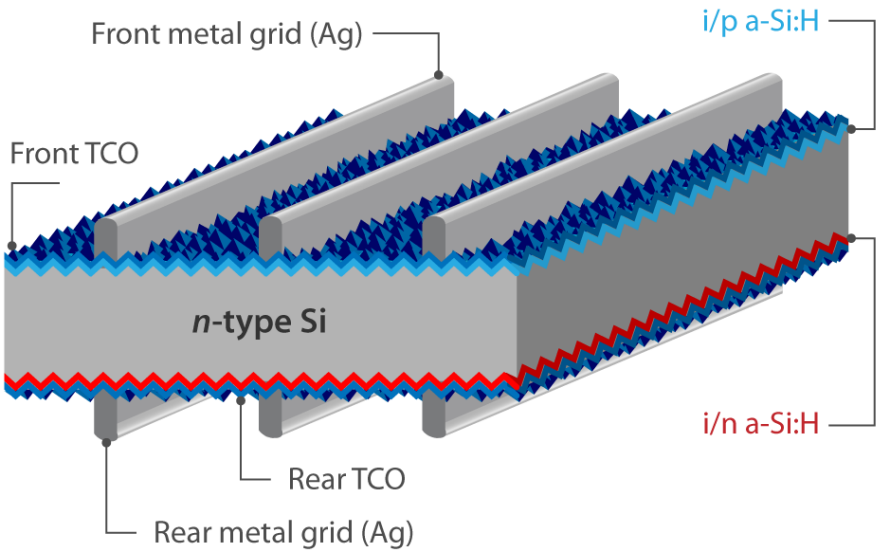

Figure 5: Typical bifacial HJT solar cells scheme in front junction configuration.

HJT technology offers other important advantages: a low temperature coefficient; compatibility with thin wafers to enable lower costs; and high bifaciality potential. The high efficiencies reported for both configurations (front-junction configuration with p-type layers at the front and rear-junction configuration with n-type layers at the front) confirm the intrinsic bifacial nature of the HIT solar cells [7]. Typically, the bifaciality factor of the HJT cells is above 92%; the potential of 100% can be reached with careful optimization.

As its most significant limitation, HJT solar cell technology experiences parasitic optical absorption in the transparent conductive oxide and a-Si:H layers, which introduces a trade-off between V_{oc} and J_{sc} of the cells [24], [30]. However, engineering plasma-enhanced chemical vapor deposition process conditions can optimize this trade-off. Today, busbar-less HJT cells fabricated in a pilot-line on mass production equipment can reach efficiencies greater than 24% [31]. With its high efficiency potential and lean manufacturing process flow, HJT cell technology is expected to gain greater global photovoltaic market share in the coming years [2].

2.5 Thermodynamic limits of a bifacial solar cell

(Muhammad A. Alam and M. Ryyan Khan)

The efficiency of single-junction monofacial solar cells has increased steadily over the years, with some cells beginning to approach the fundamental limits predicted by Shockley-Queisser (SQ) [32]. In addition, knowledge gained from volume manufacturing has allowed dramatic reductions in manufacturing and installation costs. Continued improvement in the lifetime and efficiency of the solar cells should enable further reductions in the levelized cost of energy (LCOE).

Therefore, significant effort is focused on improving solar modules and using new cell technologies, such as multijunction and bifacial solar cells. [33]. Experimentation in new cell structures and cell topologies is being driven by several encouraging factors: the intrinsic bifaciality in HIT; the availability of large bandgap material, such as perovskite (PVK) and organic solar cells; and the availability of lower-bandgap material enabled by quantum-dot cells.

The original SQ paper for single-junction solar cells and subsequent generation to multi-junction cells [34] have guided the efficiency gain of these cells towards the thermodynamic limit. Recent work has explored the thermodynamic limits of two junction (2-J) (silicon, PVK), *N*-junction bifacial solar cell, 3-J, 4-J, and 5-J concentrator PV, including the effect of series resistance. Generalization of these limits for yield optimization of food, water, and energy, and the hydrolysis of water by multi-junction tandem PV has also been analyzed [35].

Use of the SQ triangle provides an intuitive graphical approach to predict the thermodynamic limits of bifacial PV technology. The approach will explain the key intrinsic trends of bifacial gain, such as its nonlinear dependence on the cell-number and operating temperature; albedo-dependent change of the optimum bandgaps; importance of three-terminal design for variable albedo; and relevance of double-junction bifacial solar cells.

2.5.1 The SQ triangle

As described by [35], the SQ triangle approach relies on two observations regarding the current and voltage (IV) characteristics of a solar cell operating at its thermodynamic limit. The maximum power-point voltage (V_{mp}) is given by [36], [37]:

$$V_{mp} = (1 - T_D/T_S)E_g - (k_B T_D/q)\ln(\theta_D/c\,\theta_S) \equiv c_f E_g - \Delta(c) \qquad (1)$$

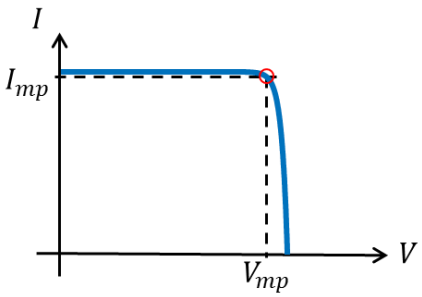

Figure 6: The current-voltage characteristic of a solar cell with bandgap, with maximum IV point indicated.

Here, T_D and T_S are the temperature of the cell and the sun, respectively. The Carnot factor is $c_f \equiv (1 - T_D/T_S) \sim 1 - 300/6000 = 0.95$. The angle entropy factor, $\Delta(c) \equiv (k_B T_D/q)\ln(\theta_D/c\,\theta_S)$, depends on the size of the solar disk (θ_S) as viewed from earth and the angular radiation from the solar cell (i.e., $\theta_D = 2\pi\ or\ 4\pi$ depending on the back reflector) and is $\Delta \simeq 0.31$ for one-sun concentration (i.e., $c = 1$). Similarly, the maximum power-point current under AM1.5G illumination (I_{mpp}) is given by [38]:

$$I_{mp} = c\,I_{sun}\left(1 - \beta'\,E_g\right) \qquad (2)$$

The current is proportional to the solar concentration, c, and I_{sun} is the projected current at $E_g \to 0$. β' is the loss-coefficient of photo-current with increasing bandgap. The linear approximation holds for $0.5\ \mathrm{eV} < E_g < 2\ \mathrm{eV}$. Any nonlinearity of I_{mp} is easily handled by a one-to-one mapping between E_g and its linear approximation [39]. Inserting Equation (1) into Equation (2), and defining $i_{mp} = I_{mp}/I_0\ and\ v_{mp} = V_{mp}/V_0$, we obtain the equation for the SQ triangle:

$$i_{mp} = 1 - v_{mp} \qquad (3)$$

Here, $I_0 \equiv cI_{sun}\,(1-\beta\Delta)$ and $V_0 \equiv (1-\beta\Delta)/\beta$, with $\beta = \beta'/c_f$. Each point on the diagonal represents a material with bandgap E_g, and the box within the triangle

$P_{mp}\,(E_g) = V_{mp}(E_g)I_{mp}(E_g)$ defines the maximum power output for the material. The maximum power-output at the thermodynamic limit from any solar cell topology (e.g., tandem, bifacial) involves maximizing the number of boxes inscribed within the triangle.

2.5.2 Thermodynamic Efficiency Limits of the Two-terminal Multijunction Solar Cell

As shown in Figure 7, the optimum bandgaps and thermodynamic efficiency of an N-junction solar cell are obtained by tiling the triangle by rectangular boxes to maximize coverage, i.e.,

$$V_{mp}^{\{i\}} = iV_0/(N+1)\;and\;I_{mp}^{\{i\}} = I_0/(N+1) \tag{4}$$

Summing over the boxes, the efficiency of N-junction tandem with illumination c is given by

$$\eta_N(c) = I_0\,V_0\,N/(2(N+1)c) \tag{5}$$

For example, for a single-junction solar cell under 1-sun illumination ($c = 1, N = 1$, and $I_{sun} = 83.5\,mA/cm^2$), shown in Figure 7(a), we find $I_0 = 71.8\,mA/cm^2$ and $V_0 = 1.92V$. Therefore, $\eta_1 = 34.3\%$ occurs at $V_{mp} = 1.92/2 = 0.96$ eV or $E_g = 1.34$ eV, as expected [34], [38]–[40]. Comparison to the thermodynamic calculator shows that Equation (5) is correct for solar cells with an arbitrary number of junctions [41].

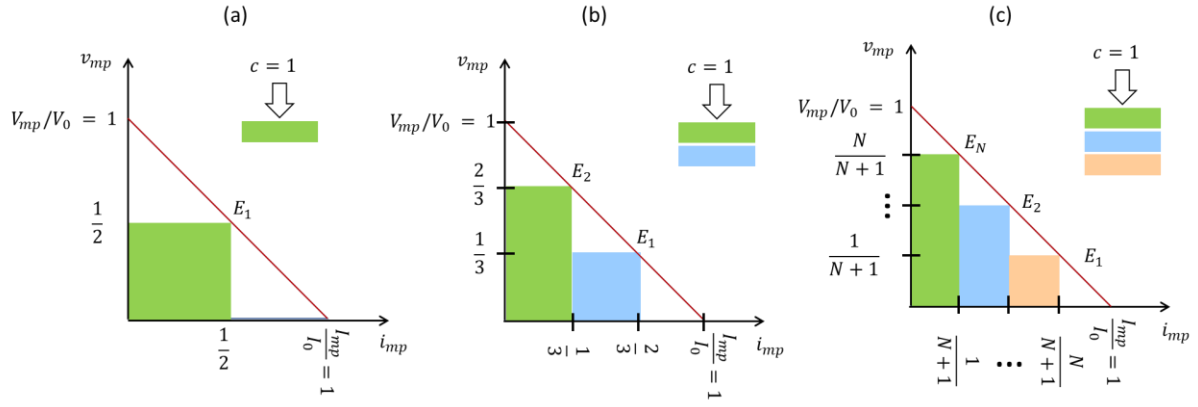

Figure 7: SQ triangle for monofacial cells: (a) Single junction, SJ; (b) double-junction, DJ, and (c) multi-junction PV. For a two-terminal configuration, the bandgaps are optimized to produce equal current.

2.5.3 Efficiency limits of bifacial tandem solar cells

Figure 8 shows the generalization needed to calculate the efficiency of a bifacial tandem cell. The extended triangle accommodates the cells illuminated both from the top (concentration, c) and the bottom (albedo, cR). In general, the cell with the smallest bandgap E_0 is surrounded by U cells above and D cell below the cell, so that $N = U + D + 1$. The sum of the boxes gives the power output: $S_N(U, D, R)$

$$s_N = \sum_{i=1}^{U} x(1-ix) + \sum_{j=1}^{D} x\left(1-\frac{jx}{R}\right) - x\left(1-Ux-\frac{x}{1+R}\right) = aNx - x^2A \qquad (6)$$

Power is maximized for the current $x_0 = I_{mp}/I_0 = N/2A$, so that

$$\eta_N/\eta_1 = (s_N/s_1) = N^2/2A \qquad (7)$$

$A \equiv U(U+1)/2 + D(D+1)/2R + U + (1/1+R)$ and $U = 2N - 3R - 1/2(1+R)$.

Maximizing (7) with respect to D, we find $N < N_{crit} \equiv 1 + R^{-1}, D = 0$,

$$\eta_N(R)/\eta_1 = 2(1+R)N^2/(N(N+1)(R+1) - 2R) \qquad (8)$$

and for $N > N_{crit} \equiv 1 + R^{-1}, D > 0, R \neq 0$)

$$\eta_N(R)/\eta_1 = (8R(1+R)N^2)/(2R(2N^2+4N+1) - 9R^2 - 1) \qquad (9)$$

Equation (8) predicts that $\eta_N(R) = (1+R)\eta_1(R=0)$, that is, the effective efficiency of a bifacial single-junction solar cell increases by a factor of $(1+R)$ compared to its monofacial counterpart, as expected. We will see later that fundamental thermal consideration reduces the gain below this limit.

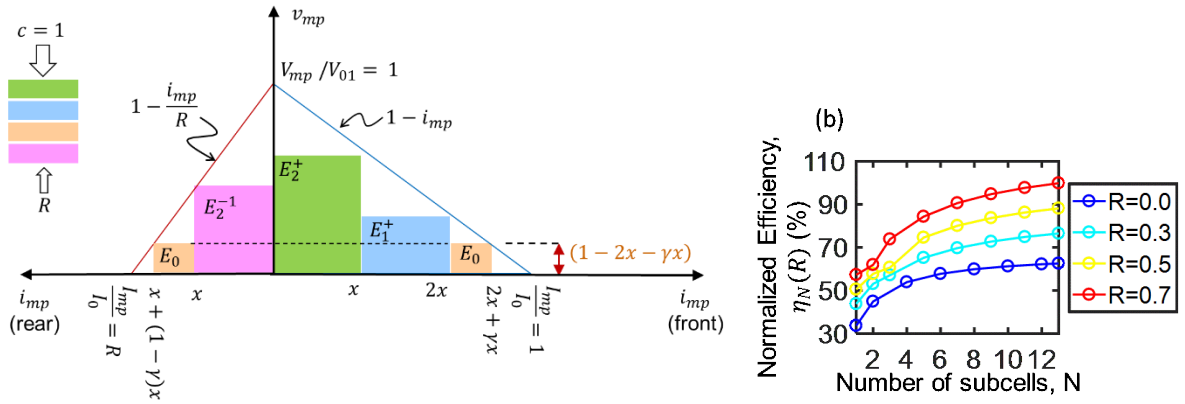

Figure 8: (left) SQ triangle for bifacial multi-junction solar cell. (right) Bifacial gain (relative to single junction monofacial limit) as a function of albedo.

2.5.4 Thermodynamic limits two-junction bifacial solar cells

As shown in Figure 8, relative gain is most significant for a smaller number of junctions, encouraging the development of simple 2-4 terminal bifacial tandem cells with two junctions (e.g., HIT-PVK). Specifically, $\eta_2(R)/\eta_1(R=0) = 4(1+R)/(3+2R)$ benefits from improved gain from 1-J to 2-J monofacial cells (e.g., a factor of 4/3), as well as more effective use of the albedo [39], [42]. Equally important, the top-cell bandgap reduces with R because the increased current from the top cell is now matched by the albedo-generated photocurrent from the bottom cell.

The thermodynamic-limit analysis reveals several practical challenges of 2-J bifacial design. For example, if the top and bottom cell bandgaps are not optimally matched for a specific albedo (e.g., $E_t = E_b 1 + R) + (1 - R))$ then the current mismatch reduces the total power output below the thermodynamic limit:

$$\eta_N \sim \frac{1}{c\ P_{in}} \left[\sum_{i=1}^{N} V_{mp}^{\{i\}} \right] min\ \{i_{mp}\}. \tag{10}$$

In practice, the current mismatch can be reduced by changing the optical thickness of the two cells [42].

The thermodynamic limit was calculated for fixed R. If the effective R is modified (due to spectral or spatial dependencies) during solar cell operation, the output will be determined by min(i_{mp}) of the top or the bottom cell. The 2-J cell will need to dissipate the excess power internally; the power output will not increase as the efficiency, but the Joule heating will reduce the cell's reliability. For example, the plot on the right side of Figure 9 shows that for an optimized HIT-PVK solar cell, the efficiency saturates to 33% for $R > 0.2$. [42]–[44]. In fact, for $R > 0.4$, a single-junction HIT would produce more output power than would the 2-J bifacial tandem. A three-terminal configuration, shown to the left of the SQ triangle in Figure 9 allows independent control of the current on the top stack (U) and bottom stack (D), with the third terminal connected to E_0, continues to benefit for $0 < R < 1$ [43].

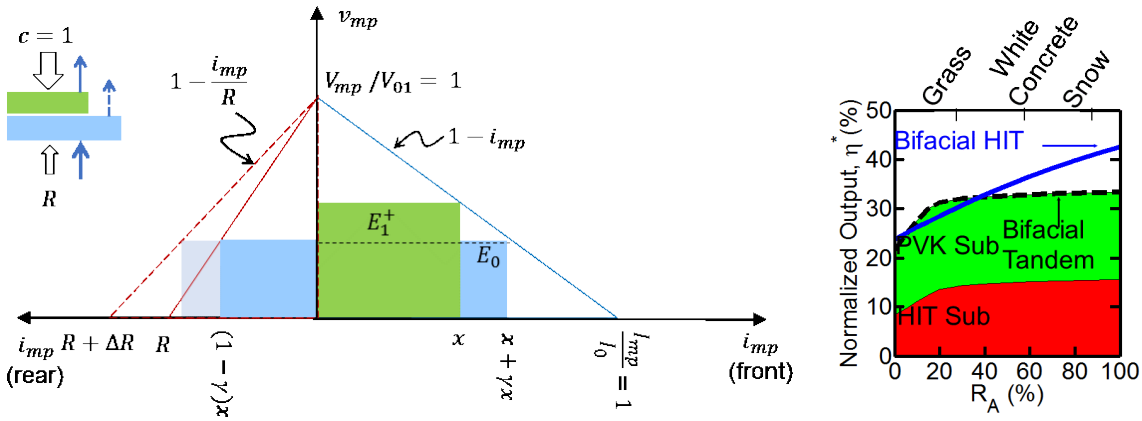

Figure 9: (left) The SQ triangle explains the sensitivity to albedo variation. Only a 3-terminal configuration can use the additional albedo. (right) Otherwise, the excess energy cannot be used by the bifacial tandem.

2.5.5 Temperature dependence of single junction solar cells

When a cell is illuminated by sunlight, the absorbed power not converted to electrical output must be dissipated within the cell. The physics of thermal flux balance requires

$$T_D = T_A + \frac{c\ P_{in}(1+R)\left(1 - \eta_N(R=0)\right)}{2h} \equiv T_A + K \cdot P_{in} \tag{11}$$

where T_A is the ambient temperature and h depends on the convection and radiative flux transfer [45], [46]. This Joule heating reduces the efficiency to

$$\eta_1 (T_D) = \eta_0 [\, 1 \, - \beta_T \, (T_D - T_A)] \tag{12}$$

The temperature of the bifacial solar cell depends on the albedo (increases temperature because a fraction of the albedo energy is converted to electricity) and subbandgap absorption (reduces temperature because subbandgap light can be transmitted). At the thermodynamic limit,

$\beta_T \, = \frac{1}{\eta_0} \left| \frac{d\eta}{dT_D} \right| \, = \beta_V \, + \, \beta_I$, where

$\beta_V \, = \, k_B \left[-\frac{E_g}{k_B T_S} - \frac{\Delta}{k_B T_D} \right] / \, (c_f \, Eg \, - \Delta)$ and $\beta_I \, = \, -\frac{\beta'}{1-\beta' \, E_g} \left(\frac{dE_g}{dT_D} \right)$.

For $E_g = 1.1$ eV, $\beta_T \, = \, -0.00172 \, + \, 0.0006 \, = \, -0.12\%$.

In practice, V_{mp} is lower than the thermodynamic limit. Using typical values, $\beta_T^{(B)} \, = \, -\, 0.25\%$ for bifacial cells, while $\beta_T^{(M)} \, = \, -\, 0.37\%$ [12] for monofacial cells. As shown in Figure 10, the relative gain of 1-J monofacial vs. bifacial solar cells is given by

$$\frac{P_o^{(B)}}{P_o^{(M)}} \, = \left(\frac{\eta_1^{(B)}}{\eta_1^{(M)}} \right) \cdot \left(\frac{1 - \beta_T^{(B)}}{1 - \beta_T^{(M)}} \right) \cdot \left(\frac{\Delta \, T_0 \, + \, K \, P_{in} (1 + R)}{\Delta \, T_0 \, + \, K \, P_{in}} \right). \tag{13}$$

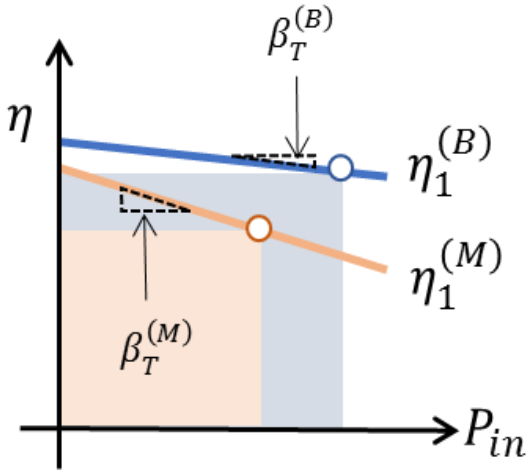

Figure 10: Bifacial gain is defined by the ratio of boxes in the $\eta - P_{in}$ plane. In intrinsic thermodynamics (β_T=const), temperature-dependence erodes bifacial gain. In practice, $\beta_T^{(B)} < \beta_T^{(M)}$ further improves bifacial gain.

In other words, the bifacial gain improves not only because $\eta_1^{(B)} / \eta_1^{(M)} \, = \, 1 + R$, but also because the reduced temperature coefficient makes $\left(1 - \beta_T^{(B)}\right) > \left(1 - \beta_T^{(M)}\right)$, so long as the temperature (as a balance between subbandgap transmission and excess absorption) remains essentially the same, i.e., $K \, P_{in} \, R \ll \Delta \, T_0 \, + \, K \, P_{in}$.

2.5.6 Conclusions

The SQ triangle enables calculation of the thermodynamic limit of the bifacial multi-junction solar cell under arbitrary sunlight concentration. The albedo R not only increases the energy output, but also relaxes the bandgap matching requirements and thickness sensitivity. A bifacial solar cell, based on PVK top cell and silicon HJT bottom cell, appears promising, espe-

cially because lower-bandgap (e.g., 1.5-1.6) needed for the bifacial tandem is more stable than higher bandgap (e.g., 1.7 eV) cells needed for monofacial tandem cells. Also, the lower temperature coefficient of bifacial cells (a consequence of higher V_{mp}) further improves the relative gain over monofacial cells. These fundamental thermodynamic advantages motivate the commercial development of bifacial solar cell technologies.

3 BIFACIAL MODULES

Differences between monofacial and bifacial cell and module design occur mostly on the rear side but can in some cases occur on the module edges. Figure 11 shows a monofacial module and solar cell on the left side and a bifacial module and solar cell on the right side. The metal grid is different for monofacial and bifacial—the grid is Al-grid for PERC and Ag-grid for nPERT, TOPCon, HJT, or IBC. The difference results in an exposed anti-reflection coating on the rear side of bifacial modules.

In bifacial modules, the rear-side cover consists of either glass or a transparent polymer backsheet. When backsheets are used, the module must be supported by an aluminum frame. However, in some cases, the rigidity of glass-glass modules makes a frame unnecessary, and the edges are merely sealed.

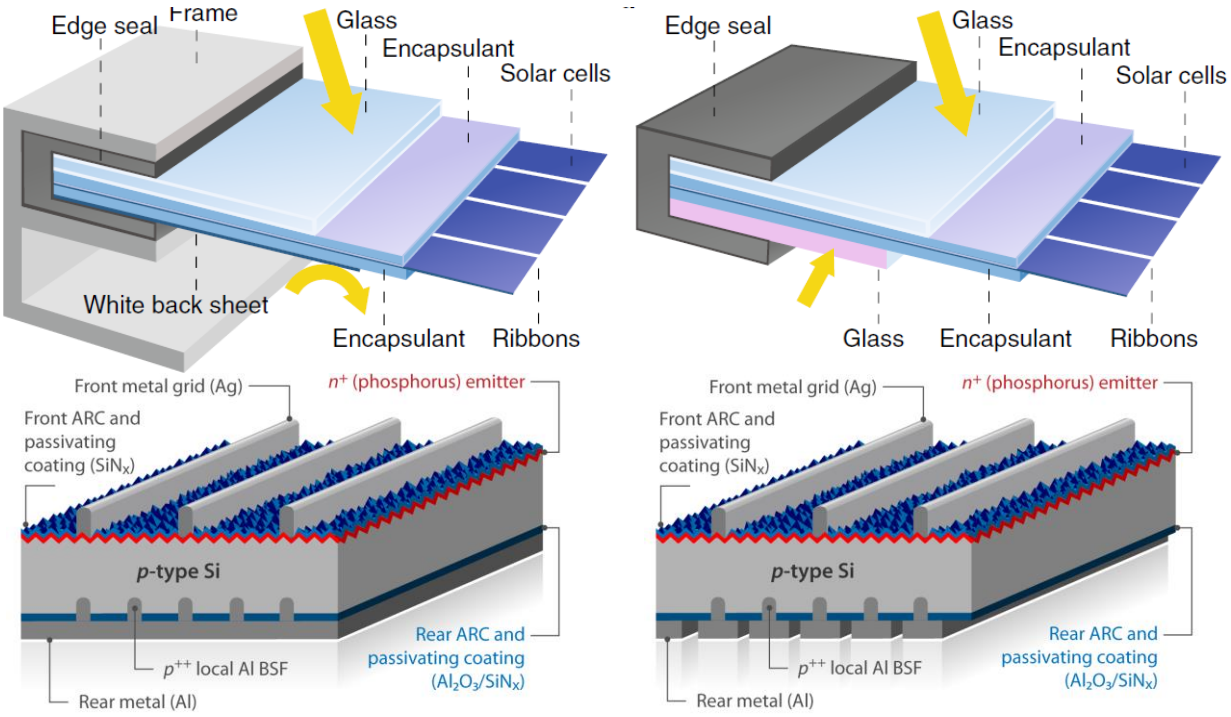

Figure 11: Differences between PV modules: monofacial (upper left) and bifacial (upper right) and differences between solar cells: monofacial PERC (lower left) and bifacial PERC+ (lower right).

3.1 Test standards and certification of bifacial PV modules

(Johanna Bonilla)

Technical Committee (TC) 82 of International Electrotechnical Commission (IEC), is responsible for PV standardization projects. Experts within the IEC-appointed working groups (WGs) of TC82 are currently reviewing existing standards and assessing the need for new standards to address bifacial PV technologies. In particular, working group 2 (WG2) is responsible for PV modules, and working group 3 (WG3) focuses on technical aspects of PV systems. Four sets of IEC standards are related to photovoltaic modules, as described in Table 1 and Figure 12.

Table 1: IEC standards related to PV modules.

Topic	IEC Standards	Changes for bifacial
Measurement issues, in particular for output power determination	IEC 60891, IEC60904-X	IEC TS 60904-1-2
Product qualification testing	IEC 61215-X, IEC 61730	Under progress
Energy Rating	IEC 61853-X	Under progress
PV materials and components	IEC 62852, IEC, 62790, IEC 62930	No changes proposed to date

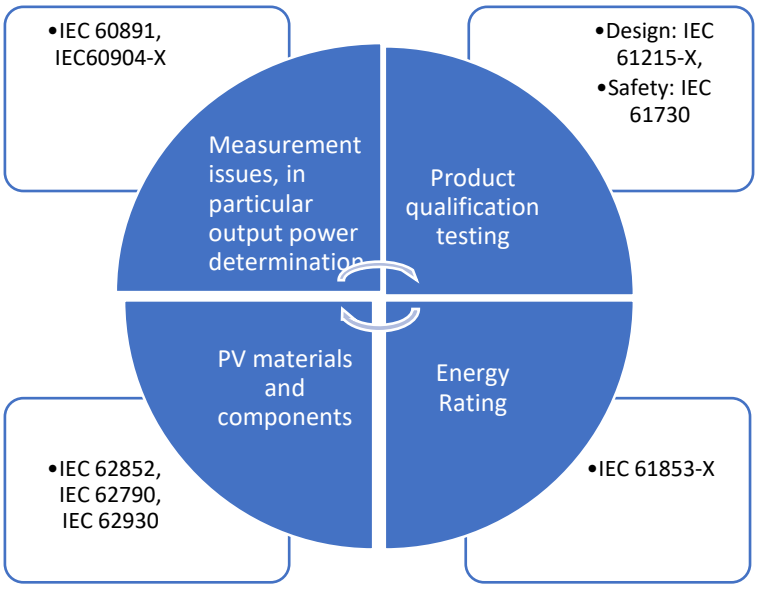

Figure 12: IEC standards related to PV modules

Despite intense discussions in the IEC working groups, the harmonization process for bifacial photovoltaics may take several years. In response to specific market needs, several practices are being adopted as "common" and will be also discussed in this section.

3.1.1 Maximum output power characterization

Specific measurement procedures to characterize the PV power output of bifacial PV modules were developed to account for their ability to generate power from both the front and the rear sides. These specifications, published in January 2019, are defined in the IEC TS 60904-1-2 [47]. The specification includes procedures for determining the bifacial output power under natural light or with a solar simulator—the device commonly used by the PV industry for cell and module performance characterization.

Characterizing the output power for bifacial PV modules with a solar simulator requires three main steps:

- Measuring bifaciality factor at standard test conditions (STC)
- Determination of rear-irradiance driven power gain yield, BiFi
- Output power determination at rear irradiances of 100 W/m² and 200 W/m²

These steps are discussed in the sections below.

Bifaciality factors at standard test conditions

The relative performance of the rear side of bifacial modules is described by bifaciality factors which are defined in IEC TS 60904-1-2 as three ratios. These ratios are determined at STC conditions: specified as 1000 W/m² irradiance level, 25°C, and an air mass of 1.5. A spectral mismatch correction according to IEC 60904-7 [48] should be applied if the front and rear sides have different spectral responses. Figure 13 shows more detail.

1. $\varphi_{P_{max}}$ = Ratio of rear to front side maximum power (P_{max}),
2. $\varphi_{V_{OC}}$ = Ratio of rear to front open-circuit voltage (V_{OC}),
3. $\varphi_{I_{SC}}$ = Ratio of rear to front short circuit current (I_{SC}).

Values of $\varphi_{P_{max}}$ typically range from 75% to 95% for n-PERT bifacial modules, from 60% to 70% for p-type PERC bifacial modules, and >90% for HJT bifacial modules.

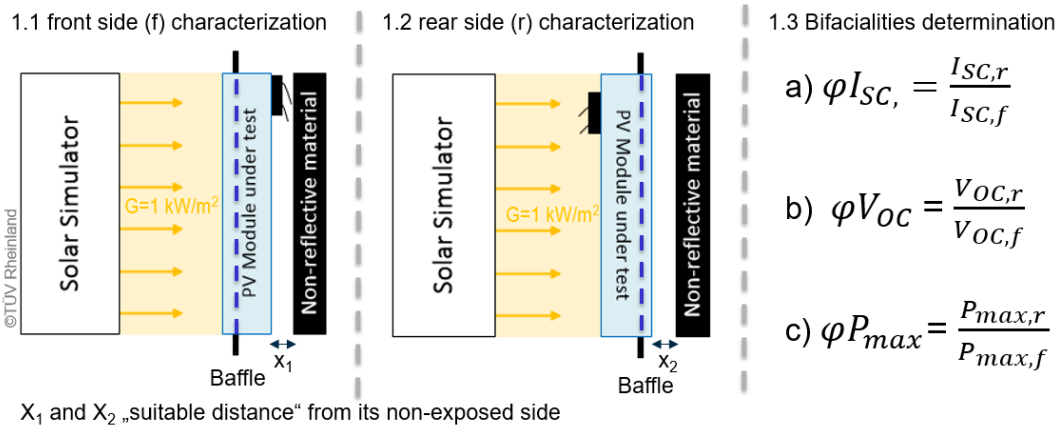

Figure 13: IEC TS 60904-1-2 test method for IV measurement of bifacial PV modules: Determination of bifaciality factor at STC. An opaque non-reflective background ensures less than 3 W/m² at any point on the non-illuminated side of the PV device.

Determination of rear irradiance driven power gain yield, BiFi

The maximum output power (P_{max}) is measured using a front irradiance of $G_f = 1000$ W/m² and different rear irradiance (G_r) levels. The G_r values shall cover **at least two of** the following ranges, which reflect the most common rear-side irradiances during field operation:

$$G_{r_{i(i=1,2,3..)}} \begin{cases} 0 < G_{r_i} < 100\ W/m^2 \\ 100 \leq G_{r_i} < 200\,W/m^2 \\ G_{r_i} \geq 200\,W/m^2 \end{cases}$$

For this purpose, the current TS IEC 60904-1-2 describes two methods: A single-side illumination and a double-side illumination, depending on the available solar simulator:

- Single-side illumination: G_E method: For solar simulators with one light source only, as defined in IEC 60904-9 [49], this method allows the measurement of the output power (P_{max}) using an equivalent irradiance G_E.

$$G_E = 1000\frac{\mathrm{W}}{\mathrm{m}^2} + \varphi * G_{r_i} \qquad (14)$$

$$\varphi = Min\left(\varphi_{I_{SC}}, \varphi_{P_{max}}\right) \quad (15)$$

- Double-side illumination method: Intended for a solar simulator with two light sources and adjustable irradiance levels, this method allows illumination of the front side with G_f= 1000 W/m² and the rear side at with at least two irradiance levels in the ranges shown above.

Regardless of the method used, a diagram P_{max} vs. G_r is required. G_r is either calculated from Equation (14) in the case of *the* G_E *method* or measured for the double-side illumination method. The linear fit of data points is forced to cross the Y-axis at $P_{max, STC}$. The slope of this graph is defined as *BiFi*, considered the bifacial power gain. Use of the BiFi slope is based on the assumption that the module's performance at front STC and any level of rear irradiance can be calculated by interpolation.

Figure 14 shows a BiFi determination of a bifacial module with bifaciality $\varphi = 0.75$. The output power (P_{max}) was measured using a single-side illumination system.

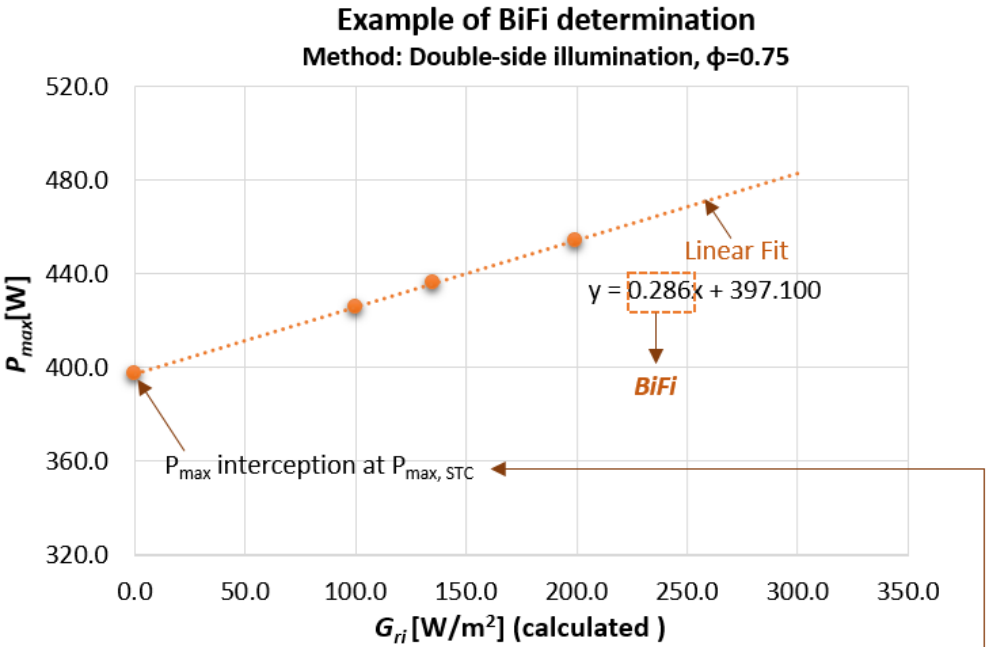

Bifaciality (ϕ)	G_f [W/m2]	G_E [W/m2]	G_r [W/m2]	P_{max} [W]	
0.75	1000.00	1000.00	0.00	397.10	STC
	1000.00	1074.98	99.97	425.75	~G_r=100W/m²
	1000.00	1101.32	135.09	435.74	~Gr=BSTC
	1000.00	1149.95	199.94	454.18	~G_r=200W/m²

Figure 14: Graph of $P_{max,}$ as a function of G_r, for determination of the BiFi parameter.

In Figure 14, BiFi is determined from the slope of the linear fit line of the measured points, as stated in Equation **(15)**. Equivalent irradiances G_E values were not completely arbitrary: values close to G_r =100 W/m² and G_r =200 W/m² were sought, as these must be reported af-

terwards. Likewise, G_r =135 W/m² corresponding to the reference bifacial test conditions (BSTC) (see the section on bifacial power rating below) was also pursued.

Output power for a rear irradiance of 100 W/m² and 200 W/m²

This step uses the BiFi slope to determine the performance of the PV module for two rear irradiance levels:

- $P_{maxBiFi100} = P_{max,STC} + BiFi * 100\ W/m^2$
- $P_{maxBiFi200} = P_{max,STC} + BiFi * 200\ W/m^2$

Table 2 shows the calculated values for the example in Figure 14.

Table 2: Calculation of $P_{maxBiFi100}$ and $P_{maxBiFi200}$ for the example in Figure 14.

BiFi	PmaxBiFi100	PmaxBiFi200
0.286	425.7	454.3

3.1.2 Bifacial power rating

The lack of a clear definition of the nominal power for bifacial PV modules is a drawback for end users. Most manufacturers relate the power rating to the commonly used STC output power of the front side, and some add an assumed contribution from the rear. There are no clearly defined reference conditions for the rated output power of bifacial photovoltaic modules and no requirements on how to incorporate the bifacial aspects on the PV module's nameplate or in the manufacturer's datasheet.

To provide transparency in the labeling practice for bifacial PV modules, IEC WG2 is considering suitable reference conditions for rated output power. TÜV Rheinland has proposed specific bifacial standard test conditions of 1000 W/m² front-side and 135 W/m² rear-side irradiance [50]. The definition of rear-side irradiance stems from work done at the National Renewable Energy Laboratory (NREL) and Sandia National Laboratories and is related to the following conditions:

- Albedo factor: 0.21 (light soil)
- Clearance height: 1 m
- Inclination angle: 37°
- Front side irradiance:1000 W/m²

The nominal output power at BSTC of the bifacial module is then measured with an equivalent irradiance of G_E =1000 W/m² + φ * 135 W/m².

The BSTC is being strongly considered by the IEC as a requirement for power rating. Figure 15 shows an example label for bifacial PV modules with power characterized at BSTC.

Electrical Data		
	STC	BSTC
Nominal Power	300 W (±3%, k=2)	330 W (± 3.5%, k=2)
Open-Circuit Voltage (V_{oc})	38.5 V (± 1%, k=2)	39 V (± 1.2%, k=2)
Short-Circuit Current (I_{sc})	9.4 A (± 2.8%, k=2)	10.2 A (± 3%, k=2)
Bifaciality (φ)	0.7 (± 0.05, k=2)	
Maximum System Voltage	1000 V IEC	
Maximum OC Protection Rating	20 A	
Power Temp Coef. (P_{mpp})	-0.4% / K (±0.05%, k=2)	
Voltage Temp Coef. (V_{oc})	-0.31% / K (±0.02%, k=2)	
Current Temp Coef. (I_{sc})	0.05% / K (±0.01%, k=2)	
STC: AM1.5G; Temp. = 25°C; Irradiance = 1000 W/m² BSTC: AM1.5G; Temp. = 25°C; Irradiance = 1000+ φ·135 W/m²		

©TÜV Rheinland

Figure 15: Example power label for a bifacial PV module rated at STC and BSTC proposed by TÜV Rheinland.

3.1.3 Product qualification testing of bifacial PV modules

Product qualification testing of PV modules is defined in two standards:

- Module design qualification testing (MQT) according. to the IEC 61215 series [51]
- Module safety qualification testing (MST) according to IEC 61730 [52]

Additional product certification requirements for bifacial PV modules are mainly related to the higher operating currents of these modules. Table 3 lists issues related to potential additional requirements for bifacial PV modules, and Table 4 summarizes the sections identified as potentially requiring test condition modifications and reasons for the modifications.

To address the additional qualification testing requirements for bifacial PV modules, TÜV Rheinland has proposed a proprietary test procedure 2PfG 2665/06.18 in 2018. This specification calls for higher test currents (I_{mpp} or I_{sc}, depending on the test) determined at an equivalent irradiance (G_E =1000 W/m² + φ * 300 W/m²) or the use of the G_E when needed. Pass/fail criteria are still based on STC measurement (1000 W/m² applies to both front and rear sides). The specification changes are detailed in Table 4.

Table 3: Issues related to potential additional requirements for quality and safety qualification of bifacial PV modules.

Test	Monofacial PV practice	Issues for bifacial testing
Thermal cycling test (MQT 11/ MST 51)	Performed in a climatic chamber with continuous temperature changes between -40°C and +85°C. To additionally stress the soldering joints, a current equal to I_{mpp} is injected.	The maximum power current must consider the contribution from the rear side.
Bypass-diode test (MQT 18/ MST 25)	The applied current is $-I_{sc}$ for the first hour and $-1.25*I_{sc}$ for the second hour.	Heating effects will be higher if the current contribution from the rear side is considered.
Hot-spot endurance test (MQT 09/MST 22)	The power dissipation at a single shaded cell is adjusted to the highest possible, which is dependent on the maximum power current (I_{mpp}) of the module.	The maximum power current must consider the contribution from the rear side.
Temperature test (MST21)	Reference temperatures of components and material are related to 1000 W/m² front irradiance and 40°C ambient temperature.	For bifacial PV modules, the additional rear-side irradiance may result in higher temperatures.
Reverse current overload test (MST26)	This test shall verify that reverse currents, which may occur during field operation, do not cause module defects due to overheating of soldering joints. Test current is 1.35 times the maximum reverse current stated by the module manufacturer on the nameplate.	The maximum reverse current should reflect the worst-case operating conditions possible in the field, i.e., 1300 W/m² front side irradiance with a high albedo and solar tracking.

Table 4: Additional requirements for bifacial PV devices regarding endurance and safety test, proposed by TÜV Rheinland.

Test	Monofacial PV	Bifacial PV
I_{mpp} applied → I_{mpp}@G_E		
MQT 11 / MST 51 – Thermal cycling test	Applied I_{mpp} in sequences	Applied I_{mpp}@G_E in sequences
I_{sc} applied → I_{sc}@G_E		
MQT 18 / MST 25 – Bypass diode test	Applied current of: 1st h @ I_{sc} 2nd h @ I_{sc} × 1.25	Applied current of: 1st h @ I_{sc}@G_E 2nd h @ I_{sc}@G_E × 1.25
Others		
MQT 09 / MST 22 – Hot spot endurance test	Irradiance shall be maintained at 1000 W/m² ± 10% during exposure	Irradiance shall be maintained at G_E ± 10% during exposure
MST 21 – Temperature test	Average irradiance shall be maintained at 1000 W/m²	Average irradiance shall be maintained at G_E ± 10%
MST 26 – Reverse current over-load test	Declared I_R by manufacturer ×1.35	To consider: (n-1) × I_{sc}@G_E × 1.25 × 1.35 (if this value is higher), where n is the maximum allowable number of strings in parallel

3.1.5 Energy rating of bifacial PV modules

The IEC 61853 standard series [53] provides a suitable framework for the energy rating of open-rack mounted monofacial PV modules. The PV industry recognizes a need to extend the energy rating to emerging applications and technologies, such as bifacial. However, the methods, measurement procedures, and related uncertainty are still under discussion.

The European EMPIR project Advanced PV Energy Rating (PV-Enerate) addressed a possible extension of the IEC 61853 standard series for bifacial devices [54]. Some outcomes are summarized in Table 5.

Table 5: Possible extension of the IEC 61853 standard series to bifacial PV modules, proposed by PV Enerate

Aspect	Monofacial PV	Bifacial PV
Mounting scenarios	Facing the equator and with an inclination angle of 20°	Add mounted east-west rack, low albedo
Rear-side irradiance	Not available	Hourly data for rear-side irradiance (Equator facing at 20°) calculated for a medium/high albedo; assumed to be uniform
Spectral correction factor	Only for front	New definition including the spectral response at the rear of the module and the spectral albedo beneath the module
Climate profiles	For front	Extended for the rear side: broadband irradiance, beam and diffuse on the rear side of the inclined plane, angle of incidence for the new planes (East-West (E-W) and rear of inclined plane), etc.

3.2 Bifacial cells in modules with white encapsulant

(Menghong Wang)

As bifacial cells become prevalent on the global solar market, new module package strategies are being developed to optimize the performance of this technology for different applications without increasing the cost or compromising the reliability. One concept being explored is the pairing of bifacial PV cells with a white reflective back encapsulant. For applications such as a close-mount rooftop with little to no rear-side irradiance, this design may increase energy yields significantly.

Similar to a white backsheet, white encapsulant reflects light that passes through or around the cells and can increase the total light available for PV conversion. Compared to common white backsheet varieties [55] or double-glass modules used with transparent encapsulants, white encapsulants feature a higher reflectivity and a shorter reflection pathway. White encapsulant has a reflectivity of ≥ 90% in the wavelength range of 1100nm to 380 nm; however, common white backsheets have reported reflectivity of ≥ 80%. White encapsulant has substantially higher reflectivity, especially between 700nm and 400nm [56].

For modules with a transparent back encapsulant (glass-glass and glass-backsheet designs), light reflected by white backsheet or transmitted through rear-side glass must pass through the rear encapsulant, which involves optical losses. Thus, white encapsulant reflects light transmitted between cells more efficiently than other options to achieve maximum performance boost.

As reported by Shanghai HiUV New Materials Co., Ltd., using white encapsulant can increase short-circuit current I_{sc} by 2.1% for bifacial PERC cells, significantly increasing their rated power. Netherlands Organization for Applied Scientific Research (TNO) has adapted a novel module design for bifacial cells that features a highly reflective gridded interlayer between and around the bifacial solar cells and laminated between the front and rear encapsulant (gridded white encapsulant) [57]. Compared to the double-glass bifacial module, a 2% higher I_{sc} is observed for the white bifacial module, which corresponds to a 2.2% higher power rating.

White encapsulant can even help monofacial cells achieve pseudo-bifaciality. According to experimental results [58], white encapsulant increased power 4.5 to 5.2 W for a 60-cell monofacial module. Hangzhou First Applied Material Co., Ltd claims that white encapsulant can increase power 7 to 10 W for double glass monofacial modules and 1.2 to 3.5 W for glass backsheet monofacial modules. As with bifacial cells, the power increase comes from an I_{sc} increase.

White encapsulant may also benefit module economics. The price of white encapsulant is in the same range as that for its transparent equivalent. However, white encapsulant blocks most of the internally transmitted front side solar radiation, reducing the requirement for UV stabilizers in the backsheet. Thus, it might be possible to avoid or reduce the use of expensive fluoropolymers, fillers, and/or UV absorbers on the cell side of the backsheet.

Although developed as early as 2012, white encapsulant was only put into mass production in recent years. Encapsulant companies have overcome numerous technical difficulties, such as the overflow of white encapsulant onto busbars or cells during the lamination process. Currently, the majority of white encapsulants on the market have been pre-processed with electron beam radiation to perform pre-crosslinking to prevent overflow or wrinkle.

However, pre-crosslinked white encapsulants might suffer from loss of peel-off strength and delamination. Moreover, a high degree of pre-crosslinking might increase cell susceptibility to cracking during lamination. Notably, some white encapsulants, especially white ethyl vinyl acetate (EVA), can be more corrosive in damp heat testing (Figure 16) [59]. The three cells (Al-BSF monofacial polycrystalline cell, PERC bifacial monocrystalline, and PERC bifacial polycrystalline cells) all show substantial corrosion in electroluminescence image when they are used with white EVA. A large R_s increase can also be seen in the I-V curves. White POE on the other hand did not show significant difference between traditional transparent encapsulants.

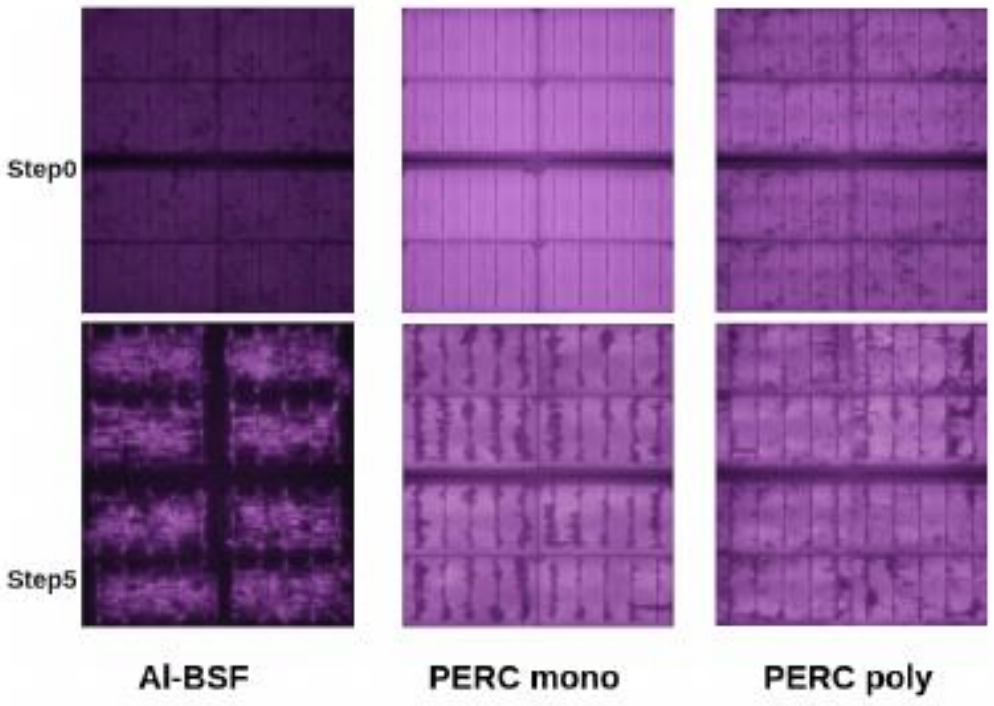

Figure 16: Electroluminescence images of various minimodules with white encapsulant before and after 2,500 hours in damp heat exposure (80°C, 85% RH).

3.3 Bifacial-specific cell and module degradation issues

(Radovan Kopecek, Ignacia Devoto, Tudor Timofte, Daniel Tune, Andreas Schneider, Andreas Halm)

Bifacial cells and modules can experience degradation processes, which are affected by their bifacial properties. Starting from inside of the module, the first important degradation is light and elevated temperature–induced degradation (LeTID), or the sum of several degradation mechanisms described below. Printing of Al- or Ag-fingers on the rear side can cause degradation effects if, for example, acetic acid is formed by decomposition of EVA encapsulant or the fingers becoming detached—for example, by 'floating' of the cell in the encapsulant.

As the anti-reflective coating is exposed to the rear side in bifacial modules, rear-side potential-induced degradation (PID) can occur and cause different effects depending on whether the solar cell has a front- or rear-side emitter. Transparent backsheet and frameless double-glass modules could be other sources for potential degradation, and an inhomogeneous illumination of the rear side could add to the hot spots that may occur due to inhomogeneous illumination on the front side. In the following, we will describe these various effects in more detail.

3.3.1 Light and elevated temperature-induced degradation in bifacial cells/modules

Processing of bifacial solar cells uses different rear dielectrics and temperatures than does processing of monofacial solar cells. The resulting LeTID of bifacial can differ significantly from the monofacial counterpart, mostly due to the contribution of hydrogen-induced degradation.

Table 6 summarizes the known and most prominent degradation mechanisms caused by the formation of boron-oxygen complexes [60], [61], hydrogenation of metallic impurities [61], [62], [63], and de-passivation of PERC´s rear side [64]. Adapting the c-Si material and solar cell process to address the causes shown in Table 6 can minimize the degradation [65]. In addition, many cell producers use a stabilization process after cell fabrication to boost the solar cell into a non-degrading state. If none of these measures is taken, the module can degrade as shown in Figure 17.

Table 6: Summary of PERC degradations and possible solutions during cell process.

Degradation mechanism	LID	HID	Passivation degradation
Cause	BO complex formation	High hydrogen concentration	Depassivation of dielectrics on undiffused surfaces
Reduction on cell level	• Low oxygen Si material • High resistivity Si material • Stabilization process • Ga-doping • N-type devices	• Use of H-poor dielectric layers • Adapted process temperature kinetics • Low firing temperatures • Thin wafers	• Use of low doped BSFs • Upgrade to PERT

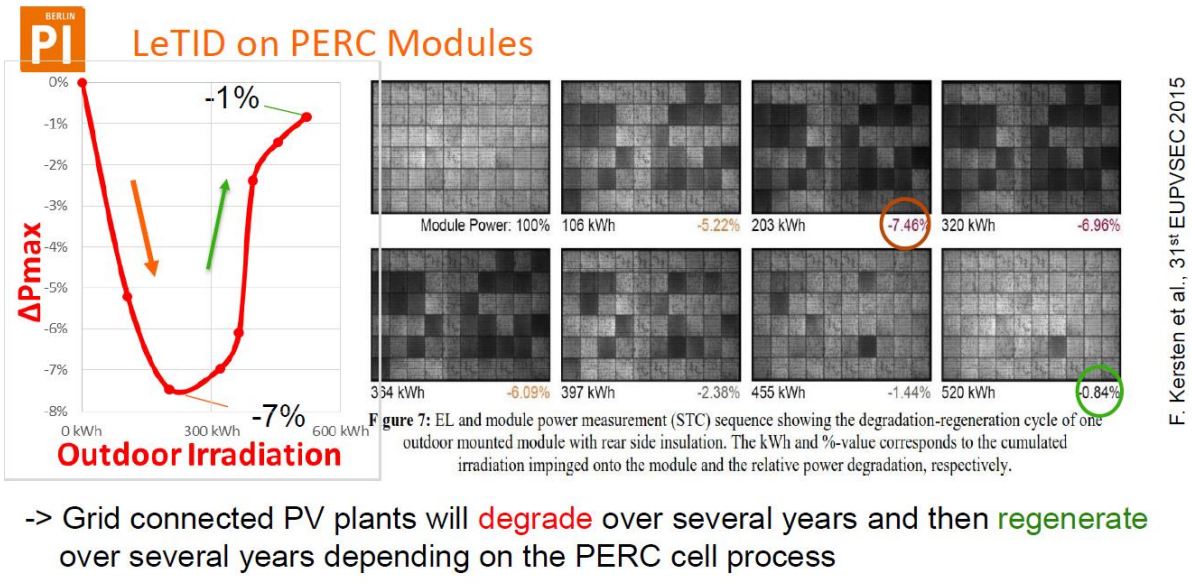

Figure 7: EL and module power measurement (STC) sequence showing the degradation-regeneration cycle of one outdoor mounted module with rear side insulation. The kWh and %-value corresponds to the cumulated irradiation impinged onto the module and the relative power degradation, respectively.

-> Grid connected PV plants will degrade over several years and then regenerate over several years depending on the PERC cell process

Figure 17: Shown are LeTID and regeneration in PERC modules with PERC cells with low quality c-Si material, which were processed with a very H-rich anti-reflective coating and not stabilized after the process.

3.3.2 Potential-induced degradation

PID arises due to a potential difference between solar cells and earth (frame and/or glass). It cannot be visually spotted, but power measurements and thermography can help identify PID onsite. Degradation due to potential differences has been seen in bifacial PV modules based on different types of bifacial solar cells: n-type [66], [67] and p-type [68], [69].

The frame, glass, encapsulant, and other module packaging components can play an important role in the extent of PID of PV modules. PID concerns are reduced when the bifacial module is frameless. Using polyolefin elastomer as encapsulant material can significantly reduce PID affection compared to using EVA [66]. In some cases, PID can be avoided at the module level by using polyolefin elastomer or by replacing glass with a transparent backsheet [67].

The structure and the substrate of the bifacial solar cell determines whether the PV module will be affected by a positive or negative potential difference. Boron-based substrates experience degradation under negative voltage (applied to the cell) [67], [68], while phosphorous-based substrates degrade under positive voltage [67]. As indicated in Figure 18, bifacial modules show two types of PID [67], [69]:

1. Shunting type (PID-s), which affects shunting resistance by shunting the junction due to ion migration into stacking faults
2. Polarization type (PID-p), a loss of surface passivation due to ion accumulation on the passivation layer

While PID-s is well understood, the PID-p mechanism is not completely clear. Sodium ions migrating from glass and affecting n-doped layers can explain PID-p. However, p-doped layers are also affected by PID-p [67], and nothing can explain the origin of the negative ion migration. Finally, modules are more affected on the front than on the rear side [67].

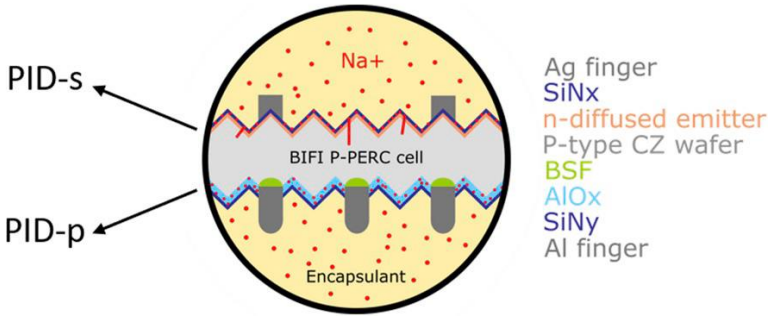

Figure 18: Bifacial PID of bifacial p-PERC solar cells when using glass/glass module: PID-s occurring at the front/emitter side and PID-p occurring at the rear side of the solar cell.

3.3.3 Metallization and encapsulant

Standard solar cells have an Ag-grid and aluminum homogeneous metallization. If Al fingers for bifacial PERC or Ag/Al fingers for nPERT are used, acetic acid formed as a degradation product of EVA can etch the fingers and lead to higher line resistance and reduction of the fill factor. Yingli Solar had some problems with this issue with their Panda modules. As another issue, the floating of cells in the encapsulant can lead to detachment of the fragile fingers.

3.3.4 Frameless modules and transparent backsheets

Currently, 90% of the bifacial modules are double-glass modules. At the beginning of the bifacial era, many double-glass modules were offered with a frameless version. Due to glass breakage during mounting and difficulties related to complicated mounting systems, double-glass modules with frames became state of the art. Some double-glass modules use an edge seal to reduce transport of moisture and other chemicals into the module. Recently, the use of edge seals has declined, raising the possibility of moisture transport into the module package, which can lead to degradation via corrosion and other chemical processes. Transparent backsheets, such as those offered by Dupont, are entering the bifacial market. Such polymers are another source of a possible degradation via moisture ingress, but they also allow acetic acid to dissipate and then reduce the corrosion and power degradation. Therefore, the pros and cons between polymer backsheet and glass is not concluded yet. For encapsulants that do not generate acetic acid, for example POE, the transmission rates of both moisture and acid do not cause the corrosion problems as in EVA. Either one is fine for modules with these encapsulants.

3.3.5 Hotspots

According to IEC 61215, “hot-spot heating occurs in a module when its operating current exceeds the reduced short-circuit current of a shadowed or faulty cell or group of cells within it. When such a condition occurs, the affected cell or group of cells is forced into reverse bias and must dissipate power, which can cause overheating” [51].

When a cell within a string is shaded or faulty, the maximum power dissipation depends on the string operating point, degree of mismatch, and cell-reverse characteristic [70]. For bifacial PV module technology, the degree of current mismatch can vary significantly depending on operating and installation conditions. Torque tube on the tracking system (or even fixed) and hanging wires induce rear-side shading [71]. Bifacial modules generate higher power and therefore higher current (assuming the use of full cell) than do monofacial modules. Therefore, cell mismatch may induce higher local temperature differences on the module. Solar cells with high breakdown voltages induce higher temperatures when operating in reverse bias (for example, under shade).

Installing two rows of bifacial modules at a specific distance from the centered tracking tube can reduce or prevent shading and installing modules with the junction-box near the tracking tube will reduce wiring shading.

4 BIFACIAL SYSTEMS

4.1 Albedo

(Bill Marion)

Albedo is the fraction of the incident sunlight that a surface reflects. It is not a constant for a surface because it varies with the spectral and angular distribution of the sunlight. These variations result from a changing sun position due to time of day, season, and latitude, and whether it is cloudy or sunny.

Except for ice, snow, and water, most surfaces exhibit an increase in albedo for wavelengths greater than about 700 nm [73]. Consequently, because the distribution of the solar spectrum shifts to longer wavelengths in early morning and late afternoon, these periods typically have slightly greater albedos than that measured at midday. Additionally, albedo may increase because the incidence angle of solar radiation to a surface is increased.

Surface conditions also influence the albedo. Dry soils have a greater albedo than wet soils, and dry vegetation has a greater albedo than green vegetation (green vegetation uses the radiation from 400 nm to 700 nm for plant growth). Surface roughness is also a factor, with rougher surfaces having lower albedos because of increased self-shading.

A range of albedo values for various surfaces is shown in Table 7 using information presented by Iqbal [73].

Table 7: Albedo ranges for different surfaces.

Surface	Albedo
Grass	0.15 to 0.26
Snow	0.55 to 0.98
Black soil	0.08 to 0.13
Clay soil	0.16 to 0.23
Sand	0.21 to 0.60
Asphalt pavement, new	0.09
Asphalt pavement, weathered	0.18

4.1.1 Measured albedo data

Albedo measurements are performed with albedometers, which consist of two horizontal irradiance sensors, such as pyranometers, one facing the sky and the other facing the ground. The albedo is the irradiance measured by the ground-facing pyranometer divided by the irradiance measured by the sky-facing pyranometer. Albedometers are typically installed one to two meters above smooth surfaces; increased height is often used in locations with unchecked vegetation or under snow conditions.

Two measurement networks measure albedo in the United States: The Surface Radiation Budget (SURFRAD) network and the AmeriFlux network. The SURFRAD network consists of seven stations and is operated by the National Oceanic and Atmospheric Administration (NOAA). Data is contributed to the AmeriFlux network by individual scientists that operate

stations in North, Central, and South America to measure ecosystem CO_2, water, and energy fluxes.

To facilitate access to measured albedo data, the National Renewable Energy Laboratory assimilated SURFRAD and AmeriFlux data and made it available for download (https://datahub.duramat.org/project/about/albedo-study) the site also includes albedo data contributed by private industry. The albedo data set includes time-series data; tabular monthly and yearly data; plots of monthly and hourly albedo values; and a user's guide. As an example, Figure 19 is a plot of monthly albedo values for Bondville, Illinois USA. The increased albedo and variability in the winter months is due to the presence of snow and its year-to-year variability.

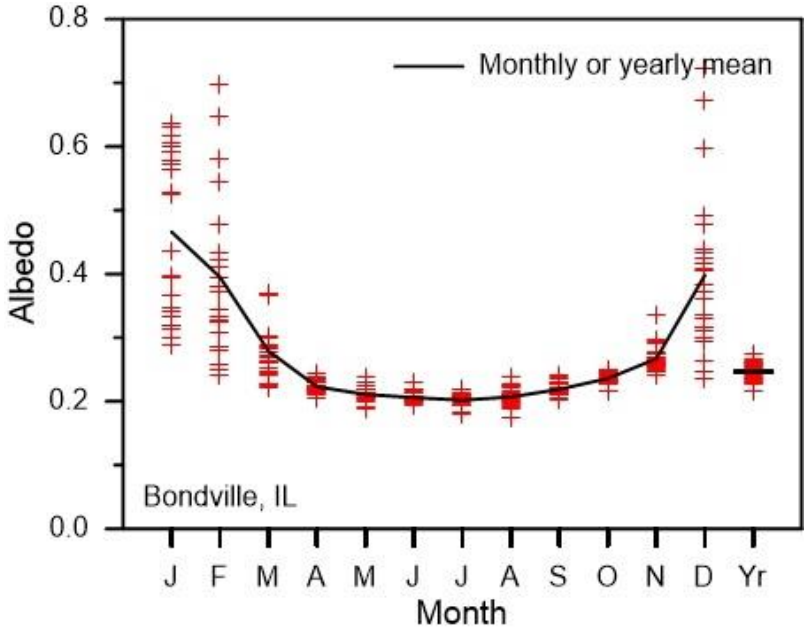

Figure 19: Monthly and yearly albedo means for Bondville, Illinois USA.

4.1.2 Satellite-derived albedo data

Numerous satellite-derived albedo databases exist, with varying spatial and temporal resolution. The primary source for the data is satellite remote-sensing work performed to facilitate the determination of Earth's energy budget. Twenty-one of these databases are listed by Gueymard et al. [74].

One of the most useful sources for the temporal and spatial needs of bifacial PV systems is the moderate resolution imaging spectroradiometer (MODIS) data measured with sensors onboard Terra and Aqua satellites. A 30 arc-second gridded albedo product from these data are derived from multi-angle measurements of surface reflectance over 16-day periods when skies are clear. The National Solar Radiation Database (NSRDB) incorporates MODIS albedo products into its data.

The NSRDB contains time-series solar radiation and meteorological data for the United States and Americas from 21°S to 60°N [75]. To match the 0.04° (4 km) spatial resolution of the NSRDB, the 30 arc-second MODIS pixels are aggregated, using the mean. Typically, from 16 to 25 MODSIS pixels are aggregated into a NSRDB pixel [76]. The NSRDB data may be downloaded via https://nsrdb.nrel.gov.

4.2 Bifacial gain

(Christian Reise)

The additional energy delivered by a bifacial PV system compared to a monofacial system at the same orientation and design is called bifacial gain (BG). This section discusses measuring this additional energy and the issues involved in these measurements.

Section 3.1 describes the measurement and characterization of bifacial modules.

On a system level, bifacial gain is defined as the ratio of the rear-side contribution to the front-side contribution of total energy output over a certain time:

$$\mathrm{BG_{sys}} = E_{\mathrm{rear}} \,/\, E_{\mathrm{front}} \tag{16}$$

BG_{sys} depends heavily on the amount and distribution of the irradiation reaching the rear module surface, which depends on several more factors than for the front surface:

- Mounting geometry (module height, module tilt angle, row-to-row distances)
- Ground albedo and its homogeneity
- Mounting structure, which also influences the homogeneity of rear-side irradiance
- Design and sizing of the balance of system (BOS) components

Given the variety of mounting concepts and other influencing factors, it is obvious that bifacial gain is not simply a property of the module, but also depends on the environmental and mounting conditions of a specific system. Each system layout must be assessed individually, and to fully account for the influencing factors, the bifacial gain can be divided as follows:

- BG_{opt}: Optical bifacial gain
- $BG_{mod:}$ Module (or direct current (DC)) bifacial gain
- BG_{sys}: system bifacial gain

Here, optical bifacial gain refers to the (average) irradiance gain from the rear surface of the module:

$$\mathrm{BG_{opt}} = G_{\mathrm{rear}} \,/\, G_{\mathrm{front}} \tag{17}$$

However, this formula greatly simplifies reality, as neither front nor rear irradiance shows a constant value across a PV module. The front-side irradiance (G_{front}) may suffer from partial shading; at the very least, some part of the diffuse irradiance is blocked by adjacent module rows in many cases. On the rear side, both the mounting geometry and racking structures are inevitable sources of inhomogeneity.

Other issues also complicate proper measurements of BG_{opt}. For example, a single sensor per module surface will not capture the complete distribution of irradiance levels over all of the solar cells. These issues are discussed and quantified further in Section 0.

The rear side of a bifacial PV module is generally less efficient than the front side. The ratio of rear-side to front-side efficiency is called bifaciality factor φ. Thus, the rear-side electricity production of any module will not be proportional to the optical gain, but will be reduced by the bifaciality factor, which leads to the bifacial gain of the module:

$$\mathrm{BG_{mod}} = (\, G_{\mathrm{rear}} * \varphi \,) \,/\, G_{\mathrm{front}} \tag{18}$$

Again, this formula implies some simplifications. A main issue is whether φ is constant or rather depends on such parameters as the irradiance level, the rear-to-front ratio, and operating temperature.

Two main non-linear mechanisms lead to further reduction of the bifacial gain when moving from the PV module to the system level: ohmic losses and clipping losses.

Bifacial PV modules produce higher currents than do monofacial modules, while the output voltage remains more or less constant. If the cable diameters are not adapted to these higher currents, the ohmic losses (for both the DC and alternate current (AC) sides) will increase proportional to the square of the current.

Often, power clipping may be a more influential factor than ohmic losses. Power clipping protects the inverter(s) from overload or is set to enforce a feed-in power limitation at the connection to the utility grid. These losses are mainly influenced by the DC to AC ratio—that is, the nominal power of the PV generator divided by the nominal power of the inverter(s) or by the power limit at the point of energy delivery.

Therefore, the additional electricity production of BG_{sys} may differ from that of BG_{mod}. The final value of BG_{sys} may be derived from two simulation runs (or two measurements), one with bifacial modules and one with monofacial modules, with identical properties:

$$\mathrm{BG}_{\mathrm{sys}} = E_{\mathrm{rear}} \,/\, E_{\mathrm{front}} = (\, E_{\mathrm{bifa}} - E_{\mathrm{mono}} \,) \,/\, E_{\mathrm{mono}} \tag{19}$$

To keep BG_{sys} close to BG_{mod}, the sizing of the BOS components should be adapted to the additional gain from bifacial modules through one of two methods:

- Method A: Use the same number of modules in the bifacial system as in the monofacial system and fit the bifacial BOS components to the increased current and yield
- Method B: Reduce the number of modules in the bifacial system to achieve the same annual yield as produced by the monofacial system

Table 8 expresses these changes in units of $+\Delta$ or $-\Delta$, where Δ is roughly equivalent to the percentage of system bifacial gain BG_{sys}. The table considers cost for both the component costs and for area-related items, such as land lease and fencing.

Table 8: Changes in the sizing of BOS components and area-related costs when shifting from monofacial to bifacial modules.

Cost affected	Method A: no change in module number; yield increased by Δ	Method B: # of bifacial modules decreased by Δ; same yield
Modules		$-\Delta$
Cables	$+\Delta$ (greater diameter)	(less length, greater diameter)
Inverter(s)	$+\Delta$	
Transformer(s)	$+\Delta$	
Area related costs		$-\Delta$

4.3 Nonuniform rear-side irradiance

(Joshua S. Stein and Christian Reise)

Because the rear side of the PV module typically faces the ground—which is usually heterogeneous (such as a mix of plants, rocks, racking, etc.) and experiences complex and changing shadow patterns—the irradiance that reaches the rear side of a PV module and array is typically far less uniform than the light that falls on the front side. This nonuniformity leads to mismatch losses within the system and represents a loss factor that is specific to bifacial PV systems.

Deline et al., [77] presented two metrics for quantifying the irradiance spatial distribution:

- Coefficient of variation (CoV)
- Relative mean absolute difference (RMD)

These metrics can be used to quantify variations in rear-side and total irradiance. The CoV (standard deviation divided by the mean) is a good metric of variability for normally distributed data while the RMD is better suited for describing nonuniformly distributed data. The total irradiance for each cell, *i* of a bifacial module is calculated as:

$$G_{\mathrm{total,i}} = G_{\mathrm{front,i}} + \phi_{\mathrm{Bifi}} G_{\mathrm{rear,i}} \tag{20}$$

where $G_{front,i}$ and $G_{rear,i}$ are the front and rear irradiance on this cell and ϕ_{Bifi} is the bifaciality of the cell.

The CoV of the irradiance across a module is:

$$\sigma[\%] = \frac{1}{\bar{G}_{\mathrm{total}}} \sqrt{\frac{\sum(\mathrm{G_{total,i}} - \bar{G}_{\mathrm{total}})^2}{n-1}} \text{ x } 100\% \tag{21}$$

where $\bar{G}_{total}$ is the mean of the total irradiance for all cells in the module and *n* is the number of cells in the module.

The RMD of the irradiance across a module is:

$$\Delta[\%] = \frac{1}{n^2 \bar{G}_{\mathrm{total}}} \sum_{i=1}^{n} \sum_{j=1}^{n} \left| G_{\mathrm{total,i}} - G_{\mathrm{total,j}} \right| \text{ x } 100\%. \tag{22}$$

Sandia built a custom irradiance distribution module (IDM) to measure the rear-side and total irradiance variability within bifacial PV arrays (Figure 20) [78]. The device was made by attaching 10 calibrated reference cells to the back of an aluminum plate sized like a standard 60-cell PV module. This plate was then placed in different positions within a bifacial array, and the rear-side irradiance distributions were measured.

In December 2016, the IDM was placed in a fixed-tilt bifacial array to measure the spatial variation of the rear-side and total irradiance across the module area. The array was a multi-row, fixed-tilt PV system that was ballasted with concrete blocks with a ground albedo of about 0.25 and a tilt angle of 35° as shown in Figure 21. Figure 22 shows the measured irradiance from this setup for two days.

The CoV and RMD were calculated for the rear-side irradiance at each time step over two example days for this setup. Figure 23 shows that the two metrics are quite similar over the example days. Note that the variation is higher for the clear day and is always much higher at the very start and end of the day, due to very high incident angles and long shadows. The prominent peak in the afternoon is caused by complex light and shadows from the ballast blocks near the IDM, which get partially illuminated in the afternoon causing nearby cells to receive more light than others. These results would likely be different in the summer when

the sun directly shines on the back of the array briefly near sunrise and sunset. Figure 24 shows the same metrics for total irradiance (assuming bifaciality = 1). Note that the variability is about an order of magnitude lower than in Figure 23, and the difference in magnitude between the clear and cloudy days has reduced significantly.

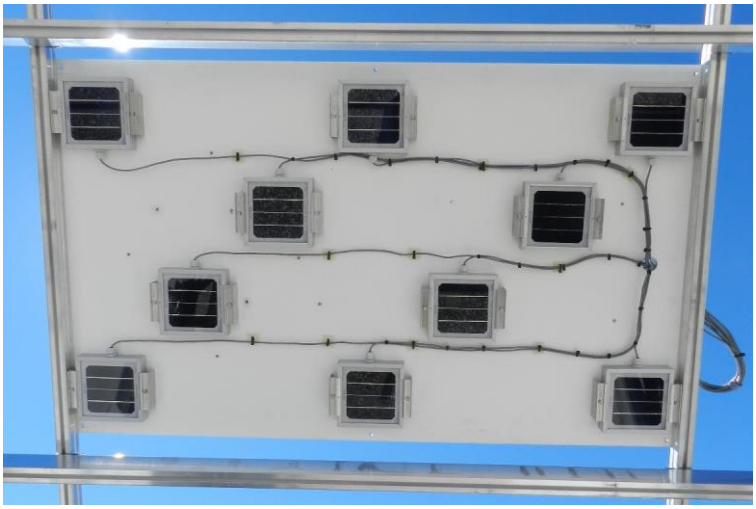

Figure 20: Rear view of the Sandia irradiance distribution module (IDM) showing the placement of the ten reference cells.

Figure 21: (left) Front side of the IDM placed in the middle of a row of modules. (right) Back side of the IDM.

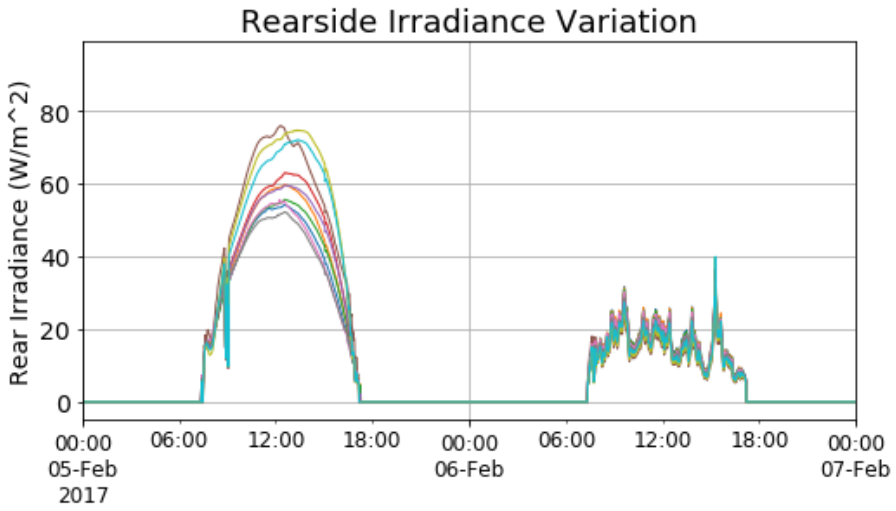

Figure 22: Rear-side irradiance as measured by the ten individual reference cells on the IDM placed in the middle of a row tilted at 35°.

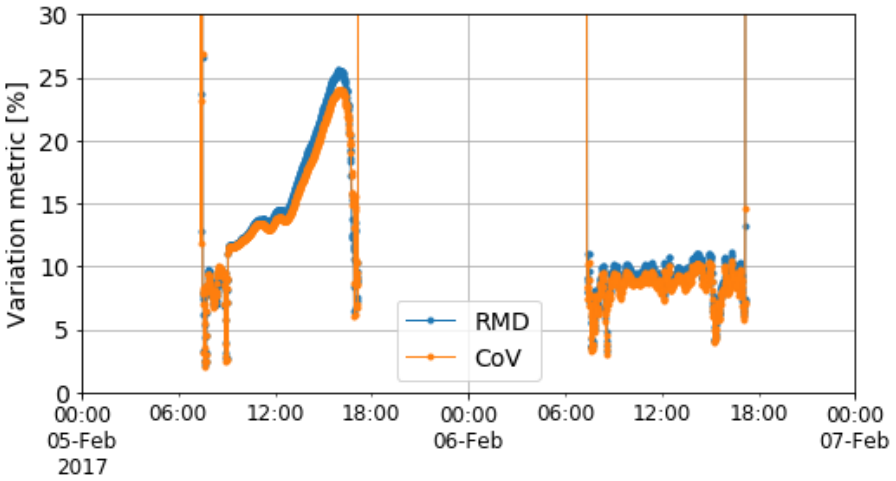

Figure 23: Spatial variation in rear-side irradiance measured at Sandia during two days in New Mexico USA.

While the evaluation shown above is based on measurements on a specific test site, similar investigations may be carried out by numerical simulation.

The example presented in the second part of this section deals with a horizontal single-axis tracked (HSAT) system situated in the desert of central Saudi Arabia. The system layout (which was subject to a commercial yield prediction done by the author) consists of tracker tables with two module rows. The modules are mounted in portrait mode, with a gap along the tracker axis. The table width (including gap) is 4.30 m, the axis-to-axis distance between the trackers is 9.08 m and the albedo is assumed to be around 30%. Module height above ground (when horizontal) is 2.20 m. Due to the optimized construction—characterized by a large distance from the system to the ground and the more homogenous ground (no plants, no concrete blocks), a smaller inhomogeneity would be expected.

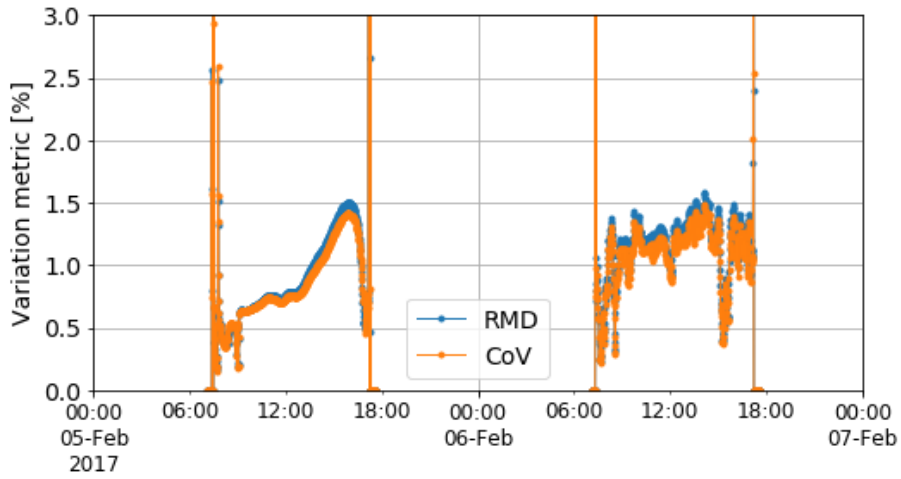

Figure 24: Spatial variation in total irradiance measured at Sandia during two days in New Mexico USA.

Figure 25 presents the front-side, rear-side and effective irradiance (with φ = 70%) for a cross-section through one tracker table, (i.e., two modules) for a given set of meteorological conditions. The rear-side irradiance decreases remarkably from the edge towards the center of the tracker table. The influence of the torque tube (in this case a rectangular tube) is negligible and seen on rear-side irradiance only. For one full day of operation, Figure 26 shows the irradiance distribution in steps of 15 minutes.

To enable a direct comparison to the fixed system shown above, the same metric CoV is utilized for the HSAT system. Figure 27 gives the spatial variation of rear-side irradiance, while Figure 28 gives the same for the effective irradiance (i.e., $G_{front} + \varphi G_{rear}$). Both figures combine the results for four different days; the CoV hardly depends on the seasons or the absolute irradiance level. In contrast to possible expectations, the values of CoV calculated for this tracker design are quite similar to those of the experimental system in New Mexico. This may lead to the conclusion that the spatial variation of rear-side irradiance is influenced mainly by overall geometry and less by single structure elements.

Further calculations on single-axis trackers showed that the inhomogeneity of the irradiation on the rear side is certainly noticeable, but together with the irradiation on the front side it only causes a variation of ±5% in the total irradiation. In the extreme case of one module in portrait mode on a single-axis tracker, the mismatch losses per module remained below 0.5%. This means that there is no significant reduction in yield per module

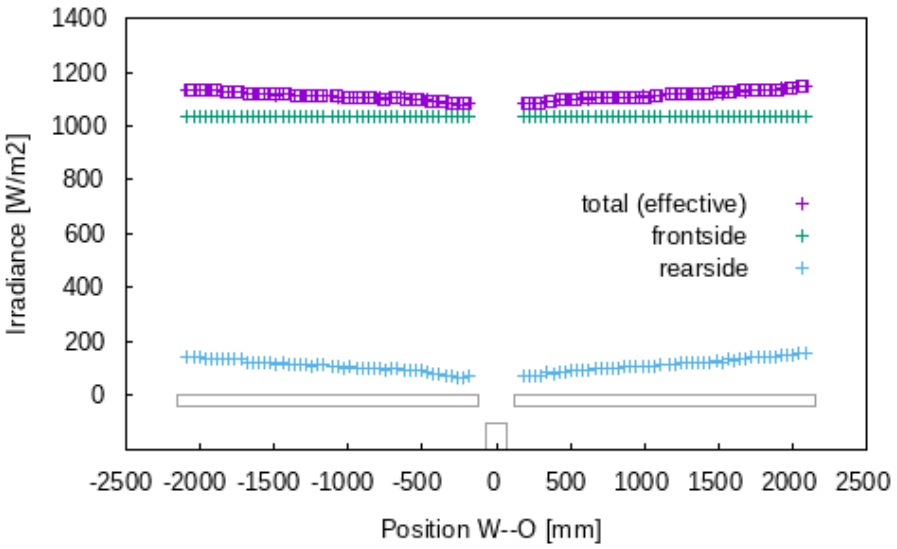

Figure 25: Irradiance levels across two modules on a horizontal single-axis tracker (2P) for one exemplary time step (noon at June 21st). Rear-side irradiance shows a mostly linear decrease from the edge towards the center of the tracker table.

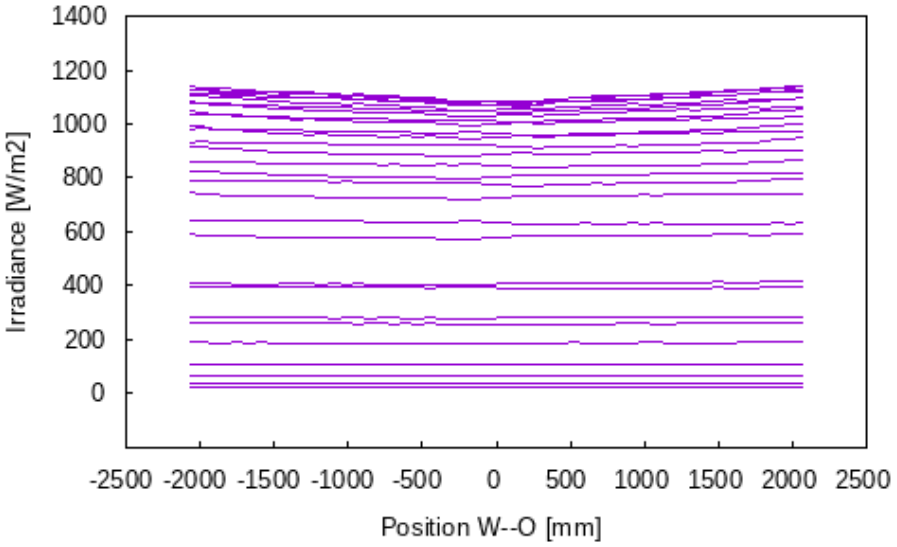

Figure 26: Irradiance levels across two modules on a horizontal single-axis tracker (2P) for all time steps of one day (June 21st). Non-uniformity is more pronounced at high irradiance levels (i.e., around noon) when the tracker position is close to horizontal.

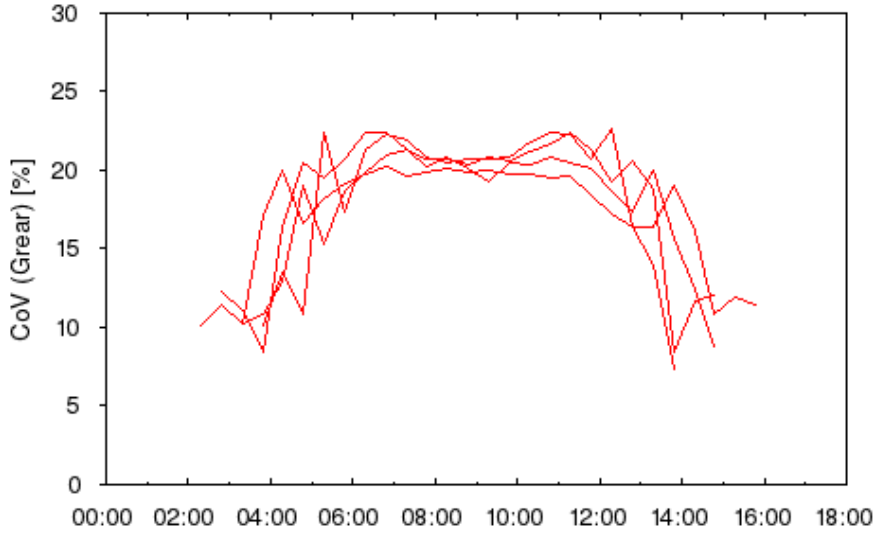

Figure 27: CoV of rear-side irradiance across two modules on a horizontal single-axis tracker (2P) for all time steps of four days (March 21, June 21, September 21, and December 21).

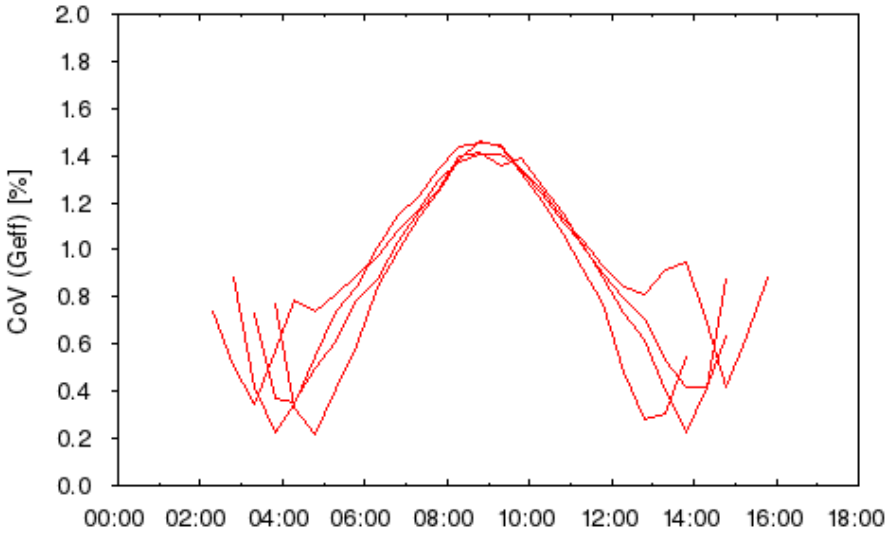

Figure 28: CoV of effective irradiance across two modules on a horizontal single-axis tracker (2P) for all time steps of four days (March 21, June 21, September 21, and December 21). The non-uniformity is more pronounced at high irradiance levels, (i.e, around noon) when the tracker position is close to horizontal.

4.4 Bifacial system maximum currents

(Joshua S. Stein and Daniel Riley)

Because bifacial photovoltaic arrays generate current from light received from the back as well as the front of the array, DC currents from bifacial systems are generally higher than for monofacial arrays, which receive light from only the front side of the array. To ensure that these higher currents do not overload bifacial system components and cause safety issues,

the factors that influence the DC current of bifacial PV modules should be considered during system design and component selection. Such factors include module performance parameters, ground albedo, and system design parameters (e.g., size, tilt, azimuth, height, number of rows, and row spacing).

Sandia National Laboratories analyzed more than three years of DC current measurements from bifacial and monofacial PV single-module systems in three different US climates to determine the frequency and magnitude of the high current events and correlate these values to system design parameters. An optical ray tracing model demonstrated the extent of edge effects that lead to the highest local currents near array edges. Model simulations allowed scaling of the observed currents to larger systems and estimate maximum currents for other sites and design parameters.

To obtain measurements, Sandia installed bifacial and monofacial modules in three locations with different climates: New Mexico, Vermont, and Nevada. Each location has 32 modules (16 bifacial and 16 monofacial) installed over a range of albedo values, tilt angles, and azimuths. In many cases, the incident irradiance causes the modules to produce power in excess of the maximum input power of their attached microinverter, resulting in inverter clipping. Of particular interest in this study is the DC maximum power current (I_{mpp}) produced by each module and the irradiance conditions at each site.

Table 9 describes the orientations and conditions at each site and summarizes the data used in the analysis. Systems 1 through 3 at each site have four monofacial and four bifacial PV modules, and systems 4 and 5 contain two monofacial and two bifacial modules. Each module is grid-connected by a microinverter and monitored for DC current and voltage. The irradiance falling on the front and rear side of all PV systems is measured by a pair of reference cells mounted near the center of each system. All monitored values are 1-min averages of measurements made every five seconds.

Table 9: Summary of site and experimental data.

	Albuquerque, New Mexico	**Henderson, Nevada**	**Burlington, Vermont**
Data Start Date	2016-02-16	2016-12-24	2017-03-29
Data End Date	2020-07-01	2020-07-01	2019-04-01
Number of observations	2,218,361	1,850,648	869,540
Natural Albedo	0.22	0.2	0.18-0.22 (depends on grass condition)
Enhanced Albedo	0.6	0.3	0.25
System 1	West-facing, 15° tilt, high albedo	West-facing, 15° tilt, high albedo	West-facing, 30° tilt, high albedo
System 2	South-facing, 15° tilt, high albedo	South-facing, 15° tilt, high albedo	South-facing, 30° tilt, high albedo
System 3	South-facing, 30° tilt, natural albedo	South-facing, 30° tilt, natural albedo	South-facing, 30° tilt, natural albedo
System 4	South-facing, 90° tilt	South-facing, 90° tilt	South-facing, 90° tilt
System 5	West-facing, 90° tilt	West-facing, 90° tilt	West-facing, 90° tilt

For each module at each site, analysts plotted measured I_{mpp} against total irradiance which is the front-side irradiance for monofacial modules and the sum of front-side and rear-side irradiance for bifacial modules. They then created a linear regression of the data, excluding current values below 0.05 A to avoid nighttime data and data from shutdown periods, as well as current values above 10.2 A (inverter self-limiting). The first term of the linear regression (slope) provides an approximate relationship between total irradiance and I_{mpp}, and analysis shows the value of the regression fit evaluated at the maximum total irradiance in the observation period, which is an estimate of the maximum current in the absence of inverter clipping (Figure 29).

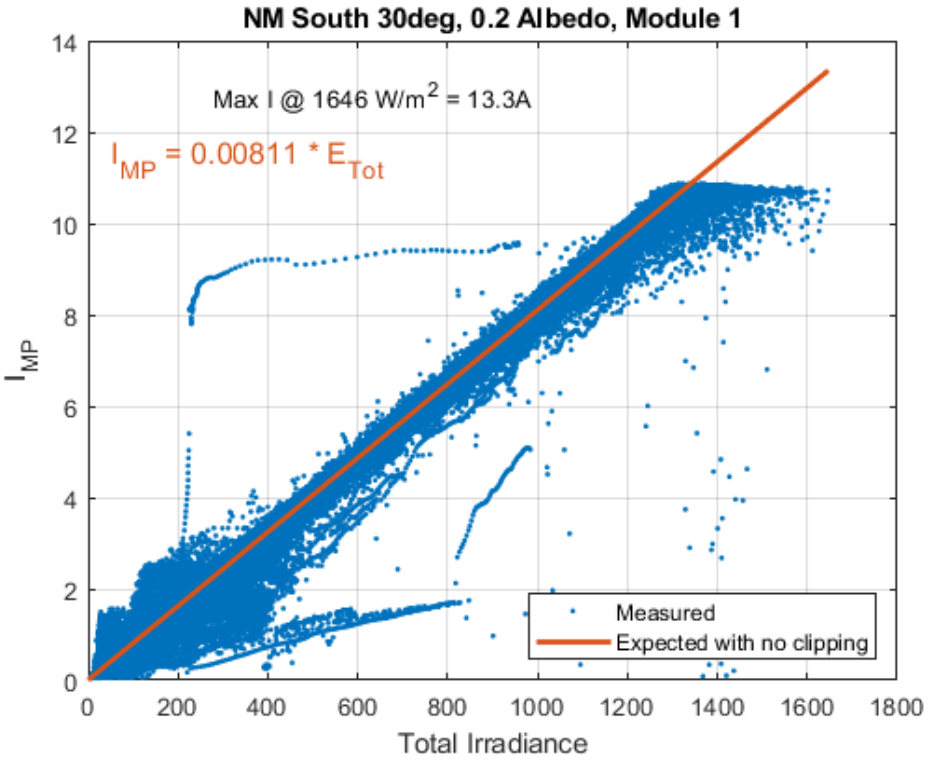

Figure 29: Example scatter plot of 1-min I_{mpp} values from a bifacial module in New Mexico plotted against total irradiance (front + rear). Red regression line extends to the maximum measured total irradiance. Maximum 1-min current is estimated from the I_{mpp} value at the maximum total irradiance.

They also analyzed empirical cumulative distribution functions for the front, rear, and total irradiance of each orientation. Analysis of the top 1% of irradiances provides a sense of the high irradiances at each site and orientation. The cumulative distribution function for total irradiance can be combined with the regression equation to estimate the probability of exceeding a given current over the observation period with a bifacial PV module. Table 10 summarizes results of 1-minute maximum currents and total irradiances for the bifacial modules.

Table 10: One-minute total irradiance measured on bifacial modules at each site and expected maximum current without inverter self-limiting.

	Albuquerque, New Mexico		Henderson, Nevada		Burlington, Vermont	
System	Max Current (A)	Max Irradiance (W/m^2)	Max Current (A)	Max Irradiance (W/m^2)	Max Current (A)	Max Irradiance (W/m^2)
1	15.3-15.9	2167	13.6-13.7	1672	12.5-13.1	1593
2	15.1-15.7	2050	13.8-14	1708	14.9-15.6	1885
3	13.3-13.4	1646	13.4-13.7	1668	14-14.7	1765
4	10.9-11	1310	11-11.1	1302	14.5	1885
5	9.6-9.8	1273	9.4	1207	11-11.1	1468

Table 11 shows the same quantities for 3-hour averages, which are important for evaluating wire sizing requirements for bifacial arrays.

These results demonstrate that bifacial PV systems operate at significantly higher DC currents than do similar monofacial systems. The highest currents occur as the result of high albedo (e.g., snowfall) and brief but very high irradiance periods likely caused by sunny conditions with cloud enhancement. These results will help PV designers optimize the designs of bifacial PV systems to minimize systems costs while creating systems able to safely handle the extra electrical current that is produced from bifacial modules.

Table 11: Three-hour average total irradiance measured on bifacial modules at each site and expected maximum current without inverter self-limiting

	Albuquerque, New Mexico		Henderson, Nevada		Burlington, Vermont	
System	Max Current (A)	Max Irradiance (W/m^2)	Max Current (A)	Max Irradiance (W/m^2)	Max Current (A)	Max Irradiance (W/m^2)
1	10.4-11.2	1520	9.9-10	1225	8.8-9.2	1120
2	11.5-11.9	1566	10.1-10.3	1254	11.3-11.8	1417
3	10.3-10.4	1276	10-10.1	1238	11.3-11.8	1415
4	9.4-9.5	1138	8.5-8.6	1012	10.5	1353
5	7.7	1009	7.6	979	8.7	1153

4.5 Fixed-tilt systems

(Cameron Stark, Sandia)

The performance of bifacial modules in a fixed-tilt orientation has been studied by many researchers [79]–[83]. However, most of these studies use field data measured from very small systems, sometimes consisting of one or a few modules in a single row (e.g., [84]). Such studies have reported very high bifacial gains and led to overly optimistic estimates of the additional energy that larger bifacial systems can deliver.

In fact, it is important to examine bifacial fixed-tilt systems in arrays, as many array design features influence fixed-tilt bifacial performance. Specifically, the amount of light that can

reach the rear side of a bifacial PV module depends on many factors, including ground albedo; height, tilt, and azimuth of the array; and the number and spacing of rows and position of the module within the row [85], [86]. The modules that receive the highest rear-side irradiance are those located nearest the end of a row and in the back row of an array. In this section, we present simulations of fixed tilt systems that demonstrate the impact of array design on performance

Sandia National Laboratories has utilized the NREL open-source Python module *bifacial_radiance* to perform parametric studies of fixed-tilt systems. The *bifacial_radiance* module is a Python wrapper for the raytrace software suite Radiance [87]. Raytracing offers the ability to model the complexities of bifacial systems. Because such simulations are computationally intensive, Sandia leveraged its array high-performance computers (HPCs) to conduct the study described here.

The range of simulations and analysis discussed in this section were run for a total of three days per month over 12 months, or 36 days, using weather data from Albuquerque, New Mexico, USA. The days are chosen from the minimum, median, and maximum daily insolation for each month. System design and site parameters were varied to explore their role in bifacial performance. Row spacing was adjusted depending on tilt angle to avoid row-to-row shading one hour before/after sunrise/sunset on the winter solstice.

4.5.1 Edge effects along rows in fixed-tilt systems

The initial set of simulations focused on the center module of a single south-facing row. The row initially consisted of only a single module with its rear irradiance simulated. A module was then added on either side of the center module for subsequent simulations of up to nine modules on either side of the central module. Albedo, tilt, and module height were held constant for this study at 0.25, 35°, and 1 meter, respectively. The results in Figure 30 show that the single isolated module is exposed to more than 45% more rear irradiation than the central module of a full row.

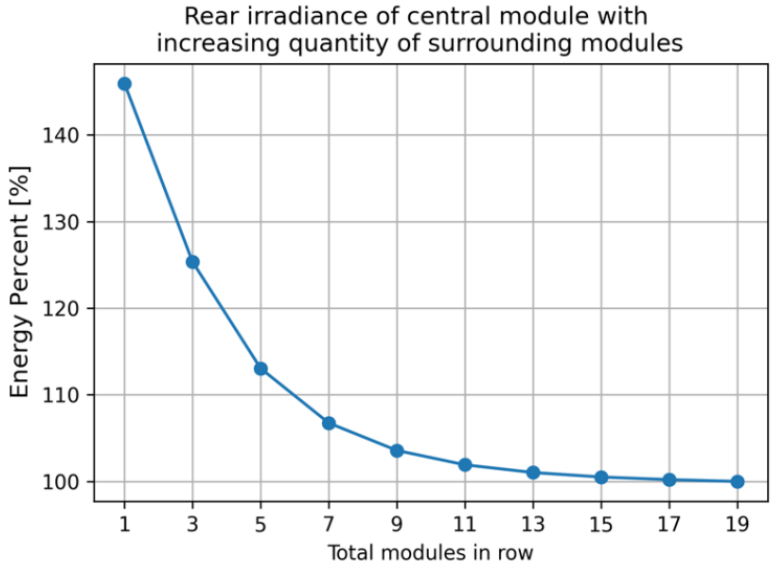

Figure 30: Relative rear irradiance for the central module in a single row of modules as a function of number of modules in the row. 100% represents the lowest irradiance in the center of a long row of modules.

The next scenario studied was a south-facing row of 49 modules with irradiation simulated on the front and back of each module from the center module to the western-most module at the end of the row. We sequentially added identical rows of modules to the north and south of the first row and observed the effect on rear irradiation on modules in the center row. The ground albedo in this example is 0.25, height is 1 m, and tilt is 35°.

Figure 31 shows two important features of fixed-tilt, multi-row bifacial systems:

- Decrease in rear irradiation as rows increase: The rear-side irradiation at the middle of the row drops by over 15% as additional rows are added. The effect is most significant between the single row and three row case. However, adding more rows continues to slightly reduce rear irradiation.
- Increase in rear irradiation in modules near row edges: In the single-row example, the module nearest the edge experiences ~25% more rear-side irradiance than do the modules in the center of the row. Interestingly, the relative increase for edge modules is higher for the multi-row examples.

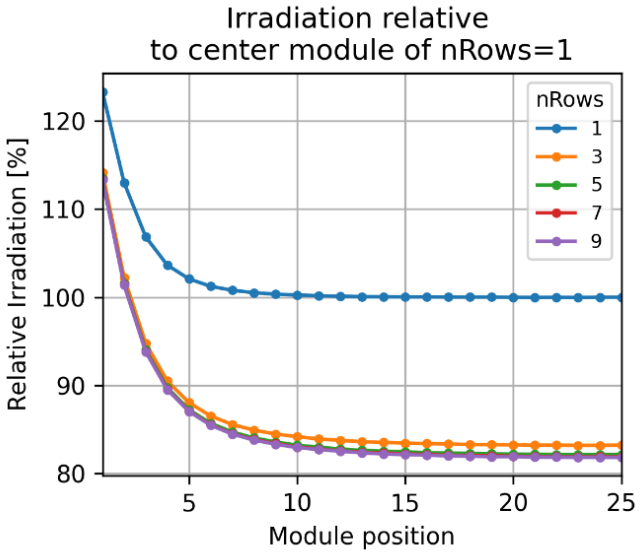

Figure 31: Percent in rear-side irradiation relative to the center-most module of a single row system for systems with differing number of rows.

4.5.2 Role of albedo in multi-row fixed-tilt systems

The next set of simulations examined the role of albedo on rear-side irradiation in multi-row, fixed-tilt systems. This scenario simulated a single row at a 35° tilt angle at three different albedo values: 0.1, 0.25 and 0.8. Figure 32 compares the run results.

Once again, there are two main conclusions from these runs. First, rear-side irradiance is highly correlated with albedo. Note that the relative increase in rear-side irradiance is slightly lower than the relative increase in albedo. This reduction is due to the self-shading around the array. Second, the magnitude of the edge effect increases with albedo. This makes sense because modules on the edge are receiving more light from unshaded ground.

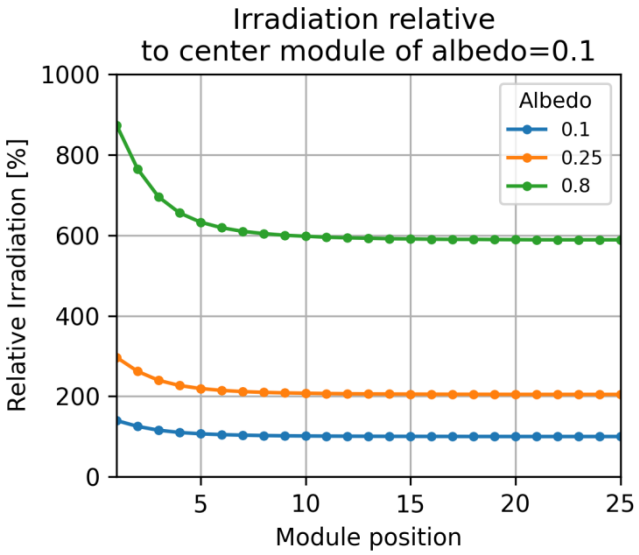

Figure 32: Percent in rear-side irradiation relative to the center-most module in the array with an albedo of 0.1.

Next we looked at the relationship of tilt angle and rear-side irradiance by simulating five rows at 0.25 albedo with different tilt angles and correlated pitch value. It is commonly known that front-side insolation is typically maximized when the array tilt is close to the latitude of the site. For the rear-side, increasing tilt angle increases the proportion of the rear irradiance coming from the sky dome. In this example, back-side irradiance increased with tilt angle because the light coming from ground reflection is lower than the diffuse light coming from the sky. In the case of higher ground albedos, this pattern will change and may reverse when ground albedo is very high (e.g., with snow). Simulation results are shown in Figure 33.

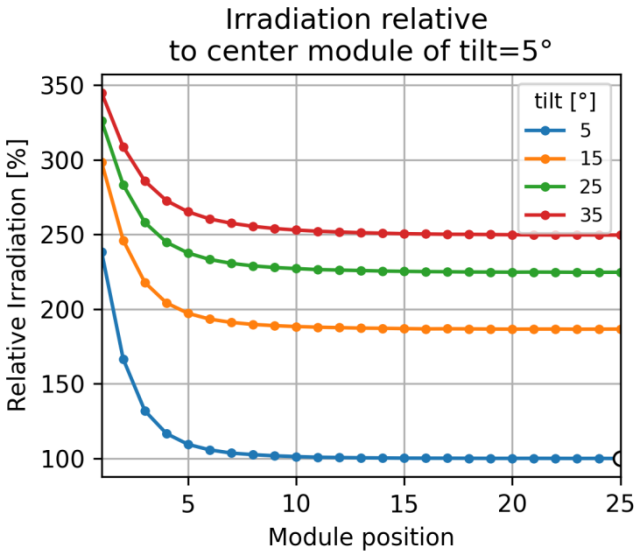

Figure 33: Percent in rear-side irradiation relative to the center-most module in the array with a tilt angle of 5°.

4.5.3 Spatial patterns of rear-side irradiance across a multi-row, fixed-tilt system

Next we ran a parametric study to show these effects across the array, not just the center row. Figure 34 shows a matrix of the western half of simulated arrays. Since the arrays are facing south, the eastern half is symmetrical to the western half. The numbers and their correlating color describe the relative percent increase in rear-side irradiance compared to the central module, considered a baseline reference as it receives the lowest rear irradiance. Each array within this matrix differs in tilt/pitch and height from the ground. Albedo is held constant at 0.8 for all arrays in this visualization but can be varied as necessary.

From this singular visualization, the radial increase in rear irradiance from the center module (row 3, column 10) can be observed. The row-to-row difference observed is most notable in the array corners. As array tilt increases, the northernmost (back) row receives more rear irradiance compared with the lower tilt angle case, which shows increased rear-side irradiance on the front row.

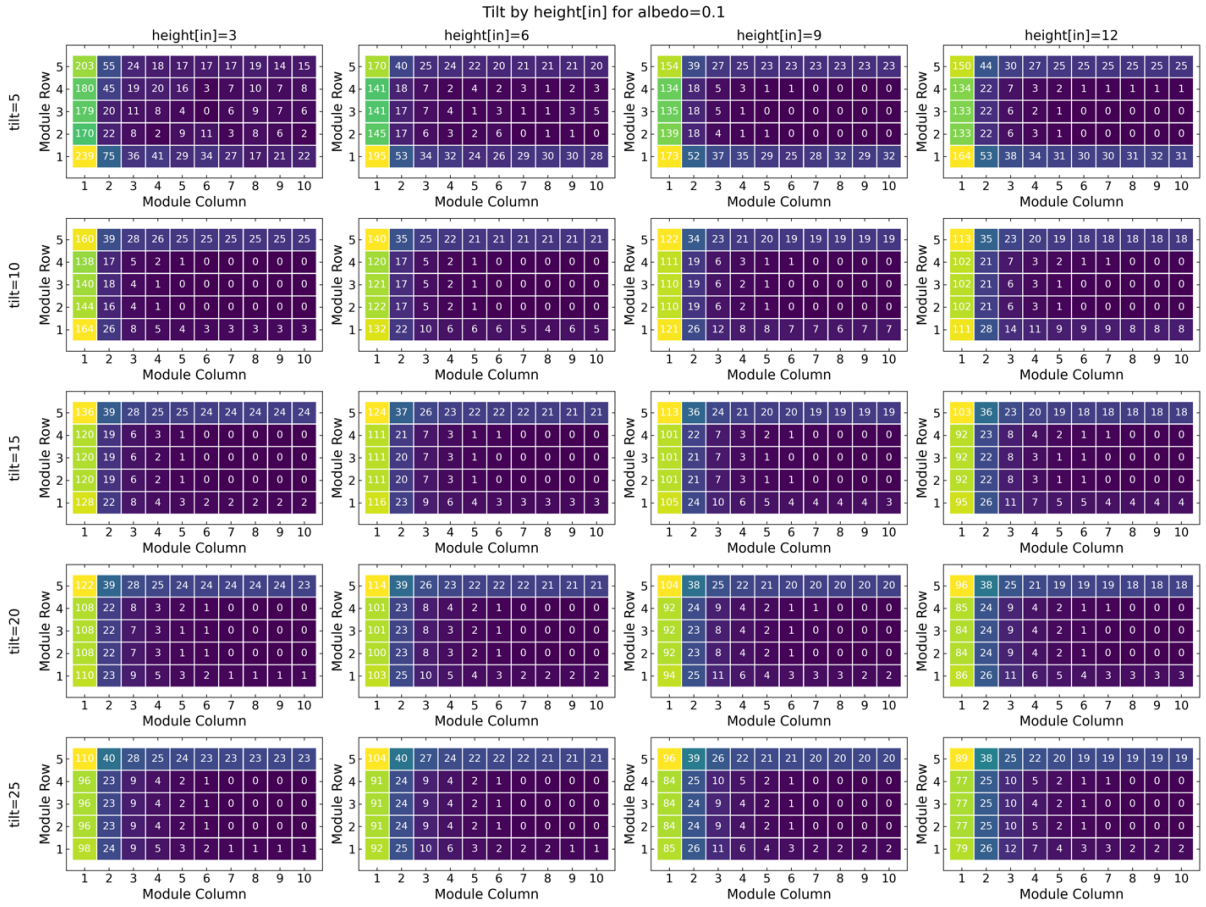

Figure 34: Matrix view of the western half of five-row systems showing percent increase in rear-side irradiation as compared with the center-most module. Each run is at a different tilt angle and pitch (row in the matrix) and module height (column in the matrix).

These matrix simulations demonstrate a saturation of rear-side irradiance for modules located away from the edges of the system. This saturation occurs within seven to nine modules from the east and west edges and within three to four rows from the north and south edges. Therefore, simulating more rows or more modules per row does not add any new information.

To take advantage of this saturation, we developed a technique to use these half-system simulations as templates to build larger systems. Figure 35 shows how small-template systems can represent larger systems. The corners and sides of the template systems surround the larger systems while center modules are simply repeated in the areas that are far enough from the edges to experience any edge effects.

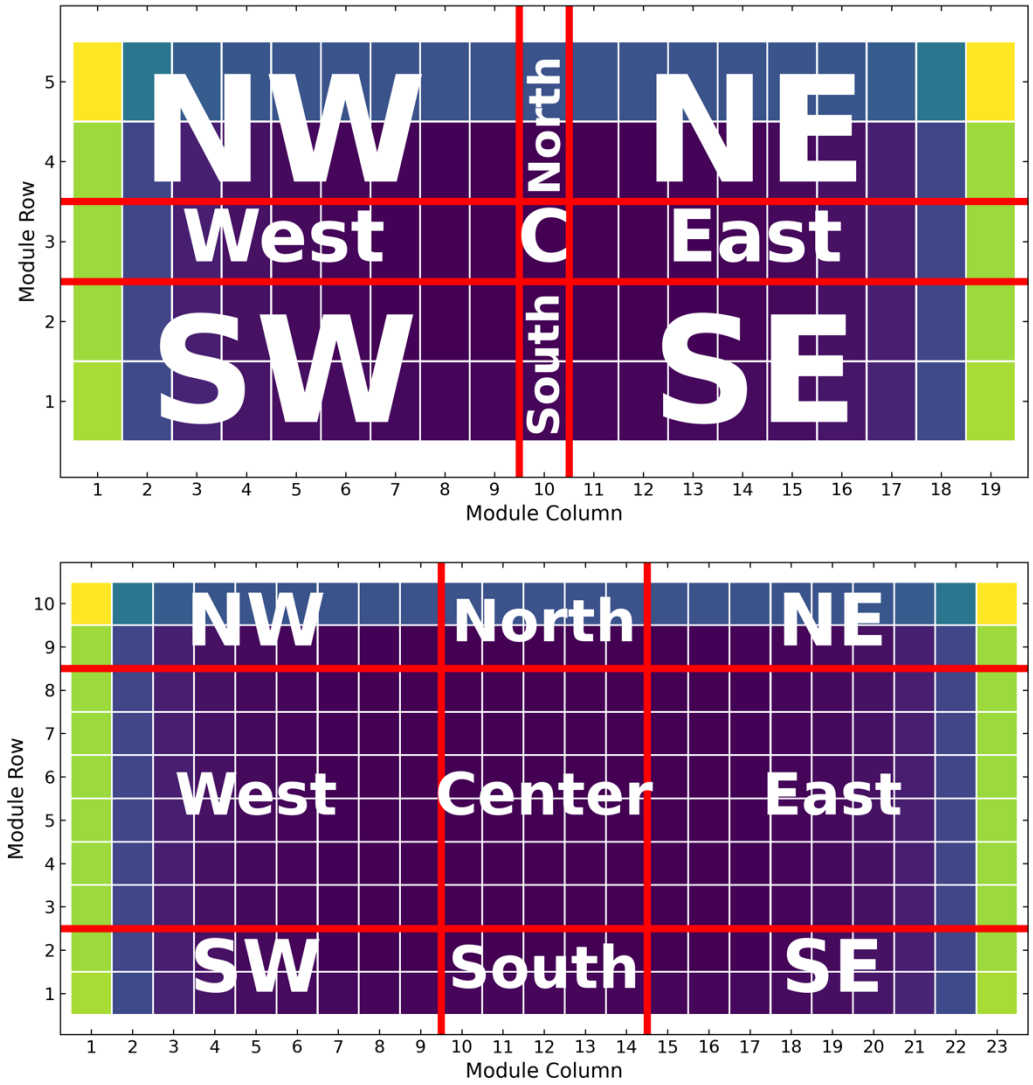

Figure 35: (top) Classification of the template system regions; (bottom) Application of classified regions to a larger array geometry.

Figure 35 demonstrates the “stretching” of the cardinal directions (north, south, east, and west) where the section above is replicated to adjacent rows or columns. The corners of the template array (north-west, south-west, south-east, north-east) stay the same size as the template since they are exposed to their unique edge effects.

Next we used this technique on the parametric simulations shown in Figure 34 to investigate the effects of edge effects on a wider variety of system configurations. We first studied the effect of the aspect ratio (number of rows vs. number of modules per row) on system bifacial gains. In this example, we examined six different system aspect ratios, two albedos, four heights, and five tilt angles. The aspect ratios we considered are listed in Table 12. Results of the impact of these factors, highlighted in Figure 36, show that albedo is of primary importance to bifacial gains, followed by tilt angle and height. The aspect ratio shows a slight increase in bifacial gain for more narrow systems east-to-west. However, this effect is more heavily dominated by system height and tilt angle.

Table 12. System aspect ratios examined in parameter study of their effect on bifacial gain.

Aspect Ratio	Number of rows	Number of modules per row
1:25	5	125
1:6	9	69
1:3	15	43
1:2	19	33
1:1	25	25
2:1	33	19

4.5.4 Implications for area constrained bifacial systems

The previous example did not consider land usage. The next example focuses on maximizing energy per area and system investment more specifically. For this example, we constrained the system to a 100 m x 100 m square area and allowed the tilt angle–based pitch calculation to determine the size of the system. The template systems were then used to describe the overall power generation.

Figure 37 shows the results of the space-constrained fixed-tilt bifacial example. Increasing tilt also increases row spacing (pitch), which lowers the total number of modules in the system and reduces the energy produced. Figure 38 shows the same results in terms of energy produced per module, which has the opposite trend. Each module produces more energy as tilt angle increases, largely due to the same factors the affect monofacial arrays. Higher albedo increases the slope of this effect. The curvature of the increase suggests that there are diminishing returns for increasing module tilt.

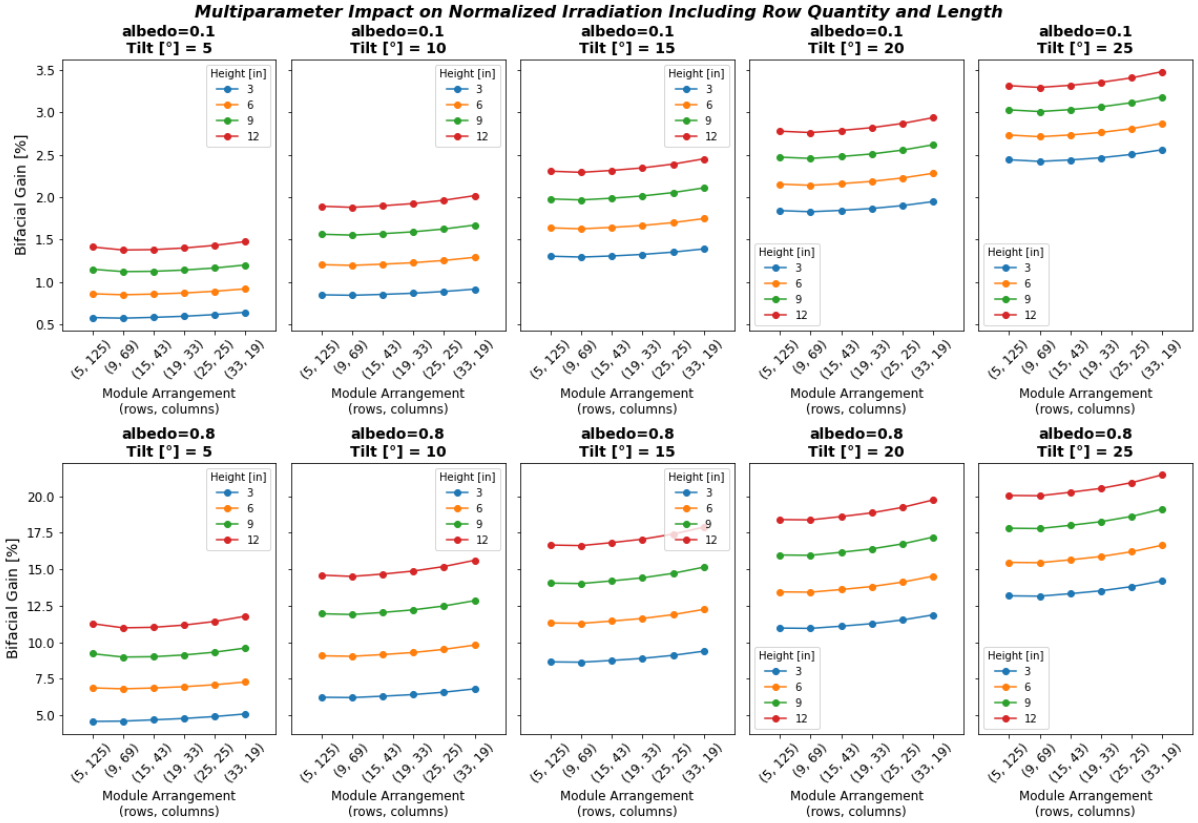

Figure 36: Annual bifacial gain for fixed-tilt systems with varying albedo (rows), tilt angle (columns), and height (lines) for different aspect ratios (x-axis).

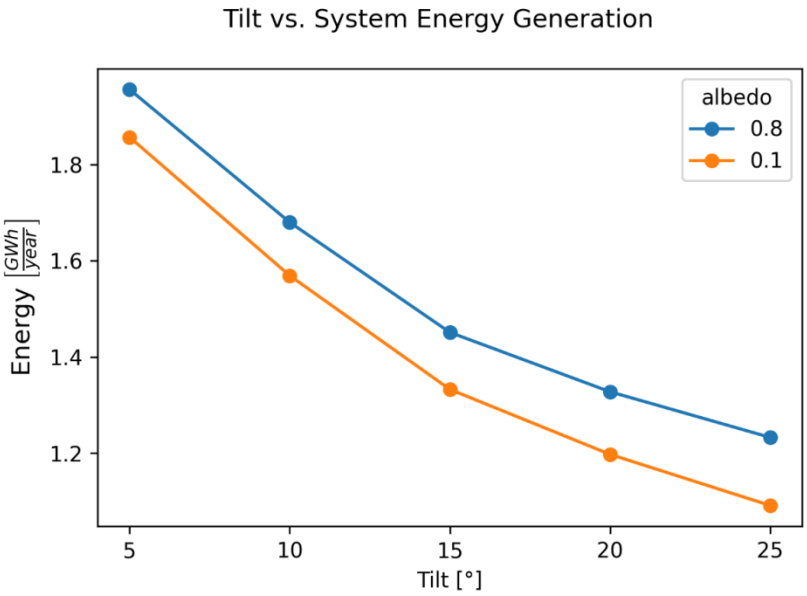

Figure 37: Bifacial array energy produced as a function of tilt angle for a fixed array area.

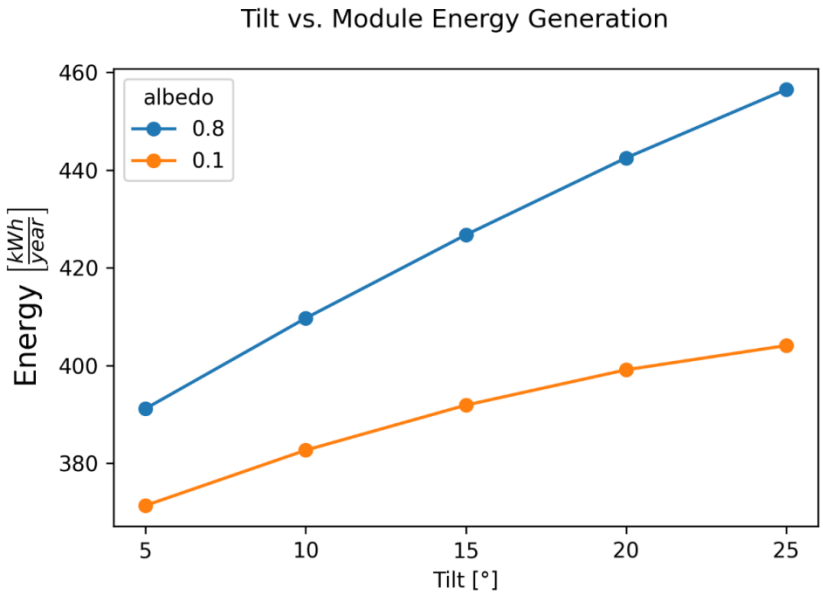

Figure 38: Bifacial energy produced per module as a function of tilt angle for a fixed array area.

These simulations underscore the importance of considering numerous factors when designing a south-facing fixed-tilt bifacial PV system. In most cases, albedo will likely be the most important factor in determining the degree of bifacial gain, but tilt and height are also key. If racking system costs allow and area is not constrained, raising the system higher off the ground (or roof) and increasing tilt angle may increase bifacial gains. Use of microinverters or DC optimizers to optimize bifacial system edge effects might increase the energy yield of a given design. Clearly, the contributing costs associated with these choices need to be weighed against the potential advantages. Overall, the studies described above provide a sense for the dynamics at play for generalized south-facing fixed tilt-bifacial systems.

4.6 Single-axis tracking systems

(Annie C. J. Russell, Christopher E. Valdivia, Karin Hinzer)

Single-axis trackers (SATs) rotate panels around an axis to optimize energy generation throughout the day. The power output of a flat photovoltaic panel decreases by a cosine factor of the angle of incidence between incident light rays and a line perpendicular to the panel surface. A SAT directs the panels toward the sun to minimize this angle and to maximize energy generation. For horizontal single-axis trackers, the axis of rotation is parallel to the ground, most commonly in the north-south direction (N-S HSAT). In this case, panels track the sun across the sky from east to west throughout the day.

Bifacial panels are frequently placed on SATs to maximize front-side irradiance while benefiting from rear-side irradiance that can drive down a project's levelized cost of electricity. The year 2018 saw a 40% increase in SAT shipments, and IHS Markit predicts that increased bifacial PV sales will be a key driver in tracker adoption in the next five years [88].

Bifacial performance on SATs depends on a variety of factors, including tracking algorithm, system design, and location-specific environmental factors (e.g., albedo, solar resource, and latitude). The following sections discuss research on these factors and reported bifacial gains seen for SATs.

4.6.1 Tracking algorithms for bifacial PV

The rotational angle of a single-axis tracked system will be dictated by one of two primary tracking algorithms: an astronomical algorithm or a light-intensity algorithm. Astronomical tracking algorithms calculate tracking angle based on the sun position to minimize the angle of incidence between direct light rays and the normal to the panel plane [89]. This mode of operation is also called *true-tracking*, and panels are referred to as *on-sun*. However, in practice, the tracker‘s mechanical system limits the available tracking range (most commonly ±60° from horizontal. For N-S HSATs, inter-row shading occurs in the morning and evening when the sun is close to the horizon; the resulting irradiance non-uniformity on the front of the panel can lead to significant current limitation and hotspots [90].

Backtracking, a common adjustment to the astronomical single-axis tracking angle, is intended to eliminate this row-to-row shading by reducing the angle of all rows toward horizontal during morning and evening hours. This adjustment results in higher cosine-losses but less electrical mismatch, creating a net increase in power output. The adjusted tracking angle is based on the elevation angle of the sun, the collector width, and the tracker pitch [91]. The conventional backtracking algorithm is designed for flat ground and does not eliminate inter-row shading for more complex terrain. Backtracking algorithms that consider the relative height of each row have been developed for use with independent row trackers. For instance, NEXTracker reports that such algorithms increase monofacial energy yield by 3.6% as compared to conventional backtracking for a field with 3% to 15% grade slopes [92]. Asgharzadeh et al. [90] found that bifacial insolation gain values for SATs were relatively similar for backtracking vs. true-tracking (without the effect of electrical mismatch caused by row-to-row shading). The paper stresses that maximizing front-side insolation should be the top priority for tracking strategies.

In contrast to astronomical algorithms, light-intensity algorithms adjust tracker position based on real-time irradiance conditions. In 2011, Kelly & Gibson [93] showed that tracking systems could position panels horizontally on cloudy days to increase the annual energy yield by 1%. NEXTracker’s whitepaper reports a similar 0.5% to 2% annual increase in energy yield due to diffuse light optimization [92]. Pelaez et al. found that similar optimization for sky conditions leads to a 0.6% to 1.1% modeled irradiance gain for bifacial single-axis trackers on 0.2 to 0.8 albedo in Albuquerque, NM [94]. This relative gain is dependent on location and increases for regions with higher diffuse content.

4.6.2 Bifacial design options for single-axis tracker geometry

For conventional single-axis trackers, a table of panels is typically bound to a torque tube—a shaft that runs along the axis of rotation, supported by vertical pilings. The tracking algorithm determines the torque tube rotation angle required to achieve the desired panel position. While the cross-sectional shape of torque-tubes vary, they are most commonly cylindrical, square, or octagonal. Panels can be installed in portrait orientation (with the short side of the panel parallel to the torque tube) or landscape orientation (with the long side parallel).

Single-axis tracker configurations are typically grouped based on the ‘X-up’ naming convention, which refers to trackers with X panels stacked in the direction perpendicular to the axis of rotation. For example, in 1P systems, a single panel lies across the torque tube. In 2P configurations, one panel lies on either side of the torque tube (e.g., for N-S HSAT, one panel is placed to the east torque tube and the other to the west). Some trackers include a space between these panels to reduce rear-side shading. Note that 1P and 2P portrait configurations have also been referred to as 1-up and 2-up, respectively, or 1MIP and 2MIP (module

in portrait). The following paragraphs provide examples of the ongoing analysis of 1P and 2P tracker performance.

Pelaez et al. [94] modeled the rear-side irradiance loss for a 1P panel in the bifacial_radiance ray-tracing software. The shading loss due to the torque tube approaches 20% of rear-incident light and reduces with increasing distance between the panels and torque tube. The panel irradiance profile also shows a brighter band at the center of the torque tube shadow, partly due to reflection off of the metallic torque tube. Another study with bifacial_radiance by Deline et al. [77] indicates that the annual electrical mismatch losses due to rear-side non-uniformity for a single-axis tracked 1P panel is less than 0.5% (under 0.2 albedo conditions).

Simulations in bifacial_radiance for 2P trackers reveal that rear-side shading factors range from 2 to 8% depending on the specific installation [95]. For example, this study shows that a 15-cm gap between 2P panels allows additional light to reflect off the torque tube, which leads to brightening on panel edges near the gap. This effect explains the disparate shading factors for reflective torque tubes and black torque tubes: 0.01% and 12%, respectively.

A Soltec analysis of field data from six fall and winter months at a test site in California found that 1P and 2P trackers achieve 14.6% and 16.8% bifacial gain, respectively [96]. The report primarily attributes the 2.2% absolute increase in bifacial gain for 2P trackers vs. the 1P trackers to a 1.3% increase due to lower average module operating temperature and a 0.7% gain from reduced torque tube shading. Ray-tracing results in this report indicate a 5.6% shading loss for the default 1P tracker in the modeling software and a 1.7% net positive increase in irradiance due to torque tube reflection for a 2P tracker with a gap between panels and a rectangular metallic torque tube.

A white paper from Array Technologies, Inc. [97] models a back-to-front irradiance ratio for 1P and 2P configurations in PVsyst with loss factors derived by PV Lighthouse's three-dimensional (3D) ray-tracing tool. The study reports that the back-to-front irradiance ratio increases with the ratio of ground clearance to collector width (called the aspect ratio), rather than with ground clearance. The paper reasons that typical 2P trackers have lower aspect ratios than 1P trackers for the same ground coverage ratio, allowing more ground-reflected light to be lost to the sky. NEXTracker has also reported that the aspect ratio is a key factor to consider when designing trackers to withstand wind-loading [98].

4.6.3 Bifacial gain on single-axis trackers

Performance results from a number of field test sites and large-scale power plants are now being reported. Bifacial gain (the increase of bifacial energy yield over monofacial energy yield) is of particular interest for these sites since this value is key in financing new projects and appears to vary significantly with location and site design. For example, 1.7 MW La Silla power plant in Chile includes side-by-side testing of monofacial and bifacial modules on single-axis trackers. Under unique desert conditions, the single-axis tracked system demonstrates 10.4-12.4% bifacial gain [99]. Canadian Solar has also presented bifacial gains for a variety of systems ranging from 11 kW to 150 kW installed capacity [100]. These gains spanned 5.2 to 8.9% for 1P trackers with 0.2 to 0.3 albedo and 17.5% for a 1P 12 kW system at 0.6 albedo.

Smaller field sites also provide insight into the performance of bifacial PV on SATs. For example, the NREL bifacial demonstration plant consists of 10 rows of 20 modules in a 1P configuration, with three monofacial strings and four bifacial strings for analysis. From initial data at 0.2 albedo, the bifacial gain was 4 to 8% for PERC modules and 6.5 to 11% for silicon heterojunction modules (which benefits from a higher bifaciality factor) [101]. For a single-

axis tracked system in California, Asgharzadeh et al. [102] reports measured bifacial energy gain is 4.1% for 0.16 albedo and 9% for 0.56 albedo. While the fixed-tilt system considered in this paper is not at the same location, it demonstrates slightly higher bifacial gains for the fixed-tilt system as compared to the SAT system. This result is expected, as front-side optimization (which occurs continuously during tracking) limits the relative contribution of rear-side irradiance. ENGIE Laborelec's El Aguila plant in the Atacama Desert shows an opposite trend with fixed-tilt gain at 8% and HSAT gain at 10% around the winter solstice when cosine losses for HSAT are most significant [81]. However, lower tracked bifacial gain is expected for an extended dataset.

The sites above are a small sample of the wide range of tracker configurations, geographic locations, and reported albedos that can impact bifacial gain and energy yield of single-axis trackers. It should be noted that bifacial gain from small-scale test sites is expected to exceed the bifacial gain in utility scale plants, since small sites have been shown to exhibit reduced self-shading and increased edge-brightening effects [81]. Further correlation of site parameters and bifacial gain, such as through the International Survey of Bifacial PV Configurations and Field Performance, should allow for more certainty in the bounds of realistic gain estimates.

4.7 Optimization and performance of bifacial solar cells: A global perspective

(Prof. Muhammad A. Alam, M. Ryyan Khan, and M. Tahir Patel)

4.7.1 Introduction

According to a thermodynamic calculation [103], bifacial solar cells will outperform monofacial cells by 15 to 20% and provide a corresponding reduction in LCOE, assuming a typical albedo of $R = 0.2 \text{ to } 0.3$ and a temperature coefficient of $\beta_T \sim 0.25\%$. The actual bifacial gain is sensitive to latitude-dependent illumination, local temperature and wind-flow defined by weather conditions and heat-island effects, the location-specific clearness-index, and seasonal albedo (as determined, for example, by snow vs. grass) [104].

Fortunately, several bifacial test sites at Sandia National Laboratories and commercial PV plants, such as the La Silla PV plant in Chile, have created a substantial database on local bifacial gain for various types of bifacial technologies. This information can be used to inform/validate the modeling efforts of the global potential of the technology. The goal of this modeling is to integrate the physics of bifacial PV with the validation data from various solar plants to suggest broad guidelines on the viability of bifacial solar plants across the world. A global model would allow location-specific comparison of the relative merits of various bifacial module technologies and system topologies. Further, a sufficiently quantitative model would inform customers and guide investment and policy decisions.

4.7.2 Determining benefits for different bifacial configurations and parameters

The ability of bifacial PV to accept sunlight from both sides introduces implications that can reduce LCOE and enable integration of PV in locations typically not suited for monofacial modules. For example, unlike monofacial, bifacial PV can be installed vertically, which reduces soiling, the amount of cleaning water needed, and the energy used for water desalination and transport to remote locations. These factors can improve the integrated energy output and help to overcome any cost premium for bifacial. These factors are also important in

deserts, where soiling-loss is significant, and for agriphotovoltaics, which requires unimpeded movement of agricultural equipment and avoidance of long-term shading.

The double-hump output seen with vertical E-W bifacial flattens the electricity demand curve and simplifies grid integration, allowing generators to make more effective use of the available energy.

An elevated south-facing bifacial PV plant typically has high yields due to ground reflected light from direct irradiance and these plants also show improved diffuse-light collection during low-clearness index periods. However, such plants may need to be optimized for tilt angle and clearance height to ensure benefits over monofacial technology. Comparing monofacial and bifacial systems that track the sun shows a significant bifacial benefit—though the benefit is smaller than that seen in non-tracking systems.

Figure 39 shows the bifacial gain—the increased energy output of bifacial vs. monofacial cells—for different bifacial plant configurations and parameters compared to their monofacial counterparts:

- East–west facing vertical bifacial plant (v-BF) with no ground sculpting (ground sculpting height (*b*) of zero)
- East–west facing ground-sculpted vertical bifacial plant (Gv-BF) with a sculpting height half the module height (h)
- South-facing optimally tilted and elevated bifacial plant (s-BF)
- East–west tracking Bf (t-BF)
- Stand-alone Bf

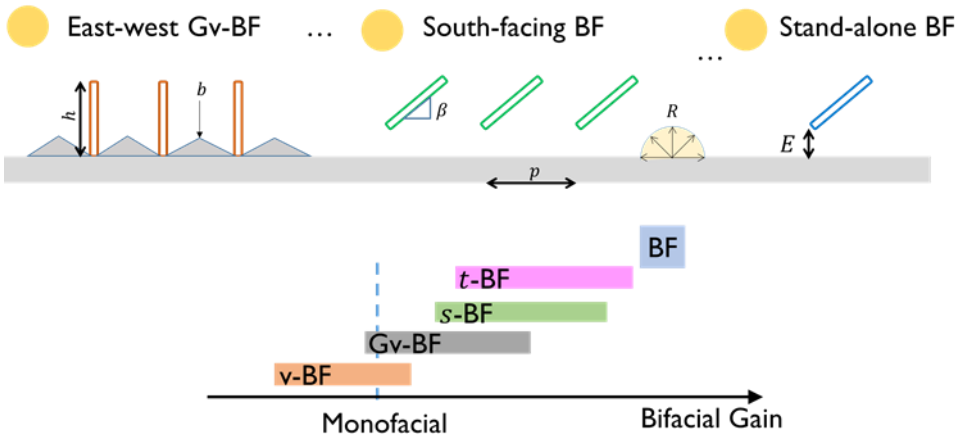

Figure 39: The top portion shows the bifacial system parameters considered (module height (h), ground-sculpting height (b), row-to-row pitch (p), tilt angle (β), and clearance height (E)) and the bifacial system configurations considered (east–west facing vertical-bifacial system ($b = 0$), east–west facing ground-sculpted vertical bifacial system ($b = h/2$), south-facing optimally tilted and elevated bifacial system, east–west tracking bifacial systems, and a stand-alone module. The bottom portion compares the bifacial gain of various system types to their monofacial counterparts. The left edge of each boxes denotes bifacial gain in hot regions close to the equator, while the right-edge shows gains as by the latitudes approach 60° N.

Other parameters not listed above but considered are row-to-row pitch (p), tilt angle (β), and clearance height (E). The comparison also considered latitude. In the bottom portion of Figure 39, the left edge of the boxes denotes bifacial gain in hot regions close to the equator, while the right-edge denotes the gain as latitudes approach 60º N.

4.7.3 Global bifacial PV simulator

Calculating the location-optimized energy yield and LCOE for any existing or emerging solar cell technology across the globe requires time-resolved and location-specific meteorological information from various databases. Other parameters, such as the intensity of sunlight, the fraction of direct vs. diffused light, ground albedo, ambient temperature, wind velocity, and moisture content, may dictate the design and output of the solar plant. Specific calculations may require analysts to synthesize information from various databases to accommodate differences in temporal resolution (e.g., minute-by-minute vs. monthly) or locations covered (North America vs. world). Additional details on various bifacial performance simulation tools can be found in Section 6.2.

For example, predicting the zenith angle in Purdue University Meteorological Tool (PUMET) [105], requires using the NREL solar position algorithm, as implemented in pvlib-python [106] or PVLIB Toolbox [107]. Next, the Haurwitz clear-sky model [108]–[110] can be used to calculate global horizontal irradiance (GHI) on a minute-by-minute basis, given the calculated solar positions. For self-consistency, integrated insolation is scaled to match the satellite-derived monthly average from the NASA surface meteorology and solar energy database.

Once the meteorological data is available as input, various solar plant modeling tools (e.g., pvlib [106], [107] and PVSyst [111], or Purdue University bifacial module calculator (PUB) calculates the technology and topology-specific bifacial energy yield. These software packages also predict the optimum configuration, as well as the direct, diffuse, and albedo components of total energy yield. Finally, this energy yield serves as an input to an LCOE-calculator, which determines the location-specific economic viability of various PV system topologies, as discussed below.

4.7.4 Simplified techno-economic analysis of solar PV plants

To simplify solar PV plant technical and economic analysis, it can be helpful to express LCOE in terms of module-scaled and land-scaled costs. Consider an analysis of a PV system installed in rows with spacing p and effective land-cost per unit area C_L. The effective cost scales with the area of the plant, including the purchase price, land-development, permits, operation, and maintenance. Next, h is the vertical dimension of the modules (either in the portrait or landscape mode) and C_M is the effective cost per unit area of the module. This cost scales with the number of modules in the plant. The traditional formula for LCOE, given by the ratio of the total cost (C_T) per unit of energy (Y_T) generated, can be rewritten in this form [112], [113]:

$$LCOE \equiv \frac{C_T}{Y_T} = \left(\frac{C_L}{\chi}\right) \cdot \frac{\left(\frac{C_M}{C_L} + \frac{p}{h}\right)}{YY_0} \equiv C_{L,\chi} \cdot LCOE^* \tag{23}$$

Here, $YY_0(p/h, E)$, the first-year energy yield of a pristine plant (normalized to the panel length (h), additionally depends on the clearance height E of the modules, and $\chi = \sum_{k=1}^{Y}(1-d)^k\,(1+r)^{-k}$ includes the yearly degradation rate d and bank-discount rate r, so that the total energy yield $Y_T \equiv YY_0 \cdot \chi \cdot h$. Given the location-specific $C_{L,\chi} = C_L/\chi$, we can compare the relative costs of various bifacial PV configurations by comparing the $LCOE^*$. In

short, the increased cost of a bifacial module increases C_M, while simultaneously increasing YY_0 as allowed by the bifacility of the solar modules. The global map of these quantities is discussed below.

4.7.5 Energy gain of stand-alone bifacial modules

The bifacial gain is most significant for optimally tilted, standalone bifacial modules, because aside from the time-dependent self-shading, these modules collect albedo light from regions extending to the horizon (i.e. $p \to \infty$). Figure 40 shows that even for $E = 0$ and a typical albedo $= 0.25$, a bifacial module outperforms a monofacial module at least by 10% everywhere in the world [4]. With elevated module fixtures, the module back-face sees a larger portion of the ground, resulting in higher light collection. For typical $E = 1$ and white concrete or sand surfaces with enhanced albedo ($R = 0.5$), the bifacial gain can increase to 30%.The optimistic projection relative to bifacial technology is justified for stand-alone PV, as indicated in Figure 40 and Table 13.

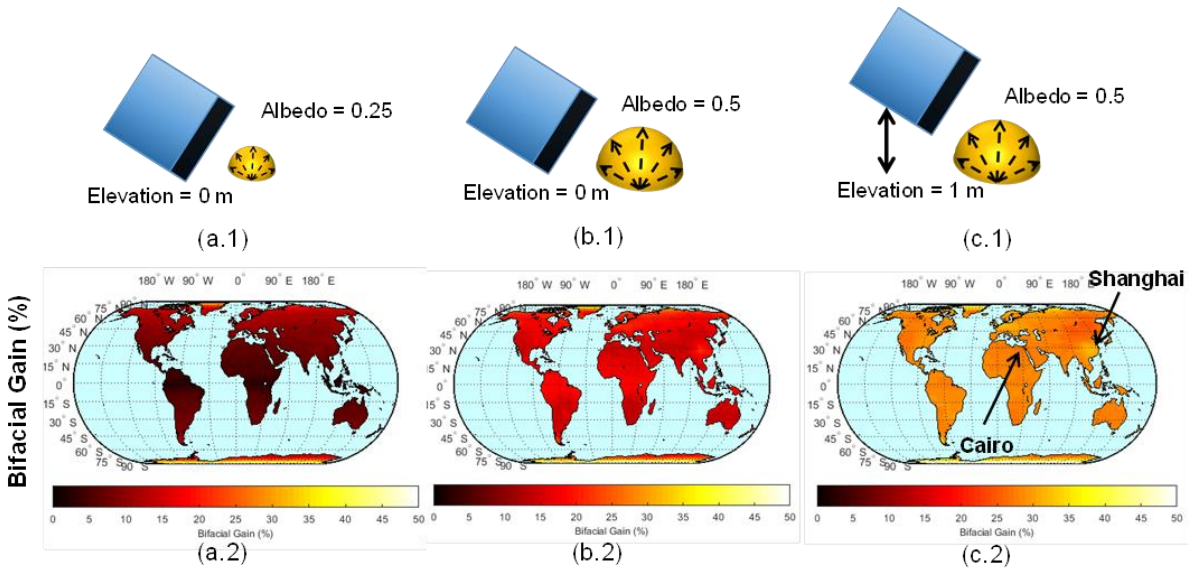

Figure 40: Global maps showing energy yield ratio of east oriented bifacial module over north–west oriented modules for three different scenarios: (a) ground-mounted with a ground albedo of 0.25, (b) ground mounted with a ground albedo of 0.5, and (c) 1 m elevated with a ground albedo of 0.

Table 13: Modeling framework validation against literature.

Location (Type)	Clearance Height / Module Height (m)	Albedo / Bifaciality	Tilt Angle / Facing	Reported Bifacial Gain (%)	Calculated Bifacial Gain (%)	Difference (%)
Cairo (Sim.)	1 / 0.93	0.2 / 0.8	26° S	11.0	11.1	–0.1
Cairo (Sim.)	1 / 0.93	0.5 / 0.8	22° S	24.8	25	–0.2
Oslo (Sim.)	0.5 / 0.93	0.2 / 0.8	51° S	10.4	13.6	–3.2
Oslo (Sim.)	0.5 / 0.93	0.2 / 0.8	47° S	16.4	22.8	–6.4
Hokkaido* (Exp.)	0.5 / 1.66	0.2 / 0.95	35° S	23.3	25.7	–2.4
Hokkaido* (Exp.)	0.5 / 1.66	0.5 / 0.95	35° S	8.6	13	–4.4
Albuquerque (Exp.)	1.08 / 0.98	0.55 / 0.9	15° S	32.5**	30.2	+2.3
Albuquerque (Exp.)	1.08 / 0.98	0.55 / 0.9	15° W	39**	36.7	+2.3
Albuquerque (Exp.)	1.03 / 0.98	0.25 / 0.9	30° S	19**	14.6	+4.4
Albuquer-que*** (Exp.)	0.89 / 0.98	0.25 / 0.9	90° S	30.5**	32.2	–1.6
Golden (Exp.) ****	1.02 / 1.02	0.2 / 0.6	30°	8.3	8.6	–0.3

* Only data from May to August were used to eliminate snow effects

** Average bifacial gain of multiple test modules was used.

*** The east-west-facing vertical modules measurement in [114] shows great discrepancy between two modules; therefore, it is not included here.

**** Bifacial measurement (12/2016 to 08/2017) performed by the National Renewable Energy Laboratory.

In general, the relative energy gain depends on the latitude $\boldsymbol{L}$ and reaches 95% of the maximum energy at clearance height $E_0^{(B)}$ for bifacial modules and at $\left(E_0^{(M)}\right)$ for monofacial modules:

$$(E\_0\text{^}((B)\,))\,/\,h = 3.3\,R + 0.4 - L\,(0.028\,R + 0.009) = E\_0\text{^}((M)\,) + R\,(3.3 - 0.028\,L) \quad (24)$$

The equation is valid for $E_0^{(B)} > 0$, and the differential gain depends on the latitude $\boldsymbol{L}$ and ground-albedo R, as expected. It is also clear that bifacial modules should be tilted at a higher angle compared to monofacial modules to more effectively collect the albedo. The optimum tilt-angle β is given by

$$\beta_{opt} = aL + b,\ (3)\ \text{where}\ a \equiv 0.86 - 0.57\,R \cdot \exp(-E/h)\ \text{and}\ b = 4.5 + 62\,R \cdot \exp(-E/h) \quad (25)$$

The exponential term suggests that difference between monofacial and bifacial tilt-angle ($\Delta\beta$) reduces rapidly at a higher clearance height. Finally, the optimum orientation changes from east–west to north–south beyond a critical latitude, given by

$$L_c = (E/h)(44\,R - 62) + 37\,R + 12.(4) \quad (26)$$

In short, a standalone bifacial module improves YY_0 and reduces $LCOE$ so significantly this technology can be beneficial all over the globe despite the increased module cost.

4.7.6 Vertical bifacial PV systems with and without ground-sculpting

Vertical bifacial PV systems provide many advantages, including flattened energy output, reduced soiling, integration with build-structures, and the potential for agriphotovoltaics. These advantages may outweigh the cost increase of bifacial compared to monofacial PV and reduced bifacial gain due to mutual shading compared to stand-alone bifacial PV.

Figure 41 shows the results of careful calculations [115], [116] to examine global implications for v-BF.

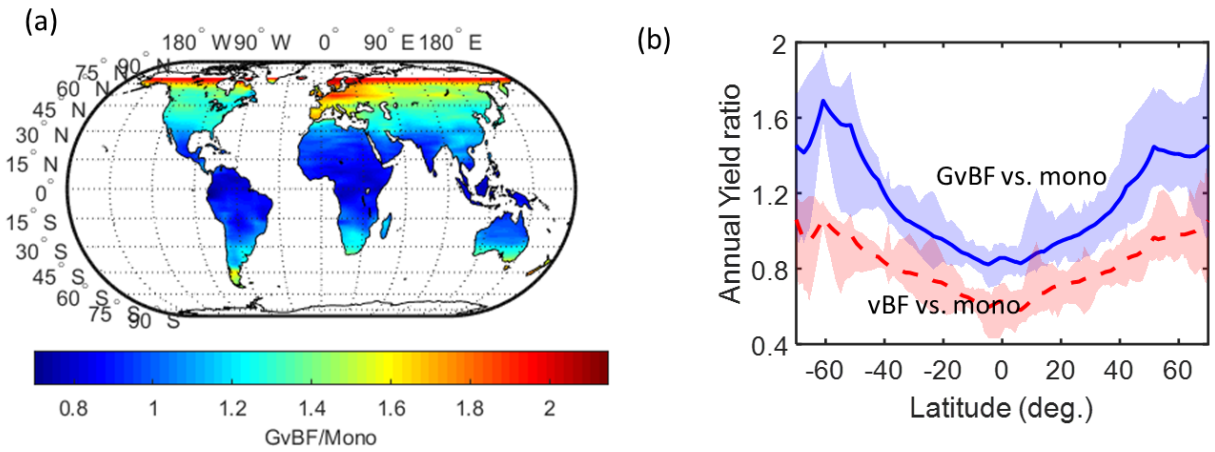

Figure 41: (left) Worldwide annual yield ratio between Gv-BF and monofacial solar cell. (right) For various latitudes, ratio of annual yields of GvBF ($R = 0.5$) vs. monofacial plant, and of v-BF ($R = 0.3$) vs. monofacial plant are shown by solid and dashed lines, respectively. The monofacial system includes a 10% soiling loss. The shaded regions, along with the lines, represent the spread in data for various longitudes.

These conclusions follow:

- Even with relatively high albedo (e.g., $R = 0.5$), bifacial gain exceeds 1 only for latitudes above 30° to 40° N and for regions with low clearness index. This result stems from the lower sensitivity of the energy yield of an east–west array to latitude compared to the energy yield of a monofacial array and the larger p/h ratio at higher latitude, which reduces mutual shading and enhances albedo collection. For example, the output of a bifacial system at 40 east longitude of approximately 200 kWh/m^2 for $-25 < L < 30$ N (with $p/h \sim 0.8$) reduces to 80 to 100 kWh/m^2 for $30 < L < 60$ N (with $p/h \sim 1.2$). For the same regions, monofacial PV output drops from 240 kWh/m^2 to 60-80 kWh/m^2.
- Second, with ground-sculpting (a poor man's concentrator), the transitional latitude decreases dramatically, and the bifacial gain becomes positive except for regions closer to the equator [116]. Equally importantly, the reduced temperature-sensitivity of

bifacial compared to monofacial further decreases the positive-gain latitude. At special high-altitude locations, significantly reduced soiling, increased p/h, and better collection of diffused light may lead to a bifacial gain of 50%.

- Third, and most important, modules in a vertical bifacial PV plant do not require being elevated. Unlike a standalone or a south-facing optimally tilted bifacial plants, elevating vertical modules always reduces the energy output, regardless of the ground-sculpting.

In short, careful consideration of such factors as geographical location, soiling rate, and ambient temperature is needed to ensure the economic viability of a vertical bifacial PV system.

4.7.7 Optimally elevated fixed-tilt bifacial PV plants

A south-facing elevated bifacial PV plant is another alternative to a monofacial design. As in the standalone bifacial PV discussed above, the combination of clearance height and lower temperature-sensitivity contribute to the bifacial gain [113], [105]. However, mutual shading erodes the bifacial gain and energy saturation occurs at lower clearance heights compared to a standalone bifacial module. Below are some key conclusions:

- For modules installed close to the ground ($E = 0$), the panels must be oriented horizontally and packed densely for locations with high land-related cost, whereas the panels should be optimally tilted for places with high module-related cost. In general, the optimum tilt-angle is a function of the location and the module vs. land cost ratio, $M_L \equiv C_M/C_L$, namely,

$$\beta_{opt} = c_1 M_L + \exp\left[c_2 (1 - (M_L - M_L^*)^{c_3}\right] \quad (27)$$

where the constants dependent on the latitude *L*. For example, $c_1 = 0.07$, $c_2 = 3.6$, $c_3 = 1.6$, and $M_L^* = 8$ for Washington, DC (38.91° N, 77.04° W). In general, for locations with |*L*| > 30° (and for places with high diffuse light fraction, such as Canada, Western Europe, Central China), the bifacial modules must be tilted ~10° to 15° higher. The additional tilt angle makes the design soiling-resistant, in turn reducing cleaning costs and further improving LCOE. The difference in the optimum tilt-angle persists even when the modules are elevated to the optimum height and energy yield has improved 5 to 15% [113], [105]. Figure 42 compares bifacial gain globally of HIT bifacial and Al-BSF monofacial systems.

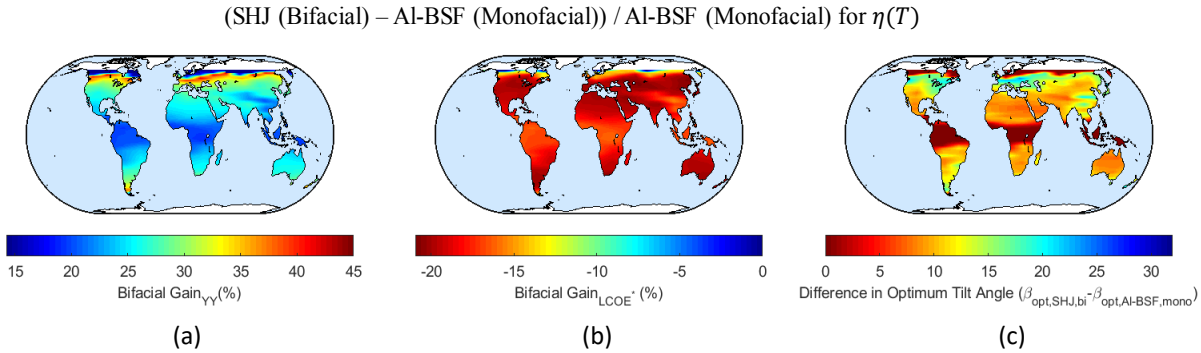

Figure 42: Global maps comparing bifacial gain in (a) yearly energy yield, (b) LCOE*, and (c) difference in optimum array tilt angle for Al-BSF monofacial ($\beta_T = 0.41\%/°C$) vs silicon heterojunction bifacial ($\beta_T = 0.26\%/°C$). Note that $R_A = 0.5$ and $M_L = 15$.

Yearly energy output of south-facing elevated bifacial PV systems improves with clearance height but degrades with the local ambient temperature. For example, in hotter regions (such

as the Sahara Desert, Mexico, and southern India), these systems show a loss in energy yield (5 to 7% below 30° N) due to temperature-induced degradation in efficiency compared to the efficiency at STC (η_{STC}). On the other hand, in colder locations (|*L*| > 30°) and in places with lower average temperatures (such as Siberia, Gobi Desert, and northern Canada and Europe), these systems show an improvement in efficiency, with respect to η_{STC}, leading to higher energy yield (5 to 12% for |*L*| > 30°). In fact, the improvement correlates almost perfectly with the average temperature map of the world. The reduced temperature sensitivity of bifacial technologies confers an important advantage over monofacial solar cells. Overall, the LCOE of an elevated optimally tilted bifacial plant should be 10 to 15% lower than a monofacial one.

4.7.8 Tracking vs. fixed-tilt bifacial PV systems

Tracking bifacial solar PV provides a dual advantage of normally incident direct light collection and albedo light collection at both the faces of a solar panel. This comes at an additional cost of the single- or double-axis trackers and inverters. However, these costs have been diminishing. Further, the dual advantage creates an energy gain sufficiently significant to potentially enable their large-scale deployment. A preliminary analysis shows the yearly energy yield of a single-axis tracking of bifacial PV to be ~5 to 10% higher than that of fixed-tilt bifacial. Moreover, the energy output of a temperature-dependent efficiency-based tracking bifacial system could be 5 to 10% lower worldwide than that of a constant temperature efficiency (η_{STC})-based tracking bifacial system.

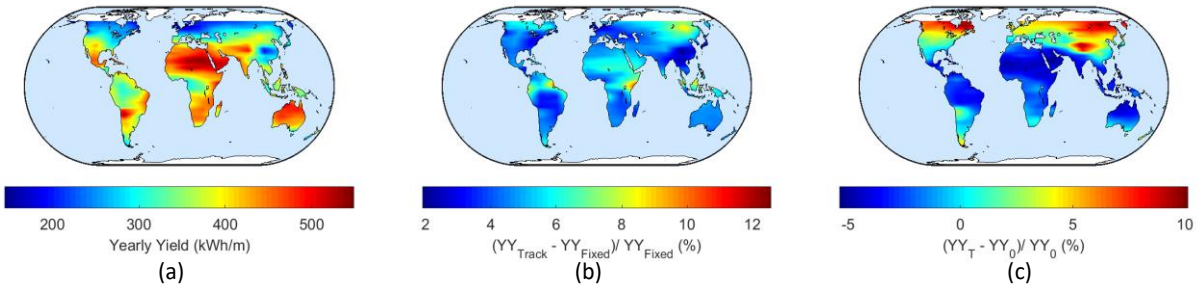

Figure 43: (a) Yearly energy yield for tracking bifacial PV with temperature-dependent efficiency (η(T)). (b) Percentage change in yearly energy yield of tracking bifacial PV vs. N-S fixed-tilt bifacial PV. (c) Percentage change in YY for tracking bifacial PV with temperature-dependent efficiency and constant efficiency (η_STC).

4.7.9 Conclusions

Bifacial solar cell technology promises to improve energy yield and reduce LCOE compared to monofacial technology. Both small-scale installations at Sandia and large-scale installations across the world support this general conclusion. A standalone bifacial module, if optimally tilted and elevated, would yield more energy than the monofacial module based on the same technology anywhere in the world. The bifacial gain of a solar PV system involves complicated trade-offs dependent on multiple factors: mutual shading, temperature-sensitivity, tilt-angle, and more. A south-facing fixed-tilt bifacial PV system produces more energy than its monofacial counterpart anywhere in the world. Substantial gain is achieved as systems move further from the equator (|*L*| > 25° to 30° N) and in regions with moderate temperature and low clearness index.

Specialized installations, such as vertical bifacial PV, yield less energy than optimally elevated, equator-facing or single-axis tracking bifacial PV and outperform monofacial systems only at high latitudes. At lower latitudes, features such as flattened energy output, increased reliability related to reduced peak temperature, reduced soiling, and ground-sculpting, make vertical designs attractive and cost-effective.

5 INTERNATIONAL SURVEY OF BIFACIAL PV CONFIGURATIONS AND FIELD PERFORMANCE

The IEA PVPS Task 13 Activity 1.2 – Bifacial Photovoltaics sent out a survey to its members to gather data on bifacial field test results from member organizations. We received completed forms from 27 systems from 9 member institutions and 13 geographic locations, including sites in Europe, Africa, Asia, and the Americas. Table 14 shows the survey form with suggested example inputs for one site.

A summary of the reported results is shown in Table 15. It is worth noting that bifacial gains are not well correlated with any of the system design parameters alone.

Table 14: International bifacial system performance survey form and example values (grayed)

No	Information	Value	Unit	Comment
1	System ID	ISE-01		For internal reference, no need to disclose site names or commercial project names
2	Task 13 contact	reise@ise.fhg.de		E-mail address of task 13 contact person for further clarifications
3	Site latitude	48.0	deg N/S	
4	Site longitude	7.85	deg E/W	
5	System size	0.35	kW_p	
6	System type	Fixed tilt		Fixed tilt / fixed vertical / HSAT / ...
7	Site albedo	25	%	
8	Bifacial gain	13	%	
9	Time period	0.1	H	Instantaneously / one day / one year / ...
10	Clearance height	0.6	M	Lower module edge above ground
11	Array tilt angle	30	Deg	if applicable
12	Array azimuth angle	135	Deg	S=180; W=270; N=0; E=90
13	Ground cover ratio	n/a	%	Ratio of module row width to row-to-row distance
14	Module bifaciality	85	%	Back-side power rating divided by front-side power rating
15	Array configuration	1-up landscape		1P, 3-up landscape, etc.
16	Electrical info	I_{sc} measurement		Central inverter, string inverter, microinverter, module optimizer?
17	Further data?	Other tilt angles		Mention availability of time series or other detailed measurements

Table 15: Summary of bifacial system field performance from IEA PVPS Task 13 members.

No	Lat (°)	Lon (°)	System Size (kW_p)	System type	Albedo (%)	Height (m)	Tilt (°)	Azimuth (°)	Module bifaciality	Bifacial gain (%)	Note
1	48.00	7.85	0.35	Fixed	25	0.6	30	135	85	13	
2	-25.75	28.27	11.3	2-axis tracker	25	4.5	n/a	n/a	56	3	
3	-25.75	28.27	11.3	2-axis tracker	70	4.5	n/a	n/a	55.8	6	
4	-25.75	28.27	0.54	Fixed	14	0.67	25	0	82.5	25	
5	-25.75	28.27	0.56	Fixed	14	0.67	25	0	55.8	12.5	
6	48.40	2.80	10.95	Fixed	32	1	15	180	84	7.6	
7	43.18	3.00	3.1	Fixed	25	1	20	180	78	7.5	
8	43.18	3.00	3.1	Fixed	25	1	20	180	59	5.9	
9	45.48	9.26	1.95	Fixed	27	1	30	180	76	15.8	
10	45.48	9.26	1.95	Fixed	10	1	30	180	76	8.5	
11	60.45	22.30	1.18	Fixed	26	0.62	90	90	90	90	
12	60.45	22.30	0.3	Fixed	30	0.5	45	225	?	?	
13	50.9	7	~0.3	Fixed	15	1	35	180	83	11	
14	33.4	-111.9	~0.3	Fixed	15	1	33.5	180	83	7	
15	22.3	39.1	~0.3	Fixed	20	1	25	180	83	9	
16	13	80	~0.3	Fixed	25	1	15	180	83	20	
17	35	-106	1.08	Fixed	25	1	30	180	90	19	
18	35	-106	1.08	Fixed	55	1	15	180	90	32.5	
19	35	-106	1.08	Fixed	55	1	15	270	90	39	
20	35	-106	0.54	Fixed	25	1	90	180	90	30.5	
21	35	-106	0.54	Fixed	25	1	90	270	90	124	
22	45.64	5.87	3.04	Fixed	40	0.95	30	180	?	9	
23	39.7	-105.2	75	SAT	26	1.5	n/a	n/a	65 to 90	8.9	(1)
24	-18.44	-69.89	12	Fixed	21	1.2	15	0	70	9.5	
25	-18.44	-69.89	12	Fixed	21	1.2	15	0	85	13.2	
26	-18.44	-69.89	12	SAT	21	1.5	n/a	n/a	70	9.3	
27	-18.44	-69.89	12	SAT	21	1.5	n/a	n/a	75	10.1	

Notes: (1): 5 different technologies

6 BIFACIAL MODELING COMPARISON

(Silvana Ayala Pelaez and Joshua S. Stein)

The IEA PVPS Task 13 bifacial activity group organized a model comparison exercise aimed at documenting current practice for modeling the performance of fielded bifacial photovoltaic systems. This activity invited participants from international research laboratories, universities, and industry to test their bifacial PV performance models on a common set of bifacial system designs, some of which have been deployed and monitored and some that are theoretical but represent a wide range of potential designs.

Participants provided a brief technical description of their model, ran their model for the scenarios described below, and provided the results to be analyzed in this report. After anonymizing submissions, the activity leads reported back to participants a summary of the relative performance of the participating models. Participants had the chance to review this summary prior to the full set of anonymized results being published here.

6.1 Description of the modeling scenarios

The following model scenarios were defined and provided to modelers, along with a diagram showing measurement locations (Figure 44).

1. Fixed-tilt, equator-facing array
    - Tilt = 20°, Azimuth = 180° (facing south)
    - Ground coverage ratio (GCR)= 0.35 (row-to-row spacing = 2.83 m)
    - Albedo = 0.62
    - Clearance height = 0.5 m
    - Size of array = 7 rows of 20 modules per row
    - Racking structure is neglected from simulation
    - Module orientation = 1-up landscape
    - Module = Prism Solar BN72-370 (size: 1.91 m x 0.989 m)
2. Fixed-tilt, west-facing array
    - Tilt = 25°, Azimuth = 270° (facing west)
    - GCR = 0.33 (row-to-row spacing = 3.0 m)
    - Albedo = 0.4 (concrete)
    - Clearance height = 0.75 m
    - Size of array = 7 rows of 20 modules per row
    - Racking structure is neglected from simulation
    - Module orientation = 1-up landscape
    - Module = Prism Solar BN72-370 (size: 1.91 m x 0.989 m)
3. Fixed-tilt, vertical east-west array
    - Tilt = 90°, Azimuth = 90° (front of modules facing east)
    - GCR = N/A (single row)
    - Albedo = 0.4 (concrete)
    - Clearance height = 0.3 m
    - Size of array = 1 rows of 20 modules
    - Racking structure is neglected from simulation

- Module orientation = 1-up landscape
- Module = Prism Solar BN72-370 (size: 1.91 m x 0.989 m)

4. Horizontal single-axis tracking array

- Azimuth axis of rotation = 180° (north-south)
- GCR = 0.35 (row-to-row spacing = 5.7 m)
- Albedo = 0.25
- Height of torque tube from ground = 1.2 m
- Size of array = 10 rows, each with 20 modules
- Torque tube diameter = 0.15 m (assume torque tube has albedo = 0%)
- Distance from back of module to center of torque tube = 0.15 m
- Module orientation = 1P
- Module = Prism Solar BN72-370 (size: 1.91 m x 0.989 m)

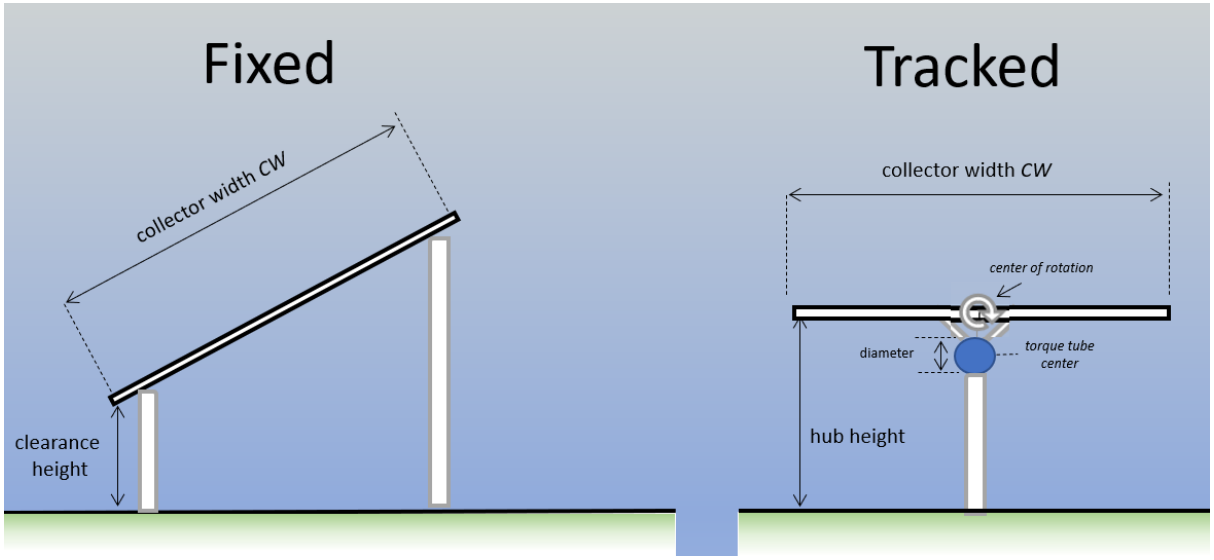

Figure 44: Diagram showing locations for measuring parameters for fixed-tilt and tracked systems.

The following value was determined for software that required more specifics: spacing between modules along same row = 0.01m.

6.1.1 Weather files used for comparison

All simulations used as inputs three weather files from International Weather for Energy Calculation (IWEC) data from the EnergyPlus website (https://energyplus.net/weather). These weather files follow the IWEC manual conventions: the data is aggregated hourly as an average from t-1 to t, as are typical meteorological year (TMY) data. Table 16 provides a summary of the weather files, as well as the corresponding order.

Table 16: Weather files for the simulations S1-S4.

Site Parameters	Abu Dhabi, United Arab Emirates	Antofagasta, Chile	Groningen, Netherlands
Latitude, Longitude (°N, °E)	24.43, 54.65	-23.43, -70.43	53.13, 6.58
Time Zone (h vs. UTC)	+4.0	–4.0	+1.0
Altitude (m)	27	120	4
Annual DNI (kWh/m^2)	2294.9	2043.7	625.2
Annual DHI (kWh/m^2)	606.7	676.5	608.5
DHI/DNI ratio	0.26	0.33	0.97
Avg. annual ambient temp. (deg C)	27.1	17.0	9.1
Avg. annual wind speed (m/s)	3.6	4.0	4.6

The quality of meteorological files was confirmed with python algorithms and PVSyst for valid values of DNI, GHI, DHI, temperature, wind speed, relative humidity, and no time shifts. Files selected did not have valid albedo values, but specific values of albedo were specified in the input parameters table for each scenario. Snow modeling was not included as part of the exercise.

6.1.2 Optional Simulations of Field Measured Irradiance and Power

Two optional simulations were included, with field-measured data for one week. Datasets were blinded for the outputs that the software tools are expected to model (front- and rear-irradiance measurements, and module power results, if corresponding). Each optional simulation is described below.

Optional Simulation 1

Optional simulation 1 simulates front and rear irradiance for a fixed-tilt testbed located on the NREL campus in Golden, Colorado, USA. Weather data is measured <60 meters from the testbed at the Solar Radiation Research Laboratory [117]. This testbed has front- and rear-irradiance sensors that collect data on the irradiance profile across the center module of the center row (Figure 45). The testbed is a scaled version of a real array, where the collector width is 2 ft (0.61 m). The testbed consists of three 20 ft (6.1 m) long rows, each with 10 modules of 2 ft (0.61 m) x 1 ft (0.305 m) in landscape. The array is facing south (azimuth = 180). Albedo for the week provided for simulation is 0.7, clearance height is 1.74 ft (0.53 m), row-to-row spacing is 3 ft (0.914 m), and modules are tilted at 10°.

Figure 45: Fixed-tilt testbed for optional simulation 1

In the testbed, irradiance was measured with two front-facing and four rear-facing reference cells across the slope of the center module. More details of the setup and original publicly released data can be found in [118].

Optional Simulation 2

One week of data was provided for the Bifacial Experimental Single-Axis Tracker field array at NREL, in Golden Colorado. Data selected spans March 02 to March 09, 2020. The field itself is further described in Section 7.8. Complete data for the field is publicly available in [119].

Teams were asked to model front and rear irradiance, with potential modeling sensors at various locations on the field. Power data for row 2, comprising 19 Prism Solar Modules Bi72-457BSTC, was also a requested output if the software could calculate it. Round-robin inputs provided were DC power, bifaciality factor, and a .PAN file.

6.2 Description of the models

Members of the bifacial community were invited to participate in this exercise with their own software tool and any tools they could access to evaluate reproducibility of the results. Participants were also asked to provide a description of their software capabilities, which are summarized below in Table 17 and expanded in the following sections.

Table 17: Overview of characteristics of software tools for modeling bifacial systems.

Name of software	Version used for simulation	Simulations run on	Modeling approach	Use
bifacial_radiance	v0.3.4	CPU-based simulation/HPC	Raytrace (Radiance)	Open source
bifacialVF	v0.1.8	CPU-based simulation	2D-VF	Open source
PVNOV	5.5.1	CPU-based simulation	3D Reverse raytrace	Internal
System Advisor Model (SAM)	2020.2.29 Revision 2 SSC 240	CPU-based simulation	2D-VF	Open source
Chudinzow Model	Matlab 2019b	Windows server 2012, min RAM 100GB for parallel computing	2D-3D VF hybrid	Internal
Pvsyst	v6.86	CPU-based simulation	2D-VF	Paid
Imec - Energy Yield Simulation Framework	14.05.2020	Linux, CPU - 24 Core Linux server, 375 GB RAM, NVIDIA Tesla GPU	Raytrace (Radiance)	Internal
DUET by SUNLAB @ University of Ottawa	v0.2	CPU-based simulation	3D-VF with rack shading	Internal
SolarFarmer	1.0.187.0	CPU-based simulation	3D Hemi-cube model, with 2D-VF for bifacial	Paid
TUAS PVPM	V0.4	CPU-based simulation	2D-VF (based on pvfactors)	Open Source
MoBiDiG hybrid	0.2.5	CPU-based simulation	Raytrace and VF hybrid, user chooses based on system size	Paid
Trifactors	May-20	CPU-based simulation	3D-VF	Paid
pvfactors	v1.4.1	CPU-based simulation	2D-VF	Open Source

Name of software	Ground Albedo	Albedo time resolution	Does the software consider spectral-dependent albedo?	Does the software consider angular-dependent reflectivity?
bifacial_radiance	isotropic	Instantaneous	Yes	BRDF possible
bifacialVF	isotropic	Instantaneous	No	No
PVNOV	isotropic	Instantaneous	No	No
System Advisor Model (SAM)	isotropic	Instantaneous, monthly, yearly	No	No
Chudinzow Model	isotropic	Instantaneous	No	No
Pvsyst	isotropic	Monthly, Yearly	No	No
Imec - Energy Yield Simulation Framework	isotropic	Instantaneous	No	Yes
DUET by SUNLAB @ University of Ottawa	isotropic	Instantaneous	In development	IAMs for front and rear module surfaces
SolarFarmer	isotropic	Monthly, yearly	No	No
TUAS PVPM	isotropic	Monthly, yearly	No	No
MoBiDiG hybrid	isotropic	Hourly	No	No
Trifactors	isotropic	Instantaneous	No	No
pvfactors	isotropic	Instantaneous	No	No

Name of software	Sky model	Irradiance Inputs	Handling of TMY3 data: For an 11 am data point, sun position is calculated at:	Does the software consider angular-dependent reflectivity for rear-side reflections?
bifacial_radiance	Perez, and Stone cumulative sky	DNI and DHI	10:30:00	Yes
bifacialVF	Perez	DNI and DHI	10:30:00	Yes
PVNOV	Isotropic or Perez	DNI / DHI; GHI /DHI; POA irradiance	11:30:00	Yes
System Advisor Model (SAM)	Perez, Isotropic, HDKR	DNI and DHI, DNI and GHI, GHI and DHI, plan of array (POA) from reference cell, POA from pyranometer	10:30:00	Yes
Chudinzow Model	Isotropic sky diffuse model	DNI and DHI or DHI and GHI	11:00:00	No
Pvsyst	Perez, Hay	A combination of two of GHI, DHI, horizontal beam irradiation or measured DNI; or measured global on plane	11:30:00	No
Imec - Energy Yield Simulation Framework	Perez	DNI and DHI	11:00:00	Yes
DUET by SUNLAB @ University of Ottawa	Perez	DNI, DHI, GHI	10:30:00	Through IAM
SolarFarmer	Hay or Perez	GHI and DHI	11:30:00	No
TUAS PVPM	Isotropic, Perez	GHI, DHI, DNI	11:00:00	No
MoBiDiG hybrid	Perez model with 1990 coefficients	GHI, DHI, DNI	10:30:00	Yes, with IAM
Trifactors	Perez	GHI, DHI and DNI	11:30:00	Yes
pvfactors	Perez	DNI, DHI and optionally GHI	11:30:00	Yes

Name of software	Does the software calculate spectral-corrected rear-side irradiance?	How does the software handle specular reflections?	Can the software calculate rear irradiance non-uniformity?	Includes shading losses from racking and other obstructions?
bifacial_radiance	Yes	Diffuse and specular component specified in each material properties	Yes	Yes
bifacialVF	No	Specular reflections are not considered.	Yes	No
PVNOV	No	All reflections considered are isotropic	Yes	Yes
System Advisor Model (SAM)	No	Specular reflections are not considered.	No	Yes
Chudinzow Model	No	By assuming a constant factor (τα, transmissivity x reflectivity) = 0.9 based on [120]	Yes	No
Pvsyst	No	Specular reflections are not considered.	No	Yes
Imec - Energy Yield Simulation Framework	No	It is optional. It is handled via Radiance	Yes	Yes
DUET by SUN-LAB @ University of Ottawa	In development	Reflection off the ground is currently Lambertian. No secondary reflections off racking or other panels are presently considered.	Yes	Yes
SolarFarmer	Yes	Not considered	No	Racks only
TUAS PVPM	No	Specular reflections are not handled, all surfaces are assumed to be diffuse reflectors	No	No
MoBiDiG hybrid	No	Considers specular reflections of the albedo	Yes	No
Trifactors	No	They are not considered (but listed on our roadmap)	Yes	No
pvfactors	No	Specular reflections are not handled, all surfaces are assumed to be diffuse reflectors	Yes	No

Name of software	Single-axis tracking	Two-axis tracking	Is power calculated?	Is module temperature accounted for?	Is electrical mismatch calculated?	Can the software calculate edge effects?
bifacial_radiance	Yes	Under development	Yes	Yes	Yes	Yes
bifacialVF	Yes	No	Yes	Yes	Yes	No
PVNOV	Yes	No	Yes	Yes	Yes	Yes
System Advisor Model (SAM)	Yes	Yes	Yes	Yes	No	No
Chudinzow Model	Yes	No	Yes	Yes	Yes	Yes
Pvsyst	Yes	Yes	Yes	Yes	Yes	No
Imec - Energy Yield Simulation Framework	Yes	No	Yes	Yes	Yes	Yes
DUET by SUNLAB @ University of Ottawa	Yes	Under development	Yes	Yes	Yes	Yes
SolarFarmer	Yes	No	Yes	Yes	Yes	No
TUAS PVPM	No	No	Yes	Yes	No	No
MoBiDiG hybrid	Yes	No	Yes	Yes	Yes	Yes
Trifactors	Yes	No	Yes	Yes	Yes	Yes
pvfactors	Yes	No	No	No	No	No

6.2.1 bifacial_radiance model

(Silvana Ayala Pelaez)

bifacial_radiance is an open-source module created by NREL in python language. It provides a set of functions and classes that comprise a workflow for simulating the performance of bifacial PV systems [121], [122] by leveraging the ray-tracing software RADIANCE [123]. A graphical user interface helps simplify the use of this modeling software. The interface or the python module allows the design and layout of PV modules and PV fields, as well as calculations of irradiance at any location in the system.

By default, bifacial_radiance monitors the irradiance at the centerline of a given module at any given amount of points. Users can select the desired module and desired row to be sampled. Full sampling of irradiance in every cell of a module is also possible. The key steps for using bifacial_radiance are as follows:

- Create characteristics ground, sky, and module inputs
- Raytrace and calculate front- and rear-side irradiances
- Post process results

To generate sky characteristics, bifacial_radiance uses a Perez distribution for the diffuse light, discretizing the sky-hemisphere into 145 patches, in the sky-model developed by [124]. The sun's direct light can either be modeled as a collimated point-source or assigned to the patch denoting the location of the sun. Skies are generated based on measured or typical MYD, with DNI and DHI as inputs. Furthermore, the software allows the use of "cumulative skies" to add skies generated for various points in time (e.g., all hours of a year) and do a single calculation. A tracking-cumulative sky algorithm is also available [125].

Reverse raytrace is an important feature of bifacial_radiance. This means the model can internally establish the source of the rays to be the location or point in the module being sampled and generate rays in all possible directions. These rays intersect with the elements in the scene until either they intersect with the sky or their power is negligible. Afterwards, the number of rays that reach each sky-patch gets weighted by each patch's power, and the total irradiance at the sampled point is the sum of all those weighted patches. Reverse raytracing is a technique that greatly reduces simulation time in raytracing software, especially for cases like these simulations that involve a detector (the module) that is much smaller than the source (the sky).

Built-in methods handle single-axis tracking and fixed-tilt applications. For tracked systems, backtracking can be enabled based on the row-to-row spacing of the field or GCR. In addition, tracking can be specified around an axis of rotation located coincident with either the center of the modules or the center of a torque tube. Torque tubes of various profiles can easily be specified (round, square, hexagonal and octagonal), which makes this tool useful for calculating shading losses from torque tubes [95] and other racking, which can be added programmatically. To consider angle of incidence losses, modules can be modeled with glass around the cells as shown in Figure 46.

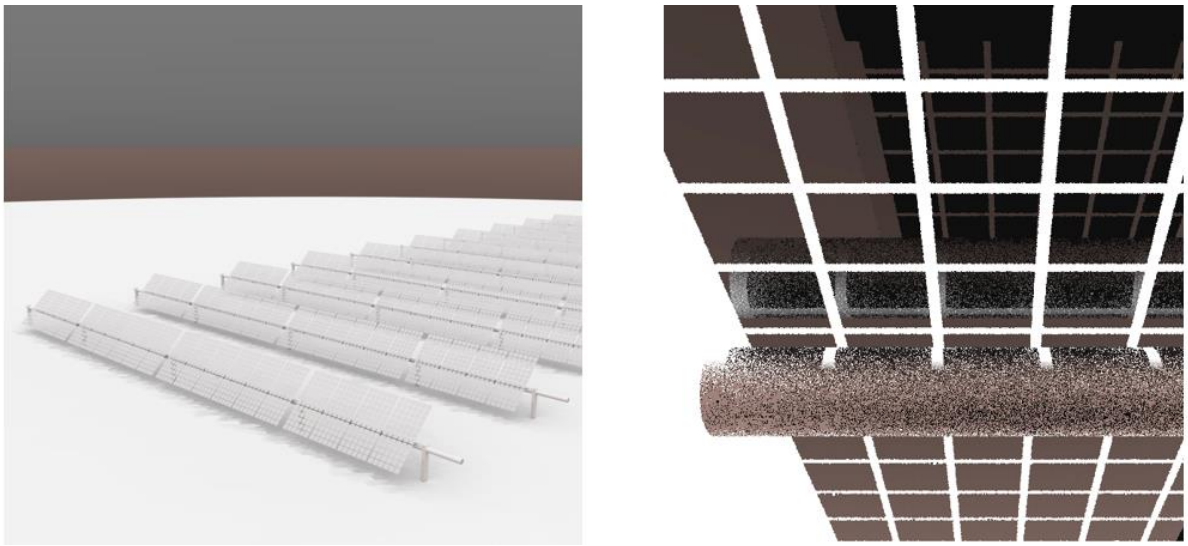

Figure 46: (left) Model in bifacial_radiance of the NREL bifacial experimental single-axis tracking field array in Golden, Colorado. (right) Close-up on a module modeled cell-by-cell, with round torque-tube and glass.

Also included in the software are functions for processing irradiance results and using them as inputs to the open-source software PVMismatch to calculate module and row power output and electrical mismatch [126]. Since bifacial_radiance can sample any location of the array, this is also an ideal tool to study edge-effects resulting from an array's size [127].

6.2.2 BifacialVF model

(Bill Marion and Mark Monarch)

The BifacialVF model is a python implementation of a model developed by the National Renewable Energy Laboratory for estimating the back-side irradiance (BSI) for bifacial PV modules [128]. It was originally coded in C++, but a python open-source is available in [129]. The model uses view factors VF, elsewhere referred to as configuration factors, to calculate the BSI. A VF is the fraction of irradiance leaving a surface that is incident on a receiving surface [73].

As an example of an equation using a VF, (28) is the familiar equation for the ground-reflected radiation, I_r, incident on the front surface of a PV module:

$$Ir = \rho \cdot \mathrm{GHI} \cdot (1 - \cos\beta) / 2 \qquad (28)$$

where ρ is the ground albedo, GHI is the global horizontal irradiance, and β is the PV module tilt angle from horizontal. The term ρ GHI is the irradiance leaving the ground surface and the VF is equal to $(1 - \cos\beta) / 2$.

The use of VF assumes that the radiation is isotropic, that is, the same intensity for all the angle-of-incidences (AOIs) considered. For ground-reflected radiation for the back side of the PV module, shadows disrupt the isotropic assumption. However, the ground area may be divided into areas with equal irradiance distribution and VF applied separately, and then summed to determine the resultant ground-reflected irradiance. A similar technique may be used to determine the diffuse sky irradiance received when the view of the sky is partially obstructed.

The model is applicable for a single row or multiple rows of PV modules of reasonable length. It calculates the BSI for each row of cells to quantify the radiation profile in the PV module slant height direction. It does not distinguish differences in BSI along the row's length, such as edge effects, which are generally not significant for systems of any size.

The model has three main objectives:

- Identify the ground that is shaded by the PV array
- Determine irradiance received by the ground by accounting for shading and restricted view of the sky
- Determine the irradiance for the rear side of the PV module

These objectives are discussed in the following sections.

Identify ground shaded by the PV array

Using the PV array dimensions and orientation, site location, and time, the sun position is calculated, and shadows are projected in the row-to-row (rtr) dimension. The rtr is divided into n segments (such as 100) and each segment identified as shaded or unshaded.

Determine irradiance received by the ground

The Perez tilted surface model [130] is used with the direct normal irradiance (DNI) and diffuse horizontal irradiance (DHI) to decompose the DHI into its circumsolar (I_{cir}), sky (I_{sky}), and horizon (I_{hor}) components. Using Equation (29), the ground-reflected irradiance (GRI) for each of the *n* segments, GRI_n, is determined.

$$\mathrm{GRI}n = a \cdot (\mathrm{DNI} + I_{cir}) + \mathrm{VF}_{sky} \cdot I_{sky} \tag{29}$$

where *a* is the cosine of the sun zenith angle if the ground segment is unshaded. If the ground segment is shaded, *a* is the cosine of the sun zenith angle multiplied by the fractional opening of the PV array due to gaps between PV cells of the PV module and gaps between PV modules of the array. VF_{sky} is determined using Equation (30) with the view angles of the sky, as shown in Figure 47. For horizontal ground segments, the contribution from I_{hor} is not significant and may be ignored.

$$\mathrm{VF}sky = ½ \cdot (\cos\theta_{S1} - \cos\theta_{S2}) \tag{30}$$

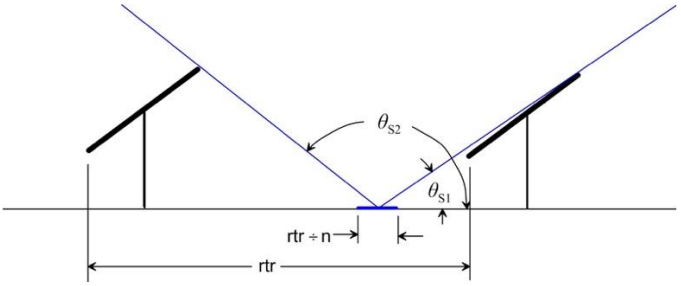

Figure 47: Field-of-view angles for determining the VF for the diffuse sky radiation incident a ground segment.

Determine irradiance received by the back side of the PV module

For the location of each row of horizontal PV cells of the PV module or panel, the back-side irradiance is determined by summing the irradiance from the sky, the irradiance reflected from the ground, the irradiance reflected from the front surface of the PV modules in the row behind, and the irradiance from the sun and circumsolar region of the sky if the AOI is less than 90°. The irradiance reflected from the front surface of the PV modules, I_{refl}, is calculated for only the diffuse radiation incident on the front surface. The reflection of the beam and circumsolar radiation from the front surface of the PV module is considered specular and not likely to be reflected to the back side of the PV module in the row to the front for typical PV array configurations.

The diffuse irradiance for the BSI is summed by dividing the field-of-view into 180 one-degree segments, and adding for each segment the product of its VF, AOI correction and the value of the source's irradiance viewed by the segment (sky, horizon, ground-reflected, or PV module–reflected). The BSI is represented by equation (31):

$$\mathrm{BSI} = b \times F_b \times (\mathrm{DNI} + I_{cir}) + \sum_{i=1^\circ}^{180^\circ} \mathrm{VF}_i \times F_i \times I_i \qquad (31)$$

where b = maximum (0, cosine of the AOI of the DNI); F_b is the AOI correction for the DNI using the air-glass model of Sjerps-Koomen et al. [131]; $\mathrm{VF_i}$ is the VF for the i^{th} one-degree segment; F_i is the AOI correction for the i^{th} one-degree segment; and I_i is the irradiance viewed by the i^{th} one-degree segment (either I_{sky}, I_{hor}, $\rho \cdot GRI_n$, or I_{ref}). The $\mathrm{VF_i}$ is represented by Equation (32):

$$\mathrm{VF}_i = {}^1\!/_2 \times [cos(i-1)] - cos(i) \qquad (32)$$

where i is in degrees with a range from 1° to 180°. The field-of-view corresponding to a $\mathrm{VF_i}$ is shown in Figure 48.

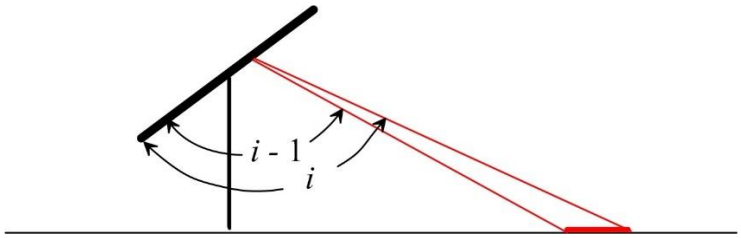

Figure 48: Field-of-view of the ground for a one-degree segment depicted by the angles *i* and *i*-1.

AOI corrections for the one-degree segments of diffuse radiation must consider that the AOI varies not only within the angular i and i-1 limits, but also for radiation originating along the length of row (into or out of the page for Figure 48). To determine a value of F_i for the one-degree segments, we used a previously developed method [128], where an elemental radiation's AOI correction is weighted by its contribution to the in-plane irradiance. The results are shown in Figure 49. Note that the F_i is always less than one because the majority of diffuse radiation is not directed normal to the surface.

Although variations in irradiance for the front side of the PV module are less, the same principles may be applied to account for inter-row shading and variations in field-of-view of the sky due to the presence of rows of other PV modules. For interior rows, the front side irradi-

ance for the bottom of the PV module may be 1 to 2% less than for the top of the PV module. Back-side irradiances have the opposite trend, with the irradiance for the bottom of the PV module being two or more times greater than for the top for some circumstances.

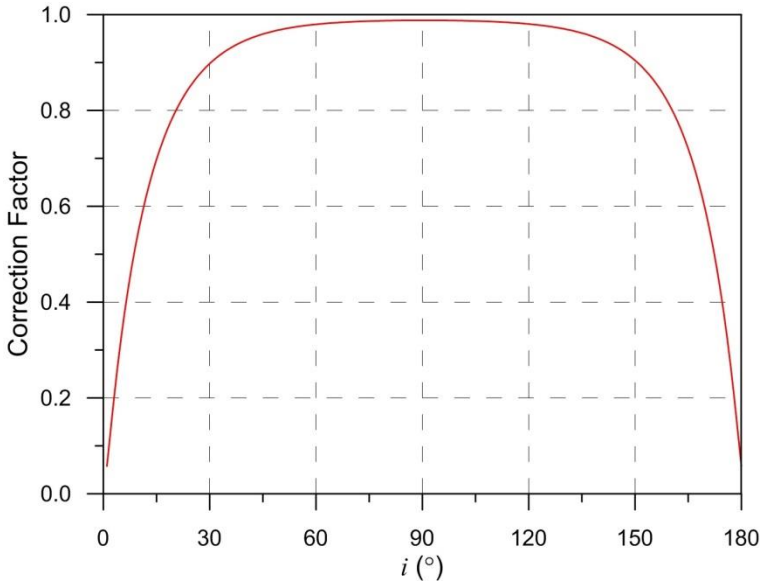

Figure 49: AOI corrections for the one-degree segments of diffuse radiation as a function of the angle *i*. For PV modules with an uncoated glass back-surface with a refractive index of 1.526.

6.2.3 PVNOV model

(Oume Lgheit Rhazi, Matthieu Chiodetti)

PVNOV is a 3D reverse ray-tracing, in-house software by Électricité de France (EDF). PVNOV is a design tool used to build numerical models of PV plants [132], [133]. It allows prediction of the theoretical yield of a future project before it is built depending on the equipment chosen. It can take into account the performance of different kinds of modules and inverters and makes it possible to study the irradiance, thermal, and electrical phenomena that affect the yield estimate. It allows accurate definition of the following PV system characteristics:

- Weather file and sky modeling (isotropic/anisotropic)
- Ground albedo and of any other 3D element of the scene (all reflections considered are isotropic)
- Topology and horizon
- Module type and its electrical/optical characteristics
- Inverter type
- Array configuration: size, orientation, tilt, row-to-row spacing
- Mounting structures definition
- Module string wiring
- Soiling on the panels
- Custom tracking algorithms
- Advanced module and cell thermal model (capacitance, infrared exchanges…)
- Multi-year degradation calculation

The sky model used is isotropic or Perez, with inputs of either DNI and DHI, GHI and DHI, or POA irradiance (global tilted irradiance). Sun position is calculated at 11:30 for a TMY3 datapoint at 11am. The input weather file has no limits or restrictions regarding the time step. Hence, the user is able to load data at finer timesteps.

PVNOV considers incident angle modifiers in the modules, with a different response for the back side than for the front side. Calculation of irradiance can be done at the cell level for each cell on the PV system or at the module level (Figure 50). Shading from any 3D elements in the scene is considered (racking, frame, buildings, row-to-row shading). The software has single-axis tracking with and without backtracking implemented.

For power, PVNOV has the same features as PVSyst and calculates the power at the inverter output (Figure 51). Power is calculated considering module temperature based on a capacitive thermal model accounting for convective, conductive, and radiative heat exchanges. Electrical mismatch is accounted for in the software based on either IV resolution or a simplified model. Edge effects are included in the calculation. PVNOV also has a batch version that enables it to be coupled or controlled by other tools.

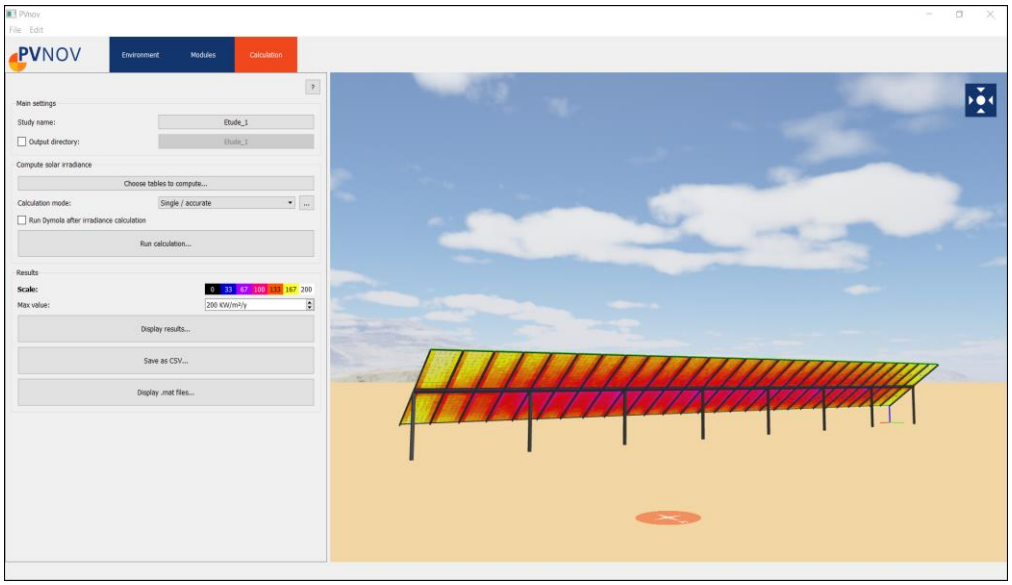

Figure 50: Calculation of irradiance for each module in a row using PVNOV.

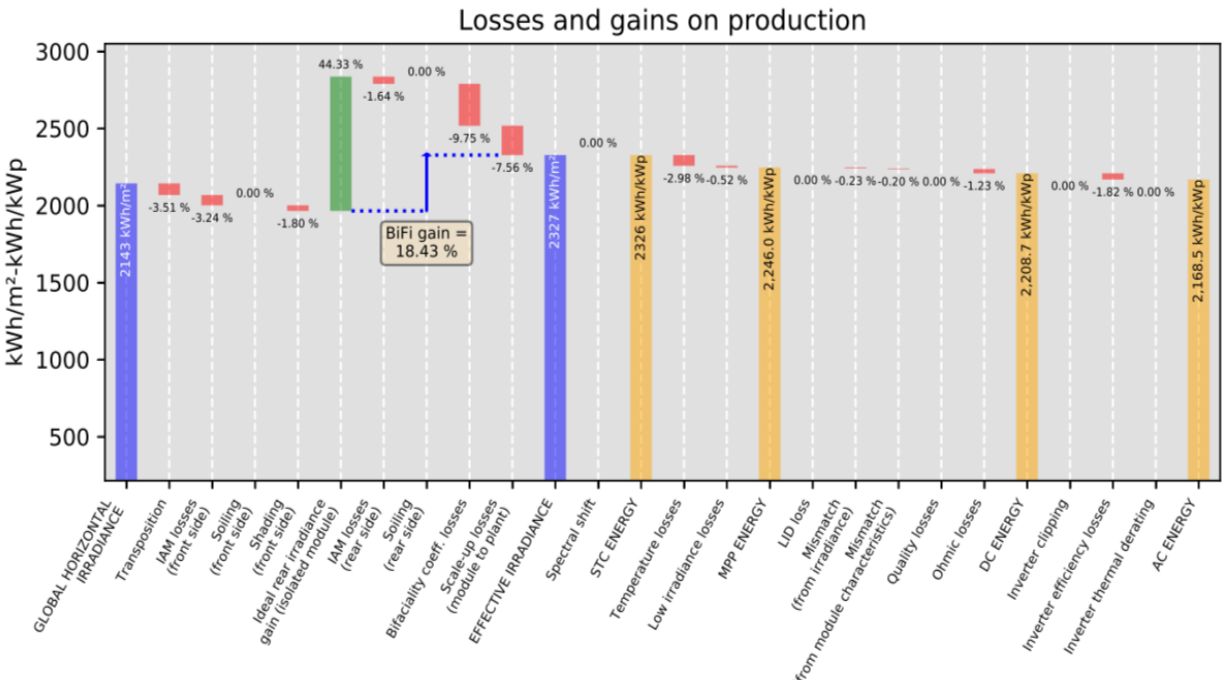

Figure 51: Losses and gains on production calculated by PVNOV.

6.2.4 System Advisor Model

(Silvana Ayala Pelaez)

System advisor model (SAM) is free software for modeling the performance and economics of renewable energy projects [134]. It was developed by NREL with funding from the US Department of Energy. It runs in Windows, OS X, and Linux; one or two new versions are delivered per year. It also has a software development kit. A version of the bifacialVF model was added to SAM in October 2018 to calculate rear-side irradiance for bifacial PV modules [135]. A 2019 Q4 release fixed known issues on the diffuse calculation of single-axis-tracked systems and the implementation now tracks closely with bifacialVF [136], [137]. As an added benefit, SAM can calculate system power performance and economics, with an extensive library of modules and algorithms.

Additional rear-side irradiance losses, such as mismatch loss between front side and rear side, shading due to mounting structure or tracking system, and soiling on the rear side can be specified as inputs to SAM. A transmission fraction can also be specified to account for spacing between modules and between cells in a module (Figure 52). The bifacial outputs of SAM are a loss diagram showing bifacial irradiance gain, as well as time series for front and rear-irradiance for each subarray and total array.

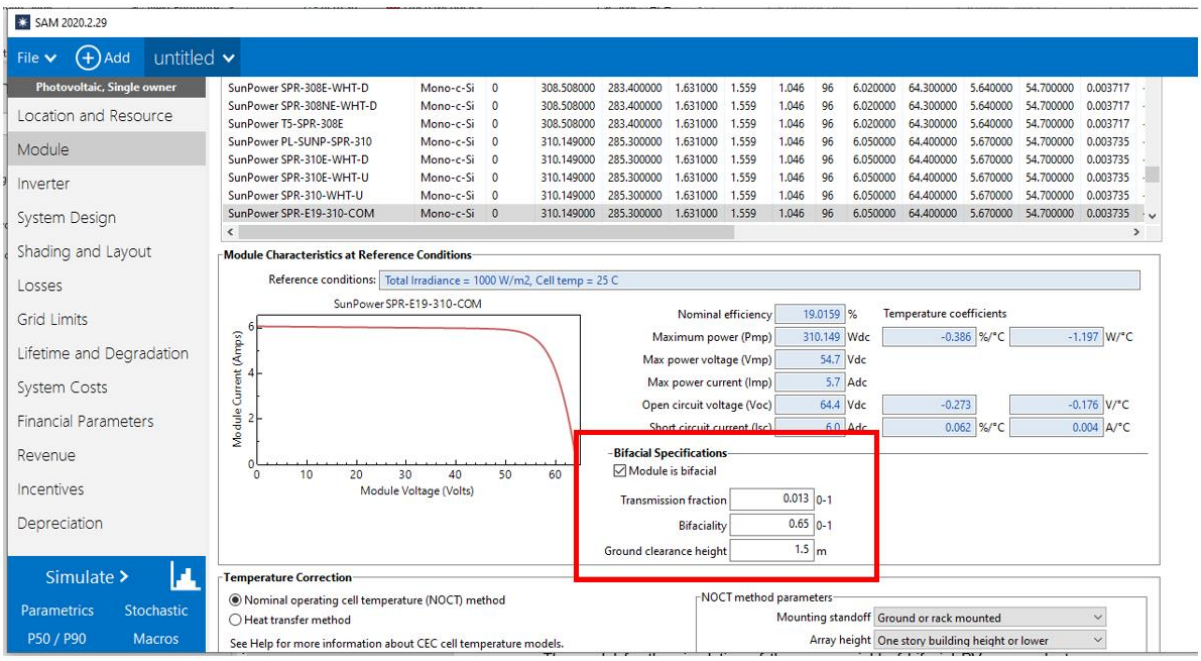

Figure 52: System Advisor Model bifacial functionality for module and simulations.

6.2.5 University of Stuttgart model

(Dimitrij Chudinzow)

The model for the simulation of the energy yield of bifacial PV power plants was developed by Dimitrij Chudinzow as part of his doctoral research at the Institute of Energy Economics and Rational Energy Use, University of Stuttgart. The model was developed in Matlab. The development process focused primarily on the optical submodel, rather than on the electrical or thermal submodels.

The model can simulate the energy yield of fixed-tilt and single-axis tracked bifacial PV power plants and distinguishes between two tracking principles:

- Azimuth tracking: To follow the azimuth angle of the sun, the axis of a module row has a north-south orientation, with the front sides of the module rows oriented east in the morning and then rotating during the day until they are oriented west in the evening.
- Elevation tracking: The axis of a module row has an east-west orientation, and the tilt angle of the module rows follows the elevation angle of the sun.

The algorithms used for the tracking calculations were taken from [120]. They were originally developed for monofacial systems and have not been adapted to bifacial PV systems in the context of this model. Backtracking to avoid self-shading is not considered. The simulations can be calculated in any temporal resolution, whereby usually an hourly resolution is chosen.

When calculating the absorbed irradiation, eight contributions are considered: DNI_{front}, DNI_{rear}, DHI_{front}, DHI_{rear}, $GRI_{DNI\text{-}front}$, $GRI_{DNI\text{-}rear}$, $GRI_{DHI\text{-}front}$, and $GRI_{DHI\text{-}rear}$, where GRI stands for ground-reflected irradiance. The absorbed DHI irradiation is calculated using the isotropic sky diffuse model. To calculate the contributions of GRI, a finite ground area is considered, and 3D view factors are calculated for the front and back of each cell string of each module. This procedure allows consideration of edge effects, but the calculation of 3D view factors in the calculation leads to a high computing effort.

Defining “view fields” allows for consideration of the detrimental influence of ground shadows on the energy yield of each row and the calculation of “edge effects” (Figure 53). The model also checks each cell string whether the front or rear is shaded, emulating a bypass diode.

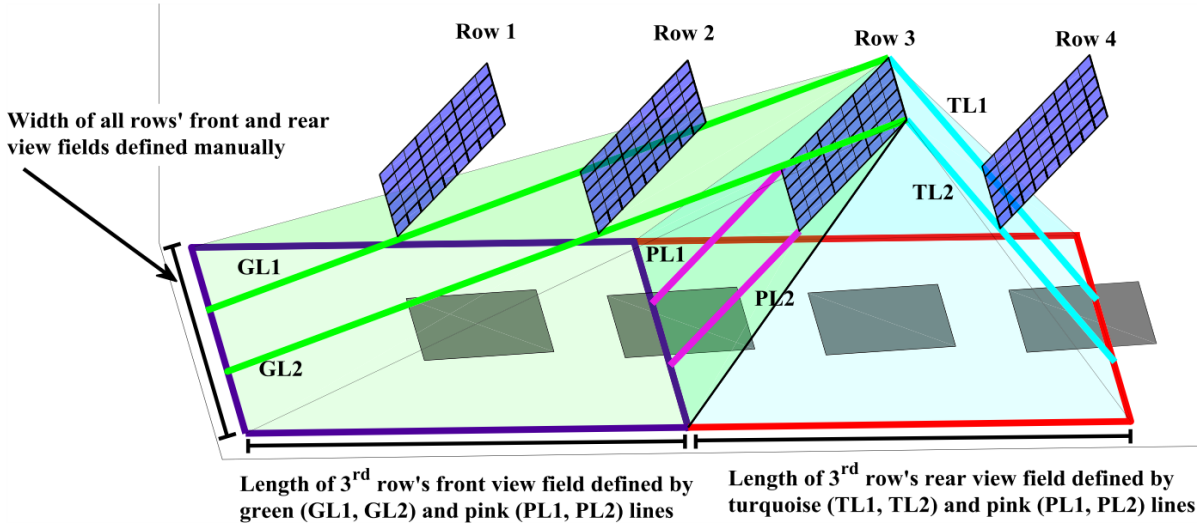

Figure 53: Exemplary definition of the front and rear view fields for module row 3. The view fields are defined for each module row. A central assumption is that the irradiance reflected from the ground outside any field of view does not contribute to the energy yield.

The GRI calculation assumes that the modules are completely opaque and that their cast ground shadows do not receive any beam irradiance. It also assumes that the modules do not attenuate the DHI irradiation that hits the cast ground shadows. Row-to-row reflections are neglected in the model.

A value of 0.9 is used in the simulation model for the effective transmittance-absorptance product τα [120]. The latest version of the simulation model calculates the electrical efficiency for both sides of a module as follows [138]:

$$\eta = \eta_{ref}\left(1 - \beta * \left(T_{amb} - T_{ref} + \left(\frac{9.5}{5.7 + 3.8 * v_{wind}}\right)(T_{NOCT} - T_{amb})\frac{I}{I_{NOCT}}\right)\right) \qquad (33)$$

Figure 54 shows exemplary results of the simulation model for the location San Felipe, Chile [139].

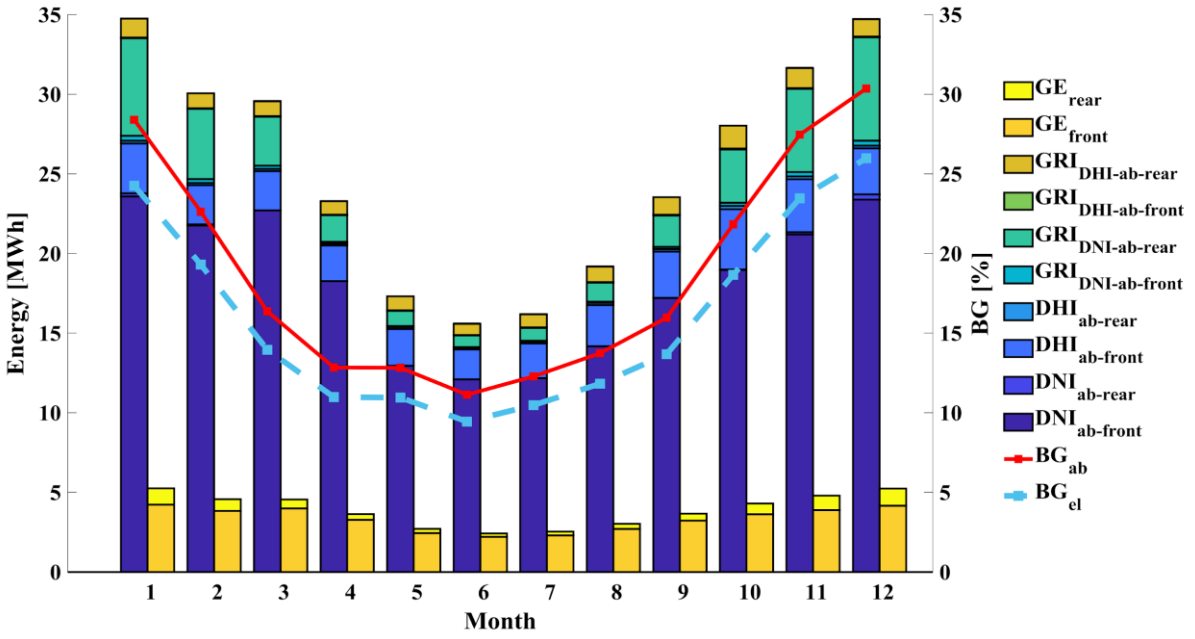

Figure 54: Breakdown of absorbed irradiation, amount of generated electricity (GE) and bifacial gain related to absorbed irradiation (BG_{ab}) and bifacial gain related to generated electricity (BG_{el}) for the location San Felipe, Chile.

Based on the presented simulation model, a techno-economic analysis of bifacial vertical PV power plants was conducted and published in [140]. The influence of field design and location on the energy yield of fixed and single-axis tracked systems was also investigated [141].

6.2.6 PVsyst model

(Jill Tymchak, Joan Haysom)

PVsyst is a software package for the study, sizing, and data analysis of complete PV systems [111]. It also models bifacial systems with the use of view factors (or “form factor”),(see Figure 55) to calculate the fraction of light effectively reaching the PV module [142], [143]

For these, PVSyst proposes two different modes for the calculation of bifacial systems:

- Simple “unlimited sheds” with a 2-dimensional calculation. This also provides a set of pedagogic tools for a deep understanding of the different irradiance contributions
- Simple “unlimited trackers” (horizontal axis) with a 2-dimensional calculation involving a full pre-calculation for several positions of the trackers.

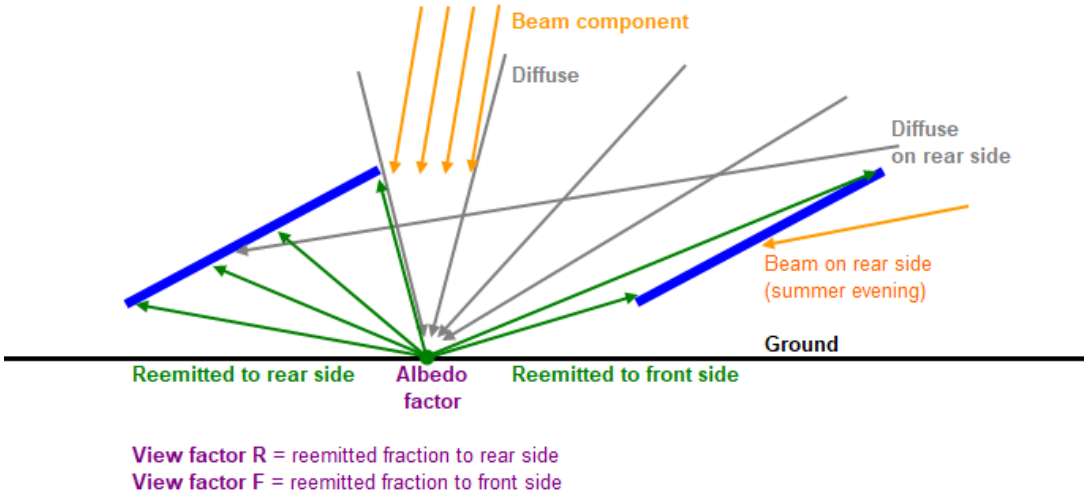

Figure 55: View factors in PVsyst

The bifacial model in PVsyst is based on three main hypotheses:

- The diffuse irradiance is isotropic.
- The re-emission of each ground point is isotropic, with a specified albedo factor.
- The additional irradiance on the rear side is added to the front irradiance for the application of the one-diode model.

The irradiance on the rear side will give rise to an increase of the global PV module output power. During the simulation, PVsyst simply adds the rear irradiance (weighted by the bifaciality factor) to the front incident irradiance before computing power using the one-diode model.

PVSyst considers a mismatch loss factor to account for the non-uniformity of the rear side of the modules and its effect on the current of the whole string. As no model exists for the estimation of this mismatch loss factor, this factor is set to 10% by default and can be changed by the user. This mismatch loss is only applied to the rear-side irradiance.

6.2.7 IMEC Energy Yield Simulation Framework model

(Santhosh Ramesh, Imre T. Horvath)

The Imec Energy Yield Simulation Framework is a complete in-house PV energy yield modeling software developed by the Interuniversity Microelectronics Center (Imec) in Belgium. The framework is developed based on a bottom-up, physics-based philosophy and its structure is shown in Figure 56. Further details are available [144], [145].

Inputs

The main model input parameters are defined in the first block. First, the climate database is loaded (i.e., time series of global horizontal, direct normal, diffuse horizontal irradiance, ambient temperature, wind speed and direction) and checked. The module lay-up is described by setting the material properties of the different layers in order to define their optical and thermal behavior. Next, the geometry and the electrical layout of the PV plant is defined using a Computer Aided Design (CAD) 3D model as shown by Figure 56.

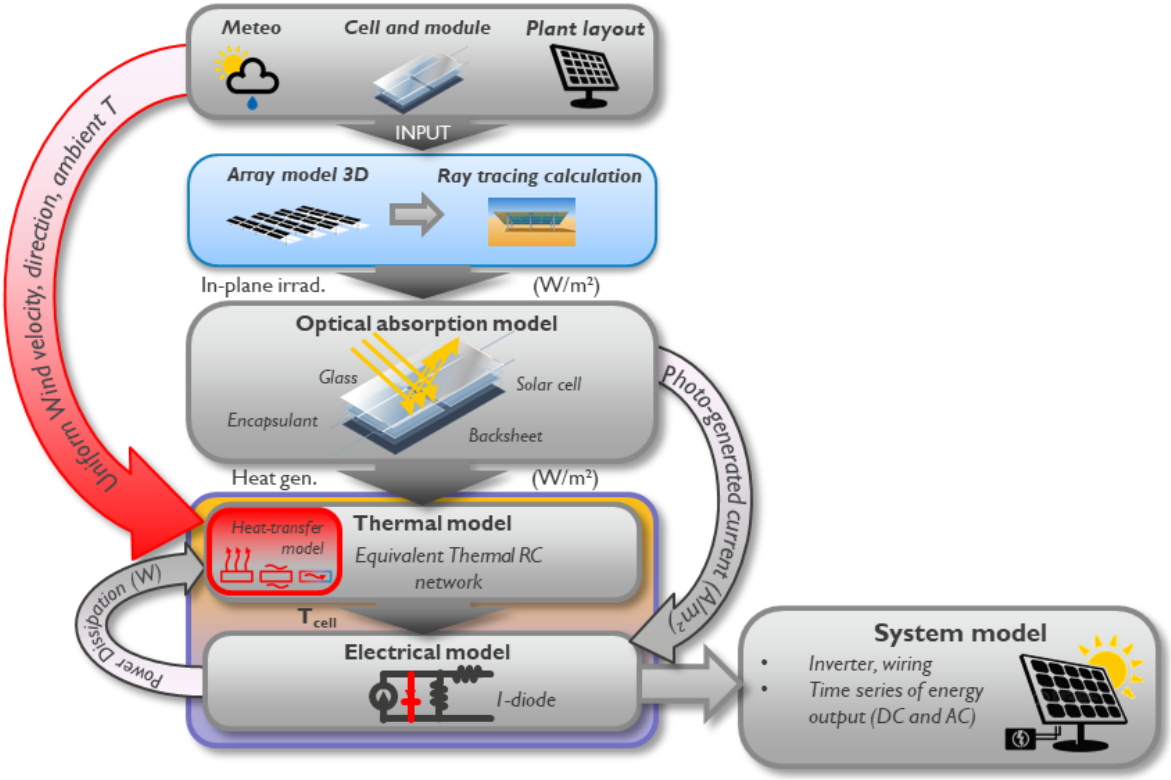

Figure 56: Structure of the Imec Energy Yield Modeling framework.

In-plane irradiance calculation

The present framework uses a ray tracing-based daylight simulation technique, to compute monofacial, bifacial and HSAT in-plane irradiance. This technique is called Daylight Coefficient Method (DCM) [146]. The DCM allows to significantly reduce computing time, while approaching the level of detail and accuracy of traditional ray tracing computations.

First, the fix parts of the simulation are defined: model geometry and the sky dome, which acts as the light source in the scene. The sky dome is defined as an assembly of finite-sized, discrete sky patches, whose time-varying direct and diffuse irradiance can be assigned based on the loaded climate data and an all-weather sky model [147]. Another parameter that can be reused for any timestep is the unchanging relationship between the radiance of any sky patch and the amount of light received by any point on the model. In other words, a unique, linear operator can be defined in matrix form, which relates sky patch radiance to irradiance of specific sensor points defined on the model. This linear operator is called Daylight Coefficient.

Time series of front and back-side in-plane irradiance $\boldsymbol{I_p}$ can be computed at any number of sensor points (*P)* on the 3D model surface, by a matrix multiplication shown by Eq. (34), between ***D*** the Daylight Coefficient Matrix and ***S*** the sky matrix describing the time series of sky patch radiance.

$$I_P = D \cdot S \tag{34}$$

The framework implements the DCM using functions of the open source Radiance [123] and Accelerad [148] packages enabling GPU-accelerated computing.

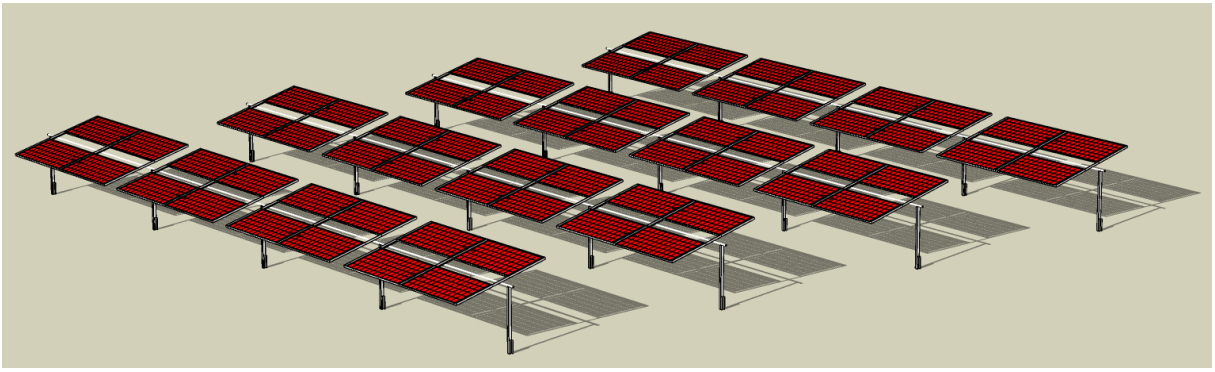

Figure 57: Example of PV array 3D model used for bifacial energy yield simulations within the Imec Energy Yield Modeling framework.

This 3D CAD-based DCM calculation method allows to perform cell, module or string level, time-resolved (from 1 second up to 1 year) front- and back-side irradiance calculations considering shading (by PV rows or any other structure), specular reflection, ground reflection, with- or without incidence angle effect, PV mounting structure, and module frame.

In-plane irradiance is calculated for every PV element present in the electrical layout of the PV system, as shown by Figure 58.

Thermal-electrical calculation

The thermal-electrical behavior of the modeled PV system is calculated next. Each PV element (cell, module, string, or any other scale) is modeled separately using two coupled electrical equivalent circuits: one to compute the electrical state using the 1-diode PV circuit model; and another one to compute the thermal state of the PV element by means of a resistive-capacitive circuit, which models heat generation (as function of meteorological input and electrical operating point), heat conduction, convection and radiation. The coupled circuits output the IV curve of the PV element, which are then combined using an IV curve superposition method, to produce the IV curve of each inverter MPPT channel input. Following this approach, the PV system electrical state is resolved on cell, module, string or any other chosen level, with the maximum time resolution of 1 second.

Mismatch caused by non-uniform irradiance is computed considering the irradiance, temperature and the electrical interactions of the mismatched PV elements.

Further information

The framework calculates sun position for TMY3 data at the timestamp provided. It computes an albedo value for each simulated time-step, based on a constant ground reflectance value. Fixed-tilt and single-axis tracking arrays can be modeled in the software, which besides calculating rear irradiance, can also provide rear irradiance non-uniformity, account for shading losses from racking and other objects, and calculate power and module temperature, edge effects, and electrical mismatch.

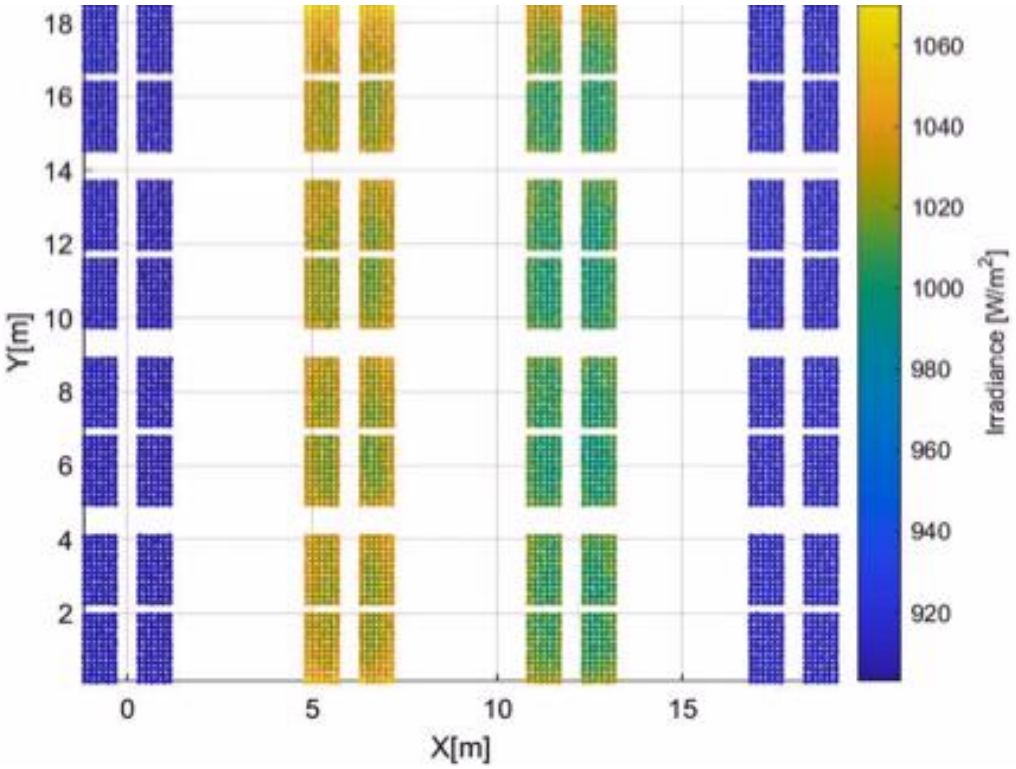

Figure 58: Result of bifacial irradiance calculation using the Imec Energy Yield Modeling framework. The plot shows solar cell-resolved non-uniformity of bifacial effective irradiance on the PV array visualized in Figure 57, around noon. The first and last rows are composed of bifacial modules with covered rear-sides and the two central rows contain bifacial modules with different bifaciality factors.

6.2.8 SUNLAB DUET model

(Annie C. J. Russell, Christopher E. Valdivia, Joan Haysom, Karin Hinzer)

Developed at the University of Ottawa's SUNLAB, DUET is a flexible 3D simulation software that incorporates sectioned view factors with rack shading to calculate performance details and energy yields for fixed-tilt and single-axis tracked monofacial and bifacial PV systems [149]–[153]. With rigorous optical and electrical simulations, parameterized cell, module, string, and array design details can be explored with a wealth of outputs to analyze the impacts of system design factors or environmental conditions. Slotting in between fast view factor models and lengthy ray tracing models, DUET balances performance detail with computational efficiency via simulation parameter settings customizable to best suit each application.

In DUET, the ground surface and panel surface are sectioned into patches. The direct and diffuse irradiance incident on each ground patch is summed. The intensity of light reflected from a ground patch (scaled by the albedo) is equal in all directions (Lambertian). Rays between all pairs of ground and panel patches are checked for intersection with shading elements (in which case the irradiance is dampened or extinguished). The irradiance arriving at the panel patch is scaled by the solid angles between patches. Ground-reflected, sky dome, and direct-beam light that is incident on the collecting surface is multiplied by incidence angle modifiers (IAM) for both the front and rear faces. The angle of incidence is based on the rela-

tive position of the transmitting and receiving patches. No secondary reflections off racking or other panels are considered.

DUET assumes input irradiance data is hour-ending and calculates sun position at the middle of the hour (e.g., 11 am datapoint, sun position is calculated at 10:30 am). However, DUET does not require hour-based time steps. In general, the software assumes period-ending data, and computes the sun position half-way between timestamps, where the period is any time step. The software can consider any IAM equation, with different modifiers for the front and rear sides. However, for the simulations provided for this report, front and rear IAM is based on the ASHRAE incidence angle modifier model.

DUET allows for a number of shading elements to be considered, including vertical posts, torque tubes, and in-plane racking pieces (frames, supports). Shading elements are simulated as planes, cylinders, and rectangular prisms. Two-dimensional (2D) front and rear irradiance profiles are available at the cell level. Furthermore, irradiance profiles can be output on an arbitrarily resolved grid, depending upon the patching applied to each cell.

Single-diode models are applied to each cell in the module to calculate current-voltage curves. Cell current-voltage curves are dependent on cell temperature (dictated by ambient temperature and cell irradiance). These curves are summed according to the intra-panel cell wiring configuration (combination of series/parallel interconnection is possible), and bypass diodes are included. The maximum power point is then extracted. IV curves can be output at each time stamp, and thus the performance of a string/array of modules can be computed in the same fashion as the module IV curve.

DUET can model the performance of a module at any location in the array to capture shading or edge effects. Multiple module locations can be modeled for the same period and IV curves are summed to the string and array levels. Electrical mismatch is automatically calculated when constructing the IV curve of the full module and of the string. Electrical mismatch factors can be calculated and output at the module, string, and array levels.

6.2.9 DNV GL SolarFarmer

(Anja Neubert, Mark Mikofski)

DNV GL has a software that combines the 3D hemicube model and 2D view factor for the bifacial simulations [154]. Albedo values are assigned monthly or yearly. The sky model can be Hay or Perez, using as inputs GHI and DHI. Sun position is calculated at midpoint of the hourly interval for handling the TMY3 data.

The software does not consider spectrally-dependent albedo, and does not consider angular-dependent reflectivity on either side of the modules. IAM rear-side reflections are also not considered, and it does not calculate rear irradiance non-uniformity. It can calculate spectrally corrected rear irradiance, and account for shading losses from racks in the bifacial simulations.

The software can calculate irradiance for fixed and single-axis tracked systems. It calculates power, considering module temperature, and accounts for electrical mismatch. The 3D shading model (not available for bifacial simulation) can also calculate edge effects.

6.2.10 TUAS PVPM model

(Samuli Ranta and Hugo Huerta)

Turku University of Applied Sciences (TUAS) PVPM open-source simulation tool with a graphical user interface was developed to predict the performance of bifacial PV systems.

The Matlab PV_LIB toolbox and the PV Array Performance Model from Sandia were used to develop a simplified model based on irradiance translation calculations performed on both sides of the array, additionally the Python pvfactors package was integrated to the interface to allow a second method to estimate the incident irradiance. With the user interface, TUAS-PVPM couples Matlab and Python PV libraries for modeling the performance of PV systems and allows an easy way to work between them. Bifacial irradiance calculations apply the view factors analytic solutions for 2D geometry representations of the PV arrays [155]. PV rows are considered to be infinitely long (edge effects assumed to be negligible). The sky model is Perez or isotropic with GHI, DHI, and DNI inputs and the sun position is calculated at the timestamp passed for TMY3 data; additional libraries allow the direct use of EnergyPlus Weather files (EPWs) and Photovoltaic Geographical Information System (PVGIS) formats. The power calculation does not consider IAM for reflections on the rear side or spectral corrections. TUAS PVPM does not account for electrical mismatch.

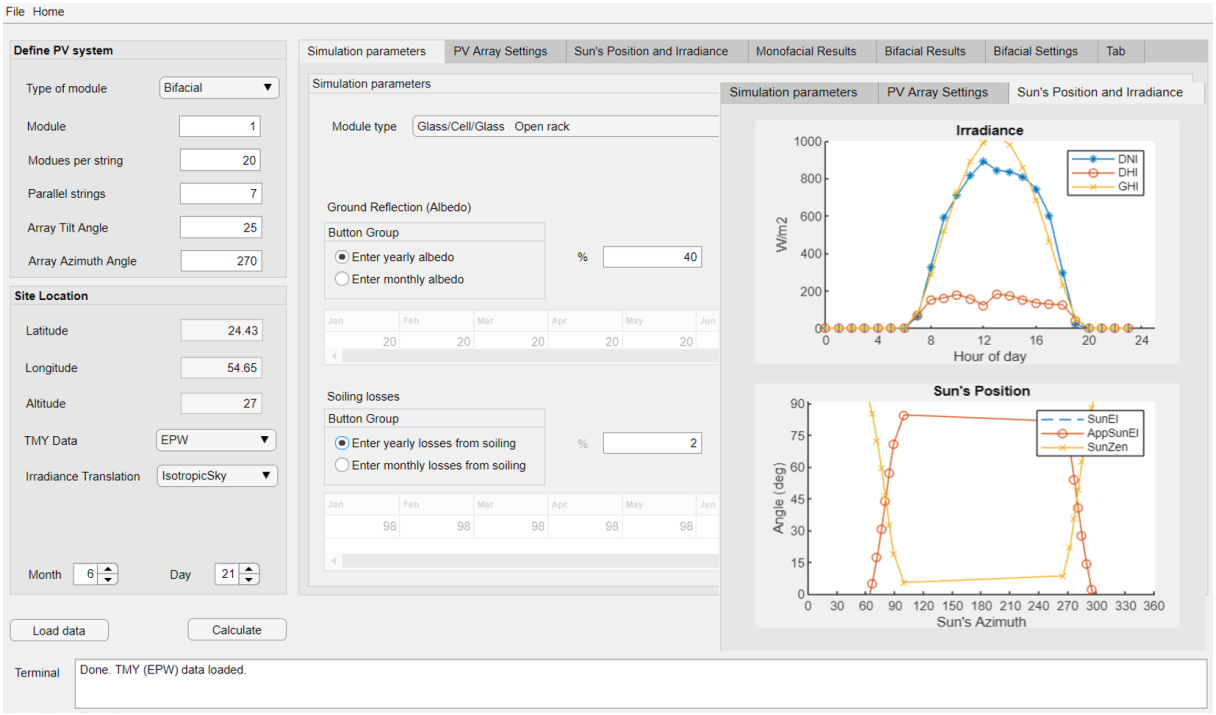

Figure 59: Screenshot of TUAS bifacial performance modeling software.

6.2.11 MoBiDiG hybrid model

(Djaber Berrian)

The MoBiDiG hybrid is paid software developed by the International Solar Energy Research Center (ISC) Konstanz [156], [157] that combines view factor and raytracing functions. Depending on the system size, the user can choose between a 2D view factor and a 3D raytracing optical model. For simulations, MoBiDiG uses a Perez sky model [130] with 1990 coefficients and GHI, DHI, and DNI as inputs. For TMY3 data, sun position is calculated at a delta half an hour before the timestamp. The hourly albedo is assumed uniform across the whole ground beneath the PV system. The reflections are assumed Lambertian. Specular reflectance of the albedo is considered, as well as IAM on rear-side reflection. Rear irradiance non-uniformity is calculated implicitly in the software. Single-axis tracking systems can also be modeled, but shading losses from racking and other obstructions are not accounted for.

The software calculates power output with module temperature, electrical mismatch, and edge effects taken into account.

6.2.12 Trifactors

(Haffner Florent and Hervé Colin)

Trifactors is paid software developed by the Alternative Energies and Atomic Energy-National Solar Energy Institute (INES) [158]. It was temporally referenced as VF3D before being renamed Trifactors. Trifactors uses a 3D VF approach: the view factors are computed once the geometry is defined and can be used in various temporal simulations without supplementary VF calculations. Notably, if various simulations are run with a given panel, the software reuses previous results to gain computation time.

Trifactors considers instantaneous isotropic diffuse albedo for each datapoint simulated. The sky model is Perez, with GHI, DHI, and DNI as inputs. For TMY3 data, time is calculated with a delta of 30 minutes after the timestamp. The software considers IAM for rear-side reflections using ASHRAE model, with b = 0.05 if there is no additional information, or measured values if available. Currently specular reflections are not handled by the software but listed in the software's roadmap. Rear irradiance non-uniformity is calculated based on the unrestricted mesh element's size. The only shading losses considered are inter-row shading. It also calculates single-axis tracking.

In Trifactors, bifacial IV curves are computed for each PV mesh element and therefore front and rear contribution to electrical production are not separated. Given that an IV curve database is built during the simulation, the more simulations run with an identical module, the quicker the results. To obtain the front-only production, the simulation must be rerun, with the hypothesis that the module is monofacial. In absence of on-site measurements of module temperature, power is calculated with a nominal operating cell temperature (NOCT) model. The software accounts for electrical mismatch and edge effects.

6.2.13 pvfactors

(Marc Abou Anoma)

pvfactors is a python open-source model [159] used to calculate the irradiance incident on surfaces of a photovoltaic array [155]. It relies on the use of 2D geometries and view factors integrated mathematically into a system of equations to simultaneously account for reflections between all of the surfaces at equilibrium. pvfactors was originally ported from the SunPower-developed 'vf_model' package [155].

The model considers albedo for each data point as a reflective uniform value for the whole ground without spectral dependence. The software assumes diffuse reflections from all surfaces; angular dependent reflectivity and specular reflections are not found. The sky model follows the Perez model implementation in pvlib with DNI and DHI as inputs. GHI can also be optionally provided. pvfactors considers angular reflection losses for rear-side reflections and does not correct for spectral irradiance.

The software only accounts for direct and diffuse inter-row shading and not for shading losses from racking and other obstructions, due to the simplicity of the 2D surfaces modeled. It can calculate rear irradiance non-uniformity in the module. The software assumes infinitely long PV rows (because of the 2D geometry) and does not account for edge effects. It can model single-axis tracked systems.

6.3 Results of the modeling comparison

(Silvana Ayala Pelaez and Joshua S. Stein)

As described in Section 6.1, four main modeling scenarios were defined: south-facing fixed-tilt (S1), west-facing fixed-tilt (S2), east-west-facing vertical (S3), and horizontal single-axis tracking (S4). In addition, there was an optional simulation based on real field data measured at NREL's bifacial single-axis tracker field.

For cumulative yearly irradiance, there is quite a variability across the results as can be seen in Figure 60. However, the relative differences between models is consistent from scenario to scenario (i.e., if a model has high rear-side irradiance it does for all scenarios).

In this exercise, information was not gathered regarding the tracking algorithm used by each modeler, which can be different and influence the results. Another important factor is how the different models represent Sun position for each time step. As shown in Table 17, differences in how time steps are interpreted can lead to sun-position divergences of up to 15 degrees. Annual cumulative irradiance on the East ("front") side of the array for Simulation 3, (E-W vertical bifacial system) are plotted in Figure 61. Similar to the other scenarios, the relative differences between models are consistent across different climates.

Selected representative results for S1-S4 are shown in Figure 62 for up to thirteen different bifacial modeling tools that were run. Front irradiance results are shown in Figure 62(a), and (b) for the spring solstice. On (a), we can see that some of the models are considering different sun positions to calculate the values, which is corrected by shifting the data on (b) to see how well the models align. By shifting the teams provided results by minus 1 hr, minus 30 mins, and plus 30 mins most of the results can be aligned up to a +-30 W/m^2 for front irradiance for most of the models. Rear irradiance results are shown in Figure 62(c), (d) and (e). Agreement between simulations varies depending on the day modeled as well as the scenario. Single-axis tracked system in (d) shows a tighter distribution of rear-irradiances, and so does the west-facing modules in simulation S2 (e).

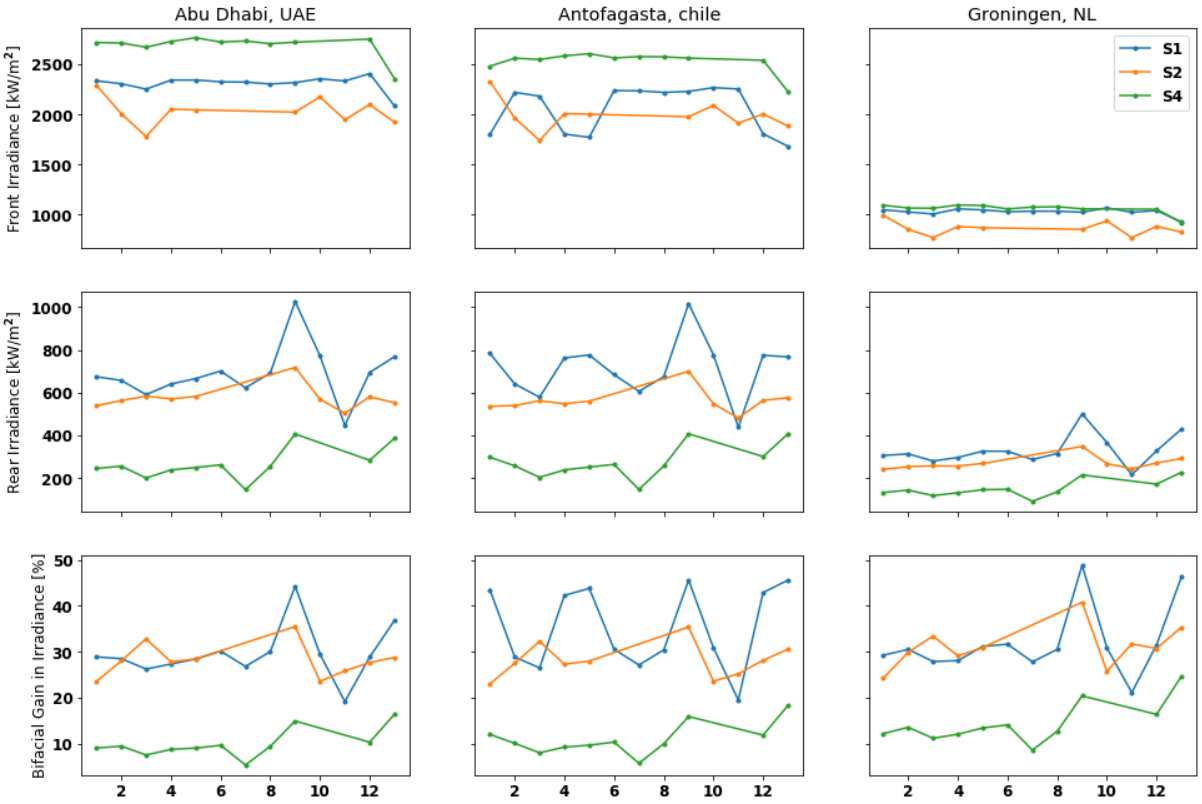

Figure 60: Cumulative yearly results for front Irradiance, rear irradiance, and bifacial gain (rear / front irradiances) for the three cities with different climates. Simulation 1 (blue) is fixed tilt Equator facing, Simulation 2 (orange) is fixed tilt West facing, and Simulation 4 (green) is single-axis tracking. The results are shown on the x-axis in the same order between plots, but they are in random order relative to the way they are presented in the report to anonymize them.

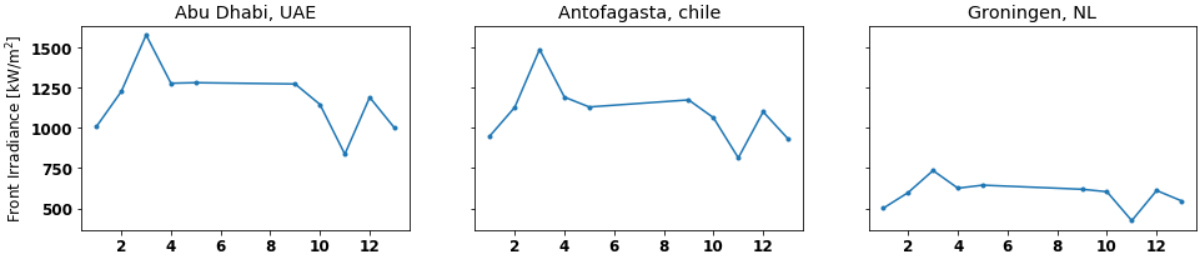

Figure 61: Vertical bifacial modules simulation for cumulative annual "front" irradiance (East facing side). The results are shown on the x-axis in the same order between plots, but they are in random order relative to the way they are presented in the report to anonymize them.

Although most of the software packages agreed on overall front and rear irradiance, there was one tool that consistently underpredicted front irradiance by almost 200 W/m^2 at solar noon; rear-irradiance values were consistent with the average of the other tools. This front under-prediction caused the bifacial gain results from this software to be about 20% above the average of the rest of the tools. This is shown in Figure 62(h), (i), and (j), which shows the bifacial gain for simulation 1 on the summer and winter solstices, and for the single-axis

tracking example. One of the view-factor models also showed 20% above average bifacial gain; looking closer at this tool, its rear irradiance results were consistently 20% above the ensemble average. This same tool's response to variations on the azimuth of the solar panels for Simulation 2 did not follow the other model's trends (as can be seen in Figure 62 (e)).

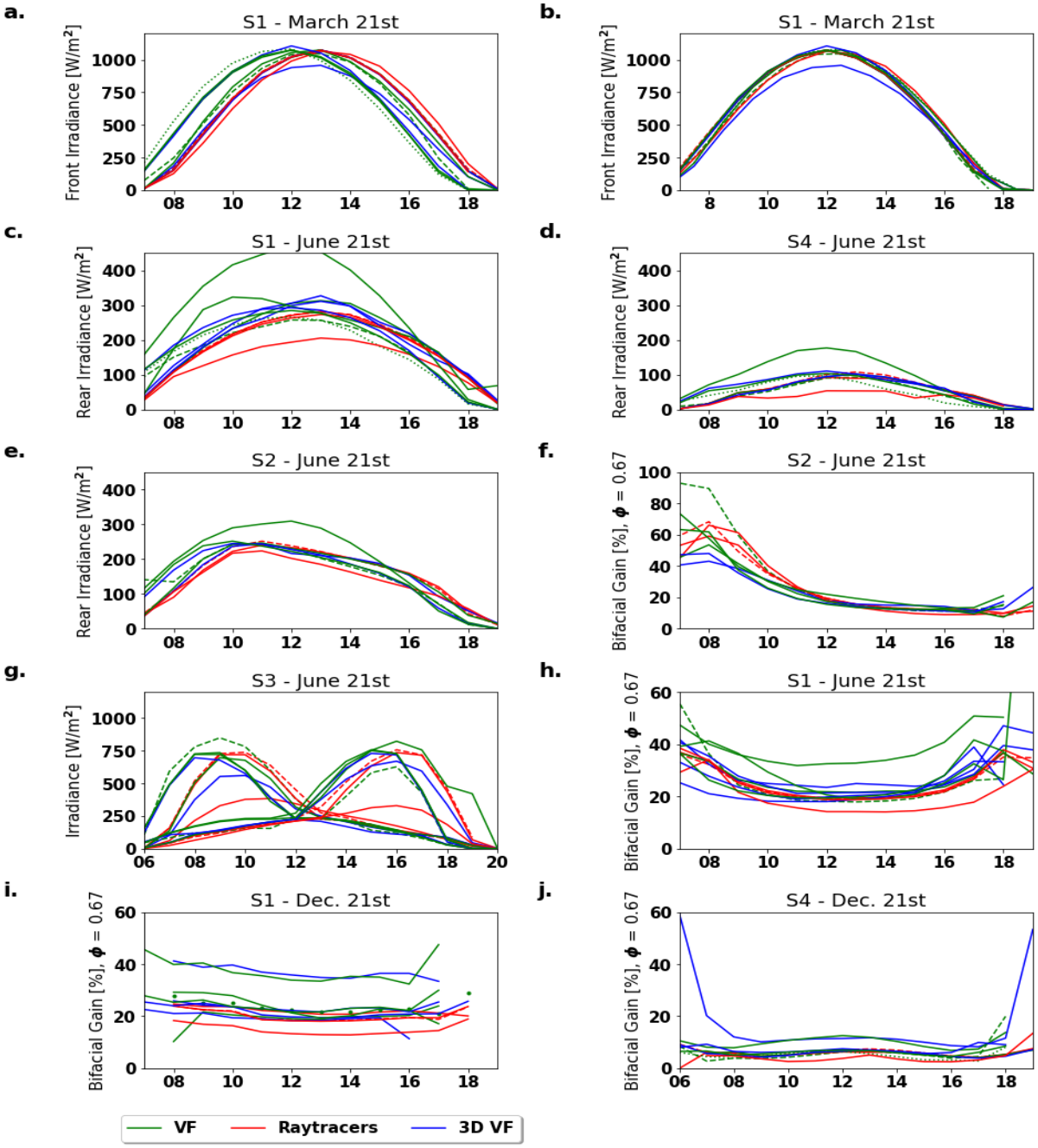

Figure 62: Results for hourly simulations by view factor models (green), raytracing models (red) and 3D VF and others (blue).

Optional Simulation 2 provided field data to compare and validate the simulations. Two raytracing models and four view factor models contributed results for this scenario. Figure 63(a) shows the Global Horizontal Irradiance data used as input to the models. GHI was also used for aligning the results of the tools. Two sunny days and four days with intermittent clouds

were modeled, with overall good agreement for front irradiance (Figure 63(b)). In Figure 63(c) and (d) we see the close-up of front irradiance for a sunny and cloudy day respectively. Three of the tools were limited to only modeling at hourly timesteps, which ignores the short-term variability in the 15-minute field data provided. Agreement between these models for front irradiance is between 30 W/m^2 for the front irradiance on the clear days.

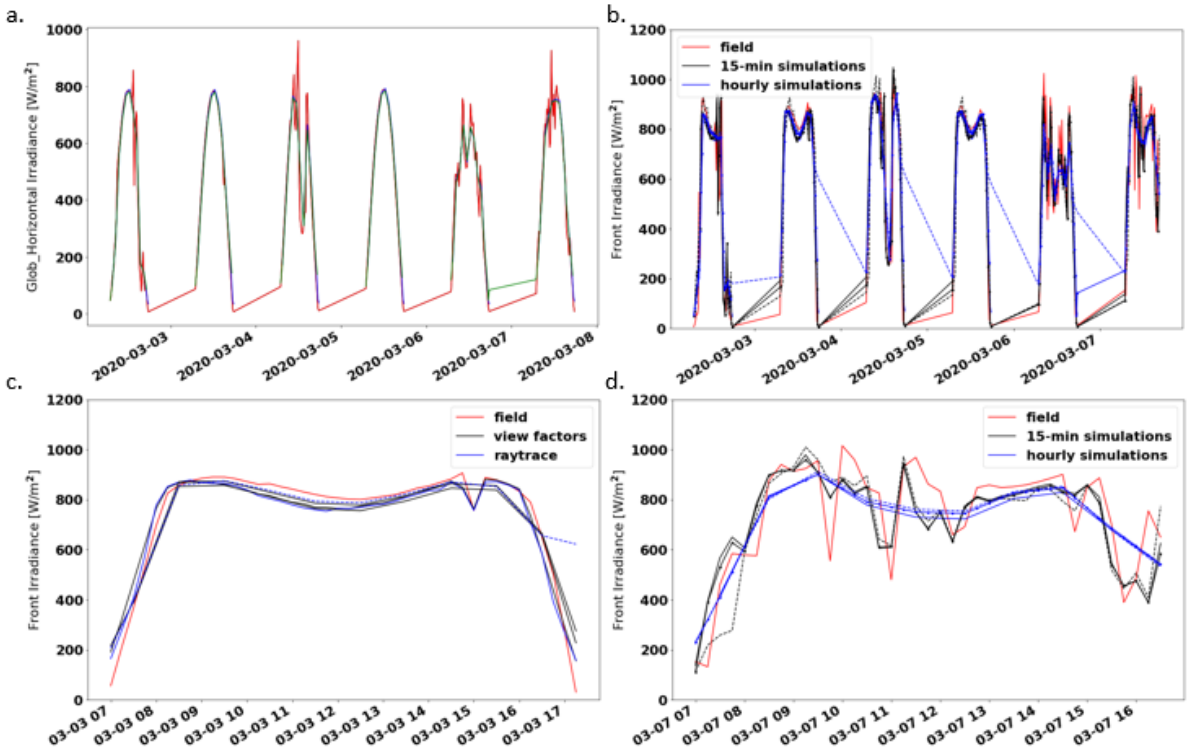

Figure 63: Results for optional simulation 2, including four view factor and 2 raytracing modeling tools. (a) Global Horizontal data was used to properly align the results of all the tools. (b) Front irradiance results for the week modeled. (c) Close-up on simulations and field data for one sunny day and for (d) one variable-cloudy day.

Figure 64(a) shows rear irradiance results for the various models for Optional Simulation 2. Albedo on the first half of the first day is very high, causing the most severe underprediction of rear irradiance for the models. Normalized power production is also shown. Figure 64(b) shows measured vs modeled results for front and rear. Rear results show a much higher deviation from measured for rear irradiances above 120 W/m^2, which are all measured on March 2nd before 1 PM. Table 18 shows the mean bias deviation (MBD), root mean square errors (RMSE) in percentage and absolute values for this week of data, excluding high albedo data (>0.5).

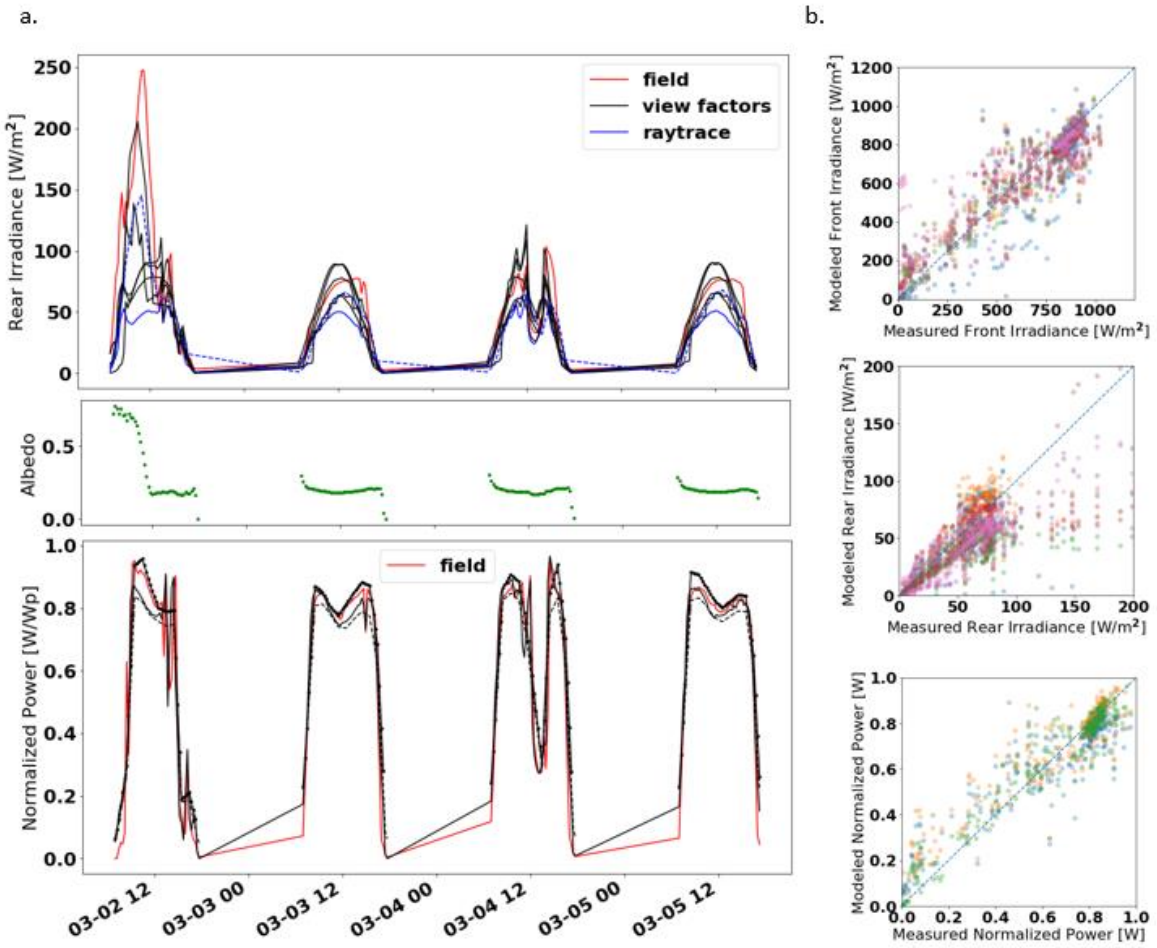

Figure 64: Optional simulation 3 results for a) rear irradiance and normalized power over four days, with albedo shown in green. b) modeled versus measured front rear irradiance and normalized power.

Table 18: Variations between the different simulation tools for Optional Simulation 2, one week of data excluding high albedo data (>0.5).

Tool	Front Irradiance				Rear Irradiance				Normalized Power			
	MBD (%)	RMSE (%)	MBD_abs (W/m²)	RMSE_abs (W/m²)	MBD (%)	RMSE (%)	MBD_abs (W/m²)	RMSE_abs (W/m²)	MBD (%)	RMSE (%)	MBD_abs (W/m²)	RMSE_abs (W/m²)
1	-0.15	15.1	-0.96	99.3	8.98	31.1	4.63	16.0				
1 (GHI)	-11.4	23.2	-75.6	153.1	5.85	26.3	3.07	13.8				
2	-1.22	14.8	-8.0	97.7	-32.6	42.4	-17.1	22.3	1.17	14.2	0.01	0.09
3	-2.73	15.5	-18.3	104.0	-4.05	24.2	-2.14	12.8	-1.92	16.4	-0.01	0.11
4	-0.13	15.7	-0.9	105.1	-25.1	34.4	-13.2	18.1	5.76	17.2	0.04	0.11
5	5.53	25.9	35.8	167.5	-19.1	32.8	-9.87	16.9				
6	-1.04	17.1	-6.9	112.7	-24.9	34.1	-13.1	18.0				
Avg	-1.59	18.2	-10.7	119.9	-13.0	32.2	-6.81	16.8	1.67	16.0	0.01	0.10
Max	5.53	25.9	35.8	167.5	8.98	42.4	4.63	22.3	5.76	17.2	0.04	0.11
Min	-11.4	14.8	-75.6	97.7	-32.6	24.2	-17.1	12.8	-1.92	14.2	-0.01	0.09
Std	4.68	4.12	30.8	26.2	15.2	5.51	7.98	2.89	3.16	1.28	0.02	0.01

7 INTERNATIONAL BIFACIAL FIELD STUDIES

7.1 USA: Sandia National Laboratories bifacial testbed

(Joshua S. Stein)

7.1.1 Description of bifacial testing

Sandia National Laboratories began installing bifacial PV test arrays in Albuquerque, New Mexico, in 2016 and has continued to maintain and monitor performance from these systems. The Sandia PV test field includes PV module- and string-level testing of 12 bifacial arrays in various orientations. For most of the arrays, the ground is composed of a gravel surface with an albedo of between 0.2 and 0.25. A few arrays have ground cover of white rocks with an albedo of 0.55 to 0.6. Table 19 lists the arrays, along with PV cell type and dates of data availability.

All bifacial arrays at Sandia include reference monofacial PV cells used to measure front- and rear-side plane-of-array irradiance, as well as measurements of module surface temperature obtained using thermocouples or RTDs. The arrays are all grid-connected, and the DC electrical performance of each system is monitored at either the string or module level. Measurements are made every second and are aggregated into 1-minute averages. Monofacial modules and strings are paired with each system for comparison. However, because these monofacial systems do not use the same cell technology as do the bifacial cells, bifacial gain calculations require temperature and spectral corrections to increase accuracy.

7.1.2 Summary of bifacial performance results

Prism Solar bifacial test arrays

The Prism Solar bifacial test arrays at Sandia National Laboratories in Albuquerque, New Mexico, began collecting performance data in February 2016. The installation consists of five different array orientations and two different ground covers. Each array orientation comprises an equal number of bifacial and monofacial PV modules, and each of the modules are individually controlled by a microinverter and monitored for DC current and voltage. Reference cells facing forward and backward are located at the center of each array. Data is saved at 1-minute intervals. Figure 65 shows a photo of the array, and the map in Figure 66 shows the placement of bifacial and monofacial modules in the array.

Table 19: Summary of bifacial PV arrays installed in Albuquerque, New Mexico

Bifacial Module	Cell type	Orientation	Albedo	# bifacial (monofacial) modules	Comments (date installed and operated)
Prism Solar	nPERT	S-facing, 35 tilt	0.24	4 (4)	All modules on microinverters. Suniva monofacial reference modules. (2/2016 to present)
Prism Solar	nPERT	S-facing, 15 tilt	0.55	4 (4)	All modules on microinverters. Suniva monofacial reference modules. (2/2016 to present)
Prism Solar	nPERT	W-facing, 15 tilt	0.55	4 (4)	All modules on microinverters. Suniva monofacial reference modules. (2/2016 to present)
Prism Solar	nPERT	W-facing, 90 tilt	0.24	2 (2)	All modules on microinverters. Suniva monofacial reference modules. (2/2016 to present)
Prism Solar	nPERT	S-facing, 90 tilt	0.24	2 (2)	All modules on microinverters. Suniva monofacial reference modules. (2/2016 to present)
Prism Solar	nPERT	S-facing, 45 tilt	0.24	7 (7)	SolarWorld monofacial reference string. (9/2016 to 5/2019)
Prism Solar	nPERT	S-facing, 25 tilt	0.24	7 (7)	SolarWorld monofacial reference string. (9/2016 to 5/2019)
Sunpreme	HIT	S-facing, 35 tilt	0.24	7 (7)	SolarWorld monofacial reference string. (9/2016 to 5/2019)
Sunpreme	HIT	S-facing, 15 tilt	0.24	7 (7)	SolarWorld monofacial reference string. (9/2016 to 5/2019)
Partner A	IBC	S-facing, 35 tilt	0.24	8 (8)	SunPower monofacial reference modules. (7/2016 to present)
Partner B	HIT	S-facing, 35 tilt	0.24	8 (8)	Silevo monofacial reference modules. (9/2016 to present)
Partner C	PERC	S-facing, 35 tilt	0.24	8 (8)	Trina monofacial modules for reference. (9/2016 to present)
			Total	68 (68)	

Figure 65: Prism Solar bifacial test array at Sandia National Laboratories in Albuquerque, New Mexico USA.

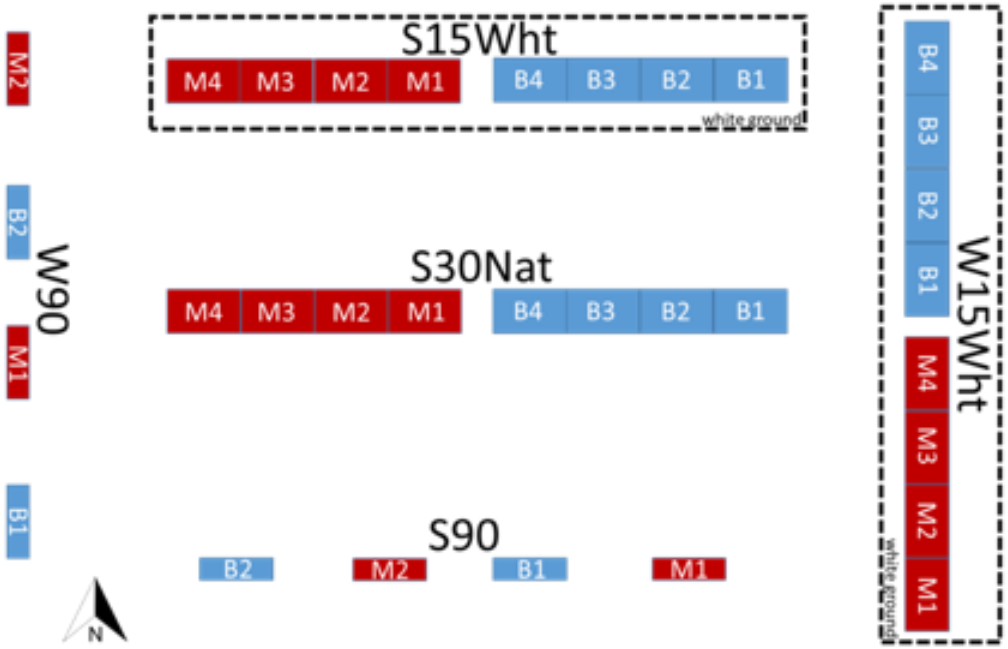

Figure 66: Map showing placement of bifacial and monofacial modules in the array.

A performance analysis of the first year of operation was published as a Sandia report [83]. This analysis yielded several important conclusions:

- Bifacial gains vary throughout the day and depend on the orientation of the array.
- As array orientation changes from equator facing, bifacial array performance does not decline as rapidly as does that of monofacial arrays. In fact, west-east-facing vertical bifacial arrays performed similarly to latitude-tilt monofacial modules.
- The south-facing, 15-tilt system over white gravel showed the highest yield, while the west-east-facing vertical bifacial modules showed the highest bifacial gains.

Figure 67 summarizes the energy yields and bifacial gains from the Prism bifacial modules for the first year of operation. Notably, these yields and bifacial gain values are higher than

would be expected from a utility-scale plant of the same orientation. Bifacial PV performance is greatly influenced by the density of the array and the shadows on the ground. Bifacial arrays with single, short rows benefit from all of the open (unshaded) ground surrounding the array and thus will see a significant performance gain compared with utility-scale plants with many long rows of modules.

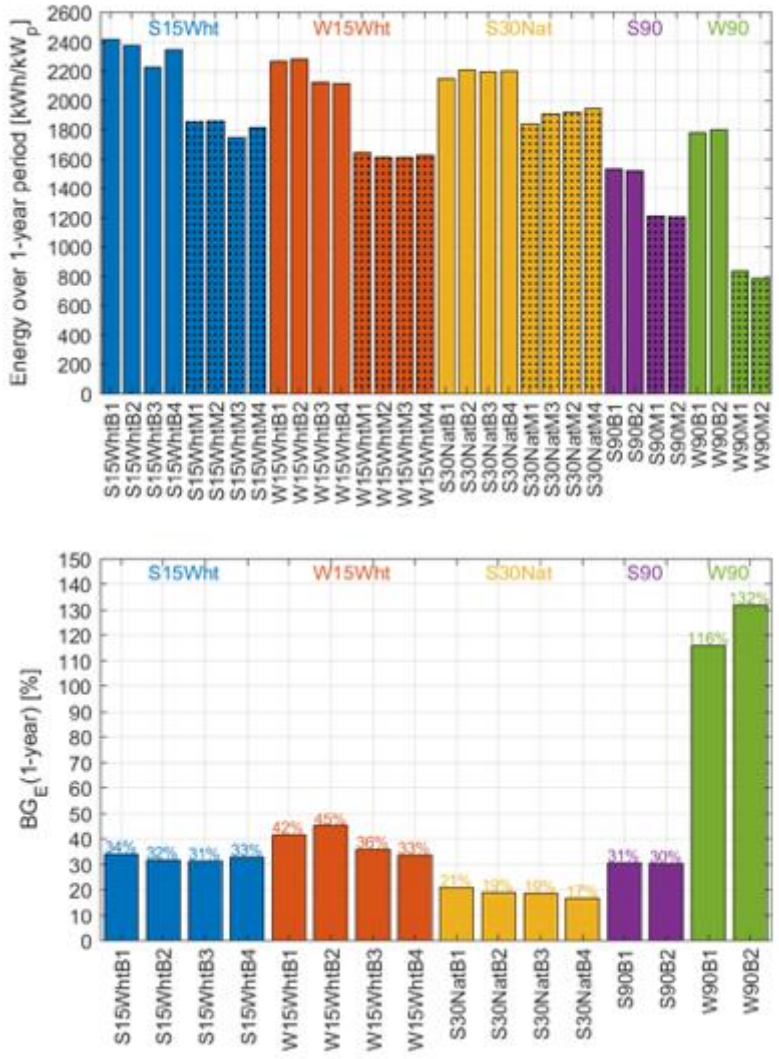

Figure 67. (top) Annual energy yields and (bottom) bifacial gains in energy for the Prism Solar bifacial test arrays at Sandia National Laboratories in Albuquerque, New Mexico USA.

Partner C bifacial test arrays

Modules from Partner C have a bifacial factor (back-to-front flash-test ratio) of 61% based on flash-test measurements made at Sandia. Figure 68 shows calculated daily bifacial gains made over several years of field exposure. On average, bifacial gain is 6%, but the value varies seasonally, with higher values in summer and lower values in winter. Days with high

diffuse irradiance fraction yield higher bifacial gains. Lower and more consistent bifacial gains occur on clear days.

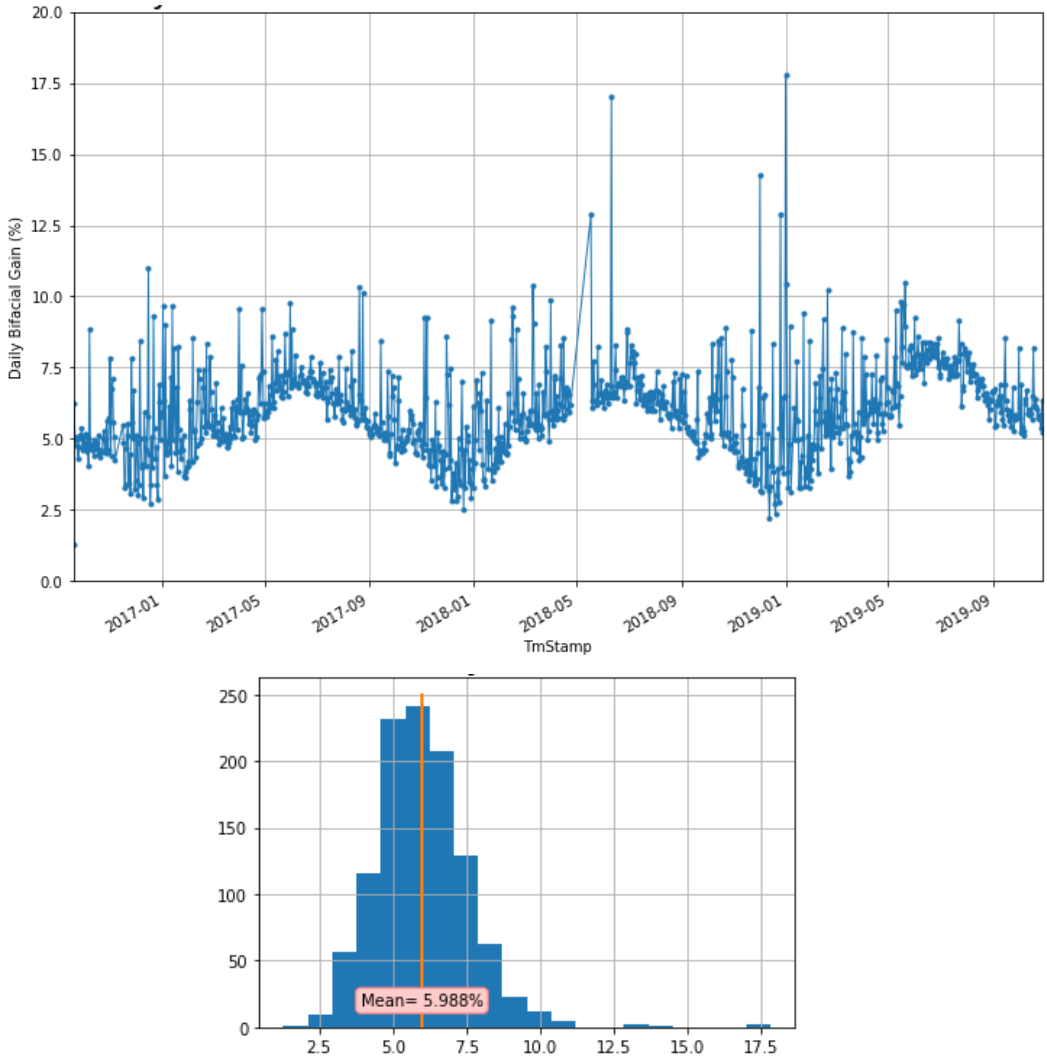

Figure 68: (top) Daily bifacial gains calculated for Partner C array. (bottom) Histogram of daily bifacial gains.

7.2 FRANCE: INES bifacial PV field test sites

(Hervé Colin)

7.2.1 Description of bifacial testing

The bifacial PV file test site is located at the National Solar Energy Institute in the French Alps, near the city of Chambéry (45.6420° N, 5.8722° E). Table 20 summarizes site characteristics. Figure 69 and Figure 70 show photos of the site.

Table 20: Characteristics of INES bifacial PV field test site

Information	Value	Comment
System size	3.04 kW_p	10 modules connected in series
System type	fixed tilt	
Site albedo	40%	Area in front of modules
Mounting height	0.8 m from installation to 03/2019 0.95 m since 03/2019	Lower module edge above ground
Array tilt angle	30°	IF applicable
Array azimuth angle	18°	S=180°; W=270°; N=0°; E=90°
Ground cover ratio	30.5%	Ratio of module row width to row-to-row distance
Module bifaciality	not known	Back-side power rating divided by front-side power rating
Array configuration	2P	
Electrical info	String inverter	Central inverter, string inverter, microinverter, module optimizer

Figure 69: View of INES bifacial PV field test site.

Figure 70: Front view of PV bifacial modules under test at INES site.

7.2.2 Summary of bifacial performance results

Over three years of monitoring, the average bifacial gain of the INES bifacial PV system (compared to a reference monofacial Al-BSF system) is 8.9%. As shown in Figure 71, this average gain decreased over the years, shifting from 10.8% in 2017 to 8.0% in 2018 and 7.2% in 2019. This decrease is likely a sign of early degradation.

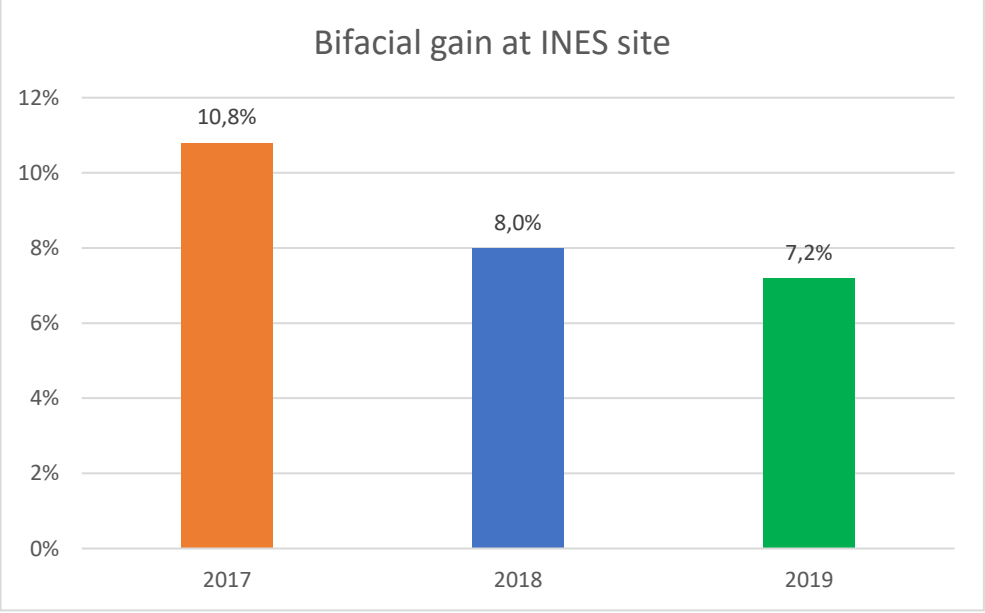

Figure 71: Decease in yearly average bifacial gain.

Figure 72 shows the rear/front-side daily irradiation ratios for 2017 and 2018. Note that seasonality in the signal, with higher values in the summer and lower values in the winter.

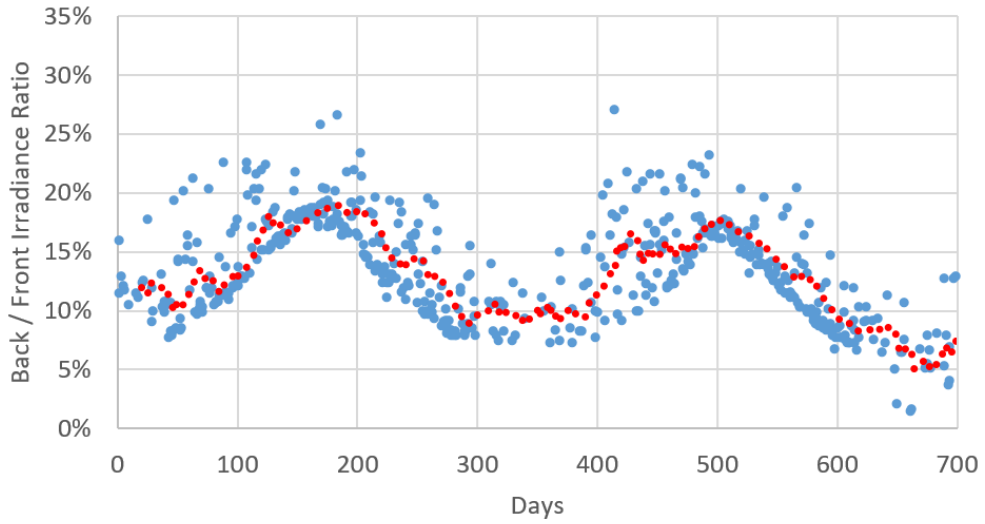

Figure 72: Rear-side to front-side irradiance ratio over the first two years of operation. Blue dots denote daily values, red dots form a 20-day moving average.

7.3 CHILE: ATAMOSTEC bifacial PV field test sites

(Elías Urrejola, Felipe Valencia, Edward Fuentealba)

7.3.1 Description of bifacial testing

Atacama Module and System Technology (ATAMOSTEC) (http://www.atamostec.cl/en/ is a private-public Chilean consortium supported by the Chilean Economic Development Agency (CORFO) and industrial partners. ATAMOSTEC develops solar PV technologies specifically for high radiation and desert conditions. The Atacama Desert is an extremely interesting landscapes for installing PV worldwide and is characterized by a very high irradiation, a high number of sun hours per year, one of the clearest skies in the world, the highest annual expected energy yield, and relatively low air temperatures.

ATAMOSTEC has at the Atacama Desert in Chile a solar platform facility (Atacama Solar Desert Platform (PSDA)) to perform outdoor testing of photovoltaic technologies: modules, cables, inverters, and mounting structures just to mention few of them. The PSDA comprises two main testing installations:

- The Lalcktur 1 MW PV power plant is an industrial solar PV plant for testing technologies at large scale.
- A complete outdoor solar test facility (OST) has monofacial and bifacial PV systems (https://bit.ly/2YC0SIM; 24.090570º S, 69.929285º E)

As can be seen in Figure 73, the PV installations are far enough from the coast to avoid issues arising from the condensation and evaporation of seawater—and thus an ideal spot for testing PV technologies designed for desert conditions. Site characteristics for the PSDA are listed below.

- Irradiation: global horizontal irradiance (GHI) reaches 2615.3 kWh/m^2, diffuse horizontal irradiance (DHI) is 366.5 kWh/m^2, and direct normal irradiance (DNI) reaches 3493.2 kWh/m^2, in average on a yearly basis.
- Average yearly sunlight hours: >4,000 h

- High UV irradiance in the whole range (171.4 kWh/m^2 for UVA and 4.6 kWh/m^2 for UVB annually.
- Average daily ambient temperature ranges between 8.86 ºC in winter to 22.39ºC in summer.
- Average annual rainfall: 2 mm
- Average daily wind speed: 3.3 m/s
- Average air pressure: 90.57 kPa
- Average relative humidity (RH) 38.75% and ranging between 10% to 72%.
- Desert climate with high soiling impact: around 1% soiling losses per month
- Flat area (no far shading)

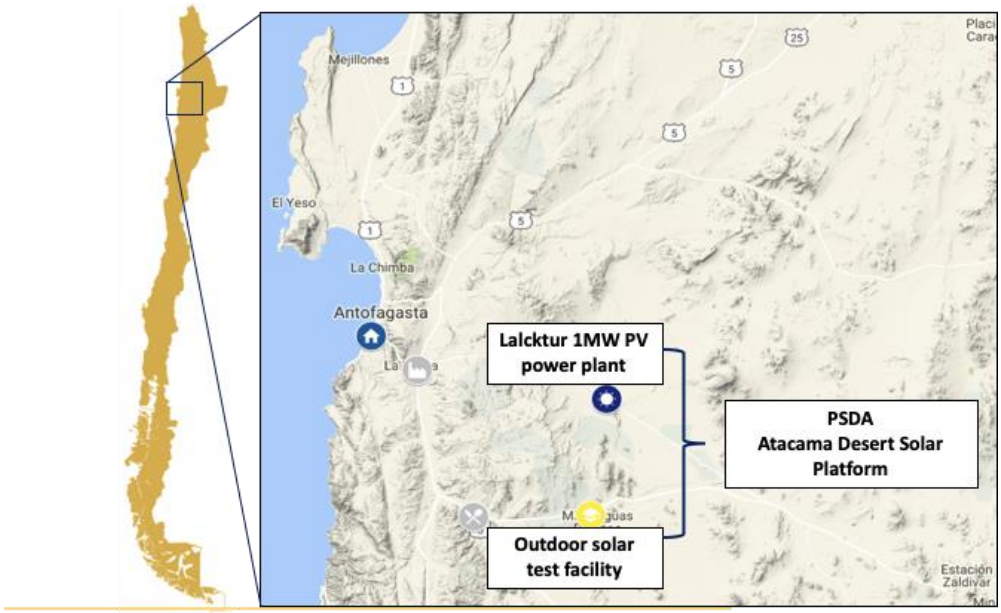

Figure 73: PSDA installation in the heart of the Atacama Desert, Chile.

The ATAMOSTEC OST site has the following features:

- A bifacial fixed-tilt system specially designed to prevent the shading of the rear side of the modules. This system is composed of five racks: one for dummy modules and the remaining four for installing bifacial modules. Monitoring allows comparison of both: module and string performance. The system is complemented with a set of sensors to measure irradiance (one in the front side and three at the rear side), temperature (one per module per side), and wind speed.
- A vertical-mounting-structure-based bifacial system. This system allows comparison of up to four different bifacial technologies at the same time. These technologies are monitored at both the module and string levels. At the edges of the system, there are dummy modules included for studying edge effects. As in the case of the fixed tilt system, this system is complemented with the following set of sensors: irradiance sensors (nine per side located at different heights), temperature sensors (one per side per module), and anemometers (two: one at the top and one at the bottom of the system), to measure the environmental conditions affecting the modules being tested.
- A single-row horizontal single-axis tracker system slated to be extended to several rows in 2020. Up to four different module technologies can be compared at the mod-

ule and string levels; dummy modules are included at the edges). Environmental monitoring on the array includes irradiance sensors (one front, three rear), temperature sensors (two per module), and wind sensors. This system is currently under upgrade, so that by beginning of 2021 a final system of five HSAT trackers will be available.

The outdoor platform tests commercial and non-commercial devices used for PV power plants, focusing mainly on disrupting technologies. Installing the modules at the OST allows identification of the best options for PV power plants and niche installations, given the modules available. Figure 74 shows the OST facilities and the placement of the different structures used for module testing. As it can be noticed, OST facilities include state-of-the-art instrumentation for measuring meteorological data, characterizing module technologies (such as bifacial modules), and evaluating tracking systems. It contains also a reference radiometric laboratory. We are currently testing our ATAMO generation 1 technology (n-type technologies: nPERT and HJT) to benchmark modules.

Figure 74: ATAMOSTEC Bifacial PV testing platform, Antofagasta, Chile

7.3.2 Summary of Bifacial Performance Results

According to the data collected by ATAMOSTEC, the "ATAMO" modules show an extra gain of 11% in annual average compared to a monofacial PERC module type installed in a 20° fixed-tilt system. Depending on the technology and the type of installation (vertical, fixed-tilt, or HSAT), bifacial gain varies from 7% to 14%. Using the "ATAMO" modules in a horizontal single-axis tracking system (SAT) further improves energy production by up to 31% extra gain. Combining these improvements, a gain of 44% on average per year is achieved, compared to a fixed monofacial module (this was simulated by PVsyst for a whole year). The installed technologies have been developed by ATAMOSTEC's international partners CEA-INES from France and ISC-Konstanz from Germany.

7.3.3 Summary of solar resource analysis

The solar spectrum and environmental conditions in the Atacama Desert are unique compared with many other climates. Therefore, the reference spectrum used to calibrate and evaluate PV devices, among other applications, might not be the best representation of conditions in the Atacama. The GHI, DHI, and DNI solar irradiation at the PSDA make this location an ideal place for deploying solar applications (see Figure 75). However, PSDA also receives a large amount of energy in the ultraviolet (UVA and UVB) wavelengths (see Figure 76). Therefore, technology components used should not be sensitive to the energy at these wavelengths to avoid significantly decreasing their lifespans—a point that should be considered in current and future investments in large-scale PV plants. PSDA also experiences noticeable fluctuations in temperature and wind speed, which can result in high thermal stress on components and structures, as well as soiling issues. All these features of the Atacama make it a great place to test and evaluate PV and bifacial PV technologies.

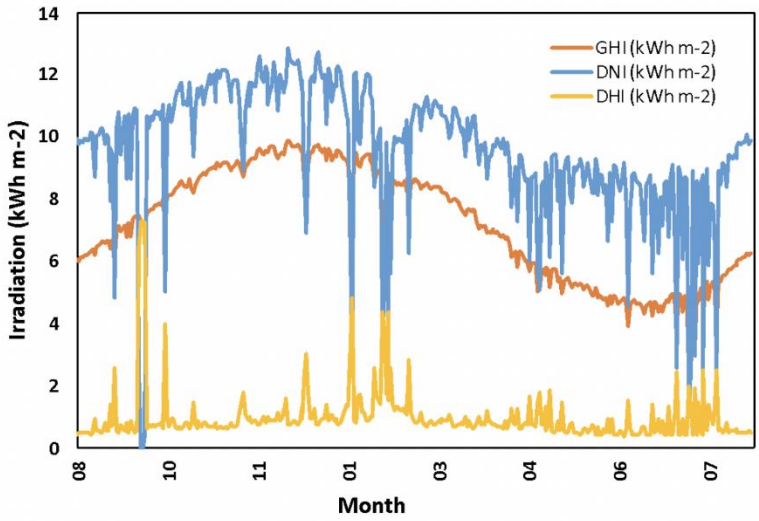

Figure 75: Measured accumulated GHI, DHI, and DNI at the PSDA (made by University of Antofagasta).

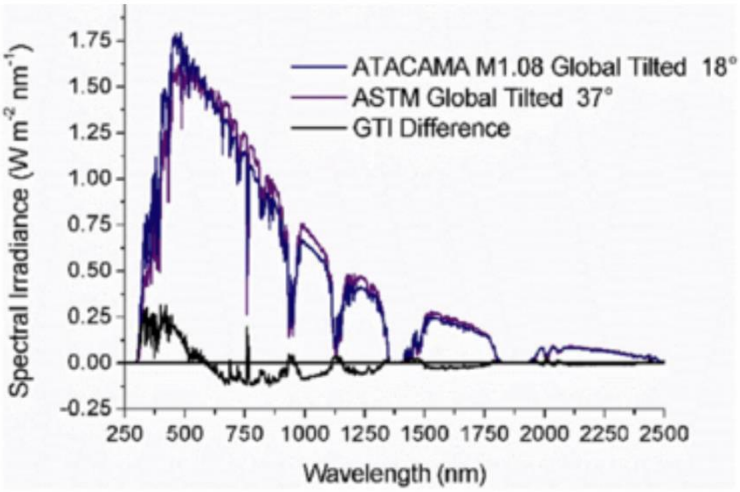

Figure 76: Normalized spectrum of the global tilted irradiance: comparison of PSDA measurements and the reference spectrum ASTM G173.

7.4 CANADA: University of Ottawa SUNLAB site

(Annie C.J. Russell, Christopher E. Valdivia, Karin Hinzer)

7.4.1 Description of bifacial testing

The Arctic Solar Photovoltaics: Innovation for Renewable Energy (ASPIRE) study at the University of Ottawa's SUNLAB examines the potential for dual-axis tracked bifacial photovoltaics in northern Canada where ground albedo is substantially improved through snow and ice cover for much of the year. The project includes the assembly of two twin R&D bifacial PV test sites, one at the University of Ottawa in Ottawa, Ontario (45° latitude), and the second at the Canadian High Arctic Research Station (CHARS) in Cambridge Bay, Nunavut (69° latitude).

Dual-axis tracking is of special interest due to the wide annual variation in solar path at high latitudes. For example, the solar elevation angle at noon in Cambridge Bay reaches just 45° at its highest, and the range of azimuth angles of direct light is 360° from mid-May to mid-July. Additional conditions that differ from low latitude environments are summarized in Table 21 [160].

Table 21: Descriptions of twin R&D bifacial photovoltaic test sites within SUNLAB's ASPIRE project.

Site Location	Site Description	Latitude	Average Temperature	Snow Coverage (months/year)
Ottawa, ON	Urban, grass	45.4°	6.6°C	4
Cambridge Bay, NU	Permafrost	69.1°	-13.9°C	9.5

Apparatus and devices

The twin test sites will feature both monofacial and bifacial PV panels installed on both south-facing fixed-tilt racking and dual-axis trackers. The sites will each include at least 1 Savanna dual-axis tracker (provided by industrial partner Morgan Solar Inc.), which features 4 tracking armatures, each equipped with a 3-panel table with portrait orientation for a total of 12 panels per tracker.

The Savanna is lightweight and serviceable without heavy equipment, which is a significant advantage for northern and remote locations. The tracker design does not require poured concrete and allows non-penetrating ballasting options, which makes installation on permafrost feasible. These trackers can also be programmed to operate in single-axis tracking mode, providing an energy-yield comparison between the two tracking modes. The Cambridge Bay study will be suspended during entirely dark periods in the winter months. The University of Ottawa solar test site is already populated with three Savanna trackers from earlier projects (two of which are shown in Figure 77) and will be expanded for this ASPIRE project.

Metrology

PV panel measurements will be simplified for dependable remote operation at the Cambridge Bay site. For the performance analysis, panels will be pre-characterized for current, voltage, and fill factor dependence on temperature. Solar resource sensors will be installed at each site including a SolarSIM spectral irradiance sensor by research partner Spectrafy Inc., pyrheliometer, GHI pyranometer, front- and rear-facing plane-of-array (POA) pyranometer, and albedometer.

The University of Ottawa site will include additional irradiance sensors to measure diffuse horizontal irradiance and panel rear-side non-uniformity. Additional environmental sensors include module temperature sensors, Lufft weather station, scene cameras, and horizontal, front, and rear POA 2π-steradian all-sky imagers. Natural albedo will be measured over the course of the experiments as ground cover varies between tundra and snow in Nunavut and grass/dirt and snow in Ottawa.

Figure 77: Two of three Savanna trackers installed at the University of Ottawa SUN-LAB field test site prior to the ASPIRE project

7.4.2 Summary of bifacial performance results

Site assembly will continue through 2021. Energy yield data from these sites will allow for analysis of the drivers of bifacial gain that are unique to intermediate and high-latitude locations, such as high fraction of snowy albedos, highly diffuse conditions, and a large range of azimuth angles. The project will report bifacial gain and other performance metrics for research-scale dual-axis tracked and fixed-tilt installations at 45° and 69° latitude and will include investigations of snow shedding, backtracking, and energy forecasting.

This small unconventional system provides a very different shading environment compared to typical utility-scale deployments. These new field results will aid in the validation of DUET, the University of Ottawa's numerical model for bifacial PV performance and energy yield, under this unique architecture. Modeling and site data from Cambridge Bay will also inform research into the diesel-displacement potential for bifacial PV in the north by research partner Dr. Michael Ross at Yukon University.

Later stages of this project will include field testing of silicon heterojunction cells optimized for high-latitude conditions. Leveraging cell fabrication and mini-module assembly at Arizona State University with research partner, Dr. Mariana Bertoni, measurements will focus on quantifying both conversion and collection efficiencies and understanding the principle conditions affecting them.

7.5 GERMANY: TÜV Rheinland outdoor bifacial module testing

(Johanna Bonilla)

7.5.1 General information

TÜV Rheinland has operated four outdoor test sites since 2013 to measure the performance of PV modules. These sites, built within the framework of the PV-CLIMATE project, were located worldwide, as shown in Figure 78, to cover the widest range of climatic conditions in areas commonly chosen for PV installations, as summarized in Table 22. The sites thus allow study of the energy performance under real conditions.

Since 2017, the test sites have also been used for comparative energy performance studies of bifacial and monofacial PV modules.

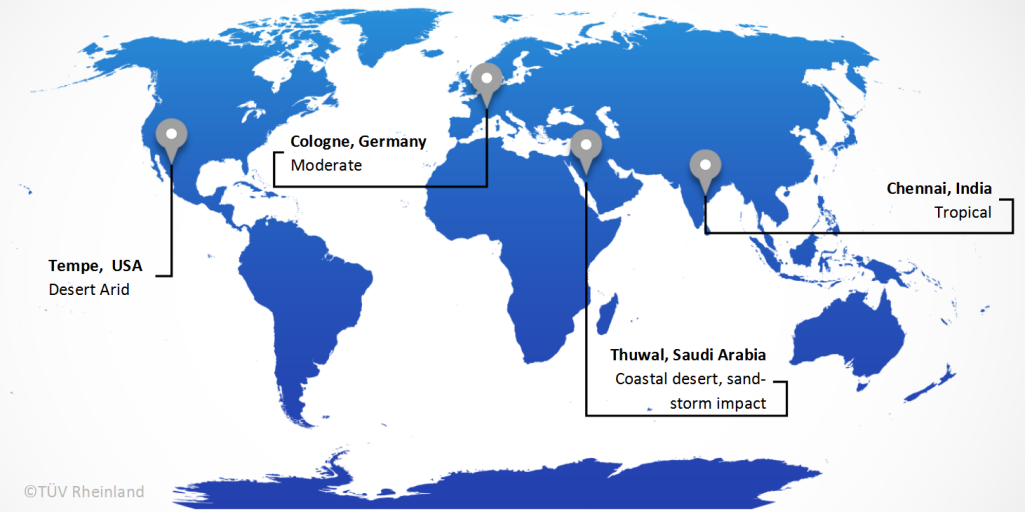

Figure 78: Worldwide locations of TÜV Rheinland for energy yield measurement of PV modules.

Table 22: Climate conditions covered by TÜV Rheinland PV test sites.

Site Parameters	Cologne, Germany	Tempe. Arizona, USA	Chennai, India	Thuwal, Saudi Arabia
Köppen-Geiger climate classification	Cfb (moderate)	BWh (desert, arid)	Aw (tropical)	BWh (desert, coastal)
Tilt angle/ ground surface	35°	33.5°	15°	25°
Annual in-plane global solar Irradiation (kWh/m^2)	1257	2396	2102	2329
Low irradiance fraction (G < 200 W/m²)	17%	5%	9%	4%
Average ambient temperature (G > 15 W/m²)	13.0 °C	25.6 °C	30.5 °C	30.2 °C
Average annual rainfall (mm)	774	219	1597	70
Average relative humidity	74.3%	33.4%	74.7%	66.8%

7.5.2 Field measurement instrumentation

All four test sites are equipped with identical hardware. The frequency of measurements and resolutions are also identical to offer the possibility of comparative energy efficiency measurements between the sites. Table 23 summarizes details.

For each test module, two Pt100 temperature sensors, one installed in the middle of the module and the other at the edge, measure the back of module temperature (T_{BoM}) at a sampling rate of 30 seconds. Individual electronic DC loads enable all test samples to operate continuously in maximum power point tracking (MPPT), with a data acquisition frequency of 30 seconds.

Table 23: Equipment and field measure frequency at TÜV Rheinland PV test sites.

Parameter	Equipment / technique	Frequency
Temperature of the module, T_{BoM}	2x Pt100 surface temperature sensors, one located at center and one at edge of each module. Special care is taken for cabling in case of bifacial PV modules.	30 sec
IV curve measurements	Electronic loads: interruption of MPPT for IV curve measurement	10 min
P_{MPP}	Electronic loads: 4-wire connection	30 sec
$G_{PoA,\,f}$, G_{Hor}, G_d, $G_{PoA,\,r}$	Pyranometers	30 sec
T_{amb}, precipitation, wind, and humidity	Sensors (instantaneous measurements)	30 sec
Spectral irradiance	Spectrometer (300–1600 nm)	1 min

Current and voltage curves are recorded at every 10 minutes. The in-plane global irradiance ($G_{PoA,f}$), horizontal (G_{Hor}), diffuse (G_d), and the in-plane rear irradiance ($G_{PoA,r}$) are measured with three pyranometers. The rear pyranometers are mounted at three different heights to determine the effect of height on the inhomogeneity of rear irradiance. The ambient temperature (T_{amb}), spectral irradiance, precipitation, wind speed, wind direction, and humidity are also measured.

Additionally, a soiling station is available at each outdoor test location. Side-by-side irradiance measurement of two mini-modules, with one mini-module cleaned manually daily, allows for soiling monitoring (see Figure 79). Dust accumulation at the surface of a soiled mini-module causes transmission loss and reduces the lower effective irradiance reaching the cells. In the Saudi Arabia location, additional mini-modules have been installed to study the impact of different cleaning schedules on the energy yield.

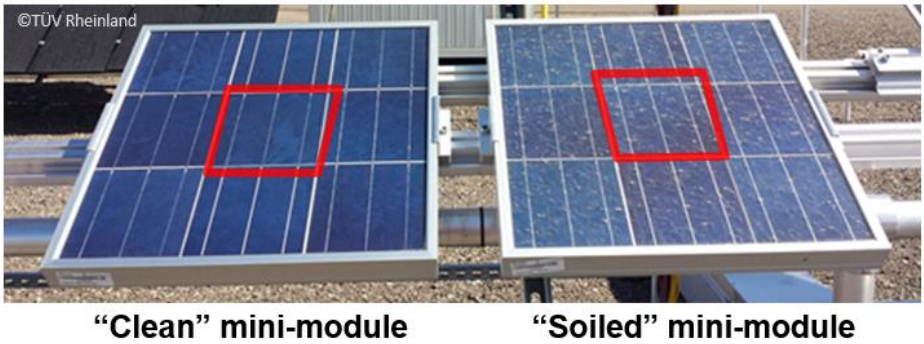

Figure 79: Soiling station at TÜV Rheinland, center cells outlined in red.

Only the center cell (measurement cell) is electrically connected, while the solar cells at the edge act as dummy cells. The center cells are acting as irradiance sensors (short-circuit operation). The mini-modules have a standard PV glazing (3.2 mm micro-structured patterned glass).

7.5.3 Laboratory tests

Before installing the bifacial PV modules at the outdoor test sites, TÜV Rheinland measured the modules in the laboratory to analyze their electrical characteristics and indoor performance. The modules were characterized according to IEC test specification 60904-1-2 [47] and the bifaciality factor, including spectral corrections [48]. Depending on the cell technology, bifacialities from 0.75 (PERC cells) to 0.91 (n-PERT cells) were measured. The spread within technologies was also depending on the cell quality and the design of the bifacial PV module.

The following energy rating measurements were also performed:

- Performance at variable temperature and irradiance [53].
- Angular response [53].
- Temperature coefficients [161].

7.5.4 Test installations and bifacial studies results

After the laboratory measurements, the test modules were mounted on the open rack installation at the four outdoor locations as shown in Figure 80, and TÜV Rheinland compared the energy yield of the installed monofacial and bifacial PV modules [161-164].

For the outdoor performance analysis, the module performance ratio (MPR) parameter is used for comparison, according to:

$$MPR = \frac{\left(\sum_{months} P_{MPP}\right) / P_{MPP,STC}}{\left(\sum_{months} G_{PoA}\right) / 1000 Wm^{-2}} .\% \qquad (35)$$

Values MPR ≠ 100% represent performance variations due to temperature, low irradiance behavior, spectral, angular effects, degradation, meta-stability, or bifacial gains. MPR=100% means that the average PV module efficiency in the period considered conforms to its STC efficiency.

To ensure equal treatment of the PV modules and minimize the impact of manufacturer sampling, power rating (label), and output power sorting, the STC output power measured in the laboratory prior is used for the MPR calculation.

For bifacial PV modules, the front output power at STC was used. Therefore, values greater than 100% are possible.

Table 24 through Table 27 summarize the results for the different studies at TÜV Rheinland.

Cologne, Germany

Arizona, USA

Thuwal, Saudi-Arabia

Chennai, India

Figure 80: TÜV Rheinland test installations for PV testing (Photos: ©TÜV Rheinland).

7.5.5 Key findings of bifacial performance at TÜV Rheinland

Key findings regarding bifacial performance at this site follow:

- The outdoor studies revealed clear advantages in the energy yield performance of bifacial over monofacial PV modules. However, the quantification of energy gain is only possible when the module performance ratio is referred to the output power of the front side.
- Bifaciality depends strongly on cell-technology, varying from 60% to 90%. However, we have seen that PV modules of the same type showed different bifaciality coefficients:
  - Bifaciality coefficients may vary from ±2.0% to ±5.0% (k=2) in production for produced modules of the same family.
  - Most of these variations are due to the sensitivity to construction variations. Even slightly soldering patterns, could affect this value.
- Once modules are under real conditions, the bifaciality factor plays a minor role in bifacial gain. Even differences between PV module types of 0.15 result in a MPR change of less than 2%.
- Correlations could be established between albedo, rear/front irradiation, and bifacial gain. Here, the bifacial gain is the group average of monofacial and bifacial PV modules. However, these correlations are only valid for the installation conditions detailed above.
- For optimized installations we have found the rear/front irradiance ratio can represent around 50% of the albedo (see Figure 81).

Table 24: TÜV Rheinland test results for location Cologne, Germany.

Location: Cologne, Germany	
Period: Aug 2017 to Jul 2018	
16 PV modules: monofacial vs. bifacial [162], [163]	
Mounting conditions	2 racks, fixed, pitch 11m
Height above ground	1.5 m
Tilt angle	35° south
Ground	Gravel (Albedo = 28%)
Annual in-plane solar irradiation $H_{POA,\ f\ (Annual)}$	1231 kWh/m²
Annual in-plane rear irradiation $H_{PoA,r}$	169.4 kWh/m²
H_{PoA_rear} / H_{PoA_front}	13.8%
Bifaciality, φ	0.85–0.89

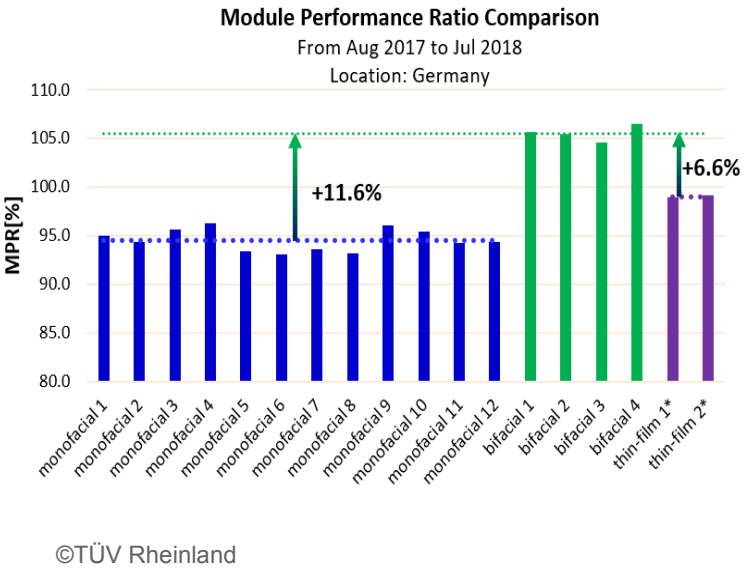

©TÜV Rheinland

Notes

Indoor laboratory PSTC, including SMM correction, was used as a reference for MPR calculations all c-Si modules. Front side P_{STC} was used for bifacial PV samples.

*Thin-film modules MPR are referred to Label PSTC.

Annual irradiation values are calculated for GPoA, f>15 W/m^2

Table 25: TÜV Rheinland test results for location Tempe, USA.

Location: Tempe, USA	
Period: Sep 2018 to Aug 2019	
11 PV modules: monofacial vs. bifacial [164]	
Mounting conditions	1 rack, fixed
Height above ground	1.3 m
Tilt angle	33.5° South
Ground	Dark gravel + sand (Albedo = 13.4%)
Annual in-plane solar irradiation $H_{POA,\,f}$	2237 kWh/m²
Annual in-plane rear irradiation $H_{PoA,r}$	229.2 kWh/m²
H_{PoA_rear} / H_{PoA_front}	10.2%
Bifaciality, φ	0.75–0.85

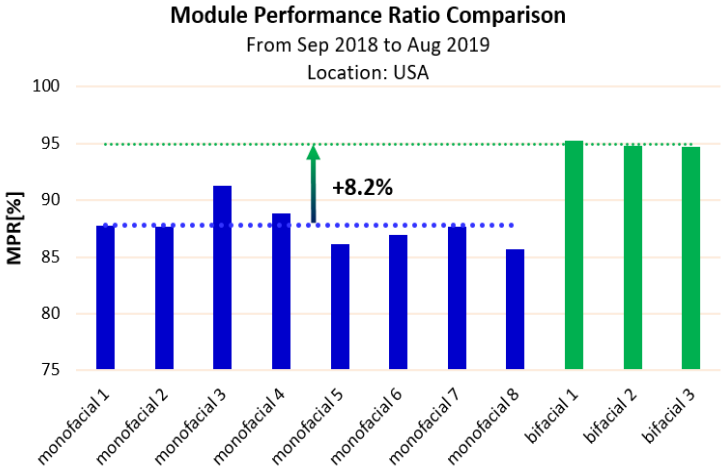

Notes

Indoor laboratory P_{STC}, including SMM correction was used as a reference for MPR calculations all c-Si modules. Front side P_{STC} was used for bifacial PV samples.

Annual Irradiation values are calculated for GPoA, f>15 W/m^2

Table 26: TÜV Rheinland test results for location Thuwal, Saudi Arabia.

Location: Thuwal, Saudi Arabia	
Period: Oct 2018 to Sep 2019	
8 PV modules: monofacial vs. bifacial [165]	
Mounting conditions	1 rack, fixed
Height above ground	1.3 m
Tilt angle	25° south
Ground	Sand with gravel (Albedo = 30.1%)
Annual in-plane solar irradiation $H_{POA,\,f}$	2029 kWh/m²
Annual in-plane rear irradiation $H_{PoA,r}$	306.3 kWh/m²
H_{PoA_rear} / H_{PoA_front}	15.1%
Bifaciality, φ	0.74–0.90

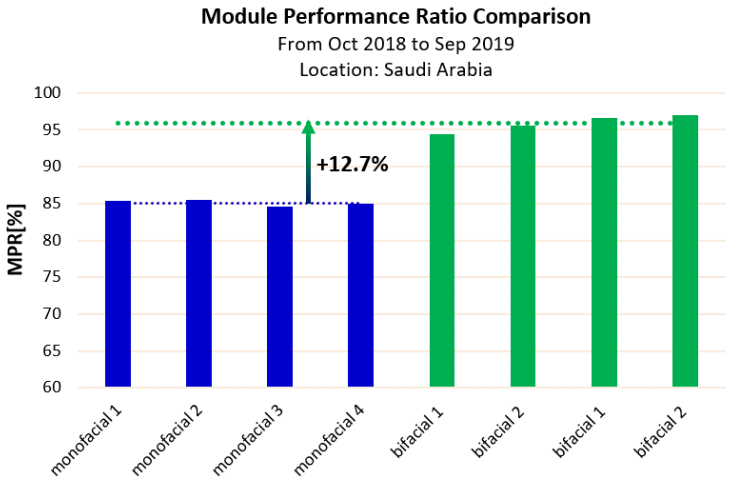

©TÜV Rheinland

Notes

Indoor laboratory P_{STC}, including SMM correction was used as a reference for MPR calculations all c-Si modules. Front side P_{STC} was used for bifacial PV samples.

Table 27: TÜV Rheinland test results for location Chennai, India.

Location: Chennai, India	
Period: Sep 2018 to Aug 2019	
11 PV modules: monofacial vs. bifacial [165]	
Mounting conditions	1 rack, fixed
Height above ground	1.3 m
Tilt angle	15° south
Ground	White stones (Albedo = 49.9%)
Annual in-plane solar irradiation $H_{POA,\,f}$	1857 kWh/m²
Annual in-plane rear irradiation $H_{PoA,r}$	472.8 kWh/m²
H_{PoA_rear} / H_{PoA_front}	25.5%
Bifaciality, φ	0.74–0.91

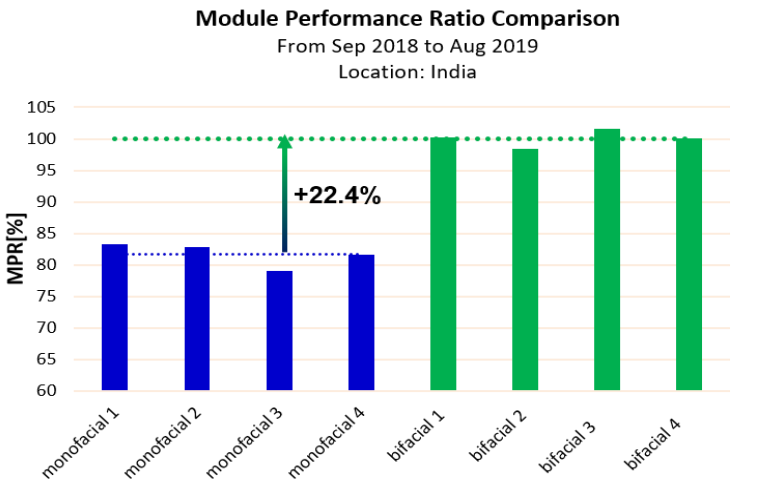

©TÜV Rheinland

Notes:

Indoor laboratory P_{STC}, including SMM correction was used as a reference for MPR calculations all c-Si modules. Front side P_{STC} was used for bifacial PV samples.

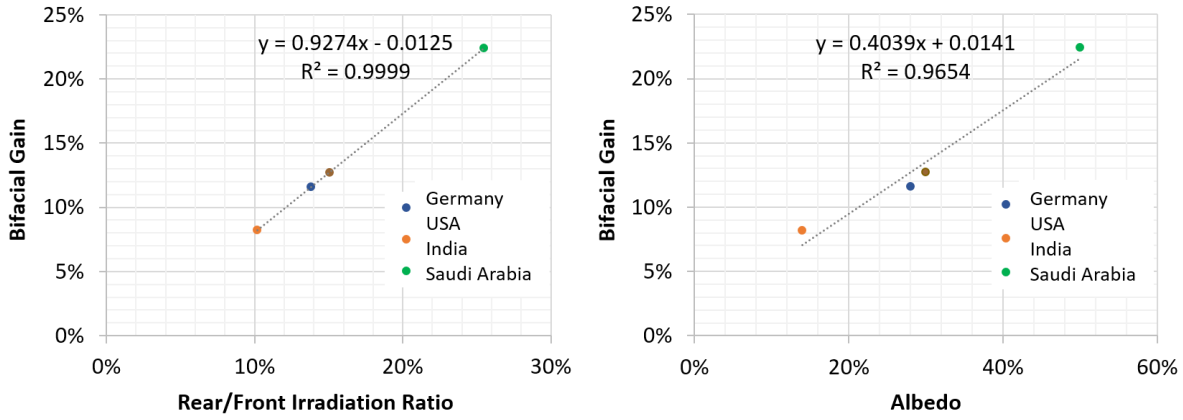

Figure 81: Correlation between rear/front irradiation ratio (left) and albedo (right) and bifacial gain.

7.6 SWITZERLAND: Zurich University of Applied Sciences bifacial test site

(Markus Klenk)

7.6.1 Description of bifacial testing

The Bifacial Outdoor Rotor Tester (BIFOROT), located on the roof of the Zurich University of Applied Science (ZHAW) in Winterthur, Switzerland, is a 3x3-module array for the systematic measurement of bifacial systems with varying mounting conditions. This array is based on commercially available, 60-cell modules (Megacell, MBA-GG60-270) with a nominal front-side power of 268 W_p and a bifaciality factor for power of 78%. Figure 82 depicts the basic set-up of the BIFOROT, and Figure 83 shows the installed test rig.

The most relevant device for this work is the bifacial module in the center of the 3x3 matrix, marked red in Figure 82 and labelled as M2 in Figure 83. This center module is ideally suited to represent the shading of a typical location in an extended bifacial PV system. As a benefit over more common test set-ups with stand-alone modules, it is highly similar to extended, real-world installations that experience direct shading by other modules and indirect shading of the reflecting ground. Additional shading elements are applied to one side. A further extension of the array was not feasible due to the limited available space on the building roof.

Three rows of modules with manually adjustable distance between the rows are mounted on vertically adjustable pillars. An important and unique feature of the BIFOROT is the automated and continuous variation of the tilt angle in certain steps. In spite of the moving modules the system is not a tracker, but rather a south-oriented test field to for analyzing tilt angle–dependent effects.

All panels change their tilt angle continuously and in a coordinated fashion with the central row. BIFOROT includes several features to analyze bifacial system properties, such as measurement of the rear-side irradiation homogeneity and of the front and rear side of bifacial modules (including modules M1, M3 in Figure 83). The modules M1 and M3 respectively have a covered front and rear side to reveal the corresponding characteristics of this feature.

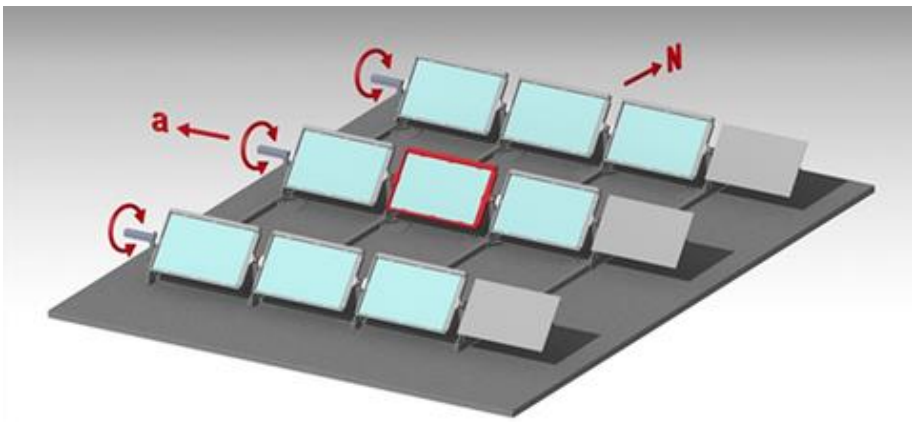

Figure 82: Measurement set-up with permanently turning modules. The center, which is best suited to represent the actual conditions in real installations, is outlined in red.

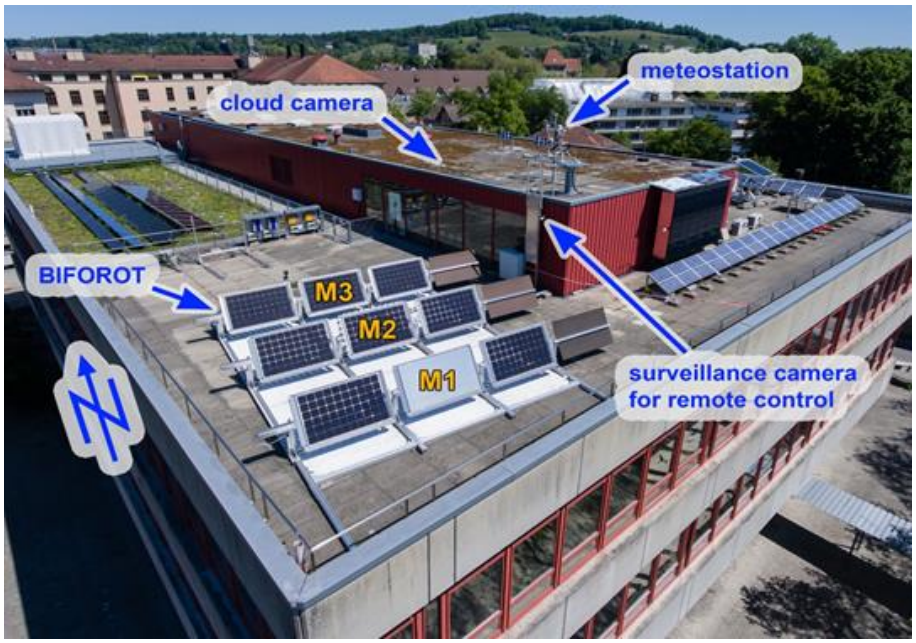

Figure 83: BIFOROT installation on the roof of the ZHAW in Winterthur. White reflecting roofing foil is placed below the array.

Weather data and environmental conditions are recorded by a weather station on the rooftop and by measurement devices applied to the test rig. The weather station includes a pyranometer to measure the global horizontal radiation, a horizontally mounted reference cell, and a pyrheliometer to measure the diffuse radiation. Another pyranometer and reference cell are installed on the rotating mounting frame of module M2.

7.6.2 Summary of bifacial performance results

Analysis is currently focused on detailed evaluation of the accuracy of simulations that are dependent on the tilt angle and specific irradiation conditions. This involved comparing results of PVSyst and the simulation tools of ECN.TNO and ISC Konstanz to the measurements at specific irradiation conditions [166]. In the experiments presented, 12 angles in the range of 0° to 90° were selected. At each step an I/V- curve of the center module M2 was measured to obtain power as a function of the tilt angle. One complete cycle takes one minute to complete. This allows IV-curve measurement for different tilt angles at otherwise virtually identical conditions and reveals the sensitivity of the simulations on the tilt.

With 60 IV-curves and Pmp values per hour for each tilt-angle position, there are 720 IV-curves and Pmp values per hour. The Pmp values can be summed over the course of the day to obtain the daily yield. The available results had been limited to specific days. Now, the study range has been expanded to encompass longer periods [167].

7.7 SWITZERLAND: SUPSI outdoor test facility

(Ruben Roldan Molinero, Gabi Friesen)

7.7.1 Description of bifacial testing

The impact of irradiance and temperature non-uniformity from white rear panels acting as a diffuse reflector were tested on bifacial HIT modules at the University of Applied Sciences and Arts of Southern Switzerland (SUPSI). Three bifacial modules supplied by the same

manufacturer were mounted on an open rack and the effect of rear panels as diffuse reflector was investigated as an alternative strategy to the classic white ground material. The rear surfaces were placed to simulate rooftops or wall reflectors for potential applications into the built environment. The test bench in Figure 84 was designed considering the best practice guidelines reported in [168]. The height of the test samples was defined at least one meter above the ground and 10 centimeters from any other object in order to promote the air circulation around the modules and minimize temperature gradients. Additional dummy modules on the left and right of the row were placed to reduce the heat propagation by convection mechanism in these module locations. A HIT monofacial module of the same technology was mounted as a reference beside the bifacial modules. Four pyranometers were placed around each bifacial module to determine the irradiance non-uniformity on the back side. The temperature in the back of the modules was measured in three in different positions with PT100 sensors. The hardware solutions used for the measurement of the module power combines IV-tracing performed in regular intervals while the module is otherwise operated at its maximum power by means of maximum power point trackers (MPPT). The activity was performed within the project ENHANCE funded by the Swiss Federal Office of Energy. Detailed results can be found in the final project report [169].

Figure 84: Bifacial test stand installed at SUPSI within the Swiss Project ENHANCE. (top row) Configuration including 3 monitored bifacial modules, 2 dummy modules, and 1 reference monofacial module in open-rack layout. (bottom row) Front view and side view, respectively, of white reflectors mounted behind bifacial PV modules.

7.7.2 Summary of bifacial performance results

The sensitivity to non-uniform irradiance in the rear of the bifacial modules mounted in the open rack without white reflector was analyzed based on the irradiance non-uniformity NU

$$\mathrm{NU}(\%) = 100 \times \frac{G_{\max} - G_{\min}}{G_{\max} + G_{\min}} \tag{36}$$

where $G_{\max}$ and $G_{\min}$ account for maximum and minimum irradiances, respectively.

The box plot matrix in Figure 85 (top) displays in the left y-axis the irradiance non-uniformities NU measured in the rear side of the three modules corresponding to columns A1, A2 and C3 respectively. The right y axis indicates day numbers J_{d} 227, 271 and 331 of the 2018 Julian calendar against the coordinated universal time (UTC) in the x axis. As shown, the non-uniformity for a specific module depends on the day of the year and is substantially lower than 10% throughout day 227 (August 15, 2018). However, the median at lower elevation angles, such as in day 331 (November 27, 2018), is closer to 10%.

The rows in the plot matrix depict the sensitivity of radiation uniformity to the position in the test bench, showing that the first and last hours of the days, with higher angle of incidences, have a greater impact on the module's position. In all cases, the uncertainty associated with the non-uniformity of solar irradiance in the rear of the bifacial modules is greater than the measurements provided by our calibrated broadband detectors.

Analogous to the case of irradiance, the temperature non-uniformity is defined as:

$$\mathrm{NU}(\%) = 100 \times \frac{T_{\max} - T_{\min}}{T_{\max} + T_{\min}} \tag{37}$$

where $T_{\max}$ and $T_{\min}$ account for the maximum and minimum temperatures, respectively, measured to the rear of the modules. Figure 85 (bottom) shows the box plot array corresponding to the temperature non-uniformity. Generally, its median is below 5%, and values for modules A2 and C3 are systematically below those of module A1.

The power densities recorded over time by the bifacial module surfaces are experimentally determined from the irradiance *G* measurements according to $H_\tau = \int_\tau G\, dt$, where the subscript τ accounts for a specific time intervals, such as $\tau = h$ or $\tau = d$, reporting per hour or day, respectively.

Figure 86 depicts the hourly front solar irradiation H_h^f and mean rear solar irradiation $\overline{H_h^r}$ corresponding to the bifacial module 16-113-A1 measured on day number 227. In this case, the fraction of mean rear irradiation $\epsilon_{\overline{H_h^r}}$ ranges from a maximum of 43.9% in the early morning to a minimum of 10.4% at noon UTC. The dispersion, measured in standard deviation $\sigma_{\overline{H_h^r}}$, in the above cases corresponds to 2.3% and 0.3% respectively.

The comparison of white reflectors vs. black panel in Figure 87 shows the hourly front solar irradiation H_h^f and mean rear solar irradiation $\overline{H_h^r}$ of bifacial module 16-113-A1 with white reflectors mounted at distance $d = 38.5\ cm$ from the module on day number 423 and the solar irradiation recorded when the reflectors were replaced with black panels mounted at the same distance on day number 447.

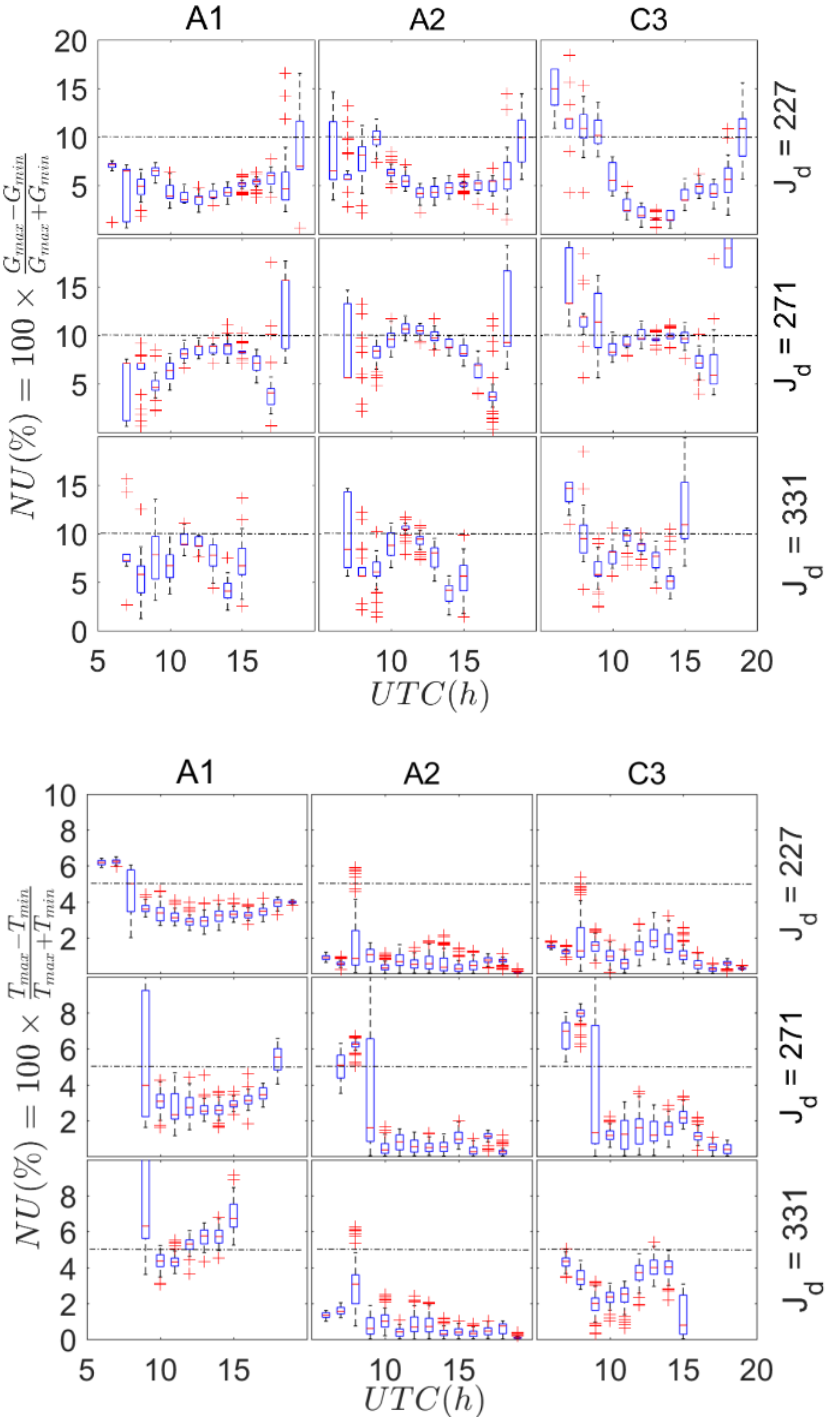

Figure 85: Box plot matrices of non-uniformity of irradiance (top) and non-uniformity of temperature (bottom) in the rear of bifacial modules 16-113-A1, 16-074-A2, and 16-074-C3, corresponding to columns A1, A2, and C3, respectively. Left y axis labels of the three rows correspond to day numbers J_d 227, 271 and 331 of the 2018 Julian calendar. In each box, the central red mark indicates the median, and the bottom and top edges indicate the 25th and 75th percentiles, respectively. The whiskers extend to the most extreme data points not considered as outliers, and the outliers are plotted individually using the '+' symbol.

The 29.6% fraction of mean rear radiant energy with white reflectors is considerably higher than the 5.1% fraction seen with the black reflectors. Mirroring the calculations done for no reflectors at the rear of the modules, the mean daily non-uniformity is calculated by integrating the measured rear irradiance for the whole day, 26.0% and 8.7% for white and black panels, respectively. The front and rear daily solar irradiation of bifacial modules 16-113-A1, 16-074-A2, and 16-074-C3 at module-to-reflector distances of 75.5 cm, 48.5 cm, and 38.5 cm are listed in Table 28.

Both white reflectors and black panels increase the non-uniformities in irradiance with respect to the initial configuration without any reflector on the rear of the modules, reaching instant mean values up to 50%. The non-uniformity in temperature distribution remained generally below 5% without significant differences seen between the mounted white reflectors and black panels. A daily relative difference generally above +15% is seen between the performance ratio MPR of the bifacial modules rated at standard test conditions with white reflectors and monofacial reference. Bifacial modules with black rear panels still outperform the monofacial reference, with relative differences below 5%.

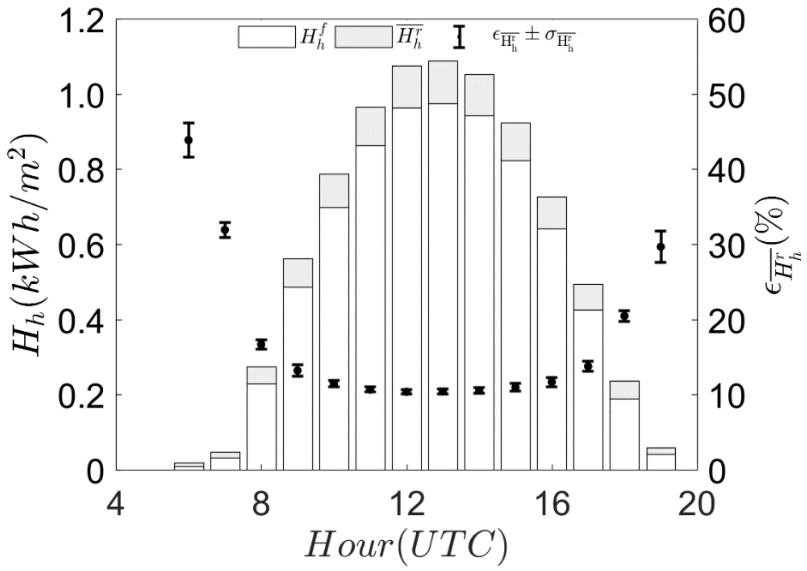

Figure 86: Available solar irradiation at module 16-113-A1 on day number 227. Left y axis: Columns chart stacking of the hourly front solar irradiation H_h^f and mean rear solar irradiation $\overline{H_h^r}$. Right y axis: Fraction of mean rear irradiation $\epsilon_{\overline{H_h^r}}$ and standard deviation $\sigma_{\overline{H_h^r}}$.

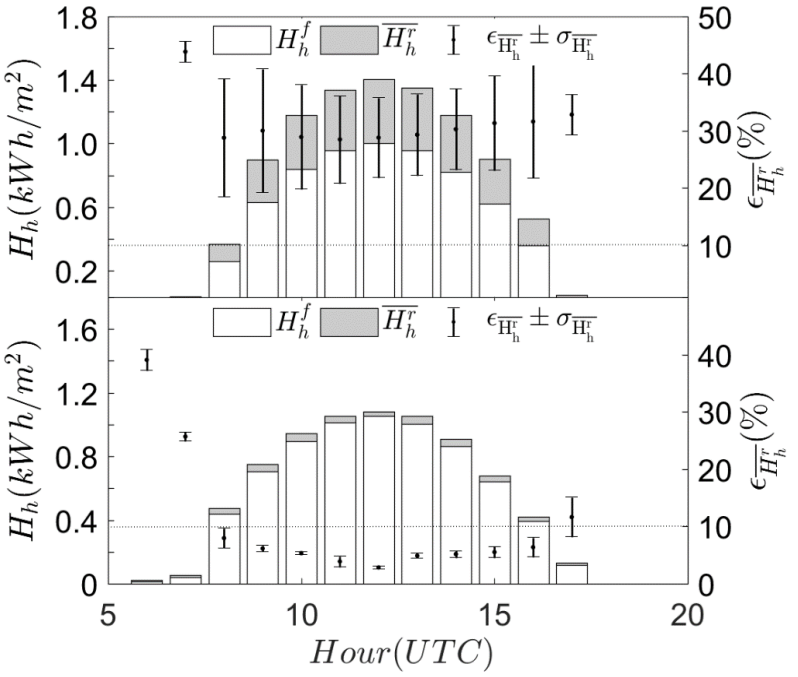

Figure 87: Available solar irradiation at module 16-113-A1 when white (top) and black (bottom) reflector panels are mounted in the rear of bifacial modules on day numbers 423 and 447, respectively. Left y axis: Columns chart stacking of the hourly front solar irradiation H_h^f and mean rear solar irradiation $\overline{H_h^r}$. Right y axis: Fraction of mean rear irradiation $\epsilon_{\overline{H_h^r}}$ and standard deviation $\sigma_{\overline{H_h^r}}$.

Table 28: Front and rear daily solar irradiation of modules 16-113-A1, 16-074-A2 and 16-074-C3.

Front		Rear A1		Rear A2		Rear C3				
H_d^f	$\cup_{H_d^f}$	$\overline{H_d^r}$	$\cup_{\overline{H_d^r}}$	$\overline{H_d^r}$	$\cup_{\overline{H_d^r}}$	$\overline{H_d^r}$	$\cup_{\overline{H_d^r}}$	d		
$(kWh \cdot m^{-2})$		$(kWh \cdot m^{-2})$		$(kWh \cdot m^{-2})$		$(kWh \cdot m^{-2})$		# day	(cm)	Reflector
4.73	0.07	1.6	0.8	1.6	0.8	1.6	0.8	342	75.5	White
4.29	0.06	1.7	0.9	1.7	0.8	1.8	0.9	372	48.5	
6.5	0.1	2.7	0.7	2.7	0.7	2.8	0.8	423	38.5	
7.2	0.1	0.41	0.03	0.39	0.03	0.40	0.02	447	38.5	Black
7.5	0.1	0.6	0.2	0.5	0.2	0.6	0.1	506	75.5	
6.9	0.1	0.4	0.2	0.4	0.2	0.4	0.2	508	48.5	

7.8 USA: NREL bifacial experimental single-axis tracking field

(Silvana Ayala Pelaez)

7.8.1 Description of bifacial testing

The Bifacial Experimental Single-axis Tracking Field (BEST) of National Renewable Energy Laboratory is located at the NREL South Table Mountain Campus, in Golden, Colorado. (39.7398341° N, -105.1727827° W). Site characteristics are listed in Table 29.

This array contains ten rows of single-axis NexTrackers, with a tracker angle limit of 60 degrees (Figure 88). Five different bifacial technologies and their monofacial counterparts for comparison have been deployed in the field. Modules (~1m x ~2m) are installed in 1P orientation, with 72-cells each. Ground coverage ratio (GCR) is 0.35. Tracker hub-height is 1 m. The ground cover of the area is grass that is mowed and maintained. Various plane-of-array sensors in rows 2 & 3 measure front and rear irradiance. The location of the sensors is highlighted in Figure 89 and Figure 90.

Weather data is available from NREL's Solar Radiation Research Laboratory station, measured at less than 100 m from the array (39.742, -105.179, 1829 m elevation). Albedo data is measured in the array itself with three albedometers (Sunkitty 1-3), two of them broadband (CM22 and Apogee Pyranometer) and one reference cell (IMT Solar). The albedometers are recorded in the data as GRI and GHI measurements.

A custom module, installed in Row 2, position 5 and referred to as "Hydra" (Figure 91), was designed and constructed to perform experiments on torque tube shading effects. The module has 12 strings of 5 cells each, tabbed out at each side along the horizontal axis, with a j-box or other connection at each row so they can be individually addressed.

Data collection for each of the strings started in December 2019. Figure 92 shows the electrical diagram and preliminary results for December on cumulative irradiance distribution, normalized.

Data for the bifacial field, including bifacial rows 2 and row 9 performance data, all front and rear facing irradiance sensors, albedometers and SRRL weather data, and Hydra Custom module data has been made publicly available in DuraMAT's website for the period of June 2019 to April 2020 [170].

An integrated bifacial gain in energy, BG_E was calculated as:

$$\mathrm{BG_E} = 100\% \times \left(\frac{\sum E_{\mathrm{bifacial}} \,/\, P_{\mathrm{STC,bifacial}}}{\sum E_{\mathrm{monofacial}} \,/\, P_{\mathrm{STC,monofacial}}} - 1 \right) \tag{38}$$

where E_{bifacial} and $E_{\mathrm{monofacial}}$ are measured yield values and $P_{\mathrm{STC,bifaical}}$ and $P_{\mathrm{STC,monofacial}}$ are front-side power ratings measured on a flash tester at STC with the back of the bifacial module covered with an opaque material. Figure 93 shows the monthly results for two of the PERC rows and the HJT string. During summer, the HJT outperforms the PERC technologies due to the high temperatures. The bifacial gain disparity is lessened when the temperature drops starting October. Both systems increase in bifacial gain due to the increased albedo from snow starting this same month.

Table 29: Characteristics of BEST bifacial PV field test site.

Information	Value	Comment
System size	75 kW_p	10 rows of 20 modules; 5 rows contain different bifacial technologies; the other 5 rows contain the equivalent monofacial technology for comparison.
System type	Single-axis trackers	Nextracker trackers, with backtracking algorithm.
Site albedo	26%	Yearly average. 1-min measurements available from 3 albedometers on site
Bifacial gain	8.9%	Based on 1-min data from Jun 2019 to April 2020
Mounting height	1.5 m	Axis of rotation of modules
Array azimuth angle	180 deg	
Ground cover ratio	0.35	
Module bifaciality	73.14%	5 different technologies, 4 PERC ranging 65 to 75% and one HJT at 90%
Array configuration	1P	
Electrical info	Row DC power, kWh, V_{DC}, I_{DC}, module's DC power	High-accuracy (0.5%) DC string monitoring. Module-level power electronics on each module (SolarEdge)
Further data	Rear irradiance, albedometers, module temperature, weather data	9 front and rear POA irradiance sensors throughout the field. 4 rear-facing reference cells along collector width on row 3 module 4. 2 rear-facing broadband irradiance meters (CM11 and Apogee Pyranometer) on row 3 module 10, east and west edges of the module, respectively. Module temperature sensors throughout the field. Albedo measured on site with CM11, IMT Solar reference cell and Apogee pyranometer. High-quality weather data available at <100m on SRRL. Time series available on Duramat.org with full data for 2 of the bifacial rows.

Figure 88: 1-axis tracker testbed for the NREL bifacial module and system performance monitoring project.

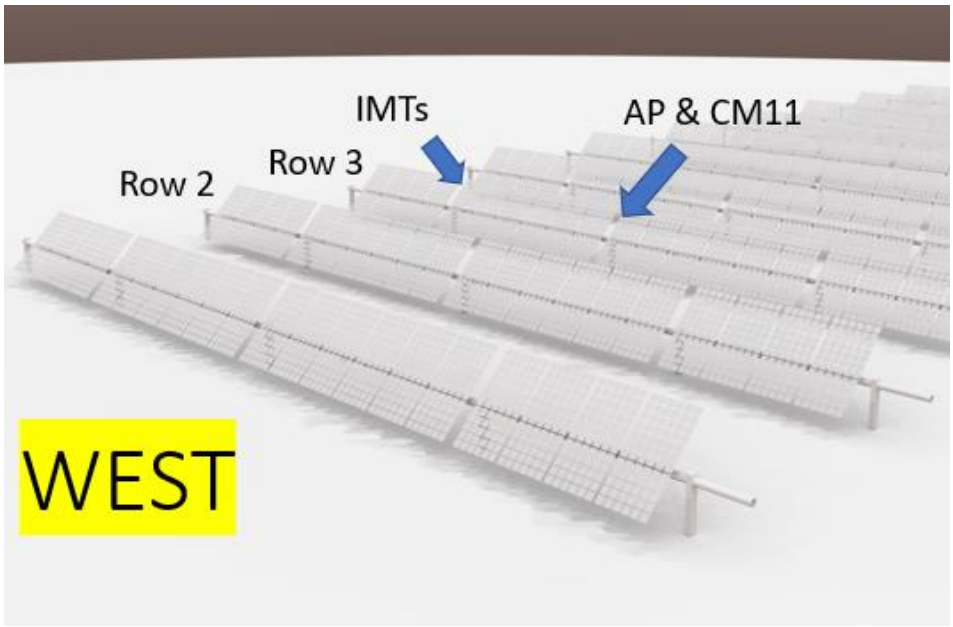

Figure 89: Schematic of the array showing rows 2 and 3, as well as location of the front- and rear-irradiance sensors on row 3.

Figure 90: Location of the front- and rear-irradiance sensors on row 3.

Figure 91: Custom module with 12 individually addressable strings mounted in the middle of NREL's bifacial PV field

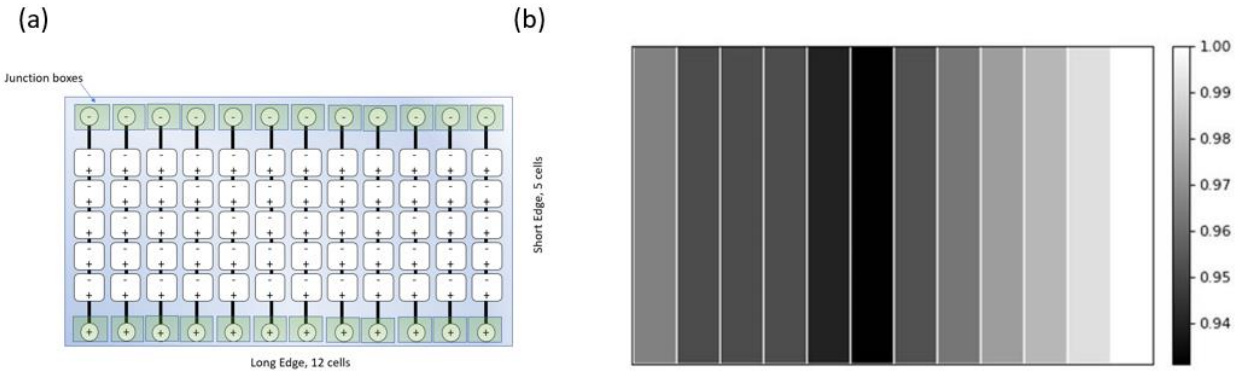

Figure 92: (a) Diagram of the custom module with 12 individually addressable strings. (b) Cumulative irradiance distribution, normalized, for the month of December.

The expected performance of the bifacial and monofacial PERC modules in the array were modeled using SAM v2018.11 and PVSyst and are shown in Figure 94, compared to the field measured bifacial gain. Just as with the rear-irradiance, the simple simulation underpredicts the field performance gain, and further adjustments to parameters are needed to better fit the data. However, SAM vs PVSyst results remain consistent to each other for most of the months. Figure 94 also shows the bifacial gain calculated from the front- and rear-irradiance measurements on the field, which shows better correlation to the bifacial gain. This highlights the importance of measuring front and rear POA irradiance on fielded systems [96].

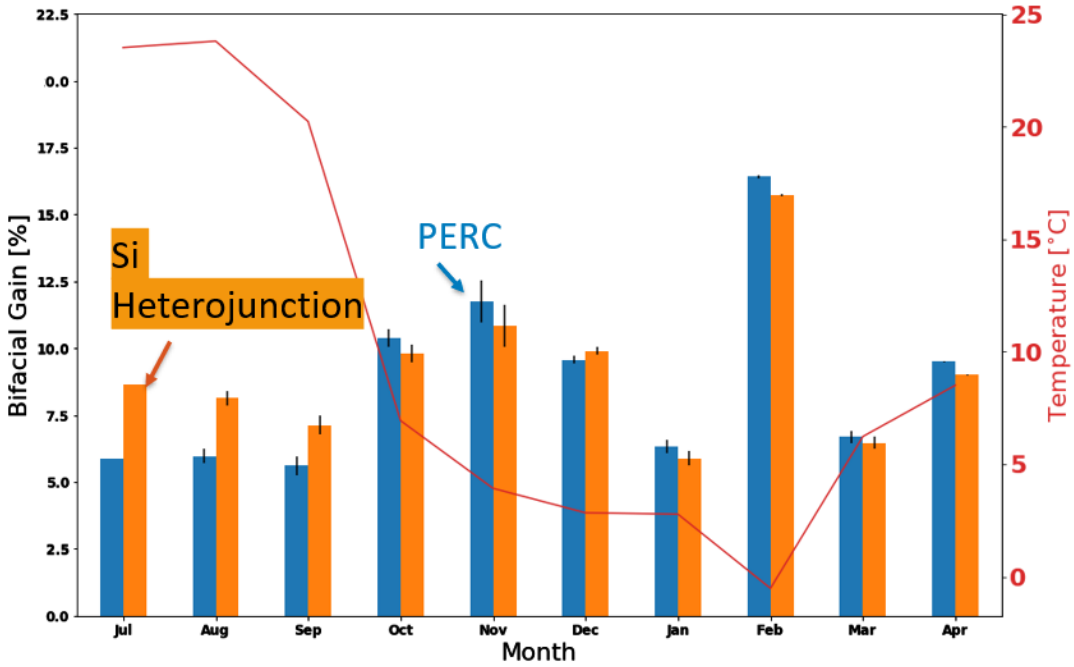

Figure 93: Monthly bifacial gain for two of the PERC technologies and a Silicon Heterojunction technology for six months of collected data. The alternating effects of temperature and snow are visible before and after beginning of October.

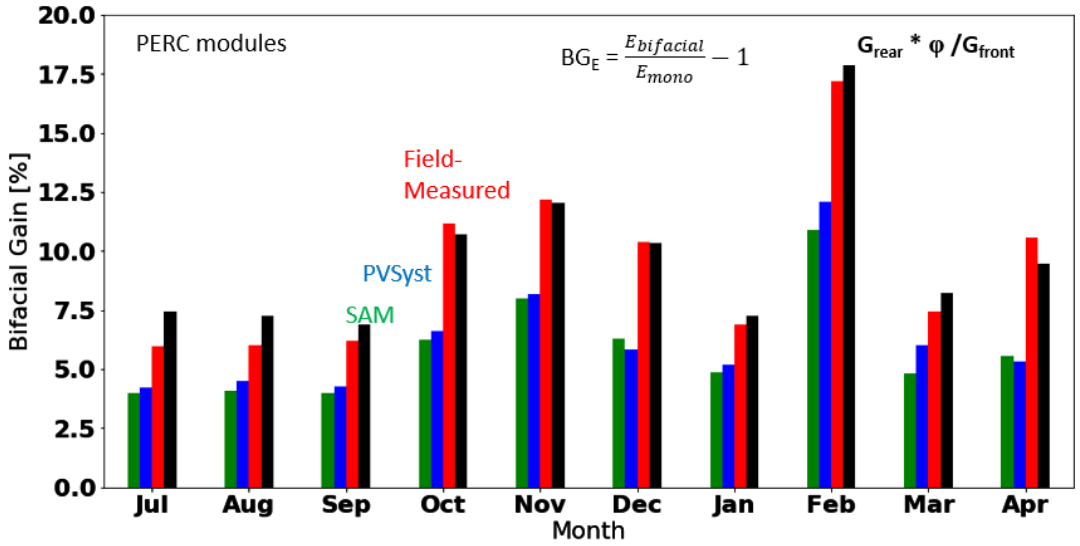

Figure 94: Field-measured bifacial gain (red) compared to bifacial gain modeled with SAM and PVSyst. In black, bifacial gain predicted from measured front and rear irradiances is plotted and shows good correlation to field-measured bifacial gain in performance.

7.9 SWEDEN: RISE bifacial test site in Piteå

(Mattias Lindh, Anna Malou Petersson)

7.9.1 Description of bifacial testing

The name of the bifacial test site, Solvåg (Sunwave), reflects the design of the solar array, which winds across a grass field surrounded by pine trees; the azimuth and inclination of the solar modules vary along the array (see Figure 95). The solar park is municipality owned through the local power company, PiteEnergi, and located at the Piteå School of Music (65.3° N, 21.5° E) in the subarctic, coastal part of Sweden. The site is the result of a regional collaboration between PiteEnergi, Norut, Luleå University of Technology, and Piteå Science Park, and it was inaugurated by the Swedish Minister for Energy in July 2018.

The Solvåg solar park is integrated into the city landscape and includes a wooden boardwalk along the modules to encourage the public to visit the site. The site's blend of solar research (through RISE) and architectural design is reflected in the custom-made wooden mounting racks.

Figure 95: Birds-eye view of the Solvåg solar site in March 2018. The red arrow denotes the North direction, and the blue circles mark trees that have been cut (September 2018) to limit issues with direct shadowing. Photo: Mikael Sundqvist (P-town Productions).

Because Piteå is in the far north, the solar elevation is low, and the solar azimuth spans almost all points of the compass during long summer days. During the very short winter days from November to January, the sun barely rises above the horizon. The yearly mean temperature in Piteå is approximately 1°C, and snow covers the ground for five to six months of the year.

Numeric models and experimental tests of bifacial modules suggest that such conditions require different mounting orientations compared to temperate mid-latitude locations. However, the published data based on real trials include only a limited range of tested orientations. Research at the Solvåg site is intended to extend this orientation range to enable experimental screening of different orientations for bifacial modules in high latitudes.

We also studied the impact of snow-enhanced albedo by coupling albedo measurements to the energy production, as well as snow shadowing of the modules with the aid of surveillance cameras and image analysis. To this end, we continuously monitored the energy production at module level, and environmental factors, such as wind speed, ambient temperature, and global horizontal, front and back-side plane-of-array irradiance (for selected modules). We also conducted occasional albedo measurements and did front- and back-side plane-of-array irradiance measurements of any module with a purpose-built mobile equipment. Technical details of the Solvåg bifacial test site are presented in Table 30.

Table 30. Technical details of the Solvåg bifacial test site.

Feature	Description	Comment
Installed power	33.9 kW_p	Based on front side STC rating
Solar modules	Prism, Bi60-362BSTC	117 pieces, front side STC rating 290 W; frameless, glass/glass.
Inverter	SolarEdge	Module level monitoring through optimizers
Mounting rack	Wooden “lounge chair” with adjustable inclination	Custom-designed for this solar site
Surveillance cameras for snow coverage detection	Hikvision, DS-2CD2655FWD-IZS	Four cameras monitoring different sections (front- and back-side) of the solar array
Module inclinations	0 to 90°	
Module azimuths	0 to 98° and 171 to 360°	N = 0°, clockwise increasing
Site topology	Grass/Urban	Grassy field with surrounding pine trees and buildings
Global horizontal irradiance sensor	Kipp & Zonen, SMP10-A Mencke & Tegtmeyer, Si-01TC	Horizontal mount; one class A pyranometer and one Si-ref cell
Front- and back-side plane-of-array sensors	Mencke & Tegtmeyer, Si-420TC & Si-01TC and Hukseflux, SR05-D1	Si-ref cells (continuous measurements for selected modules); class C pyranometers, two pieces (occasional measurement for any module)
Ambient temperature sensors	Mencke & Tegtmeyer, Ta-V-4090	Pt-1000, two pieces
Wind speed sensor	Thies, Vwind-420	Anemometer
Albedo measurements	Hukseflux, SR30-D1	Heated class A pyranometers, two pieces

7.9.2 Summary of bifacial performance results

The energy production, sensor, and camera data from Solvåg have not yet been fully analyzed. The preliminary results for 2019 and 2020 presented below show the importance of orientation on the yearly yield, the snow shadowing dependence on module inclination, and insights from albedo and irradiance measurements. Onsite measurements indicated that 2019 was warmer than usual in Piteå, both in terms of the average (3.0°C) and maximum (34.9°C) annual temperatures. Nonetheless, snow covered the ground for about six months, according to photographs from onsite surveillance cameras.

The orientations of the installed modules at Solvåg are unevenly distributed, as seen by the marker positions in Figure 96(a). Unfortunately, data from the south to east sector is missing, which obstructs and limits the analysis. The uneven distribution of orientations results in a non-trivial distribution of yearly yields for the different modules, presented for front-side STC

power rating of the modules for 2019 in Figure 96(b). The front-side STC power of the installed modules is normally distributed (verified through flash tests before installation, P = 290.1±0.7 W), and the yield distribution results from the uneven spread of azimuths. A more detailed, possibly multivariate, statistical analysis is apparently required to separate azimuth from inclination effects.

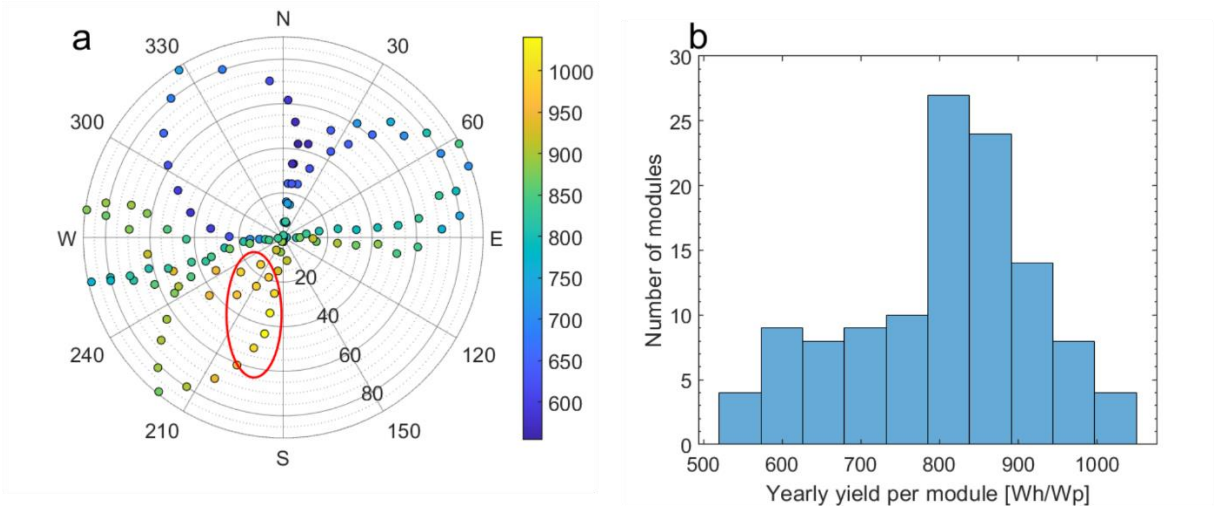

Figure 96: (left) Distribution of the module orientations with azimuth and inclination on the polar and radial axes, respectively. Each marker represents an individual module, and the color corresponds to the annual yield for the front-side STC power rating (Wh/Wp). The red ellipse indicates the best orientations for yield. (right) Histogram of the module yields for 2019.

The marker colors in Figure 96(a) reveal that the yearly yield depends on both the azimuth and the inclination, and the azimuth appears to be the most important variable. Qualitatively, south-facing modules perform better than those facing east and west, which in turn perform better the north-facing modules—a distinct trend for all inclinations. The orientations with highest yearly yield are marked by the red ellipse in Figure 96(a). The two champion modules for 2019, on par with each other, are installed at an azimuth of 190°, and inclinations of 35 and 45°, respectively.

It is important to mention that the Solvåg solar site is affected by shading from nearby pine trees and the lounge chair mounting rack. Further, the layout of the array implies some shading by nearby modules (Figure 97). The shading impact is complex: different modules are affected to varying extent and in different ways during the year. The effects direct shading from trees, mounting racks, and nearby modules have been omitted from the analysis of the results presented here.

The influence from a different kind of shading—snow covering the modules—was studied from January to May 2019, and preliminary results were presented at the *36th European PV Solar Energy Conference and Exhibition* [171]. In summary, a group of modules with similar azimuth (204 to 239°) and varying inclination (0 to 90°) were selected, as shown in Figure 97. With a daily resolution, the modules were primarily either fully covered or completely free of snow; they were partially covered only during approximately 5% of the days in the study period, as shown in Figure 98.

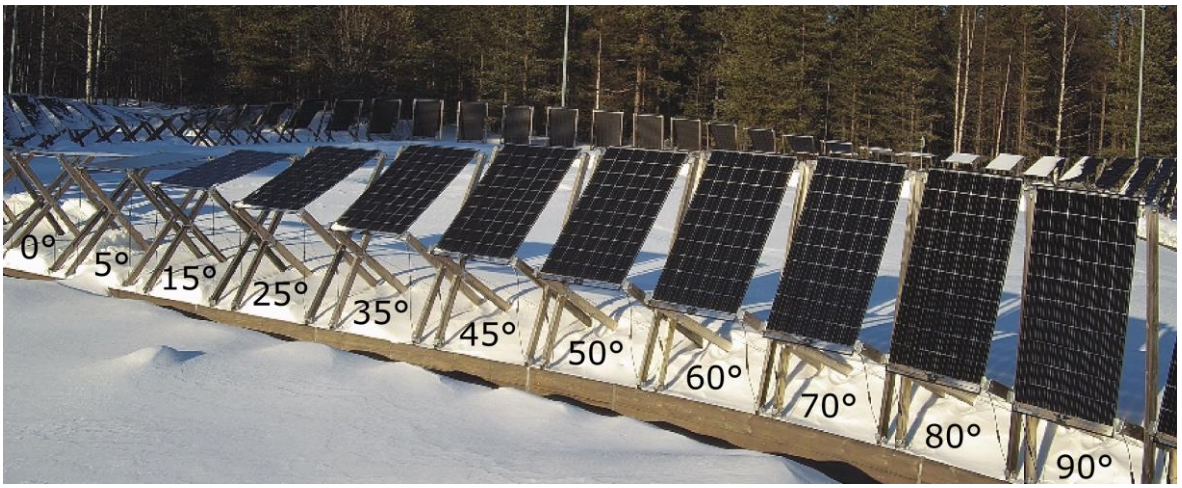

Figure 97: Photograph of the selected section of Solvåg with the inclination presented below each module.

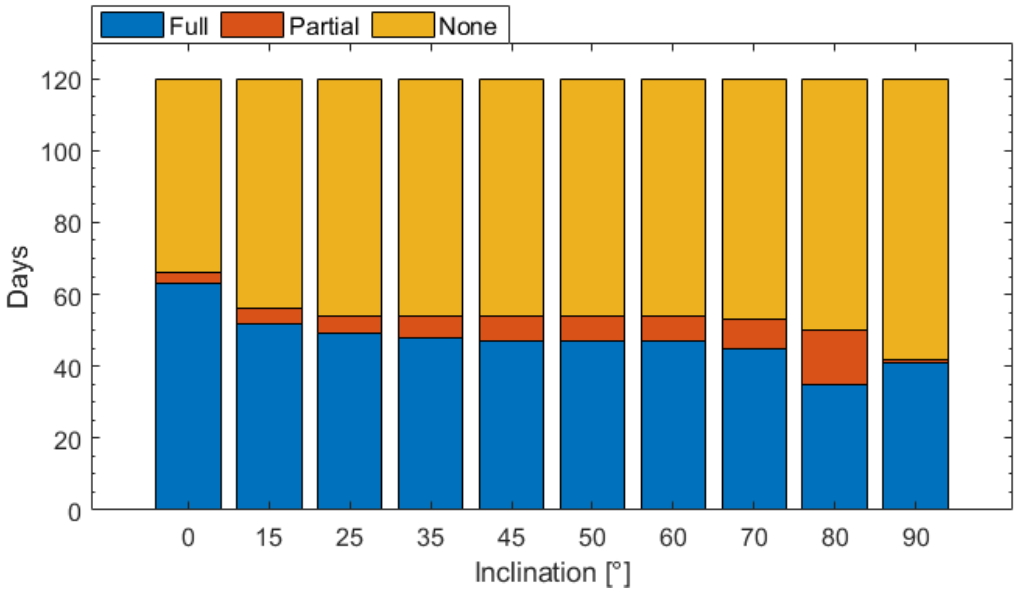

Figure 98: Number of days with and without snow cover from January to April 2019 for modules at different inclinations.

This binary snow coverage behavior can be understood by observing the process of snow removal. Sliding was the predominant mode for modules at inclinations between 25º and 90°, whereas snow melted away for modules at lower inclinations — a significantly slower process. Interestingly, sliding also occurred at sub-freezing temperatures, attributed tentatively to module heating from back-side irradiation.

During February and March, the energy production was similar for modules at inclinations between 25º and 90°. However, in April, the modules at 35° and 45° began to outperform those at other inclinations from a year-to-date energy production perspective, as seen in Figure 99. This observation holds true for southward orientations during the remains of the year, as seen in Figure 96a.

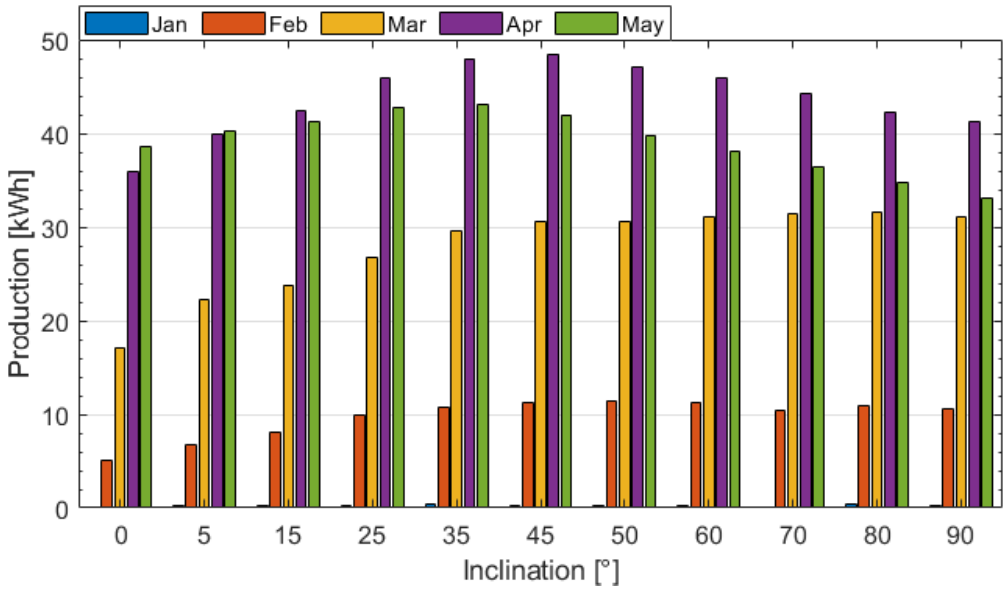

Figure 99: Monthly production of selected south oriented modules from January to May 2019.

The lack of monofacial reference modules at the Solvåg site makes it difficult to reliably measure the bifacial gain. However, combining front- and back-side plane-of-array irradiance measurements with the front- and back-side conversion efficiency of the modules enables an estimate of the *expected* bifacial gain. In mid-February 2020, when the snow covered the ground, the albedo measured 0.79±0.02. During this period, irradiance measurements for a southward module (azimuth=190°) with an inclination of 35° indicated a bifacial gain of 18±3% and 30±5% (averaged over two hours) on a mostly clear and an overcast day, respectively.

These estimates are conservative, given that they are from a south-facing module in the middle of the day. Notably, however, the ground cover ratio for the Solvåg site is lower than what would be expected in a bifacial solar production site with multiple rows. We intend to extend the analysis of bifacial gain to different times of the year, to account for factors that vary over the year, such as differences in the albedos of grass and snow, as well as different orientations of the modules.

7.10 DENMARK: Risø bifacial test site

(Nicholas Riedel-Lyngskær)

7.10.1 Description of bifacial testing

This test site located in Roskilde, Denmark (55.6°N, 12.1°E) is a collaborative project between European Energy A/S and the Technical University of Denmark (DTU). The objectives of the joint project are to validate the accuracy of bifacial PV simulations; investigate bifacial performance under various installation conditions of such factors as albedo, tilt angle, pitch; and test new bifacial PV technologies.

The test facility at this site consists of eight horizontal single-axis trackers, labelled T1–T8 in Figure 100 and eight south-facing static-tilt structures, labelled T9–T16 in the figure. All 16 substructures (including the south-facing units) are HSATs from the same manufacturer, but T9 to T16 have been oriented southward and programmed for a static-fixed tilt. Tilt angles

from 0° to 60° from horizontal are possible. Each PV substructure holds 88 PV modules, either monofacial or bifacial.

The cell types within modules are either 156 mm x 156 mm p-PERC or half-cell p-PERC. The 88 modules in each substructure are divided into four strings, where each string consists of 22 series connected modules. There is one 50 kW dual MPPT inverter for every two trackers (i.e. for every 8 strings) and therefore the operating point of the 88 panels on each substructure is determined by a single MPPT. As an advantage, all substructures at this site have dimensions analogous to those found in utility-scale PV installations.

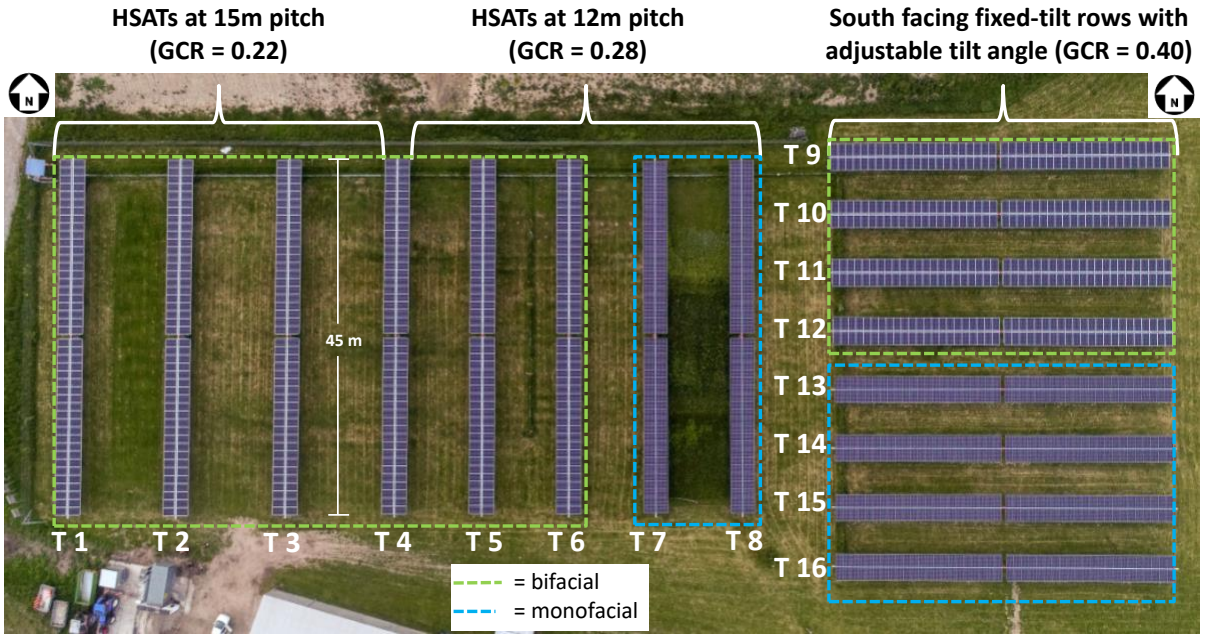

Figure 100: Aerial view of the bifacial test facility at DTU. Annotations show tracker number, substructure type, pitch, and module type.

7.10.2 Summary of bifacial performance results

The monitoring system provides maximum power point current (IMP) and maximum power point voltage (VMP) data from all 64 strings in the park at a one-minute sampling frequency using sensors with galvanic isolation. Digital filters are applied to the data to remove noise, such as fluctuations from inverter switching. Albedo data from upward and downward facing spectrally flat class A pyranometers, as well as from Class C photodiode sensors are available onsite. One year of data from the pyranometer-based albedometer is openly available on NREL's DuraMat webpage.

Figure 101 shows the albedo experiments on fixed-tilt and HSAT strings. A shortcoming of these experiments is that the experimental ground cover is not wide enough to be representative of uniform field conditions. In other words, a significant amount of the ground reflected light reaching the back side of the PV arrays comes from the grass, not the experimental cover. We have determined that for cells near the torque tube, roughly 80% of the ground reflected light comes from the experimental cover, but this amount can be as low as 50% for the cells highest (3m) from the ground. Therefore, these experiments have not proved to be useful for validating reduced-order models that do not have the capability to

simulate such localized albedo enhancements. The utility of these experiments is therefore largely to observe energy production gains that can be achieved from modifying the ground.

Figure 101: Ground cover (albedo) experiments on fixed-tilt strings (left) and equivalent experiments on HSAT strings (right).

Figure 102 shows the daily bifacial gain recorded on all the bifacial arrays at the site from July to September 2019. Data from 24 individual bifacial (6.5 kW) strings are presented in the plots. Please note that the HSAT monofacial reference systems (T7 and T8) are at a 12 m pitch. Therefore, the bifacial data from systems with a 15 m pitch have been removed, except for T2 where the white tarp and gravel are placed. The data points show the daily average bifacial gain for a given ground cover and substructure. The error bars represent the standard deviation of the daily bifacial gain when multiple strings are tested over the same ground cover. The highest bifacial gains occur under diffuse conditions when the daily DNI dose is < 1kWh/m^2. Table 31 shows a statistical summary of the bifacial gains observed over the three months. The 7.2% bifacial gain on the HSAT system above grass, versus the 5.9% gain on the fixed tilt system over the same albedo, is likely due to the fact that the HSAT system has a lower GCR and therefore experiences less self-shading.

Broadband DHI, DNI, and GHI measurements from spectrally flat class A pyranometers are made onsite at the campus solar radiation monitoring station located roughly 400 m south of the bifacial test site (Figure 103, left). These high-quality irradiance measurements - in conjunction with ambient temperature and wind speed - are used to create meteorological files for PV simulations of the test site.

In [172] the onsite meteorological data were used as input to eight different bifacial performance tools, and the outputs from all simulations were compared to field measurements when available. The work placed emphasis on validating modeled rear POA irradiance against measurements (Figure 103, right), but comparisons of DC power and bifacial gain were also presented. Figure 104 shows one month of results from four software tools that implement 2D view factor methods described previously in this report. Please note that the x-axis in the regressions report the average of two pyranometer measurements. That is, the average of pyranometer measurements made on the top and bottom of the array are used for fixed tilt systems, and for HSAT systems, the average of the east and west mounted pyranometers are used.

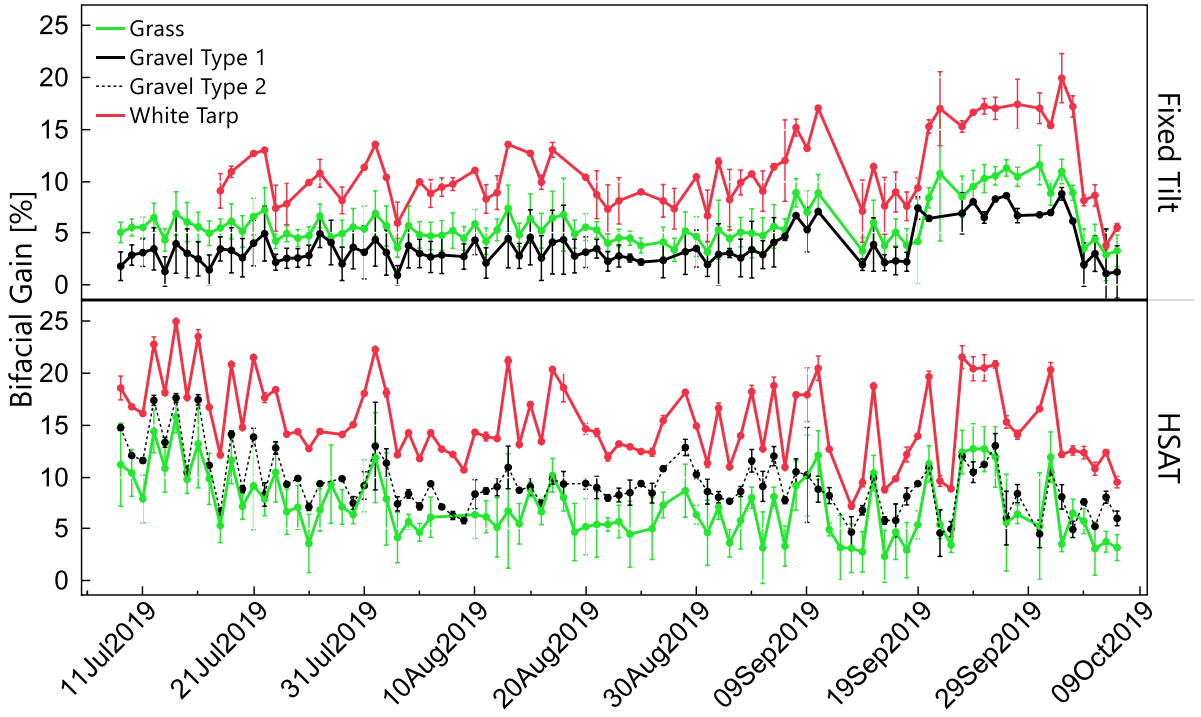

Figure 102: Daily bifacial gain of 35 individual 6.5 kW bifacial PERC systems mounted on 25° fixed tilt (top) and HSAT (bottom) substructures. Results from testing three different ground covers during 2019 are shown.

Table 31. Bifacial gain summary during three months of testing at the Risø site.

Substructure	Ground Cover	GCR	Avg Albedo (%)	Strings Tested	Avg Bifacial Gain (%)	St.Dev Bifacial Gain (%)
25° Fixed Tilt	Natural Grass	0.40	22%*	8	5.89	2.65
	Gravel Type 1	0.40	20%†	2	3.73	2.24
	White Tarp	0.40	60%*	2	11.02	3.82
HSAT	Natural Grass	0.28	22%*	8	7.23	3.84
	Gravel Type 2	0.22	26%†	2	9.32	2.87
	White Tarp	0.22	60%*	2	15.37	3.98

* Albedo measured with pyranometers.

† Albedo measured with Si photodiodes (reference cells).

Figure 103: (left) Direct normal, diffuse horizontal, and global horizontal radiation measured at the campus solar radiation monitoring station. (right) Spectrally flat class C pyranometers installed on the backside of a fixed tilt array T11.

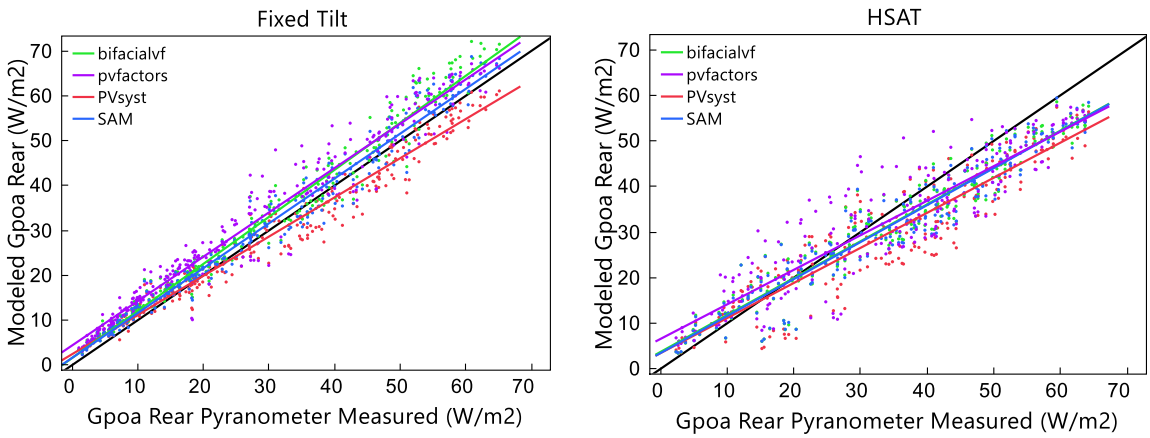

Figure 104: Regressions of modeled versus simulated rear plane of array irradiance from four view factor models simulating two system types (fixed tilt and HSAT). The unity 1:1 line is shown in black. One month of data from March 2020 is shown in each plot.

The results from the fixed tilt simulations show better agreement to measurements than the single-axis tracker simulations. This could possibly be related to the changing roll angle of the tracker that causes the view factors to change more dynamically than for the fixed tilt system. The mean bias error (MBE), mean absolute error (MAE) and root mean squared error (RMSE) are shown in Table 32. The negative MBE of the tracker simulations means that the models are underestimating the measurements. Edge brightening effects are not considered to be the cause of this underestimate since the sensors are located at least 10 m away from the nearest array edge, and according to [94], this distance should be sufficient to represent a “semi-infinite” assumption. The MAE is between 2.6 to 5.0 W/m^2 for fixed tilt simulations and 4.8 to 6.7 W/m^2 for tracker simulations. When considering total (i.e. front and back) irradiance on a clear-sky day, this error would contribute roughly 0.5% uncertainty to the bifacial PV modeling chain.

Table 32. Goodness of fit summary from the regressions shown in Figure 104.

	Fixed Tilt			HSAT		
Software	MBE (W/m^2)	MAE (W/m^2)	RMSE (W/m^2)	MBE (W/m^2)	MAE (W/m^2)	RMSE (W/m^2)
bifacialvf	2.9	3.4	4.3	-2.9	4.8	5.8
pvfactors	4.0	5.0	5.7	-1.8	6.4	7.6
PVsyst	-1.1	3.0	3.8	-4.5	6.7	7.9
SAM	1.6	2.6	3.3	-3.0	4.8	5.8

Figure 105 shows the monthly simulated and measured bifacial gains for two system types (HSAT = T6, Fixed Tilt = T12) at the test site above natural grass. The measured data are normalized in two ways: to the manufacturer nameplate values, and to the indoor flash IV measurements made at DTU before light soaking. The simulated bifacial gain is calculated as the ratio of G_{POA} rear to G_{POA} front, and adjusted for the module bifaciality (0.67), rear mismatch (0.025), and structural shading (0.07). In other words, no electrical modeling is used to obtain the simulated bifacial gains shown here. The bifacial gains from the fixed tilt simulations are all within about ±1% to the measured DC power normalized to indoor flash IV measurements. In all cases, the measured bifacial gains best agree to simulations when they are normalized to the flash measurements. The results from the HSAT simulations show errors as high as 3% in July, but as low as 1% in September. This could be because the measured bifacial gain is derived from the DC power measurements while no electrical model is used in calculating the simulated values.

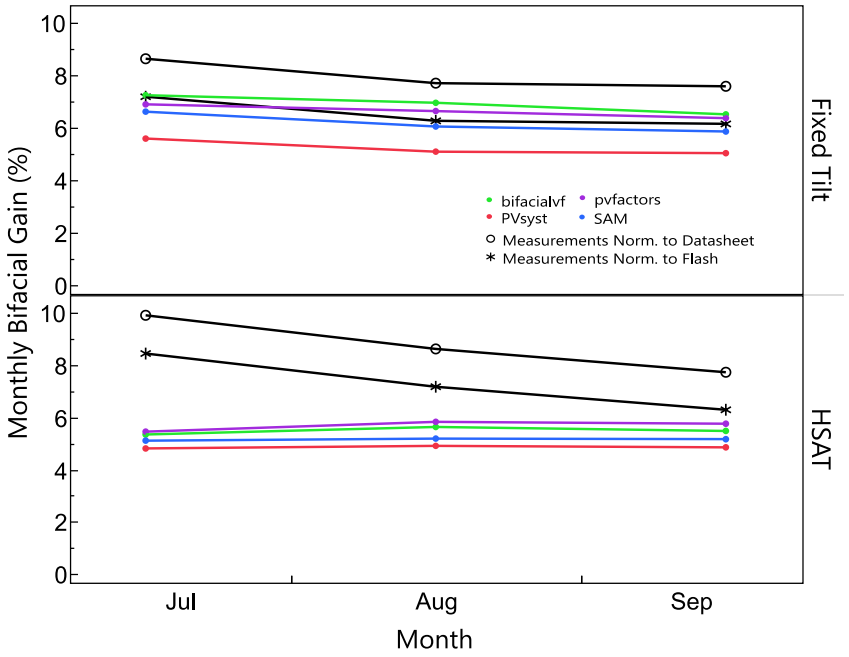

Figure 105: Simulated and measured bifacial gains of two system types (fixed tilt and HSAT) over grass for the three month period shown in Figure 102.

The DTU site includes a custom-built monitoring setup that consists of forty large-area (156.25 cm^2) PV cells laminated into four separate PV panels. The custom panels are installed at four locations on T5, with two panels on the south edge and two panels toward the center (Figure 104). This configuration was selected to investigate edge-brightening effects. The custom panels are moveable, which allows for investigations of the non-uniformity of light intensity and the subsequent impact on electrical mismatch as performed in [173].

7.11 ITALY: RSE bifacial PV field test sites

(Giosuè Maugeri)

7.11.1 Overview

Ricerca sul Sistema Energetico (RSE) is a non-profit research organization fully owned by Gestore Servizi Energetici SpA. The mission of RSE is to conduct public interest research and development programs that address national energy, environmental, and economic goals, with an open view to European Union research initiatives. RSE focuses on the development of high-efficiency and low-cost flat PV systems that help optimize the energy production of PV plants installed in the Italian territory (see Figure 106). Studies on new operation and maintenance strategies based on automatic diagnostic tools are carried under the framework of European research projects and the Italian government.

Figure 106: PV array used in research and development by RSE.

7.11.2 Description of bifacial testing

The bifacial PV system under test is located in the north of Italy, Milan (45°28'35.7"N 9°15'41.2"E) and it has a nominal power of 1.95 kW. The PV system is installed on a structure specially designed for modifying the tilt and azimuth of the entire PV string. Table 33 lists the main characteristics of the PV system under test.

The PV test plant is placed on concrete of a homogeneous light-grey color and an albedo of 27%. The monitoring system installed consists of the following:

- One unit for DC parameter monitoring.
- One unit for weather data monitoring.
- One-meter unit for AC electrical parameters monitoring and the transmission of data to the central server.
- Two monocrystalline silicon reference cells: one for measuring the incident solar radiation on the plane of the PV modules and one for measuring radiation on the rear side of the PV modules. Both reference cells have been positioned on the lower side of the PV modules in accordance with the standard IEC 60904-1-2 [47].
- One temperature probe for measuring temperatures of rear side of PV modules.

Table 33: Bifacial PV system main characteristics.

PV module characteristics		PV system characteristics	
Pnom (kW)	390	Plant ID	MI-GFV24
N°of PV module	5	Pnom (kW)	1.95
Vmpp (V)	41.4	N°of PV module	5
Impp (A)	9.4	Vmpp (V)	207
Voc (V)	49.2	Impp (A)	9.4
Isc (A)	10.15	Voc (V)	246
Module Eff (%)	18.5	Isc (A)	10.2
Bifaciality Coefficient (%)	70 ±5		
N. cells	72		

To analyze the influence of installation details on PV system performance, the tilt and ground albedo of a string of five PV modules were modified periodically to create the following three test conditions:

- Test condition 1: South-facing PV modules tilted 30° with 27% ground albedo (light grey concrete) (see Figure 107 left)
- Test condition 2: South-facing PV modules tilted 15° with 27% ground albedo (light grey concrete)
- Test condition 3: South-facing PV modules tilted 30° with 10% ground albedo (synthetic green grass) (see Figure 107 right)

Figure 107: Bifacial PV system under test; South-facing PV module on light grey concrete tilted 30°(left); South-facing PV modules on synthetic green grass tilted 30° (right).

Analysis results discussed below were based on six months of monitoring of the five-module string. This six-month monitoring period does not represent the entire spectrum of climatic conditions that can occur over a year. Moreover, the configurations monitored represent only a limited example of the countless cases that can be found in the field. Therefore, more investigation will be conducted.

7.11.3 Summary of bifacial performance results

Radiation on the rear side of the PV modules

Figure 108 shows the effect of the albedo decrease on the PV modules, while maintaining the same tilt and azimuth. A reduction that is directly proportional to incident radiation on the rear side is evident. Analysis of the trend of daily incident radiation on the rear side as a function of the incident radiation on the front side shows an almost linear dependence between the two quantities, with a greater slope associated with a higher level of albedo.

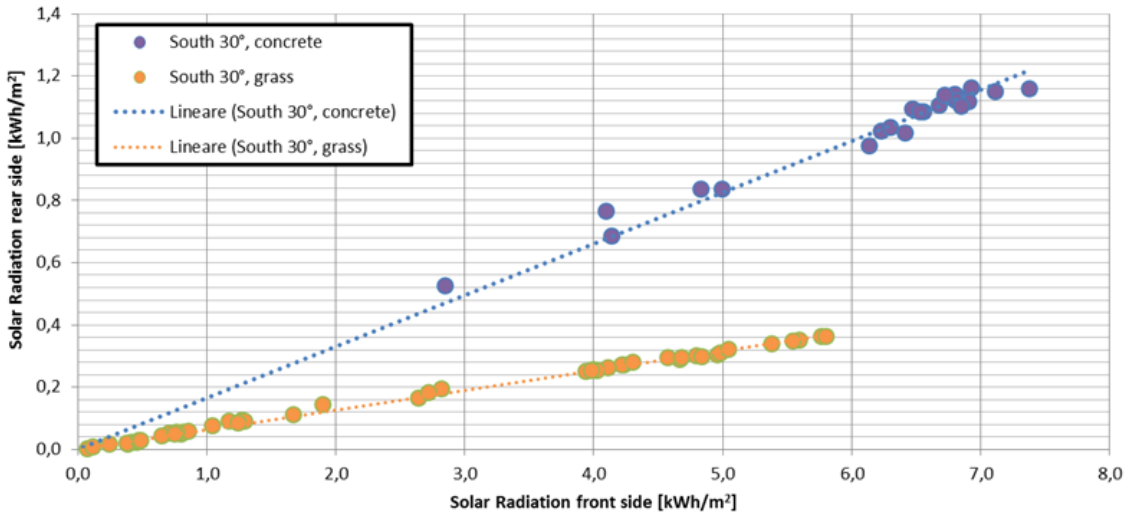

Figure 108: Trend of daily incident solar radiation on front and rear side with change in ground albedo under the PV system.

Analysis of the three test conditions showed a significant lack of homogeneity in rear solar radiation values. Specifically, the average radiation detected on the upper edge of the PV modules is more than 40% higher than on the module lower edges. Likewise, the radiation detected on the modules located furthest from the center of the string (right and left) is on average 16% higher than that on the PV module in the central position. Figure 109 shows the measurements for test condition 3 used in this analysis.

88	81	73	70	68	69	70	70	71	66	71	72	74	76	80	<- rear side
893	893	893	881	881	883	886	886	885	873	876	877	868	867	867	<- front side
63	58	52	50	51	53	47	45	45	47	50	52	51	53	59	<- rear side
893	894	891	887	889	891	881	883	883	883	881	880	866	867	868	<- front side

<- position of the solar radiation sensors used for the period of monitoring

Figure 109: Measurement of the solar radiation inhomogeneity incident on the rear side of the PV modules for the test condition 3, South, 30° tilt, grass.

Performance of the PV bifacial system

Table 34 shows the findings regarding the performance on the RSE bifacial PV system for each test configuration.

Table 34: Results of the RSE bifacial PV system monitoring for each test configuration

Test Configuration	AC energy (kWh)	DC energy (kWh)	Irrad front (kWh/m²)	Irrad back (kWh/m²)	back/ front (%)	PR (%)	PR_{DC}* (%)
1) South, 30° tilt, 27% ground albedo (concrete)	273.6	288.1	141.4	23.4	16.6	99.2	104.5
2) South, 15° tilt, 27% ground albedo (concrete)	136.0	143.5	72.6	12.5	17.3	96.1	101.4
3) South, 30°tilt, 10% ground albedo (grass)	222.1	235.7	125.6	8.1	6.4	90.7	96.2

Performance ratio in DC (PR_{DC}) highlights the overall effect of losses in DC power generated from the photovoltaic system due to module temperature, the incomplete exploitation of solar radiation, and component inefficiencies or faults (including the decoupling between the strings and any shading on the modules).

The energy performance comparison highlights the impact of decreasing ground albedo from 27% in test condition 1 to 10% in test condition 3. This decrease led to a drop in the back/front radiation ratio from 16.6% to 6.4%, which in turn reduced the performance ratio in DC (PR_{DC}) value from 104.5% to 96.2%.

The graph in Figure 110 compares the PR_{DC} of the bifacial modules under the three test configurations with the PR_{DC} of the highest performing monofacial modules among those monitored by RSE. These monofacial modules are installed on a 30° fixed-tilt structure facing south. The average bifacial gain during the monitoring period was slightly higher than 10%.

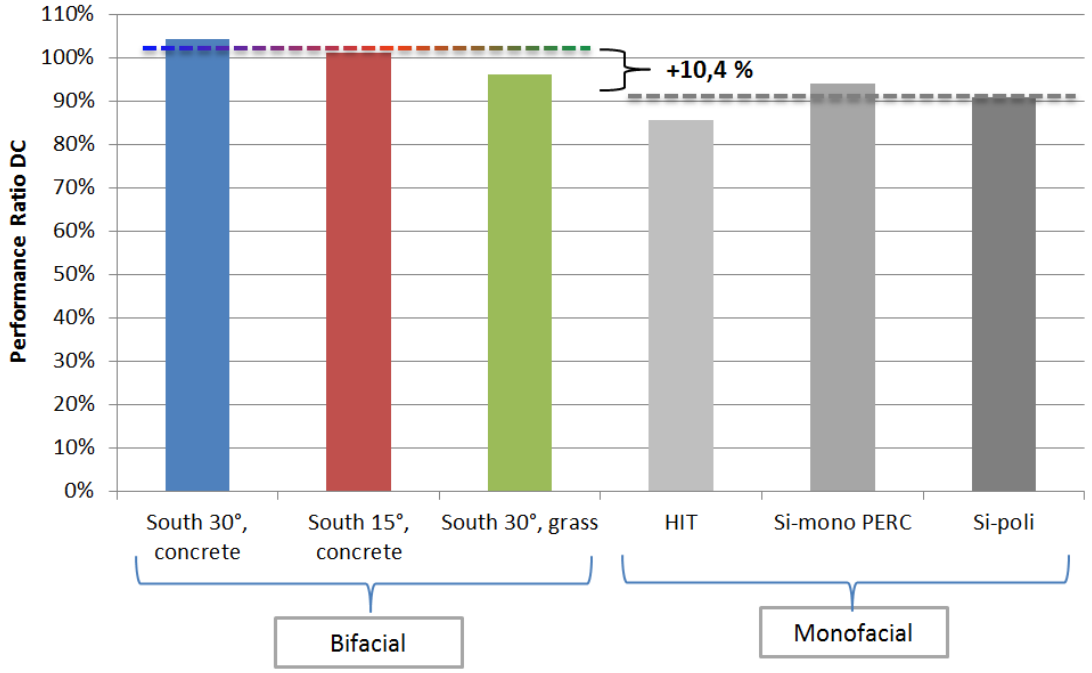

Figure 110: PR_{DC} of the bifacial modules in the three test configurations and the highest- performing monofacial modules monitored by RSE.

7.12 FINLAND: TUAS Outdoor Test Facility

7.12.1 Description of Bifacial Testing

TUAS Outdoor Test Site is located on the roof of the TUAS premises (Turku University of Applied Sciences) in Turku, Finland (60.4491°N, 22.2962°E). The field test system shown in Figure 111, consisting of four Prism Solar 295 Wp bifacial modules, was installed on the TUAS rooftop in June 2017. System was installed to the in-house developed aluminum racking that is designed to give as little shading for either side of the module as possible. The roof surface is bituminous membrane which is a common watertight layer used on commercial rooftops in Finland and whose albedo is very low. At wintertime when there is snow cover, much higher albedo is however expected. Another system in the same location is a South-West facing latitude-tilt system where several monofacial modules as well as two bifacial modules are installed.

PV Module measurements are carried out by DC-energy meters connected between modules and DC Optimizers, which keep the modules in MPP state. Voltage, current, power and energy readings are read by a PI 3B+ based DAQ system once every minute from all meters simultaneously. Time stamp for the measurement is added from dedicated time server to ensure correct time. Data is then copied to the server running the SQL database using wired Ethernet. Before the installation, modules are characterized for current, voltage, and power by triple Class A+ solar simulator (Figure 112).

Solar resource monitoring, including diffuse horizontal irradiance (DHI), direct normal irradiance (DNI), global horizontal irradiance (GHI), UV-E and the Long Wave Ratio from spectrally flat class A devices are made onsite with the solar radiation monitoring station. On top of this, several crystalline monitoring cells are also installed and measured every second by

RaspberryPI 3B+ based DAQ and average values are written to database every minute. Additional environmental sensors include module temperature sensors and a Vaisala weather station.

Figure 111: TUAS Outdoor Test Site located on the roof of the TUAS premises (Turku University of Applied Sciences) in Turku, Finland (60.4°N, 22.3°E).

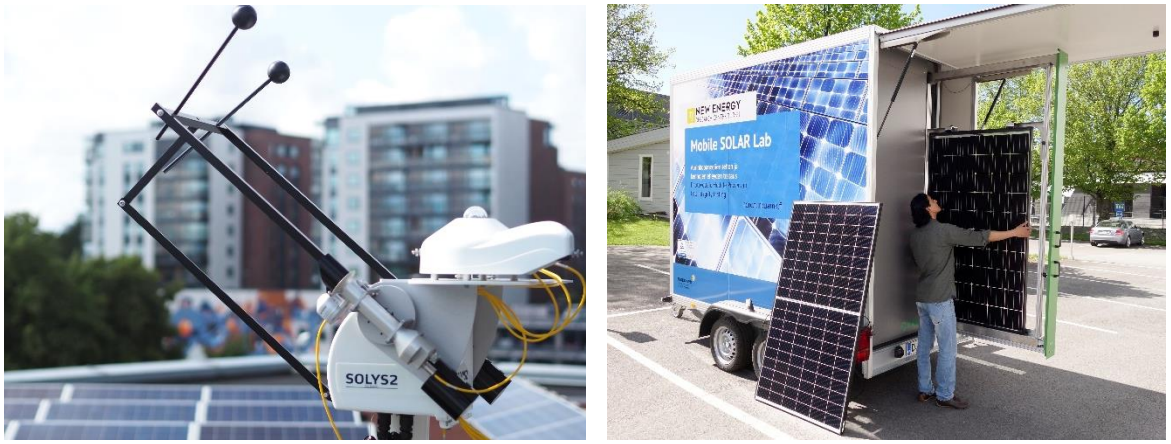

Figure 112: (left) Solar irradiance monitoring, including diffuse horizontal irradiance (DHI), direct normal irradiance (DNI), mounted south of tracker. (right) Modules are characterized by triple A+ Mobile Solar Simulator.

7.12.2 Summary of Bifacial Performance Results

The East-West Prism Solar Array started to collect data in August 2017 and has been monitored since then. The performance analysis was done for 2018 and published in 2019 [174]. The analysis of the data indicates that the bifacial gains average 5% for the different evaluated scenarios.

The data also shows the benefits of this type of modules with the East-West Vertical (EWV) setup in Nordic conditions, for instance an early peak production of 75% of the nameplate power during February, which can be attributed to high albedo from the snow. Compared with ordinary monofacial setups, under these conditions and at these latitudes, monofacial modules are often covered by snow, resulting in zero production.

The results from the analysis also showed the benefits for the residential self-consumption. The benefits from this type of array can be seen in Table 35 and in Figure 113. In general, for

most of the months during the year, the EWV array presented a better self-consumption ratio.

Table 35: Self-consumption ratios during the year for the different types of modules and arrays (3 kW systems).

	Profile 1		Profile 2		Avr of 8	
	MoF 1	Bifi 1	MoF 2	Bifi 2	MoF A	Bifi A
Jan	1.00	1.00	0.99	1.00	1.00	1.00
Feb	0.75	0.86	0.77	0.86	1.00	1.00
Mar	0.61	0.71	0.70	0.80	0.92	0.98
Apr	0.60	0.66	0.75	0.80	0.90	0.96
May	0.44	0.42	0.58	0.65	0.70	0.81
Jun	0.51	0.52	0.59	0.66	0.74	0.80
Jul	0.60	0.63	0.61	0.66	0.72	0.75
Aug	0.68	0.80	0.55	0.65	0.62	0.73
Sep	0.89	0.94	0.66	0.79	0.78	0.89
Oct	0.95	0.98	0.84	0.91	0.89	0.96
Nov	1.00	1.00	0.87	0.99	0.96	1.00
Dec	1.00	1.00	0.90	1.00	1.00	1.00
Year	0.62	0.66	0.65	0.72	0.78	0.84
Gain		4%		7%		6%

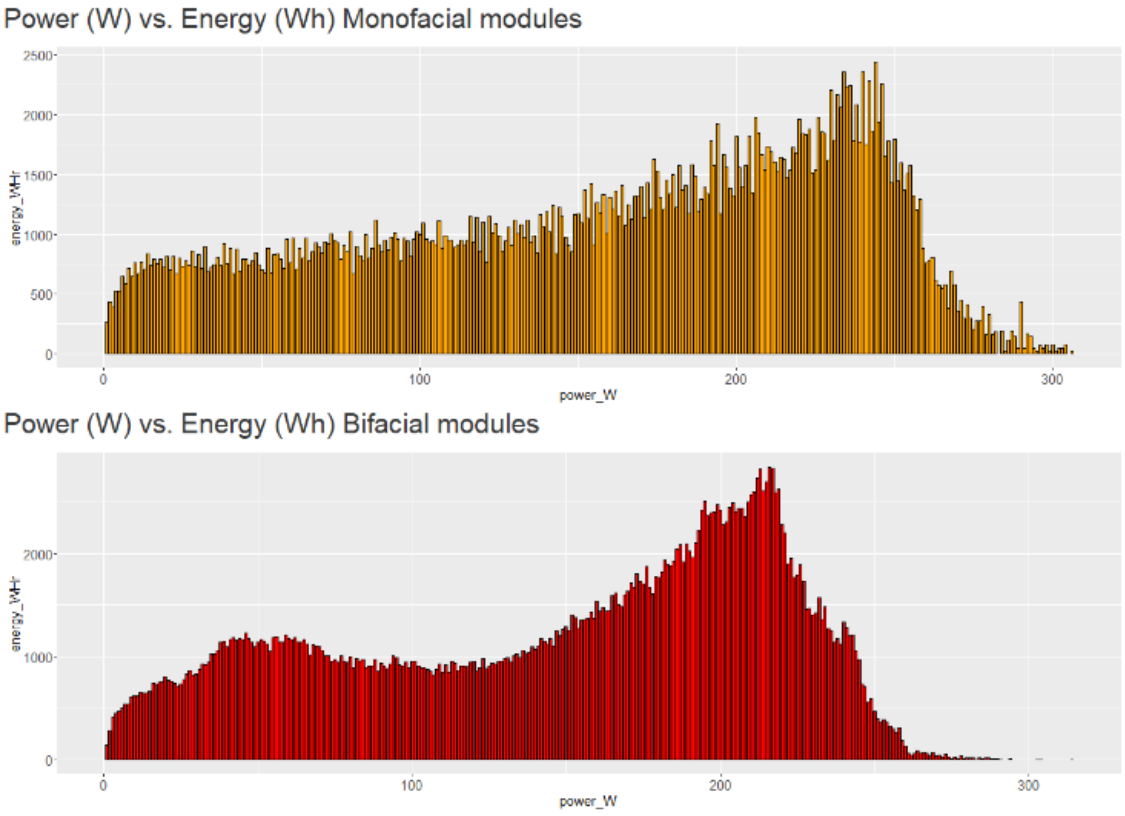

Figure 113: Power vs. energy for monofacial (top) and bifacial (bottom) modules during 2018.

REFERENCES

[1] C. D. Rodríguez-Gallegos *et al.*, "Global techno-economic performance of bifacial and tracking PV systems," *Joule*, vol. 4, pp. 1–28, 2020.

[2] "International Technology Roadmap for Photovoltaic (ITRPV) - Results 2019," Apr. 2020. [Online]. Available: http://itrpv.vdma.org/.

[3] T. Dullweber and J. Schmidt, "Industrial Silicon Solar Cells Applying the Passivated Emitter and Rear Cell (PERC) Concept—A Review," *IEEE Journal of Photovoltaics*, vol. 6, no. 5, pp. 1366–1381, 2016.

[4] X. Sun, M. R. Khan, C. Deline, and M. A. Alam, "Optimization and performance of bifacial solar modules: a global perspective," *Appl. Energy*, vol. 212, pp. 1601–1610, 2017.

[5] C. Deline, S. A. Peláez, B. Marion, B. Sekulic, M. Woodhouse, and J. Stein, "Bifacial PV System Performance: Separating Fact from Fiction," presented at the IEEE-PVCS-46, Chicago, 2019.

[6] A. Cuevas, "The Early History of Bifacial Solar Cells," presented at the 20th European Solar Energy Conference, Barcelona, Spain, 2005.

[7] I. Romijn *et al.*, "Bifacial Cells," in *Bifacial Photovoltaics: Technology, applications and economics*, J. Libal and R. Kopecek, Eds. IET, 2019.

[8] H. Mori, "Radiation energy transducing device," Oct. 1966.

[9] A. W. Blakers, A. Wang, A. M. Milne, J. Zhao, and M. A. Green, "22.8% efficient silicon solar cell," *22.8% efficient silicon solar cell*, vol. 55, no. 1363, 1989.

[10] T. Dullweber *et al.*, "Present status and future perspectives of bifacial PERC+ solar cells and modules," *Japanese Journal of Applied Physics 57*, vol. no. 8S3, 2018.

[11] "Trina Solar press release," Mar. 06, 2020. https://www.trinasolar.com/us/resources/newsroom/trina-solar-announces-2339-perc-solar-cell-made-standard-fabrication-equipment.

[12] "LONGi Solar press release," Jan. 16, 2019. https://www.pv-tech.org/news/longi-solar-has-bifacial-monoperc-solar-cell-world-record-verified-at-24.0.

[13] C. Messmer, A. Fell, F. Feldmann, J. S. N. Wöhrle, and M. Hermle, "Efficiency Roadmap for Evolutionary Upgrades of PERC Solar Cells by TOPCon: Impact of Parasitic Absorption," *IEEE Journal of Photovoltaics*, vol. 10, no. 2, pp. 335–342, Mar. 2020.

[14] J. Schmidt, K. Bothe, and R. Bock, "N-type silicon- the better material choice for industrial high-efficiency solar cells," presented at the 22nd European Photovoltaic Solar Energy Conference, Milan, Italy, 2007.

[15] S. W. Glunz, S. Rein, J. Y. Lee, and W. Warta, "Minority carrier lifetime degradation in boron-doped Czochralski silicon," *J. Appl. Phys.*, vol. 90, pp. 2397–2404, 2001.

[16] L. Tous *et al.*, "Progress on bifacial Ni/Ag plated NPERT cells for module fabrication with SWCT," Brussels, Belgium, 2018, pp. 439–443.

[17] J. Rodriguez, E.-C. Wang, and N. Chen, "Towards 22% efficient screen-printed bifacial n-type silicon solar cells," *Sol Energy Mater & Sol Cells*, vol. 187, pp. 91–96, 2018.

[18] J. H. Zhao, A. H. Wang, P. P. Altermatt, M. A. Green, J. P. Rakotoniaina, and O. Breitenstein, "High efficiency PERT cells on n-type silicon substrates," New Orleans, 2002, pp. 218–221.

[19] Y. Liu, "nPERC and nIBC Solar Cell Technology," presented at the Presentation at the 8th n-type PV workshop, Lausanne, Switzerland, 2018.

[20] IMEC, "IMEC Press Release," Apr. 2019, [Online]. Available: https://www.imec-int.com/en/articles/imec-and-jolywood-achieve-a-record-of-23-2-percent-with-bifacial-n-pert-solar-cells.

[21] A. Richter, J. Benick, F. Feldmann, A. Fell, M. Hermle, and S. Glunz, "n-Type Si solar cells with passivating electron contact: Identifying sources for efficiency limitations by wafer thickness and resistivity variation," *Sol. Energy Mater. Sol. Cells*, vol. 173, pp. 96–105, 2017.

[22] JinkoSolar, "JinkoSolar press release," Jan. 25, 2019. https://www.pv-tech.org/news/jinkosolar-pushes-n-type-topcon-solar-cell-to-record-24.2-conversion-efficiency.

[23] D. Ding, G. Lua, Z. Lia, Y. Zhanga, and W. Shena, "High-efficiency n-type silicon PERT bifacial solar cells with selective emitters and poly-Si based passivating contacts," *Solar Energy*, vol. 193, pp. 494–501, 2019.

[24] R. V. K. Chavali, S. De Wolf, and M. A. Alam, "Device physics underlying silicon heterojunction and passivating-contact solar cells: A topical review," *Prog Photovolt Res Appl*, vol. 26, no. 4, pp. 241–260, Apr. 2018, doi: 10.1002/pip.2959.

[25] W. Fuhs, K. Niemann, and J. Stuke, "Heterojunctions of Amorphous Silicon and Silicon Single Crystals," 1974, vol. 345, pp. 345–350.

[26] M.Tanaka *et al.*, "Development of New a-Si/c-Si Heterojunction Solar Cells: ACJ-HIT (Artificially Constructed Junction-Heterojunction with IntrinsicThin-Layer)," *Japanese Journal of Applied Physics*, vol. 31, 11R vols., p. 3518, 1992.

[27] A. Descoeudre *et al.*, "The versatility of passivating carrier-selective silicon thin films for diverse high-efficiency screen-printed heterojunction-based solar cells," *Progress in Photovoltaics*, 2019.

[28] K. Masuko, M. Shigematsu, and T. Hashiguchi, “Achievement of more than 25% conversion efficiency with crystalline silicon heterojunction solar cell,” *IEEE J Photovoltaics*, vol. 4(6), pp. 1433–1435, 2014.
[29] K. Yamamoto *et al.*, “Record-breaking efficiency back-contact heterojunction crystalline Si solar cell and module,” Amsterdam, 2017, pp. 201–204.
[30] R. V. K. Chavali *et al.*, “Multiprobe Characterization of Inversion Charge for Self-Consistent Parameterization of HIT Cells,” *IEEE J. Photovoltaics*, vol. 5, no. 3, pp. 725–735, May 2015, doi: 10.1109/JPHOTOV.2014.2388072.
[31] M. Burger, “Meyer Burger press release,” Mar. 11, 2019. https://www.meyerburger.com/en/company/media-center/news/meyer-burger-announces-record-hjt-cells-with-efficiencies-over-24-at-pv-celltech/.
[32] O. D. Miller, E. Yablonovitch, and S. R. Kurtz, “Strong Internal and External Luminescence as Solar Cells Approach the Shockley–Queisser Limit,” *IEEE J. Photovoltaics*, vol. 2, no. 3, pp. 303–311, Jul. 2012, doi: 10.1109/JPHOTOV.2012.2198434.
[33] F. I. for S. E. S. ISE, “Fraunhofer ISE Sets Two Records for the Efficiency of Silicon-Based Monolithic Triple-Junction Solar Cells,” Aug. 29, 2019. .
[34] C. H. Henry, “Limiting efficiencies of ideal single and multiple energy gap terrestrial solar cells,” *Journal of Applied Physics*, vol. 51, no. 8, pp. 4494–4500, Aug. 1980, doi: 10.1063/1.328272.
[35] E. Gençer *et al.*, “Directing solar photons to sustainably meet food, energy, and water needs,” *Scientific Reports*, vol. 7(1), p. 3133, 2017.
[36] L. C. Hirst and N. J. Ekins-Daukes, “Fundamental losses in solar cells,” *Prog. Photovolt: Res. Appl.*, vol. 19, no. 3, pp. 286–293, May 2011, doi: 10.1002/pip.1024.
[37] A. Polman and H. A. Atwater, “Photonic design principles for ultrahigh-efficiency photovoltaics,” *Nature Mater*, vol. 11, no. 3, pp. 174–177, Mar. 2012, doi: 10.1038/nmat3263.
[38] M. A. Alam and M. R. Khan, “Shockley–Queisser triangle predicts the thermodynamic efficiency limits of arbitrarily complex multijunction bifacial solar cells,” *Proceedings of the National Academy of Sciences*, vol. 116(48), pp. 23966–23971, 2019.
[39] M. A. Alam and M. R. Khan, “Thermodynamic efficiency limits of classical and bifacial mb] ulti-junction tandem solar cells: An analytical approach,” *Applied Physics Letters*, vol. 109(17), p. 173504, 2016.
[40] W. Shockley and W. J. Queisser, “Detailed Balance Limit of Efficiency of p-n Junction Solar Cells,” *Journal of Applied Physics*, vol. 32(3), p. 510, 1961.
[41] M. R. Khan, X. Jin, and M. A. Alam, “PVLimits: PV thermodynamic limit calculator,” 2016.
[42] R. Asadpour, R. V. K. Chavali, M. Ryyan Khan, and M. A. Alam, “Bifacial Si heterojunction-perovskite organic-inorganic tandem to produce highly efficient (ηT* ∼ 33%) solar cell,” *Appl. Phys. Lett.*, vol. 106, no. 24, p. 243902, Jun. 2015, doi: 10.1063/1.4922375.
[43] H. Imran, I. Durrani, M. Kamran, T. M. Abdolkader, M. Faryad, and N. Z. Butt, “High-Performance Bifacial Perovskite/Silicon Double-Tandem Solar Cell,” *IEEE J. Photovoltaics*, pp. 1–8, 2018, doi: 10.1109/JPHOTOV.2018.2846519.
[44] H. Chung, X. Sun, and P. Bermel, “Optical approaches to improving perovskite/Si tandem cells,” *MRS Adv.*, vol. 1, no. 14, pp. 901–910, 2016, doi: 10.1557/adv.2016.33.
[45] X. Sun, Y. Sun, Z. Zhou, M. A. Alam, and P. Bermel, “Radiative sky cooling: fundamental physics, materials, structures, and applications,” *Nanophotonics*, vol. 6, no. 5, pp. 997–1015, Jul. 2017, doi: 10.1515/nanoph-2017-0020.
[46] X. Sun, T. Silverman, Z. Zhou, M. Khan, P. Bermel, and M. Alam, “Optics-based approach to thermal management of photovoltaics: selective-spectral and radiative cooling,” *IEEE Journal of Photovoltaics*, vol. 7(2), pp. 566–574, 2017.
[47] “IEC TS 60904-1-2: Photovoltaic devices - Part 1-2: Measurement of current-voltage characteristics of bifacial photovoltaic (PV) devices,” International Electrotechnical Commission, 2019.
[48] “IEC 60904-7: Photovoltaic devices; part 7: Computation of the spectral mismatch correction for measurements of photovoltaic devices,” International Electrotechnical Commission.
[49] “IEC 60904-9: Photovoltaic devices - Part 9: Solar simulator performance requirements,” International Electrotechnical Commission, 2007.
[50] W. Herrmann, M. Schweiger, and J. Bonilla Castro, “Performance characteristics of bifacial PV modules and power labeling,” presented at the 4th Bifi PV Workshop, Konstanz, Germany, 2017.
[51] “IEC 61215: Terrestrial photovoltaic (PV) modules - Design qualification and type approval,” International Electrotechnical Commission, 2016.
[52] “EC 61730: Photovoltaic (PV) module safety qualification,” International Electrotechnical Commission, 2016.
[53] “IEC 61853: Photovoltaic (PV) module performance testing and energy rating,” International Electrotechnical Commission, 2018.
[54] A. Gracia-Amillo, “Challenges of energy rating of bifacial and BIPV modules - Possible extension of the IEC 61853 standard series to bifacial and BIPV devices,” *Advanced PV Energy Rating (PV-Enerate)*. https://www.pv-enerate.ptb.de/16eng02-

blogsingle.html?&tx_ttnews%5Btt_news%5D=804&cHash=8d12bea539af2a236e393c107e1f4bbb (accessed Mar. 05, 2020).
[55] Kim *et al.*, "Reflection and Durability Study of Different Types of Backsheets and Their Impact on C-Si PV Module Performance.," *Solar Energy Materials and Solar Cells*, vol. 146, pp. 91–98, Mar. 2016.
[56] M. C. López-Escalante, M. Fernández-Rodríguez, L. J. Caballero, F. Martín, M. Gabás, and J. R. Ramos-Barrado, "Novel encapsulant architecture on the road to photovoltaic module power output increase," *Applied Energy*, vol. 228, pp. 1901–1910, Oct. 2018, doi: 10.1016/j.apenergy.2018.07.073.
[57] J. a. M. van Roosmalen, S. L. Luxembourg, J. Liu, L. a. G. Okel, and B. B. V. Aken, "White Bifacial Modules – Improved STC Performance Combined with Bifacial Energy Yield," Munich, Germany, Jul. 2016, pp. 42–47.
[58] M. C. López-Escalante, M. Fernández-Rodríguez, L. J. Caballero, F. Martín, M. Gabás, and J. R. Ramos-Barrado, "Novel Encapsulant Architecture on the Road to Photovoltaic Module Power Output Increase," *Applied Energy*, vol. 228, pp. 1901–1910, 2018, doi: 10.1016/j.apenergy.2018.07.073.
[59] A. J. Curran *et al.*, "Degradation of Bifacial PERC and Al-BSF Cell Minimodules with White and Clear Encapsulant Combinations in Modified Damp Heat," presented at the IEEE 47th Photovoltaic Specialist Conference, Calgary, Canada, 2020.
[60] J. Schmidt and A. Cuevas, "Electronic properties of light-induced recombination centers in boron-doped Czochralski silicon," *Journal of Applied Physics*, vol. 86, no. 6, pp. 3175–3180, Sep. 1999, doi: 10.1063/1.371186.
[61] K. Bothe, R. Sinton, and J. Schmidt, "Fundamental boron-oxygen-related carrier lifetime limit in mono- and multicrystalline silicon," *Prog. Photovolt: Res. Appl.*, vol. 13, no. 4, pp. 287–296, Jun. 2005, doi: 10.1002/pip.586.
[62] D. Bredemeier, D. Walter, S. Herlufsen, and J. Schmidt, "Lifetime degradation and regeneration in multicrystalline silicon under illumination at elevated temperature," *AIP Advances*, vol. 6, no. 3, p. 035119, Mar. 2016, doi: 10.1063/1.4944839.
[63] A. C. nee Wenham *et al.*, "Hydrogen-Induced Degradation," in *2018 IEEE 7th World Conference on Photovoltaic Energy Conversion (WCPEC) (A Joint Conference of 45th IEEE PVSC, 28th PVSEC & 34th EU PVSEC)*, Waikoloa Village, HI, Jun. 2018, pp. 0001–0008, doi: 10.1109/PVSC.2018.8548100.
[64] A. Herguth, C. Derricks, and D. Sperber, "A Detailed Study on Light-Induced Degradation of Cz-Si PERC-Type Solar Cells: Evidence of Rear Surface-Related Degradation," *IEEE J. Photovoltaics*, vol. 8, no. 5, pp. 1190–1201, Sep. 2018, doi: 10.1109/JPHOTOV.2018.2850521.
[65] R. Kopecek, "Is LeTID degradation in PERC cells another degradation crisis even worse than PID?," *PVTech*, Nov. 19, 2018.
[66] M. Barbato *et al.*, "Durability of Bifacial Solar Modules under Potential Induced Degradation: Role of the Encapsulation Materials," *32nd European Photovoltaic Solar Energy Conference and Exhibition; 1879-1883*, p. 5 pages, 6555 kb, 2016, doi: 10.4229/EUPVSEC20162016-5BV.1.26.
[67] I. Devoto and A. Halm, "Comprehensive Study of PID Mechanisms for n-Type Bifacial Solar Cells," *36th European Photovoltaic Solar Energy Conference and Exhibition; 1106-1113*, p. 8 pages, 18659 kb, 2019, doi: 10.4229/EUPVSEC20192019-4AV.1.61.
[68] W. Luo *et al.*, "Elucidating potential-induced degradation in bifacial PERC silicon photovoltaic modules," *Prog Photovolt Res Appl*, vol. 26, no. 10, pp. 859–867, Oct. 2018, doi: 10.1002/pip.3028.
[69] J. Carolus, J. A. Tsanakas, A. van der Heide, E. Voroshazi, W. De Ceuninck, and M. Daenen, "Physics of potential-induced degradation in bifacial p-PERC solar cells," *Solar Energy Materials and Solar Cells*, vol. 200, p. 109950, Sep. 2019, doi: 10.1016/j.solmat.2019.109950.
[70] M. I. Devoto Acevedo, "Solar module characterization via visual inspection in the field, I-V curve and thermal-image analysis," Univeristy of Chile, Santiago, Chile, 2018.
[71] J. Melendez, "Bifacial PV Tracking Designing Bifacial PV Projects," 2018, [Online]. Available: https://16iwyl195vvfgoqu3136p2ly-wpengine.netdna-ssl.com/wp-content/uploads/2018/10/2018-10-25-Bifacial-Webinar-SOLTEC.pdf.
[72] "QCells: Hot-Spot Protect prevents solar module fire," 2020. https://www.q-cells.eu/products/technology/hot-spot-protect.html.
[73] M. Iqbal, *An introduction to solar radiation*. Toronto ; New York: Academic Press, 1983.
[74] Gueymard *et al.*, "Surface albedo and reflectance: Review of definitions, angular and spectral effects, and intercomparison of major data sources in support of advanced solar irradiance modeling over the Americas," *Solar Energy*, vol. 182, pp. 194–212, 2019, doi: 10.1016/j.solener.2019.02.040.
[75] Sengupta *et al.*, "The national solar radiation data base (NSRDB)," *Renewable and Sustainable Energy Reviews*, vol. 89, pp. 51–60, 2018, doi: 10.1016/j.rser.2018.03.003.
[76] G. Maclaurin, M. Sengupta, Y. Xie, and N. Gilroy, "Development of a MODIS-Derived Surface Albedo Data Set: An Improved Model Input for Processing the NSRDB," NREL/TP--6A20-67306, 1335471, Dec. 2016. doi: 10.2172/1335471.
[77] C. Deline, S. Ayala Pelaez, S. MacAlpine, and C. Olalla, "Estimating and parameterizing mismatch power loss in bifacial photovoltaic systems," *Prog Photovolt Res Appl*, p. pip.3259, Mar. 2020, doi: 10.1002/pip.3259.

[78] C. W. Hansen *et al.*, “A Detailed Model of Rear-Side Irradiance for Bifacial PV Modules,” in *2017 IEEE 44th Photovoltaic Specialist Conference (PVSC)*, Washington, DC, Jun. 2017, pp. 1543–1548, doi: 10.1109/PVSC.2017.8366707.
[79] T. S. Liang *et al.*, “A review of crystalline silicon bifacial photovoltaic performance characterisation and simulation,” *Energy Environ. Sci.*, vol. 12, no. 1, pp. 116–148, 2019, doi: 10.1039/C8EE02184H.
[80] I. Shoukry, D. Berrian, J. Libal, and F. Haffner, “Simulation models for energy yield prediction of bifacial systems,” in *Bifacial Photovoltaics: Technology, applications and economics*, J. Libal and R. Kopecek, Eds. Institution of Engineering and Technology, 2018, pp. 119–151.
[81] J. S. Stein, D. Riley, M. Lave, C. Hansen, C. Deline, and F. Toor, “Outdoor Field Performance from Bifacial Photovoltaic Modules and Systems,” in *2017 IEEE 44th Photovoltaic Specialist Conference (PVSC)*, Washington, DC, Jun. 2017, pp. 3184–3189, doi: 10.1109/PVSC.2017.8366042.
[82] J. S. Stein, D. S. Riley, M. Lave, C. Deline, F. Toor, and C. W. Hansen, “Outdoor Field Performance from Bifacial Photovoltaic Modules and Systems,” *33rd European Photovoltaic Solar Energy Conference and Exhibition; 1961-1967*, p. 7 pages, 6649 kb, 2017, doi: 10.4229/EUPVSEC20172017-6CO.13.3.
[83] J. Stein, L. Burnham, and M. S. Lave, “One Year Performance Results for the Prism Solar Installation at the New Mexico Regional Test Center: Field Data from February 15 2016 - February 14 2017.,” SAND2017-5872, Jun. 2017. doi: 10.2172/1367463.
[84] I. Shoukry, J. Libal, R. Kopecek, E. Wefringhaus, and J. Werner, “Modelling of Bifacial Gain for Stand-alone and in-field Installed Bifacial PV Modules,” *Energy Procedia*, vol. 92, pp. 600–608, 2016, doi: 10.1016/j.egypro.2016.07.025.
[85] C. Deline, S. MacAlpine, B. Marion, F. Toor, A. Asgharzadeh, and J. S. Stein, “Assessment of Bifacial Photovoltaic Module Power Rating Methodologies—Inside and Out,” *IEEE J. Photovoltaics*, vol. 7, no. 2, pp. 575–580, Mar. 2017, doi: 10.1109/JPHOTOV.2017.2650565.
[86] S. Ayala Pelaez, C. Deline, S. M. MacAlpine, B. Marion, J. S. Stein, and R. K. Kostuk, “Comparison of Bifacial Solar Irradiance Model Predictions With Field Validation,” *IEEE J. Photovoltaics*, vol. 9, no. 1, pp. 82–88, Jan. 2019, doi: 10.1109/JPHOTOV.2018.2877000.
[87] G. W. Larson and R. Shakespeare, *Rendering with Radiance: the art and science of lighting visualization*. San Francisco: Morgan Kaufmann, 1998.
[88] C. Barati, “A record year for trackers,” *pv-magazine.com*, Mar. 27, 2020.
[89] S. Racharla and K. Rajan, “Solar tracking system–a review,” *International Journal of Sustainable Engineering*, vol. 10, 2 vols., no. 2, pp. 72–81, 2017.
[90] A. Asgharzadeh Shishavan, “Bifacial photovoltaic (PV) system performance modeling utilizing ray tracing,” Doctor of Philosophy, University of Iowa, 2019.
[91] E. Lorenzo, M. Pérez, A. Ezpeleta, and J. Acedo, “Design of tracking photovoltaic systems with a single vertical axis: SINGLE-AXIS TRACKING PV SYSTEMS,” *Prog. Photovolt: Res. Appl.*, vol. 10, no. 8, pp. 533–543, Dec. 2002, doi: 10.1002/pip.442.
[92] V. Abbaraju and A. Daly, “Optimizing Your Energy Yield,” *NEXTracker*, Jun. 2018. https://www.nextracker.com/2018/06/white-paper-optimizing-your-energy-yield/.
[93] N. A. Kelly and T. L. Gibson, “Increasing the solar photovoltaic energy capture on sunny and cloudy days,” *Solar Energy*, vol. 85, no. 1, pp. 111–125, Jan. 2011, doi: 10.1016/j.solener.2010.10.015.
[94] S. Ayala Pelaez, C. Deline, P. Greenberg, J. S. Stein, and R. K. Kostuk, “Model and Validation of Single-Axis Tracking With Bifacial PV,” *IEEE J. Photovoltaics*, vol. 9, no. 3, pp. 715–721, May 2019, doi: 10.1109/JPHOTOV.2019.2892872.
[95] S. Ayala Pelaez, C. Deline, J. S. Stein, B. Marion, K. Anderson, and M. Muller, “Effect of torque-tube parameters on rear-irradiance and rear-shading loss for bifacial PV performance on single-axis tracking systems,” 2019.
[96] J. Guerrero-Perez and J. N. Berbel, “BiTEC: How to simulate bifacial projects,” Jul. 2019.
[97] J. Crimmins, K. McIntosh, L. Creasy, and K. Lee, “Field testing meets modeling: validated data on bifacial solar performance,” *Array Technologies*, 2020. https://arraytechinc.com/field-testing-meets-modeling-white-paper/.
[98] A. Roedel and S. Upfill-Brown, “Designing for the wind,” *NEXTracker*, Sep. 2018. https://www.nextracker.com/2018/06/white-paper-designing-for-the-wind/.
[99] F. Bizzarri, G. Leotta, and A. D. Stefano, “La Silla PV plant as a utility- scale side-by-side test for innovative modules technologies,” Nov. 2017, pp. 1978–1982, [Online]. Available: http://www.eupvsec-proceedings.com/proceedings? paper=44211.
[100] J.-N. Jaubert, “LCOE-driven method for selection and layout optimization of albedo enhancer materials,” presented at the BifiPV Workshop, Amsterdam, NL, Sep. 2019.
[101] C. Deline, S. Ayala Peláez, B. Marion, B. Sekulic, M. Woodhouse, and J. S. Stein, “Bifacial Tracking Testbed at NREL,” presented at the BifiPV Workshop, Amsterdam, NL, Sep. 2019, [Online]. Available: http://npv-workshop.com/fileadmin/layout/images/bifiPV/presentations2019/bifiPV2019_POSTER_NREL_Deline.pdf.

[102] A. Asgharzadeh *et al.*, “A Benchmark and Validation of Bifacial PV Irradiance Models,” in *2019 IEEE 46th Photovoltaic Specialists Conference (PVSC)*, Chicago, IL, USA, Jun. 2019, pp. 3281–3287, doi: 10.1109/PVSC40753.2019.8981272.
[103] M. T. Patel, R. A. Vijayan, R. Asadpour, M. Varadharajaperumal, M. R. Khan, and M. A. Alam, “Temperature-dependent energy gain of bifacial PV farms: A global perspective,” *Applied Energy*, vol. 276, p. 115405, Oct. 2020, doi: 10.1016/j.apenergy.2020.115405.
[104] M. T. Patel, M. Ryyan Khan, A. Alnuaimi, O. Albadwawwi, J. J. John, and M. A. Alam, “Implications of Seasonal and Spatial Albedo Variation on the Energy Output of Bifacial Solar Farms: A Global Perspective,” in *2019 IEEE 46th Photovoltaic Specialists Conference (PVSC)*, Chicago, IL, USA, Jun. 2019, pp. 2264–2267, doi: 10.1109/PVSC40753.2019.8981163.
[105] B. Zhao, X. Sun, M. R. Khan, and M. A. Alam, “Online Simulation Tools for Global Photovoltaic Performance: Purdue University Meteorological Tool (PUMET) and Bifacial Module Calculator (PUB),” presented at the 7th World Conference on Photovoltaic Energy Conversion, 2018.
[106] W. F. Holmgren, C. W. Hansen, and M. A. Mikofski, “pvlib python: a python package for modeling solar energy systems,” *JOSS*, vol. 3, no. 29, p. 884, Sep. 2018, doi: 10.21105/joss.00884.
[107] J. S. Stein, W. F. Holmgren, J. Forbess, and C. W. Hansen, “Open source photovoltaic performance modeling functions for Matlab and Python,” presented at the 43rd photovoltaic specialists conference, Portland, OR, 2016.
[108] B. Haurwitz, “Insolation in Relation to Cloudiness and Cloud Density,” *Journal of Meteorology*, vol. 2, pp. 154–166, 1945.
[109] B. Haurwitz, “Insolation in Relation to Cloud Type,” *Journal of Meteorology*, vol. 3, pp. 123–124, 1946.
[110] J. S. Stein, C. W. Hansen, and M. J. Reno, “Global horizontal irradiance clear sky models: implementation and analysis.,” SAND2012-2389, 1039404, Mar. 2012. doi: 10.2172/1039404.
[111] A. Mermoud and B. Wittmer, *Pvsyst User’s Manual*. PVSyst SA, 2014.
[112] Horowitz *et al.*, “An analysis of the cost and performance of photovoltaic systems as a function of module area (No. NREL/TP-6A20-67006),” *National Renewable Energy Lab (NREL)*, 2017.
[113] Patel *et al.*, “A worldwide cost-based design and optimization of tilted bifacial solar farms,” *Applied Energy*, vol. 247, pp. 467–479, 2019.
[114] J. S. Stein, L. Burnham, and M. Lave, “Performance Results for the Prism Solar Installation at the New Mexico Regional Test Center: Field Data from February 15 - August 15, 2016,” 2017.
[115] Khan *et al.*, “Vertical bifacial solar farms: Physics, design, and global optimization,” *Applied energy*, vol. 206, pp. 240–248, 2017.
[116] Khan *et al.*, “Ground sculpting to enhance energy yield of vertical bifacial solar farms,” *Applied energy*, vol. 241, pp. 592–598, 2019.
[117] T. Stoffel and A. Andreas, *NREL Solar Radiation Research Laboratory (SRRL): Baseline Measurement System (BMS); Golden, Colorado (Data)*. National Renewable Energy Lab (NREL), Golden, CO, US, 1981.
[118] S. Ayala Pelaez and C. Deline, “Bifacial PV test-bed irradiance measurements.” National Renewable Energy Laboratory, 2019, doi: 10.7799/1578176.
[119] S. Ayala Pelaez and C. Deline, “BEST Field Data.” DuraMAT Datahub, 2020.
[120] J. A. Duffie and W. A. Beckman, *Solar engineering of thermal processes / John A. Duffie, William A. Beckman*, 4th ed. Hoboken: John Wiley, 2013.
[121] S. Ayala Pelaez and C. Deline, “bifacial _ radiance: a python package for modeling bifacial solar photovoltaic systems,” *Journal of Open Source Software*, vol. 5, no. 2020, pp. 1–5, 1865, doi: 10.21105/joss.01865.
[122] C. Deline and S. Ayala, “bifacial_radiance.” Dec. 2017.
[123] G. J. Ward, “The RADIANCE lighting simulation and rendering system,” in *21st Annual Conference on Computer Graphics and Interactive Techniques*, 1994, pp. 459–472, doi: 10.1145/192161.192286.
[124] D. Robinson and A. Stone, “Irradiation modelling made simple: the cumulative sky approach and its applications,” in *PLEA Conference, Eindhoven, Netherlands*, 2004, pp. 19–22.
[125] S. Ayala Pelaez, C. Deline, P. Greenberg, J. S. Stein, and R. K. Kostuk, “Model and validation of single-axis tracking with bifacial PV,” *IEEE Journal of Photovoltaics*, vol. 9, no. 3, pp. 715–721, 2019, doi: 10.1109/JPHOTOV.2019.2892872.
[126] C. Deline, S. Ayala Pelaez, S. MacAlpine, and C. Olalla, “Estimating and parameterizing mismatch power loss in bifacial photovoltaic systems,” *Progress in Photovoltaics: Research and Applications*, pp. 1–13, 2020, doi: 10.1002/pip.3259.
[127] S. Ayala Pelaez, C. Deline, S. Macalpine, B. Marion, J. S. Stein, and R. K. Kostuk, “Comparison of bifacial solar irradiance model predictions with field validation,” *IEEE Journal of Photovoltaics*, vol. 9, no. 1, pp. 82–88, 2019, doi: 10.1109/JPHOTOV.2018.2877000.
[128] B. Marion, “Numerical method for angle-of-incidence correction factors for diffuse radiation incident photovoltaic modules,” *Solar Energy*, vol. 147, pp. 344–348, 2017.
[129] NREL, “BifacialVF,” 2020, [Online]. Available: http://github.com/NREL/bifacialvf.
[130] R. Perez, P. Ineichen, R. Seals, J. Michalsky, and R. Stewart, “Modeling daylight availability and irradiance components from direct and global irradiance,” *Solar Energy*, vol. 44, no. 5, pp. 271–289, 1990, doi: 10.1016/0038-092X(90)90055-H.

[131] E. A. Sjerps-Koomen, E. A. Alsema, and W. C. Turkenburg, “A simple model for PV module reflection losses under field conditions,” *Solar Energy*, vol. 57, no. 6, pp. 421–432, Dec. 1996, doi: 10.1016/S0038-092X(96)00137-5.
[132] M. Chiodetti, J. Kang, C. Reise, and A. Lindsay, “Predicting Yields of Bifacial PV Power Plants - What Accuracy is Possible?” 2018.
[133] M. Chiodetti, O. Rhazi, E. Boyere, P. Dupeyrat, M. Bila, and G. Terrom, “A ray-tracing based 3D tool for accurate prediction of PV plants yield,” 2019.
[134] P. Gilman, “SAM Photovoltaic Model Technical Reference Update,” *National Renewable Energy Laboratory, NREL P-6A20-64102*, vol. 3, no. 1, pp. 1–93, 2018, doi: NREL/TP -6A20- 64102.
[135] N. DiOrio and C. Deline, “Bifacial simulation in SAM,” 2018.
[136] NREL, “bifacialVF.” GitHub, 2019.
[137] B. Marion *et al.*, “A practical irradiance model for bifacial PV modules,” in *44th IEEE Photovoltaic Specialists Conference (PVSC), Washington, DC.*, 2017, pp. 1537–1542, doi: 10.1109/PVSC.2017.8366263.
[138] S. Dubey, J. N. Sarvaiya, and B. Seshadri, “Temperature Dependent Photovoltaic (PV) Efficiency and Its 138Effect on PV Production in the World – A Review,” *Energy Procedia*, vol. 33, pp. 311–321, 2013, doi: 10.1016/j.egypro.2013.05.072.
[139] D. Chudinzow, J. Haas, G. Díaz-Ferrán, S. Moreno-Leiva, and L. Eltrop, “Simulating the energy yield of a bifacial photovoltaic power plant,” *Solar Energy*, vol. 183, pp. 812–822, May 2019, doi: 10.1016/j.solener.2019.03.071.
[140] D. Chudinzow, S. Nagel, J. Güsewell, and L. Eltrop, “Vertical bifacial photovoltaics - A complementary technology for the European electricity supply?” *Applied Energy*, vol. 264, p. 114782, 2020, doi: 10.1016/j.apenergy.2020.114782.
[141] D. Chudinzow, M. Klenk, and L. Eltrop, “Impact of field design and location on the techno-economic performance of fixed-tilt and single-axis tracked bifacial photovoltaic power plants,” *Solar Energy*, vol. 207, pp. 564–578, Sep. 2020, doi: 10.1016/j.solener.2020.06.096.
[142] A. Mermoud and B. Wittmer, “Bifacial shed simulation with PVSyst,” *4th Bifi PV Workshop, Konstanz, Germany*, 2017.
[143] B. Wittmer and A. Mermoud, “Yield simulations for horizontal axis trackers with bifacial PV modules in PVSyst,” 2018.
[144] I. T. Horvath *et al.*, “Next Generation Tools for Accurate Energy Yield Estimation of Bifacial PV Systems – Best Practices, Improvements and Challenges,” *36th European Photovoltaic Solar Energy Conference and Exhibition; 1261-1265*, p. 5 pages, 4854 kb, 2019, doi: 10.4229/EUPVSEC20192019-5DP.2.2.
[145] I. T. Horváth *et al.*, “Photovoltaic energy yield modelling under desert and moderate climates: What-if exploration of different cell technologies,” *Solar Energy*, vol. 173, pp. 728–739, Oct. 2018, doi: 10.1016/j.solener.2018.07.079.
[146] J. Mardaljevic, “Daylight simulation: validation, sky models and daylight coefficients,” De Montfort University, Leicester, 2000.
[147] R. Perez, R. Seals, and J. Michalsky, “All-weather model for sky luminance distribution—Preliminary configuration and validation,” *Solar Energy*, vol. 50, no. 3, pp. 235–245, Mar. 1993, doi: 10.1016/0038-092X(93)90017-I.
[148] N. Jones and C. Reinhart, “Accelerad | Daylighting Simulation on the GPU,” 2020. https://nljones.github.io/Accelerad/.
[149] M. R. Lewis *et al.*, “Impact of bifacial photovoltaic cell characteristics on module energy yield in high-latitude locations (Conference Presentation),” in *Physics, Simulation, and Photonic Engineering of Photovoltaic Devices IX*, San Francisco, United States, Mar. 2020, p. 31, doi: 10.1117/12.2546583.
[150] M. R. Lewis *et al.*, “Angular Dependence of Textured Bifacial Silicon Heterojunction Solar Cells for High Latitudes,” in *2019 IEEE 46th Photovoltaic Specialists Conference (PVSC)*, Chicago, IL, USA, Jun. 2019, pp. 1919–1923, doi: 10.1109/PVSC40753.2019.8980857.
[151] A. C. J. Russell, C. E. Valdivia, M. R. Lewis, J. E. Haysom, and K. Hinzer, “Modelling Bifacial Solar Energy Yield for Single-Axis Tracked Systems with Racking,” 2019, pp. 61–62.
[152] A. C. J. Russell, C. E. Valdivia, M. R. Lewis, J. E. Haysom, and K. Hinzer, “Modelling Energy Yield Including Rack Shading for Single-Axis Tracked Bifacial Solar Panels,” in *2019 Photonics North (PN)*, Quebec City, QC, Canada, May 2019, pp. 1–1, doi: 10.1109/PN.2019.8819539.
[153] C. E. Valdivia *et al.*, “Bifacial Photovoltaic Module Energy Yield Calculation and Analysis,” in *2017 IEEE 44th Photovoltaic Specialist Conference (PVSC)*, Washington, DC, Jun. 2017, pp. 1094–1099, doi: 10.1109/PVSC.2017.8366206.
[154] M. A. Mikofski, M. Lynn, J. Byrne, M. Hamer, A. Neubert, and J. Newmiller, “Accurate Performance Predictions of Large PV Systems with Shading using Submodule Mismatch Calculation,” in *2018 IEEE 7th World Conference on Photovoltaic Energy Conversion (WCPEC)*, 2018, pp. 3635–3639, doi: 10.1109/PVSC.2018.8547323.
[155] M. A. Anoma, D. Jacob, B. C. Bourne, J. A. Scholl, D. M. Riley, and C. W. Hansen, “View Factor Model and Validation for Bifacial PV and Diffuse Shade on Single-Axis Trackers,” in *2017 IEEE 44th Photovoltaic*

Specialist Conference (PVSC), Washington, DC, Jun. 2017, pp. 1549–1554, doi: 10.1109/PVSC.2017.8366704.
[156] D. Berrian, J. Libal, and S. Glunz, "MoBiDiG: simulations and LCOE," 2017.
[157] D. Berrian, J. Libal, M. Klenk, H. Nussbaumer, and R. Kopecek, "Performance of bifacial PV arrays with fixed tilt and horizontal single-axis tracking: Comparison of simulated and measured data," *IEEE Journal of Photovoltaics*, vol. 9, pp. 1583–1589, 2019, doi: 10.1109/JPHOTOV.2019.2924394.
[158] T. Capelle, F. Araya, F. Haffner, J. Sayritupac, and H. Colin, "A comparison of bifacial PV system modelling tools," in *6th BifiPV Workshop, Amsterdam, NL*, 2019, pp. 1–21.
[159] "SunPower, 'pvfactors,'" 2018. https://sunpower.github.io/pvfactors/.
[160] "Canadian Climate Normals 1981-2010 Station Data," *Environment and Climate Change Canada, Government of Canada*. https://climate.weather.gc.ca/climate_normals/.
[161] "IEC 60891: Photovoltaic devices – Procedures for temperature and irradiance corrections to measured I-V characteristics," International Electrotechnical Commission, 2009.
[162] J. Bonilla Castro, M. Herz, C. Monokroussos, and M. Schweiger, "Energy Yield Comparison between Bifacial and Monofacial PV Modules - Real-world measurements and validation with bifacial simulations," presented at the 35th EUPVSEC, Brussels, 2018.
[163] J. Bonilla Castro, "Energy Yield Comparison between Bifacial and Monofacial PV Modules," presented at the PV Module Forum 2019, TÜV Rheinland, Cologne, Germany, 2019.
[164] J. Saal, J. Bonilla Castro, and M. Schweiger, "Energy Yield Comparison between Bifacial and Monofacial PV Modules - Real World Measurements in Desert climate," presented at the 36th EU PVSEC, Marseille, 2019.
[165] J. Bonilla Castro and G. Friesen, "Photovoltaic Module Energy Yield Measurements: Existing Approaches and Best Practice," presented at the IEA PVPS Task 13 Webinar, Mar. 12, 2020.
[166] H. Nussbaumer *et al.*, "Accuracy of simulated data for bifacial systems with varying tilt angles and share of diffuse radiation," *Solar Energy*, vol. 197, pp. 6–21, Feb. 2020, doi: 10.1016/j.solener.2019.12.071.
[167] D. Berrian, J. Libal, M. Klenk, H. Nussbaumer, and R. Kopecek, "Performance of Bifacial PV Arrays With Fixed Tilt and Horizontal Single-Axis Tracking: Comparison of Simulated and Measured Data," *IEEE J. Photovoltaics*, vol. 9, no. 6, pp. 1583–1589, Nov. 2019, doi: 10.1109/JPHOTOV.2019.2924394.
[168] G. Friesen, W. Herrmann, G. Belluardo, and B. Herteleer, *Photovoltaic module energy yield measurements: existing approaches and best practice: International Energy Agency Photovoltaic Power Systems Programme: IEA PVPS Task 13, Subtask 3: report IEA-PVPS T13-12:2018*. Paris: International Energy Agency IEA, 2018.
[169] R. R. Molinero, G. Friesen, and M. Caccivio, "FInal Report ENHANCE - Next Generation Photovoltaic Performance," Swiss Federal Office of Energy SFOE, 2019. [Online]. Available: https://www.aramis.admin.ch/Default.aspx?DocumentID=64923.
[170] S. Ayala Pelaez, "BEST Field Data," 2020. https://datahub.duramat.org/dataset/best-field-data.
[171] A. Granlund, J. Narvesjö, and A. M. Petersson, "The Influence of Module Tilt on Snow Shadowing of Frameless Bifacial Modules," *36th European Photovoltaic Solar Energy Conference and Exhibition; 1646-1650*, p. 5 pages, 7619 kb, 2019, doi: 10.4229/EUPVSEC20192019-5CV.4.36.
[172] N. Riedel-Lyngskær *et al.*, "Comparison of Large Scale Bifacial PV Test Field Performance to Commercially Available Software, Research-Based and Open Source Tools," presented at the European Photovoltaic Solar Energy Conference and Exhibition (EUPVSEC), 2020.
[173] N. Riedel-Lyngskær, M. Petit, D. Berrian, P. Poulsen, J. Libal, and M. Jalobsen, "A Spatial Irradiance Map Measured on the Rear Side of a Utility-Scale Horizontal Single-axis Tracker with Validation using Open Source Tools," presented at the IEEE 47th Photovoltaic Specialists Conference (PVSC), 2020.
[174] S. Ranta, J. S. Stein, H. Huerta, A. Heinonen, and E. Whitney, "Self-consumption rate achieved by the bifacial east-west vertical PV system compared to the conventional south facing system in nordic conditions," presented at the EU PVSEC, Marseille, France, 2019.

Technology Collaboration Programme
by iea

ISBN 978-3-907281-03-1